Inter-atomic/molecular Decay in Doped Helium Nanodroplets Induced by Extreme-ultraviolet Radiation

A thesis

Submitted in partial fulfilment of the requirements

Of the degree of

Doctor of Philosophy

By

Suddhasattwa Mandal

Registration ID : 20153413

INDIAN INSTITUTE OF SCIENCE EDUCATION AND RESEARCH PUNE

2023

To

my parents

and

teachers

CERTIFICATE

We certify that the work incorporated in the thesis entitled, 'Inter-atomic/molecular Decay in Doped Helium Nanodroplets Induced by Extreme-ultraviolet Radiation', submitted by Suddhasattwa Mandal was carried out by the candidate, under our supervision. The work presented here or any part of it has not been included in any other thesis submitted previously for the award of any degree or diploma from any other University or institution.

Date: January 9, 2023

Dr. Bhas Bapat (Thesis Supervisor),
Professor, Department of Physics,
Indian Institute of Science Education and Research (IISER) Pune,
Pune, India

Dr. Vandana Sharma (Thesis Co-supervisor),
Associate Professor, Department of Physics,
Indian Institute of Technology (IIT) Hyderabad,
Kandi, India

DECLARATION

I, Suddhasattwa Mandal, declare that the work presented in the thesis entitled, 'Inter-atomic/molecular Decay in Doped Helium Nanodroplets Induced by Extreme-ultraviolet Radiation', is my own and is original, and where others' ideas have been included; I have adequately cited and referenced the original sources. I solely own the responsibility of the originality of the entire content. This work (in part or in full) has not been submitted to any University or institution for the award of any degree or diploma. I also declare that I have adhered to all principles of academic honesty and integrity and have not misrepresented or fabricated or falsified any idea/data/fact/source in my submission. I understand that violation of the above will be cause for disciplinary action by the Institute and can also evoke penal action from the sources which have thus not been properly cited or from whom proper permission has not been taken when needed.

Date: January 9, 2023

(Suddhasattwa Mandal)

ACKNOWLEDGEMENTS

First and foremost, I would like to express my gratitude towards my thesis supervisor, Dr. Bhas Bapat, and co-supervisor, Dr. Vandana Sharma. I am immensely enriched by their guidance and constant support. I have extensively learnt about the basics of experimental atomic molecular research, as well as effective science communication skills from them. They have tremendously helped me in shaping the research topic, presented in this thesis. I would also like to thank them for allowing me to pursue my research work at Elettra Synchrotron Facility in Italy, as well as for giving me opportunities to participate and learn from several other experiments with my lab-mates and colleagues at Tata Institute of Fundamental Research (TIFR), Hyderabad, and Inter University Accelerator Center (IUAC), Delhi. Here, I would also like to thank Dr. M Krishnamurthy for arranging my long-term stay at TIFR, for giving me access to his laboratory and for his research inputs.

I am deeply indebted to Dr. Sivarama Krishnan and Dr. Marcel Mudrich for introducing me to helium nanodroplets spectroscopy. I have learnt a lot about the experimental strategies in this topic from multiple discussions with them. I thank Dr. Vandana Sharma and Dr. Sivarama Krishnan for arranging the financial support for my multiple experimental visits to Italy from Department of Science and Technology, India, and Elettra Synchrotron Facility, Italy. I thank all the people who helped me in conducting these experiments, specially to Dr. Robert Richter, Dr. Ram Gopal, and Dr. Marcelo Coreno. I would like to acknowledge Dr. Robert Richter for his invaluable support with the experimental setup and scientific insights. Running these experiments continuously during beamtimes would not have been possible without the help from Dr. Mykola Shcherbinin, Dr. Ltaief Ben Ltaief, Hemkumar Srinivas and Dr. Alessandro D'Elia.

I cherish the time spent and many fruitful discussions with my lab-mates and colleagues, Arnab, Deepak and Sumit at IISER Pune, SoubhikDa, AnganaDi, Sanket, and Abhishek at TIFR Hyderabad. I am grateful for getting the company of Anweshi, Projjwal, Banibrata, BhanuDa, and Arijeet among others who created a home away from home for me.

Lastly, I would like to thank my parents for their love and continuous support in my journey and for giving me the freedom to choose my path.

Contents

Abstract **xv**

1 Introduction **1**

1.1 Electronic decays in isolated atom or molecule 4

1.1.1 Decay of outer valence vacancy 4

1.1.2 Decay of inner valence vacancy 7

1.1.3 Decay of core shell vacancy 10

1.2 Electronic decays in loosely-bound cluster 12

1.2.1 Resonant energy transfer 12

1.2.2 Penning ionization 14

1.2.3 Charge transfer 15

1.2.4 Inter-atomic/molecular Coulombic decay 16

1.2.5 Electron transfer mediated decay 24

1.3 Probing inter-atomic/molecular decay 27

1.4 The model system - doped helium nanodroplets 30

1.4.1 Outline and motivations 32

2 Experimental Methodology **37**

2.1 Generating clusters of atoms and molecules 37

2.1.1 Supersonic expansion in free-jet 37

2.1.2 Conditions for rare gas clusterization 38

2.1.3 Creating helium nanodroplets 39

2.2 Doping of foreign atoms and molecules 44

2.3 Synchrotron radiation 47

2.4 Co-axial electron and ion spectrometer 51

2.4.1 Coincident detection of electrons and ions 55
2.5 Data analysis 61
2.5.1 Time of flight data 61
2.5.2 Velocity map imaging data 62

3 Acetylene Doped Helium Nanodroplets 67
3.1 Experimental Methods 67
3.1.1 Doping process 67
3.1.2 Spectrometer configuration 69
3.2 Dopant ionization at different photon energies 69
3.2.1 Inter-atomic/molecular decays 69
3.2.2 Interior localization of acetylene 72
3.2.3 Product ions 73
3.3 Dopant ionization at $n = 2$ droplet excitation band 75
3.3.1 Penning ionization electron spectra 77
3.3.2 Clusterizations of neutral and ionic dopants 81
3.3.3 Structures of dopant clusters 82
3.4 Dopant ionization upon droplet autoionization 84
3.4.1 Competing Penning ionization from $n = 4$ droplet excitation 84
3.5 Dopant ionization upon droplet direct ionization 88
3.6 Summary 89

4 Heavy Alkali Doped Helium Nanodroplets 91
4.1 Experimental Methods 91
4.1.1 Doping process 91
4.1.2 Spectrometer configurations 92
4.2 Dopant ionization at different photon energies 93
4.2.1 Inter-atomic/molecular decays 93
4.2.2 Surface localization of alkali 94
4.2.3 Product ions 95
4.2.4 Degree of ionization of the dopants 96
4.2.5 Identifying single and double ionization processes 98
4.3 Dopant ionization upon droplet excitation 99

4.3.1 Long-range interatomic Coulombic decay 100
4.3.2 Short-range interatomic Coulombic decay 101
4.3.3 Double inter-atomic/molecular Coulombic decay 104
4.3.4 Cascaded inter-atomic/molecular Coulombic decay 108
4.4 Dopant ionization following droplet direct ionization 113
4.4.1 Electron transfer mediated decay 115
4.4.2 Charge transfer followed by interatomic Coulombic decay 117
4.5 Discussion on dopant double ionization 122
4.6 Summary 127

Summary and Future Prospects **129**
4.7 Summary 129
4.8 Future Prospects 131

Publications **133**

Bibliography **137**

Abstract

This thesis concerns with experimental investigations of *inter*-atomic/molecular decays in nanometer-sized van der Waals clusters of helium (He), or in He nanodroplets, doped with a few foreign atoms and molecules. Acetylene (C_2H_2) molecules which are embedded inside, and heavy alkali atoms, rubidium (Rb) and cesium (Cs), which attach to the surface of the host droplet, are chosen as dopants. The doped He droplet is perturbed by tunable extreme ultraviolet (EUV) synchrotron radiation, wherein the host is resonantly photoexcited to different droplet excitation bands derived from He* ($1s\ np,\ n \geq 2$) (> 21 eV), as well as photoionized above the autoionization threshold (~ 23 eV). Insights into different dopant ionization processes, induced by both the excited and ionized host, are gained by measuring kinetic energies of the ejected electrons and product-ions in coincidence using a co-axial time of flight and velocity map imaging spectrometer.

In case of C_2H_2 doping, upon resonant photoexcitation to the first droplet excitation band ($n = 2$) at 21.6 eV, C_2H_2 oligomers are found to be singly ionized via interatomic/molecular Coulombic decay (ICD), conventionally known as Penning ionization, from $1s2p\ ^1P$, as well as from internally relaxed metastable $1s2s\ ^{3,1}S$, He* states. The loosely-bound structures of embedded neutral C_2H_2 oligomers, and the formation dynamics of oligomer ions are revealed from the dopant-ion correlated Penning ionization electron spectroscopy (PIES). This establishes PIES as effective experimental technique for investigating the structures of dopant oligomers which can be easily created inside He nanodroplets. Moreover, upon photoexcitation to $n = 4$ droplet excitation band at 23.9 eV, Penning ionization channels leading to highly excited $C_2H_2^+$ ($C^2\Sigma_g^+$, 23.33 eV and $D^2\Sigma_g^+$, 23.53 eV) due to relaxation of $1s4p\ ^1P$ He* state are identified. These newly discovered Penning channels compete with the known dominant dopant charge transfer (CT) ionization channel following autoionization of the host droplet. This observation opens up

possibilities to probe higher lying excited states of various dopant-ions through Penning ionization following the photoexcitation to $n = 4$ droplet excitation band, which are not accessible upon photoexcitation to $n = 2$ droplet excitation band, in similar system.

In case of Rb and Cs dopants, both single and double ionization are observed in the dopants following photoexcitation to the first droplet excitation band and direct photoionization of the host. For double ionization of the alkali dimers, attached to the surface of the host cluster, novel *inter*-atomic/molecular decays through intermediate inner valence ionization of the alkali atoms are reported. The inner valence p-shell of one of the alkali dimer constituents is ionized through resonant ICD from He^* ($1s2s\ ^{3,1}S$, and $1s2p\ ^1P$), and via CT ionization from He_2^+, following excitation and ionization of the host by the incident photon, respectively. This leads to an excited alkali dimer cation which decays via a subsequent ICD resulting in a doubly ionized dimer, that eventually undergoes Coulomb explosion. These two-step double ionization processes, cascaded-ICD and CT followed by ICD, compete with the known one-step ionization mechanisms, double-ICD and electron transfer mediated decay (ETMD) leading to the same product-ions, respectively.

Thus, in this thesis, *inter*-atomic/molecular ionization processes in two different types dopants following photoexcitation and ionization of the host He nanodroplets are identified, wherein novel single and double ionization channels are presented, while PIES is demonstrated to be a useful tool to probe the structure of embedded dopant oligomer in the host cluster.

Chapter 1

Introduction

Almost till the end of nineteenth century, all the matter around us were known to be constituted from the smallest building block, atoms. Later with the discoveries of subatomic particles, we realised that atoms are actually made up of electrons, protons and neutrons, which are arranged in a particular way. At the centre of the atom, protons and neutrons form a positively charged nucleus and the negatively charged electrons revolve around the nucleus in particular electronic orbitals. Equal number of electrons and protons makes the atom neutral, while the number of these particles in an atom decides its physical and chemical properties. Now, when two or more atoms come closer, a few electrons from the outer orbitals of each atom can be shared in such a way that the nuclei and the electron-cloud around them create an equilibrium stable geometry, to form a molecule. The formation of molecules is also interpreted in terms of creation of chemical bonds between the atoms, which are of two kinds: covalent [1] and ionic [2, 3] bonds. For atoms with similar electronegativities, covalent bonds are usually formed between the neighbours through creation of shared electron pairs. In each pair, electrons from neighbouring atoms contribute. Whereas, for atoms with largely different electronegativities, usually a certain number of electrons are transferred between them. This makes opposite polarities between the neighbouring atoms, which are then electrostatically attracted towards each other to form ionic bonds. Atoms aggregated in these fashions have low interatomic separations of a few angstroms and high binding energies up to a few electronvolts (eV) per bond. Thus, the correlations between the valence electrons of neighbouring atoms in a molecule are very strong, while the core-shell electrons are usually localized close to each

nucleus. Note that, this simplistic view on bond formation allowed chemist to estimate the strength of different chemical bonds. However, from the point of view of quantum mechanics, bonds formed between atoms are explained in terms of more sophisticated theories, such as, molecular orbital theory [4], where both covalent and ionic natures exist in various degrees.

Over the years, investigating the molecular structure, bond formation dynamics as well as multi-electron correlations within a molecule, using external perturbations such as interaction with light or the impact of charged particles, has been an intriguing subject of research. Due to the perturbation, molecule undergoes structural changes in its energetic ground state configuration by absorbing energy from the external agent. Consequently, the absorbed energy is shared between the electronic and nuclear degrees of freedom. Electronically, some of the electrons can get excited to the high-energy orbitals leaving holes in their previously occupied ones, or if energy permits, they can even go to the continuum which is the process of ionization. Typically for light-matter interactions, these transitions from the ground to excited electronic states are Franck-Condon transitions, wherein the transitions take place instantaneously without any change in the nuclei positions within the molecule. The molecule can go to different vibrational and rotational (ro-vibronic) states as compared to its ground ro-vibronic energy level. Depending on which excited state the molecule is populated, de-excitation occurs in different excited state manifolds where nuclear dynamics play important role. Following the excitation, due to the instability of these excited states, the molecule relaxes to low energy states by emitting photons and/or electrons, as well as the molecule can undergo structural rearrangement or even fragmentation. Thus, the relaxation energy is distributed among the energies of emitted photons, the kinetic energies of electrons, fragment -ions and -neutrals, as well as among their internal energies. One can gain knowledge about the structure of the molecule, as well as about its response to the external perturbation by experimentally measuring these energies. Both the relaxation mechanism and the associated time-scale are important to fully understand the underlying decay dynamics. Depending on the energy imparted by the external agent, single to multi electron excitations occur in the system, and the system is excited to different excited states. For instance, in an isolated atom or molecule wherein *intra*-atomic/molecular multi-electron correlations are pertinent, a single electron excitation from the valence orbital usually decays radiatively on

a slower timescale (∼nanosecond), while a single electron excitation from the core shell leads to faster relaxation processes, such as, X-ray emission and Auger decay [5, 6], occurring on a faster timescale (∼femtosecond). Whereas, a single electron excitation from the inner valence orbital can decay via slow radiative photoemission as well as via fast autoionization process depending on the participating energy levels. Note that, the radiative decay rate depends on the excited and decaying state properties. However, typically the higher the energy level of the excited state is compared to that of the decaying state, the faster radiative decay process becomes. Note that, non-radiative decay processes, such as, internal conversions in isolated molecules are much faster decay processes. For multi electron excitation in an isolated atom or molecule by external perturbation, the more complex relaxation processes can be observed.

However, there exists a different type of bonding, arising due to weak van der Waals forces between all atoms and molecules, whose binding energy per bond is only a few meV, unlike the covalent and ionic bonds existing in a molecule. The origin of this van der Waals force is the polarization of one neutral atom or molecule, due to another one in the neighbourhood. Originally, it was thought that only atoms and molecules having permanent electric moments can induce such weakly-attractive forces [7, 8, 9]. It was later revealed that rapidly fluctuating transient electric moments in the neighbouring atoms or molecules are also responsible for these van der Waals forces [10]. Naturally, atoms and molecules, clustered through the van der Waals forces, have large inter-atomic/molecular separations. Thus, correlations between electrons from the neighbouring entities are relatively weak in this case, compared to the same in a molecule. In spite of that, electronic excitation or ionization in one of the constituent atoms or molecules in these loosely-bound clusters, can decay through excitation or ionization in the neighbour. Furthermore, these *inter*-atomic/molecular relaxation processes are often found to be highly efficient compared to the *intra*-atomic/molecular counterpart in weakly-bound aggregate, following a local electronic excitation in a constituent atom or molecule. Since these van der Waals aggregates are ubiquitous in biological and astrophysical environments, understanding how external perturbations, such as, photons or energetic charged particles, impact these systems through propagation of an induced local perturbation to its neighbourhood is of fundamental interest.

The focus of this thesis is to experimentally investigate *inter*-atomic/molecular elec-

tronic decays in loosely-bound nanometer-sized van der Waals clusters of helium (He), commonly known as He nanodroplets, doped with a few foreign atoms or molecules, when the host droplets are resonantly photoexcited or photoionized by extreme ultra-violet (EUV) photons. In this chapter, first, correlated electronic decays in an isolated atom or molecule are discussed, when a single electron is excited from different orbitals under the influence of external perturbation. The knowledge of underlying *intra*-atomic/molecular processes, occurring at the individual atomic or molecular level, should help us to further understand the correlated decays in the loosely-bound clusters of atoms and molecules. Then, relevant *inter*-atomic/molecular processes and corresponding experimental techniques to investigate them are presented. Then, the model system of doped He nanodroplets, along with the choice of dopants, are presented. Finally, the outline and motivations of this investigation are laid out.

1.1 Electronic decays in isolated atom or molecule

Multi-electron correlations are present between different electronic orbitals in a neutral atom or molecule. Thus, disturbing any electron in the system from its stable ground state configuration will affect rest of system. In this section, lets look into the electronic decays in an isolated atom or molecule upon creation of an electronic vacancy in the valence or core orbital by the external perturbation. This should lay the ground to compare the competing *inter*-atomic/molecular processes, relevant in loosely-bound clusters, as discussed later in section 1.2.

1.1.1 Decay of outer valence vacancy

If a vacancy is created in the outer most electronic orbital or the outer valence (ov) orbital of an isolated atom or molecule (A), either by electronic excitation to an excited orbital (np), or by direct ionization, the created vacancy (ov^{-1}) can be directly filled in two possible pathways: a) by de-excitation of the electron from the excited orbital to the initial vacancy in case of an excited metastable atom or molecule ($A^*(ov^{-1}\ np)$), and b) by capturing an external electron from the environment to the initial vacancy in case of

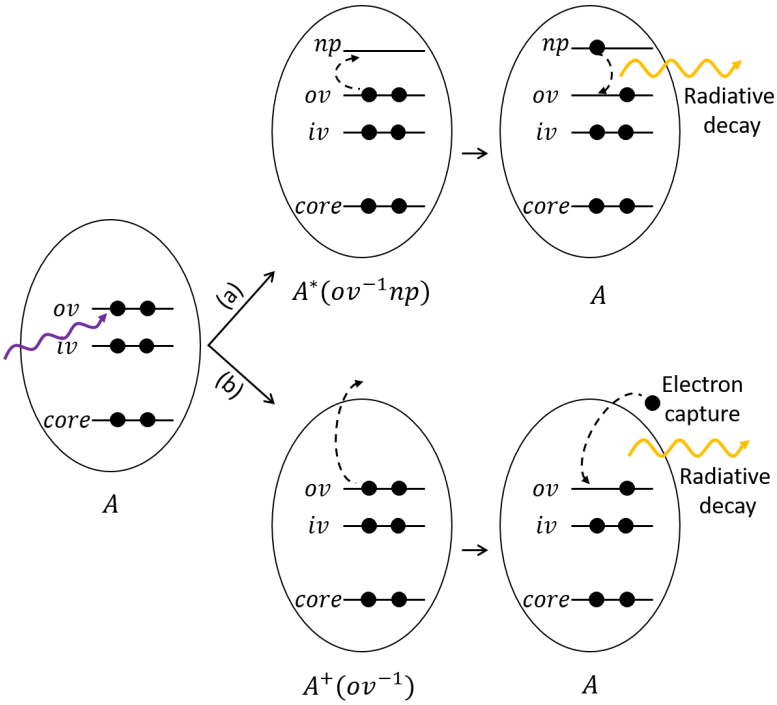

Figure 1.1: Schematic of outer valence (ov) excitation and relaxation processes where the corresponding vacancy is directly filled in an isolated atom or molecule (A). Pathway (a) shows the excitation of the outer valence electron to an excited orbital (np) and subsequent de-excitation of the same to the ground state, while pathway (b) shows direct ionization of the outer valence electron and capture of an external electron for relaxation of the corresponding vacancy in $\mathrm{A}^{+}(ov^{-1})$. In both the decay processes, the excess energies released are insufficient to further ionize the system, thus the corresponding decay processes are radiative in nature.

ionized species ($\mathrm{A}^{+}(ov^{-1})$) (see Fig. 1.1), as shown below.

$$\mathrm{A}^{*}(ov^{-1}\ np) \rightarrow \mathrm{A} + \Delta E \tag{1.1}$$

and

$$\mathrm{A}^{+}(ov^{-1}) + e^{-} \rightarrow \mathrm{A} + \Delta E \tag{1.2}$$

In both these cases, the excess energies (ΔE) are equal to the differences between the final and initial state energies as follows:

$$\Delta E = E(\mathrm{A}^{*}(ov^{-1}\ np)) - E(\mathrm{A}) \tag{1.3}$$

and

$$\Delta E = E(\mathrm{A}^{+}(ov^{-1})) - E(\mathrm{A}) \tag{1.4}$$

where, $E(\mathrm{A})$, $E(\mathrm{A}^*(ov^{-1}\ np))$, and $E(\mathrm{A}^+(ov^{-1}))$ are the energies of A, $\mathrm{A}^*(ov^{-1}\ np))$ and $\mathrm{A}^+(ov^{-1})$, respectively. Thus, in the electron capture process, the excess energy released is equal to the ionization energy of A which is equal to $E(\mathrm{A}^+(ov^{-1}))$ minus $E(\mathrm{A})$, whereas in case of direct de-excitation of the excited state, the excess energy released is less than the ionization energy, since $E(\mathrm{A}^*(ov^{-1}\ np))$ is always less than $E(\mathrm{A}^+(ov^{-1}))$. This implies that in both the cases, the released excess energies (ΔE) are insufficient to further ionize the system, through autoionization, as these final states are not energetically accessible in these decays of outer valence vacancy. Therefore, the underlying decay processes here are usually radiative in nature, wherein the excess energy is released by emission of a photon, see below.

$$\mathrm{A}^*(r) \rightarrow \mathrm{A} + h\nu \tag{1.5}$$

and

$$\mathrm{A}^+(ov^{-1}) + e^- \rightarrow \mathrm{A} + h\nu \tag{1.6}$$

The radiative relaxation of the outer valence excited atom or molecule usually takes place on a slower timescale ($\sim$ nanosecond), depending on the lifetimes of the excited state. Whereas, the electron capture process, which is similar to time reversal photoionization, is a much faster relaxation mechanism occurring in attosecond timescale.

Note that, here only the single step relaxation processes are presented following the excitation or ionization of an outer valence electron where the de-excitation or electron capture directly leads to ground state atom or molecule. This is to show that the maximum energies released in these relaxations are insufficient for autoionization of the system, since the autoionizing states are energetically inaccessible through excitation of an outer valence electron. However, there can be multi step radiative and non-radiative de-excitation processes involved for metastable outer valence excited system, wherein the initial outer valence vacancy can be filled through relaxations to multiple lower lying excited states. In these cases, the energy released in each step is lower than what are shown by equation 1.3. Similarly for an outer valence ionized system, an electron from the environment can be captured by a higher lying excited orbital than by the orbital where the initial vacancy is created. Thus the energy released in the electron capture process can be lower than what is presented in equation 1.4. Subsequently, the metastable excited atom or molecule following the electron capture can undergo single or multi step de-excitations.

1.1.2 Decay of inner valence vacancy

An inner valence vacancy (iv^{-1}) created due to ionization by the external perturbation in an isolated atom or molecule (A) can be filled by both radiative decays and decay via further ionization. Fig.1.2 i) schematically shows these relaxation pathways, where pathway a) presents the following radiative decay mechanisms.

$$A^{+*}(iv^{-1}) \rightarrow A^{+}(ov^{-1}) + \Delta E \tag{1.7}$$

and,

$$A^{+*}(iv^{-1}) \rightarrow A^{+*}(ov^{-2}\ np) + \Delta E \tag{1.8}$$

where, in the first process an outer valence electron fills the vacancy in the inner valence orbital, while in the second process due to transfer of the outer valence electron to the initial vacancy, another electron from the outer valence orbital is excited to a higher lying orbital (np). The excess energies (ΔE) released by photoemissions in these processes are shown below for the first and second process, respectively.

$$\Delta E = E(A^{+*}(iv^{-1})) - E(A^{+}(ov^{-1})) \tag{1.9}$$

and,

$$\Delta E = E(A^{+*}(iv^{-1})) - E(A^{+*}(ov^{-2}\ np)) \tag{1.10}$$

where, $E(A^{+*}(iv^{-1}))$, $E(A^{+}(ov^{-1}))$ and $E(A^{+*}(ov^{-2}\ np))$ are the energies of $A^{+*}(iv^{-1})$, $A^{+}(ov^{-1})$ and $A^{+*}(ov^{-2}\ np)$ states, respectively. The energy of the $A^{+*}(ov^{-2}\ np)$ state lies above the energy level of $A^{+}(ov^{-1})$, see Fig.1.2 ii) where relevant energy levels of A are depicted. Thus, the excess energy released in the second process is lower than the same from the first process.

In Fig. 1.2 i), pathway (b) shows the decay through further ionization from the outer valence shell due to transfer of an outer valence electron to the inner valence vacancy, also see below.

$$A^{+*}(iv^{-1}) \rightarrow A^{2+}(ov^{-2}) + e^{-} \tag{1.11}$$

This decay leading to further ionization can occur when the energy level of $A^{+*}(iv^{-1})$ is

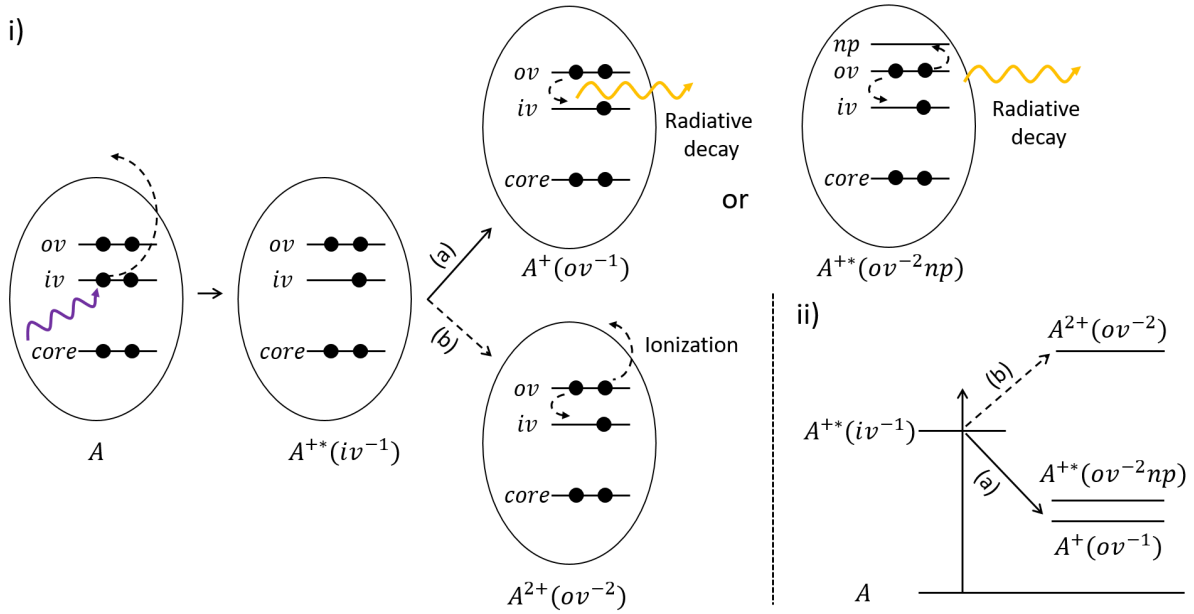

Figure 1.2: i) Schematic of inner valence (iv) ionization and decay of the corresponding vacancy in an isolated atom or molecule (A). Pathway (a) shows radiative decays upon transfer of an outer valence (ov) electron to the inner valence vacancy (iv^{-1}), while pathway (b) shows ionization of an outer valence electron following the transfer of an outer valence electron to the inner valence vacancy. ii) The relevant energy levels of A for the processes (a) and (b) to occur.

higher than that of the decaying state, $\mathrm{A}^{2+}(ov^{-2})$, *i.e.*,

$$E(\mathrm{A}^{+*}(iv^{-1})) > E(\mathrm{A}^{2+}(ov^{-2})) \tag{1.12}$$

However, it is very unlikely that the energy level of an inner valence ionized atom or molecule is higher than the energy level of the dicationic state of the same, see Fig. 1.2 ii). Therefore, autoionization leading to doubly ionized state, following inner valence ionization, is usually energetically forbidden in an isolated atom or molecule.

Furthermore, other than direct ionization, an inner valence vacancy in an isolated atom or molecule (A) can also be created by excitation of an inner valence (iv) electron to a higher lying orbital (np). The corresponding excitation and de-excitation processes are presented in Fig. 1.3 i), where pathway (a) shows the radiative relaxation of the initially excited electron from the excited orbital (np) to the inner valence vacancy (iv^{-1}), see below.

$$\mathrm{A}^{*}(iv^{-1}\ np) \rightarrow \mathrm{A} + \Delta E \tag{1.13}$$

This de-excitation of initially excited electron from np orbital to the inner valence vacancy

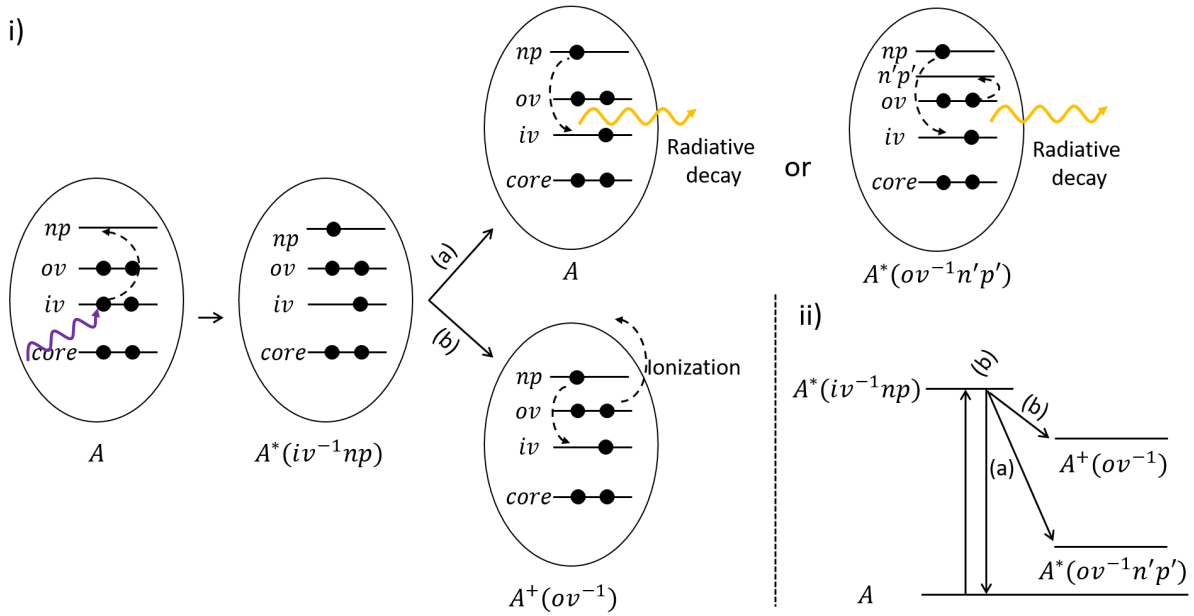

Figure 1.3: i) Schematic of the excitation of an inner valence (iv) electron to the higher lying excited orbital (np), and corresponding de-excitation processes in an isolated atom or molecule (A). Pathway (a) shows radiative decay of the electron from the excited orbital (np) to the inner valence vacancy (iv^{-1}), while pathway (b) shows ionization of an outer valence (ov) electron following the transfer of the initially excited electron to the inner valence vacancy. ii) The relevant energy levels of A for the processes (a) and (b) to occur.

can also lead to excitation of an outer valence (ov) electron to an higher lying excited orbital ($n'p'$), see below.

$$\mathrm{A}^*(iv^{-1}\ np) \rightarrow \mathrm{A}^*(ov^{-1}\ n'p') + \Delta E \tag{1.14}$$

The excess energies (ΔE), as shown below, are released by photoemission in these processes.

$$\Delta E = E(\mathrm{A}^*(iv^{-1}\ np)) - E(\mathrm{A}) \tag{1.15}$$

and,

$$\Delta E = E(\mathrm{A}^*(iv^{-1}\ np)) - E(\mathrm{A}^*(ov^{-1}\ n'p')) \tag{1.16}$$

where, $E(\mathrm{A}^*(iv^{-1}\ np))$, $E(\mathrm{A})$ and $E(\mathrm{A}^*(ov^{-1}\ n'p'))$ are the energies of $\mathrm{A}^*(iv^{-1}\ np)$, A and $\mathrm{A}^*(ov^{-1}\ n'p')$ states, respectively. These radiative de-excitation processes are energetically accessible, since the energies of the final states are lower than that of the initial inner valence excited state, see Fig. 1.3 ii).

Moreover, unlike excitation from outer valence orbital, excitation from inner valence

orbital can result in ionization of another outer valence electron, see below.

$$\mathrm{A}^*(iv^{-1}\ np) \rightarrow \mathrm{A}^+(ov^{-1}) + e^- \tag{1.17}$$

This autoionization leading to cationic state, shown in pathway (b) of Fig. 1.3 i), is energetically allowed, since the energy of the autoionizing final state ($\mathrm{A}^+(ov^{-1})$) is lower than that of the initial excited state ($\mathrm{A}^*(iv^{-1}\ np)$). The autoionizing electron carries the excess energy (ΔE), see below, as its kinetic energy.

$$\Delta E = E(\mathrm{A}^*(iv^{-1}\ np)) - E(\mathrm{A}^+(ov^{-1})) \tag{1.18}$$

The relevant energy levels of A for these de-excitation processes are presented in Fig. 1.3 ii).

Note that, depending on the energy levels, following autoionization from an inner valence excited atom or molecule, $\mathrm{A}^*(iv^{-1}\ np)$, the resulting product ion can also be produced in an excited state, $\mathrm{A}^{+*}(ov^{-2}\ n'p')$, which eventually can undergo further radiative decay.

1.1.3 Decay of core shell vacancy

Finally, if the external perturbation leads to ionization from the core orbital of an isolated atom or molecule (A), the corresponding core shell vacancy ($core^{-1}$) can be filled by an electron transfer from the inner valence (iv) or outer valence (ov) orbital. Thus, the excess energy released in this process is given by,

$$\Delta E = E(\mathrm{A}^{+*}(core^{-1})) - E(\mathrm{A}^+(ov^{-1}/iv^{-1})) \tag{1.19}$$

where, $E(\mathrm{A}^{+*}(core^{-1}))$ and $E(\mathrm{A}^+(ov^{-1}/iv^{-1}))$ are the energies of the core shell ionized and valence shell ionized atom or molecule, respectively. Since, the energy required to ionize a core shell electron is very high, usually hundreds of eV to a few KeV, as compared to the ionization energy of an atom or molecule which is a few eV, this excess energy (ΔE) is sufficient to further ionize the atom or molecule. Therefore, the corresponding decay processes can lead to both photoemission and multiple ionization of the atom or molecule, as shown in Fig. 1.4. As the excess energy released is in the KeV range, the corresponding

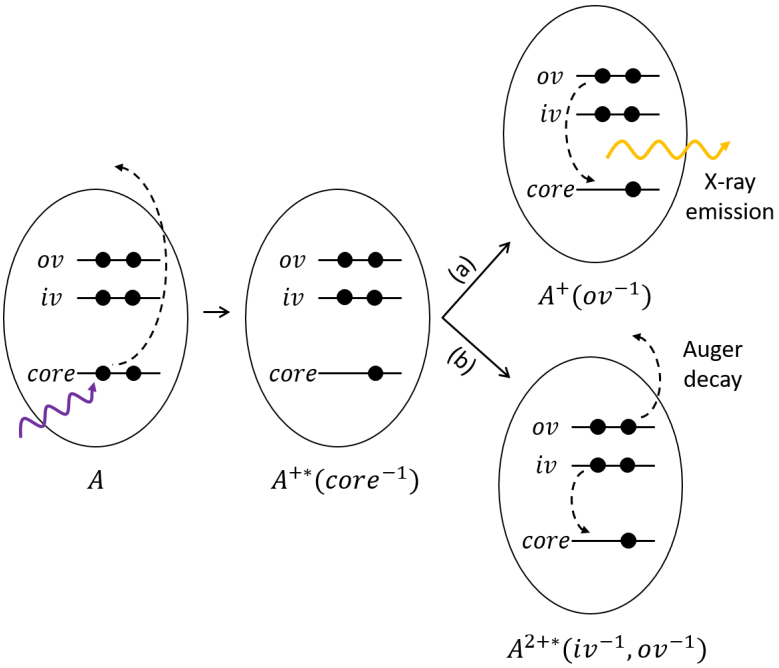

Figure 1.4: Schematic of core shell excitation and decay of the corresponding vacancy in an isolated atom or molecule (A). Pathway (a) shows X-ray emission upon transfer of an outer valence (ov) electron to the core shell vacancy ($core^{-1}$), while pathway (b) shows ionization of an outer valence electron following the transfer of an inner valence (iv) electron to the core shell vacancy in an Auger decay process.

photoemission process is known as X-ray emission, see below.

$$\mathrm{A}^{+*}(core^{-1}) \rightarrow \mathrm{A}^{+}(ov^{-1}) + h\nu \text{ (X-ray)} \tag{1.20}$$

The other possible pathway is the further ionization through Auger decay. In this case, an electron from the valence shell fills the core shell vacancy, and the corresponding excess energy is utilized to ionize single or multiple electrons from the valence orbitals, depending on the excess energy released upon decay of the core shell vacancy. The electrons emitted in the process are known as Auger electrons and the kinetic energies of these electron are decided by the energies of the participating electronic states. For example, if in an Auger decay, one electron from the inner valence orbital is transferred to core shell vacancy, to ionize another electron from the outer valence orbital, see below,

$$\mathrm{A}^{+*}(core^{-1}) \rightarrow \mathrm{A}^{2+*}(iv^{-1}, ov^{-1}) + e^{-}_{Auger} \tag{1.21}$$

then, the kinetic energy (KE) of the Auger electron (e^-_{Auger}) can be written as

$$\mathrm{KE}(e^-_{Auger}) = [E(\mathrm{A}^{+*}(core^{-1})) - E(\mathrm{A}^{+*}(iv^{-1}))] - [E(\mathrm{A}^{2+*}(iv^{-1}, ov^{-1})) - E(\mathrm{A})] \quad (1.22)$$

where, $E(\mathrm{A}^{+*}(core^{-1}))$ and $E(\mathrm{A}^{+*}(iv^{-1}))$ are the energies of core and inner valence ionized cations, respectively, while $E(\mathrm{A}^{2+*}(iv^{-1}, ov^{-1}))$ is the energy of doubly ionized product-ion and $E(\mathrm{A})$ is the energy of the neutral atom or molecule. Since in this example, the product-ion ($\mathrm{A}^{2+*}(iv^{-1}, ov^{-1})$) has an inner valence vacancy, it can undergo further relaxations. It should be noted that, both the X-ray emission and Auger decay occur on femtosecond timescale, as the lifetime of the core ionized atom or molecule is very short.

To summarize, for an isolated atom or molecule, an electronic vacancy in the outer valence orbital usually decays radiatively, while an vacancy in the core shell decays either radiatively via X-ray emission or through Auger decay leading to multiple ionization. For, an inner valence excited or ionized atom or molecule, de-excitation usually leads to either radiative decay or autoionization to singly ionized state. Now, lets look into the corresponding decay processes in loosely-bound clusters of atoms or molecules.

1.2 Electronic decays in loosely-bound cluster

In loosely-bound atomic or molecular aggregates, along with the *intra*-atomic/molecular decays, discussed earlier in section 1.1, *inter*-atomic/molecular decays also become active following the excitation or ionization in a constituent atom or molecule. When the initial excitation or ionization propagates to the neighbouring atom or molecule, the neighbour can get excited or ionized, depending on the electronic structures of the involved entities, the amount of energy transferred, and the underlying relaxation mechanism. Thus, one can classify these *inter*-atomic/molecular decays into several categories, which are determined by the initial and final charge states of the participating neighbours, as presented below.

1.2.1 Resonant energy transfer

This *inter*-atomic/molecular decay takes place between an excited atom or molecule (A^*) and its neighbour (B), when the involved energy states are resonantly coupled, *i.e.*, when

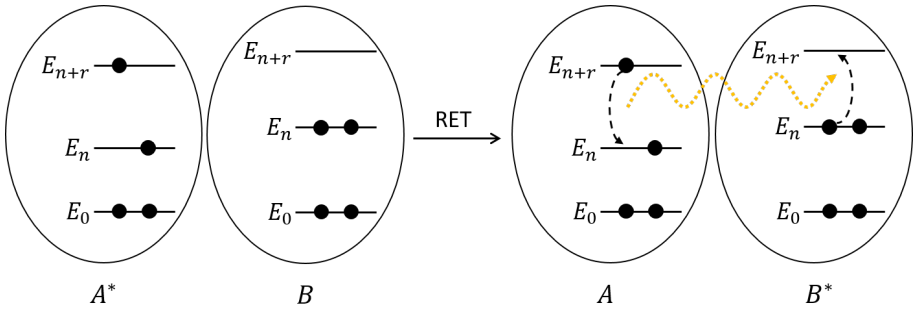

Figure 1.5: Schematic of the resonant energy transfer (RET) process between the excited atom or molecule (A^*) and its neighbour (B), resulting in de-excited A and excited B^*.

the de-excitation energy of (A^*) exactly matches with the excitation energy of B, see below.

$$A^* + B \rightarrow A + B^* \tag{1.23}$$

The charge states of both the neighbours do not change in this resonant energy transfer (RET) process, only the electronic excitation is transferred between the neighbours (see Fig. 1.5). There are two mechanisms responsible for the excitation transfer process, as follows: 1) energy transfer through dipole-dipole interaction and 2) energy transfer via electron exchange.

In the dipole-dipole interaction, the radiative decay pathway of the initially excited atom or molecule is quenched and the relaxation energy is transferred via electric dipole-dipole interaction. In other words, the relaxation energy is transferred to the neighbour via a virtual photon exchange. Due to the involved dipolar interaction, the decay efficiency falls as R^{-6}, where R is the separation between the two entities. Furthermore, along with the energy matching condition, the dipole selection rule should be satisfied in this process. This means only the dipole allowed transitions between the ground and excited states are observed in the neighbours. These decays via virtual photon transfers are also known as Förster resonant energy transfer (FRET), named after Th. Förster, who first reported these processes in 1948 [11]. Recent reviews on FRET can be found in ref.[12, 13].

D. L. Dexter, in 1953, proposed a novel RET process involving transfer of two electrons between the neighbours, wherein one electron from the neighbour fills the vacancy in the excited atom or molecule, and another electron from the later gets transferred to the valence shell of the former [14]. Since, electrons are transferred between the neighbours, here no dipolar selection rule needs to be followed. Thus, in this process, a wide range of

excitations in the neighbour are accessible as compared to the previous case. However, the electron transfer process requires sufficient overlap between the participating electronic orbitals of the neighbouring entities. Therefore, in this case, the decay rate falls exponentially with the increase in the inter-atomic/molecular distance.

1.2.2 Penning ionization

The energy resonance condition between participating electronic states of the neighbours, applicable for bound to bound transitions in RET, is however not required when the energy transferred from the excited atom or molecule leads to excitation of an electron to the continuum in the neighbour. Frans Penning, in 1927, first reported this type of *inter*-atomic/molecular decay, wherein following the de-excitation of an excited atom or molecule (A^*), the neighbouring entity (B) undergoes ionization [15], see below.

$$A^* + B \rightarrow A + B^+ + e^-_{PI} \tag{1.24}$$

This type of reactions, also known as Penning ionization, has been widely studied in crossed atomic or molecular beam setup, where excited metastable atoms or molecules are collided with neutral ones [16]. The kinetic energy (KE) of the ejected Penning electron (e^-_{PI}) can be calculated as

$$\mathrm{KE}(e^-_{PI}) = V(A^* + B)|_{r'} - V(A + B^+)|_{r'} \tag{1.25}$$

where, the $V(A^* + B)|_{r'}$ and $V(A + B^+)|_{r'}$ are the potential energies of the initial and final states at the inter-atomic/molecular distance (r') where the Penning ionization takes place, see Fig. 1.6 a). The above equation 1.25 can also be written as,

$$\mathrm{KE}(e^-_{PI}) = [E(A^*) - E(A)] - [E(B^+) - E(B)] + \Delta E \tag{1.26}$$

where, $E(A)$ and $E(A^*)$ are the internal energies of the neutral and excited A, respectively, and $E(B)$ and $E(B^+)$ are the internal energies of neutral and ionized B, respectively. The value of ΔE can be determined from the potential energy curves of incoming and outgoing channels at r'.

Note that, Penning ionization usually takes place at lower inter-atomic/molecular dis-

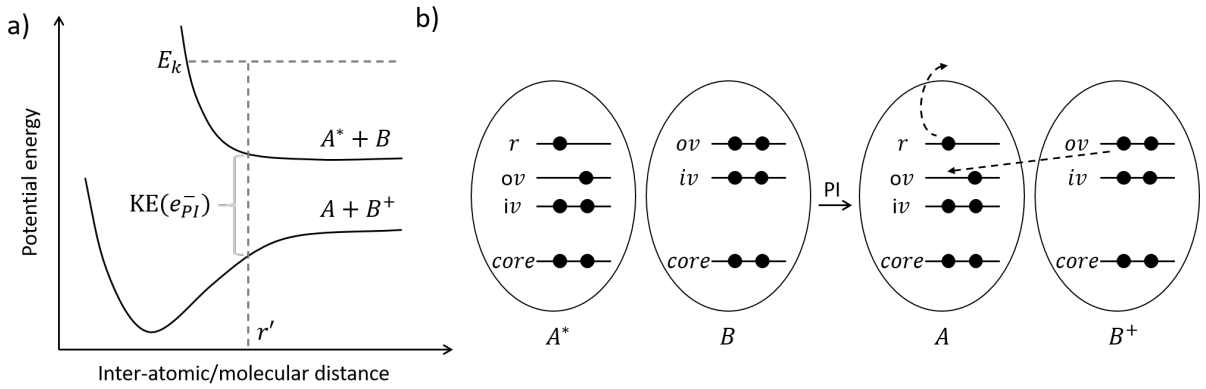

Figure 1.6: a) Potential energy curves of the initial (A^* + B) and final (A + B^+) states of Penning ionization, wherein the Penning ionization takes place at the inter-atomic/molecular distance of r'. b) The underlying electron transfer mechanism in Penning ionization, where the valance shell vacancy of A^* is filled by a valence electron from the neighbour B, which in turn ionizes the excited electron from the A^*, creating A and B^+.

tance, wherein the underlying decay process is initiated by an electron transfer from the valence orbital of the neighbour to the valence shell vacancy of the excited atom or molecule, resulting in ionization of the excited electron from the later, see Fig. 1.6 b). The Penning ionization efficiency, thus, largely depends on the overlap between participating electronic orbitals of the neighbours. Therefore, the collisional kinetic energy (E_k) of the neighbours becomes an important parameter determining the Penning ionization cross section [17].

1.2.3 Charge transfer

Although the *inter*-atomic/molecular decays, discussed above, result from an exited neutral atom or molecule, similar processes can be also observed from an ionized one. In a loosely-bound atomic/molecular cluster, an electronic vacancy in one of the constituents (A^+) can decay via transfer of an electron from the neighbour (B) to the initial vacancy, to relax into a lower energy final state, see below.

$$\mathrm{A}^+ + \mathrm{B} \rightarrow \mathrm{A} + \mathrm{B}^+ \tag{1.27}$$

In this charge transfer (CT) process, the excess energy between the initial and final states is released either radiatively via photoemission or non-radiatively via potential energy curve crossing [18, 19, 20, 21]. Since the electron exchange process requires overlap

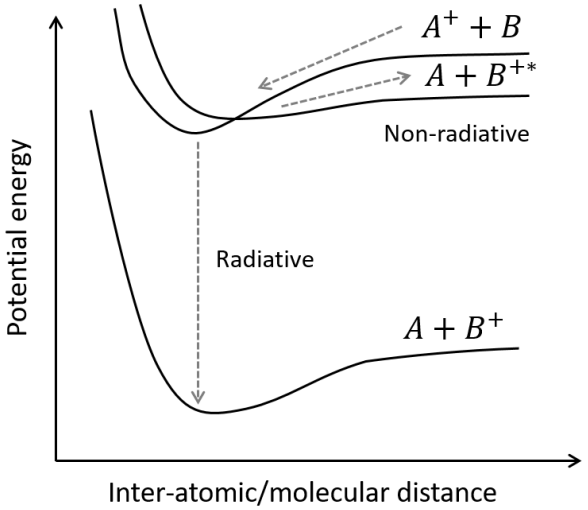

Figure 1.7: Schematic of radiative and non-radiative charge transfer processes, in terms of the potential energies between the participating states of A and B.

between the participating electronic orbitals of the neighbours, nuclear dynamics plays an import role here. Fig. 1.7 schematically shows both the radiative and non-radiative CT processes in terms of the potential energies between the participating states of A and B. Among these processes, the non-radiative CT process usually produces an excited neighbour-ion (B^{+*}), and is more efficient decay mechanism than the radiative one in which a ground state neighbour-ion (B^+) is created. Note that, the total charge state of the neighbours remains the same in CT processes. However, subsequent secondary ionization or photoemission in the system can be observed, when the excited neighbour-ion relaxes. In the following sections, lets look into the *inter*-atomic/molecular decays, where the total charge state of the system increases.

1.2.4 Inter-atomic/molecular Coulombic decay

Cederbaum *et al.*, in their pioneering work in 1997, theoretically demonstrated a novel relaxation pathway, known as inter-atomic/molecular Coulombic decay (ICD) [22], in small loosely-bound clusters of atoms and molecules, wherein upon inner valence ionization of one of the constituents, the system relaxes via further ionization in the neighbour. These ICD processes were first predicted in H-bonded homogeneous clusters of water (H_2O) and hydrogen fluoride (HF), upon inner valence O2s and F2s ionization, respectively [22, 23]. Following the ionization, the inner valence 2s-vacancy is filled by an outer valence 2p-electron and another 2p-electron from the neighbour is ionized, thereby leaving the clus-

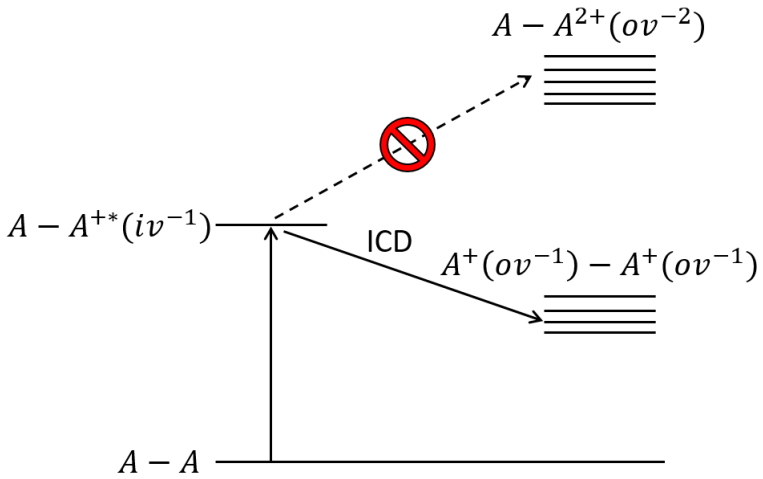

Figure 1.8: Energy levels of a loosely-bound atomic or molecular dimer (A−A). Following the inner valence ionization of the dimer, A−$A^{+*}(iv^{-1})$ state relaxes via ICD into $A^{+}(ov^{-1})$-$A^{+}(ov^{-1})$ final state, when the energy of final state is lower than that of the initial state. Double ionization of the same atom or molecule, where the initial inner valence vacancy is located in the dimer, is often energetically forbidden, since the energy level of A−$A^{2+*}(ov^{-2})$ is usually higher than the same of A−$A^{+*}(iv^{-1})$.

ter in a doubly-ionized state wherein two positive holes are located on the neighbouring molecules. This eventually results in Coulombic fragmentation into two cations.

The opening of this new decay channel upon inner valence ionization can be realized in terms of the energy levels of an atomic or molecular dimer (A−A), as shown in Fig. 1.8. Initially, due to the creation of the inner valence vacancy in one of the dimer constituents, the dimer is formed in the A−$A^{+*}(iv^{-1})$ energy level. Other than radiative decay, there are two possible relaxation pathways for this inner valence ionized dimer: 1) via ionization of an outer valence electron from the same dimer constituent where the inner valence vacancy is located, and 2) via ionization of an outer valence electron from the other dimer constituent in the neighbour. Pathway 1) leads to a doubly ionized A−$A^{2+}(ov^{-2})$ state. However, from the earlier discussion on the decay of inner valence vacancy of an isolated atom or molecule in section 1.1.2, one can argue that this process is usually energetically forbidden, since the energy of A−$A^{2+}(ov^{-2})$ state is often greater than the same of the initial A−$A^{+*}(iv^{-1})$ state. The second pathway, where due to the relaxation of initial vacancy the neighbour is ionized, can be energetically accessible. This is due to the fact that the spatially separated locations of the positive holes on two neighbours reduces the internal repulsive Coulombic energy between the holes in the final dicationic state, $A^{+}(ov^{-1})$-$A^{+}(ov^{-1})$, as compared to the case where two holes are located on the same

atom or molecule. Thus, the energy of the final doubly ionized state, $A^+(ov^{-1})$-$A^+(ov^{-1})$, can be at a lower level than the same for initial inner valence ionized state, $A{-}A^{+*}(iv^{-1})$. When the above-mentioned condition is satisfied, the ICD becomes the mode of decay of the inner valence vacancy in loosely bound dimer, see below.

$$A{-}A^{+^*}(iv^{-1}) \rightarrow A^+(ov^{-1}) - A^+(ov^{-1}) + e^-_{ICD} \tag{1.28}$$

Furthermore, these ICD processes are found to be highly efficient decay mechanisms in loosely-bound clusters, occurring on ultrafast time scale [24, 25]. Detailed theoretical descriptions of the ICD processes can be found in ref.[26]. In the following discussions, the origin of this high efficiency and the underlying mechanisms are briefly described.

The initially ionized excited state from which the ICD proceeds can be represented by the wavefunction $\mid \phi_i \ \phi_k\rangle$, where ϕ_i and ϕ_k denote the initial vacancy and the scattering wavefunction of the ionized free-electron created due to external perturbation, respectively. The final state is represented by $\mid \phi_f \ \phi_{f'}\rangle$, where ϕ_f and $\phi_{f'}$ denote the final vacancies located at two neighbouring atoms or molecules. Thus, the decay rate can be calculated from the electron-electron Coulomb matrix element,

$$V_{f,f',i,k} = \langle \ \phi_f \ \phi_{f'} \mid V \mid \phi_i \ \phi_k \ \rangle \tag{1.29}$$

where, V is the Coulombic potential between two electrons. Ignoring the complexity of the strongly correlated states, the decay rate, also quantified from the decay width (Γ) can be approximated to the leading term according to the Fermi's golden rule, as

$$\Gamma \propto |V_{f,f',i,k} - V_{f,f',k,i}|^2 \tag{1.30}$$

where, the matrix elements, $V_{f,f',i,k}$ and $V_{f,f',k,i}$, result from direct and exchange contributions due to the indistinguishability of the electrons, respectively.

Qualitatively, these two terms represent two different underlying mechanisms which lead to the same final state, as shown in Fig. 1.9. The direct term indicates, transfer of an outer valence electron to the initially created vacancy from the same dimer constituent (left constituent in Fig. 1.9). The released energy in this relaxation process is then utilized

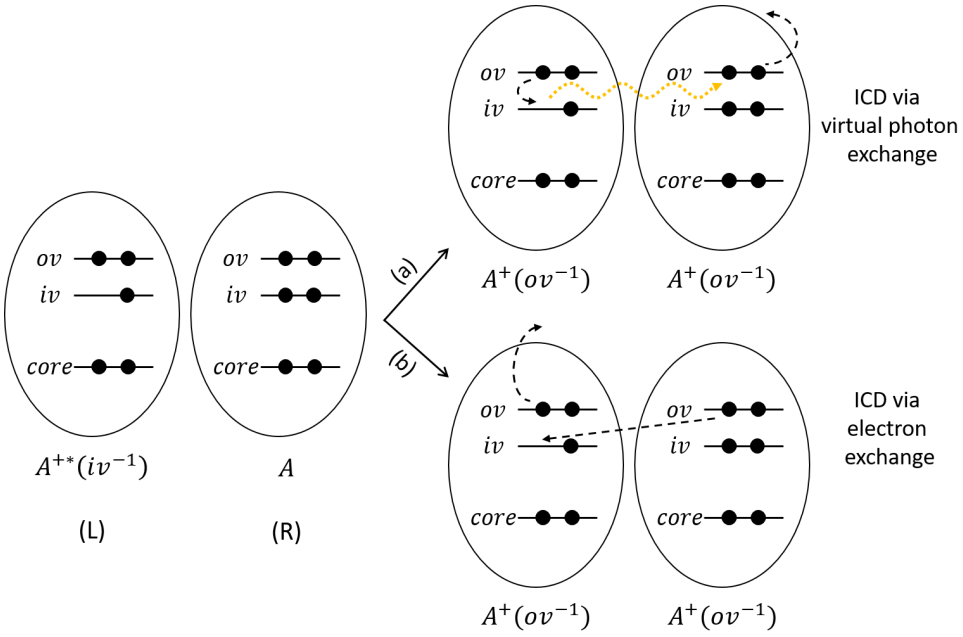

Figure 1.9: Schematics of ICD channels by virtual photon transfer and electron exchange in atomic/molecular dimer upon inner valence (iv) ionization. The inner valence vacancy of the initially ionized constituent (A) is filled by an outer valence (ov) electron of the same, resulting in ionization from the outer valence orbital of the neighbour (B) in virtual photon transfer ICD, shown in process (a). Whereas, the inner valence hole of A is filled by an outer valence electron of the neighbour B, leading to ionization of another outer valence electron of A, in electron exchange ICD, shown in process (b).

to ionize an outer valence electron from the neighbour (right constituent in Fig. 1.9). This ICD mechanism is also know as ICD via virtual photon exchange, since a radiative decay in one constituent is quenched by ionization in other (see process (a) in Fig. 1.9). The dipole selection rule must also be followed here by the initially ionized dimer constituent while relaxation. Whereas, the exchange term indicates transfer of an outer valence electron from the neighbour to the initial vacancy, which leads to ionization of an outer valence electron from the same constituent where the initial vacancy was located. This process is also know as the ICD via electron exchange (see process (b) in Fig. 1.9).

According to the ICD schematic shown in Fig. 1.9, the direct and exchange terms in equation 1.30 can be written as

$$V_{Lf,Rf,Li,k} = \int\int \phi^*_{Lf}(\bar{r}_1)\ \phi_{Li}(\bar{r}_1)\ \frac{e^2}{|\bar{r}_1 - \bar{r}_2|}\ \phi^*_{Rf}(\bar{r}_2)\ \phi_k(\bar{r}_2)\ d\bar{r}_1\ d\bar{r}_2 \tag{1.31}$$

$$V_{Lf,Rf,k,Li} = \int\int \phi^*_{Lf}(\bar{r}_1)\ \phi_k(\bar{r}_1)\frac{e^2}{|\bar{r}_1 - \bar{r}_2|}\ \phi^*_{Rf}(\bar{r}_2)\ \phi_{Li}(\bar{r}_2)\ d\bar{r}_1\ d\bar{r}_2 \tag{1.32}$$

where, L and R represent the dimer constituents on the left and right, respectively, while f, f' and i are replaced by Lf, Rf and Li, respectively.

From equation 1.31, one can see that only overlap between participating electronic orbitals, ϕ_{Li} and ϕ_{Lf} in the dimer constituent where the initial vacancy was located, along with the dipole selection rule, is sufficient for non-zero contribution of the direct term. Thus, ICD via virtual photon exchange proceeds even for well separated neighbours. Moreover, since this ICD process is mediated by dipole-dipole interaction between neighbours, the associated decay rate falls as R^{-6}, where R is the distance between the neighbours.

However, from equation 1.32, it is evident that overlap of the electronic orbitals, ϕ_{Li} and ϕ_{Rf}, of two neighbours between which the electron transfer takes place is necessary for efficient ICD via electron exchange. Thus, in case of ICD via electron exchange, the decay rate falls as $\exp(-R)$, much quicker than the same for ICD via virtual photon exchange.

The orbital overlap between neighbours can dramatically enhance the decay rate by $2-3$ orders of magnitude than the case where orbital overlap is neglected [27]. Therefore, the nuclear dynamics initiated by the ionization of neutral dimer, which affects the overlap of electronic orbitals between the neighbouring atoms or molecules plays a crucial role determining the ICD efficiency [28, 29, 30, 31]. Moreover, large number of open channels ($\mid \phi_f \; \phi_{f'}\rangle$) also adds up to the effective ICD decay rate. If the size of the loosely bound cluster is increased from dimer to higher order, the number of interacting atoms or molecules in the vicinity of the initially ionized excited species increases and the number of open channels is also expected to increase accordingly [32, 33, 34]. For example, Santra *et al.* theoretically demonstrated effect of cluster size on the ICD rate for Ne clusters upon inner valence ($2s$) ionization in ref.[28], where the decay lifetimes were found to decrease from hundreds of femtosecond for Ne_2 to less than ten femtosecond for Ne_{13}. Interestingly, in case of Ne_2, the same ICD lifetime was found to decrease by 6 times in the presence of a He atom at a distance of 4 Å between the Ne atoms, wherein the He atom acts as as a bridge atom to enable efficient energy transfer between the Ne atoms via virtual states of the same. This novel ICD mechanism is termed as superexchange ICD [35, 36, 37].

In Fig. 1.10, the ICD process is schematically shown in terms of potential energies of

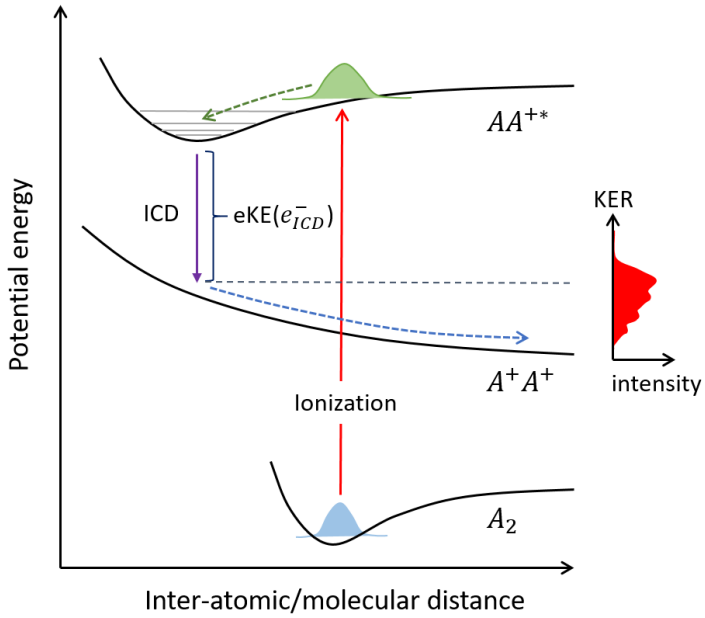

Figure 1.10: Schematic of ICD in loosely-bound dimer (A_2), and relevant transitions between different electronic states.

the relevant electronic states of the atomic/molecular dimer (A_2) and transitions between them. Upon inner valence ionization, A_2 undergoes vertical transition to the excited AA^{+*} state. Depending on the nature of potential energy curve of the excited state, the inter-atomic/molecular distance of AA^{+*} can reduce which effectively increase the efficiency ICD process as discussed above. Thus, ICD takes place in AA^{+*} leading to the Coulombic potential energy curve of A^+A^+ at a certain inter-atomic/molecular distance, r'. Therefore, the kinetic energy of the ejected electron (e^-_{ICD}) from the above process is given by,

$$\mathrm{KE}(e^-_{ICD}) = E(\mathrm{AA}^{+*})|_{r'} - E(\mathrm{A}^+\mathrm{A}^+)|_{r'} \tag{1.33}$$

where, $E(\mathrm{AA}^{+*})|_{r'}$ and $E(\mathrm{A}^+\mathrm{A}^+)|_{r'}$ are the energies of the initial and the final states, respectively, at the inter-atomic/molecular distance, r'. Thus, similar to Auger decay in isolated system, $\mathrm{KE}(e^-_{ICD})$ is also a characteristic energy which is governed by the involved electronic states of loosely-bound system (see equations 1.22 and 1.33). However, unlike Auger decay which is initiated by core shell ionization, the kinetic energy of the ICD electron is only a few eV, since only the valence orbitals of the constituent atoms or molecules participate in the later case.

In the Coulombic potential energy curve, the resultant ion (A^+A^+) fragments into two A^+ ions, wherein the total kinetic energy release (KER) by the fragmented ions can be

calculated from,

$$\mathrm{KER}(\mathrm{A}^+ + \mathrm{A}^+) = E(\mathrm{A}^+\mathrm{A}^+)|_{r'} - 2 \times E(\mathrm{A}^+) \tag{1.34}$$

where, $E(\mathrm{A}^+)$ is the internal energy of the fragmented ion A^+. Since the Coulombic potential energy between fragmented ions is converted to their kinetic energies, the total KER can be approximated from $14.4/r'$ in eV, where r' is expressed in angstrom (Å). Thus, by measuring the KER spectrum, one can get insight about the inter-atomic/molecular distance, r', at which the ICD takes place. Furthermore, as the initially ionized AA^{+*} can be populated in different vibrational states, the KER spectrum can contain the corresponding vibrational structure. Thus, oscillations in the KER spectrum can arise from the interplay between wave packet dynamics and inter-atomic/molecular distant dependent ICD decay rates [38, 39, 40].

Note that, ICD type decay processes can be observed, not only upon ionization of the inner valence (iv) electron, but also upon resonant excitation of the same to an excited state ($n'l'$) in one of the constituents of a loosely-bound homogeneous cluster. For the later case, when the inner valence vacancy (iv^{-1}) is filled by an outer valence (ov) electron, the de-excitation energy is utilized to ionize another outer valence (ov) electron from the neighbour, see below:

$$\mathrm{A}^*(iv^{-1}\ n'l') \cdot \mathrm{A} \rightarrow \mathrm{A}^*(ov^{-1}\ n'l') \cdot \mathrm{A}^+(ov^{-1}) + e^-_{ICD} \tag{1.35}$$

Contrary to ICD, discussed earlier, wherein charge separated dication is created, in this ICD which is induced by resonant excitation, an excited cation $[\mathrm{A}^*(ov^{-1}\ n'l') \cdot \mathrm{A}^+(ov^{-1})]$ is produced. In this way, these resonant ICD processes are similar to Penning ionization, discussed earlier in section 1.2.2. However, Penning ionization usually proceeds upon outer valence excitation in heterogeneous system which energetically allows for a de-excitation in an outer valence excited constituent to ionize an outer valence electron from a neighbour with largely different energy levels. In case of homogeneous cluster, outer valence ionization in the neighbour due to de-excitation of an outer valence excited constituent is usually energetically forbidden.

Moreover, these ICD processes are not unique to the homogeneous loosely-bound clusters, they can also be observed in heterogeneous clusters upon excitation of an inner

valence electron [41, 42]. In case of heterogeneous cluster, due to differences in energy levels of the constituent atoms or molecules, excitation from both the outer and inner valence orbital can also decay via ICD. Since the overlaps between outer valence orbitals of neighbours in a loosely-bound cluster is stronger than the same with inner valence orbitals, ICD becomes even more efficient relaxation pathway following outer valence excitation in heterogeneous clusters [43]. At the same time, it should be noted that the outer valence orbitals of an atom or molecule are more perturbed in the presence of neighbours than the inner valence orbitals of the same. Thus, due to stronger electronic correlations, determinations of outer valence energy levels are theoretically more challenging than the same for inner valence energy levels. Other than the energetics, this was one of the reasons for reporting ICD processes following inner valence ionization for the first time by Cederbaum *et al.* [22]. Moreover, in heterogeneous loosely-bound cluster due to large differences in the energy levels of the constituents, a variety of ICD processes can be observed. For example, Lorenz S. Cederbaum also reported a novel ICD process wherein a vibrationally excited molecule in its electronic ground state can efficiently ionize an anionic neighbour, by transferring its vibrational energy to the anion [44]. In case of endohedral fullerene complex (X@Cn) such as Ne@C_{60}, following the inner valence 2*s*-ionization of Ne, a double ICD channel where two ICD electrons are emitted from C_{60}, has been theoretically proposed [45].

Furthermore, due to highly localized core orbitals in an atom or molecule in loosely-bound cluster, the correlations of core shell electrons of the same with the electronic orbitals of the neighbours are much weaker. Thus, although the decay of core shell vacancy in one of the constituents energetically allows for subsequent ionization in the neighbour through ICD, core shell excitation usually leads to *intra*-atomic/molecular X-ray emission or Auger decay. However, ICD becomes a dominant decay channel for the inner valence ionized product-ion in the cluster, following the Auger decay [46, 47, 48, 49, 50, 51]. Even though the ICD efficiency from a core shell ionized state is low, similar processes are theoretically reported in liquid water [52, 53, 54, 55], microhydrated LiOH [56] and ammonia cluster [57, 58]. Therefore, these non-local decay processes upon core-shell ionization become extremely relevant for structural analysis of biological samples by X-ray photoelectron spectroscopy [59] and coherent X-ray diffraction imaging [60].

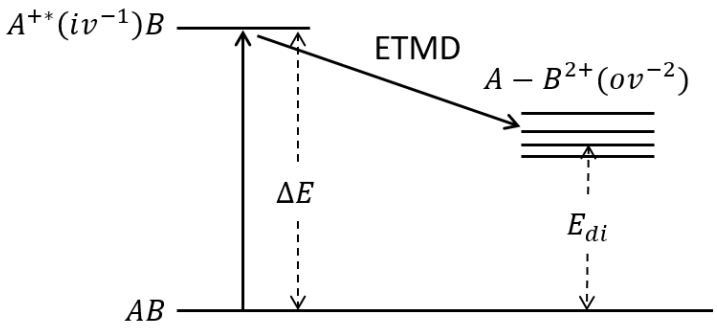

Figure 1.11: Energy levels of a loosely-bound heterogeneous atomic or molecular dimer (AB). Following the inner valence ionization of the dimer constituent (A), $A^{+*}(iv^{-1})B$ state relaxes via ETMD into A-$B^{2+}(ov^{-2})$ final state, when the neutralization energy released (ΔE) upon transfer of an outer valence electron from the neighbour (B) to the initial inner valence vacancy is higher than the double ionization threshold (E_{di}) of the dimer leading to A-$B^{2+}(ov^{-2})$.

1.2.5 Electron transfer mediated decay

For loosely-bound heterogeneous dimers, Zobeley *et al.*, in 2001, theoretically reported a new type of *inter*-atomic/molecular relaxation process known as electron transfer mediated decay (ETMD) [61], wherein upon inner valence ionization in one of the dimer constituents, the system relaxes through further ionization in the neighbour similar to the ICD processes. However, in this case, the initially ionized constituent ($A^{+*}(iv^{-1})$) is neutralized due to transfer of an outer valence electron from the neighbour (B) to the initial vacancy, and the neutralization energy released in this process is used to ionize another outer valence electron from the neighbour, see below.

$$A^{+*}(iv^{-1})\ B \rightarrow A\ B^{2+}(ov^{-2}) + e^{-}_{ETMD} \tag{1.36}$$

The double ionization of the neighbour through ETMD is possible in case of heterogeneous dimer due to the largely different electronic energy levels of the dimer constituents. In Fig. 1.11, the energy levels of the AB are presented to realize this process. Initially the system is created in $A^{+*}(iv^{-1})B$ state. If the neutralization energy (ΔE) of $A^{+*}(iv^{-1})B$ is higher then the double ionization energy (E_{di}) of AB which leads to $AB^{2+}(ov^{-2})$, ETMD becomes a plausible decay channel.

Since electron transfer between neighbours mediates the decay process in ETMD, sufficient overlaps between the participating electronic orbitals of the neighbours are required,

like we have seen for ICD via electron exchange. Thus, the nuclear dynamics in the cluster upon initial ionization plays a vital role determining the ETMD efficiency [62]. Furthermore, similar to ICD, the ETMD decay rate also depends on the number of open channels available in the neighbourhood of the initially ionized entity and is found to increase with the increasing number of neighbouring atom or molecule [63].

This ETMD process is schematically shown in terms of potential energies of relevant electronic states of AB and transitions between them in Fig. 1.12. Upon external perturbation, AB is ionized vertically from its ground state to the excited state, $A^{+*}B$, where nuclear dynamics can be effective to decrease the inter-atomic/molecular distance and enhance the ETMD efficiency. The subsequent ETMD occurring at a lower inter-atomic/molecular distance, r', leads to AB^{2+} which undergoes either trapping into AB^{2+} or dissociation into A and B^{2+}. Thus, the kinetic energy of e^-_{ETMD} can be calculated as,

$$\mathrm{KE}(e^-_{ETMD}) = E(\mathrm{A}^{+*}\mathrm{B})|_{r'} - E(\mathrm{AB}^{2+})|_{r'} \tag{1.37}$$

where, $E(\mathrm{A}^{+*}B)|_{r'}$ and $E(\mathrm{AB}^{2+})|_{r'}$ are the energies of the initial $A^{+*}B$ and final AB^{2+} states, respectively, at the inter-atomic/molecular distance, r'. Similar to the discussion for ICD, this ETMD electron kinetic energy is also decided by the participating energy levels of the dimer. Whereas the total kinetic release (KER) by the product-ions and neutrals is decided by the interplay between wave packet dynamics and inter-atomic/molecular distance dependent ETMD efficiency of the initially excited $A^{+*}B$ state. Thus, by measuring the $\mathrm{KE}(e^-_{ETMD})$ and KER, one can gain insights into the underlying decay mechanism.

Note that, the above described ETMD process is not limited to a single atomic or molecular neighbour (B). For higher order cluster, it is also possible that instead of ionizing the same neighbour (B) from which an outer valence electron is transferred to neutralize $A^{+*}(iv^{-1})$, another neighbour(B) is ionized from the outer valence shell, see below.

$$\mathrm{A}^{+*}(iv^{-1})\ \mathrm{B}\ \mathrm{B} \rightarrow \mathrm{A}\ \mathrm{B}^{+}(ov^{-1})\ \mathrm{B}^{+}(ov^{-1}) + e^-_{ETMD} \tag{1.38}$$

This ETMD process where three interacting neighbours are involved is known as ETMD(3), while the earlier discussed ETMD process involving two interacting neighbours is known as ETMD(2). Theoretical descriptions of ETMD(2) and ETMD(3) can be found in ref.[63].

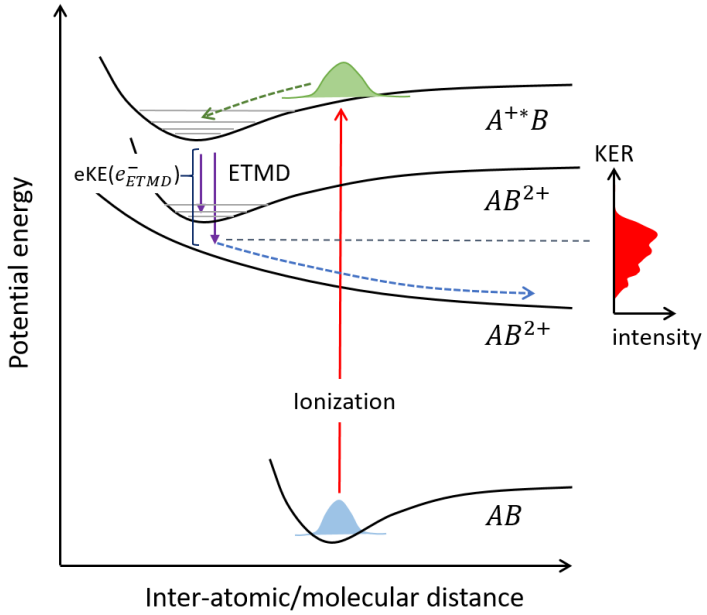

Figure 1.12: Schematic of ETMD in loosely bound dimer (AB), and relevant transitions between different electronic states.

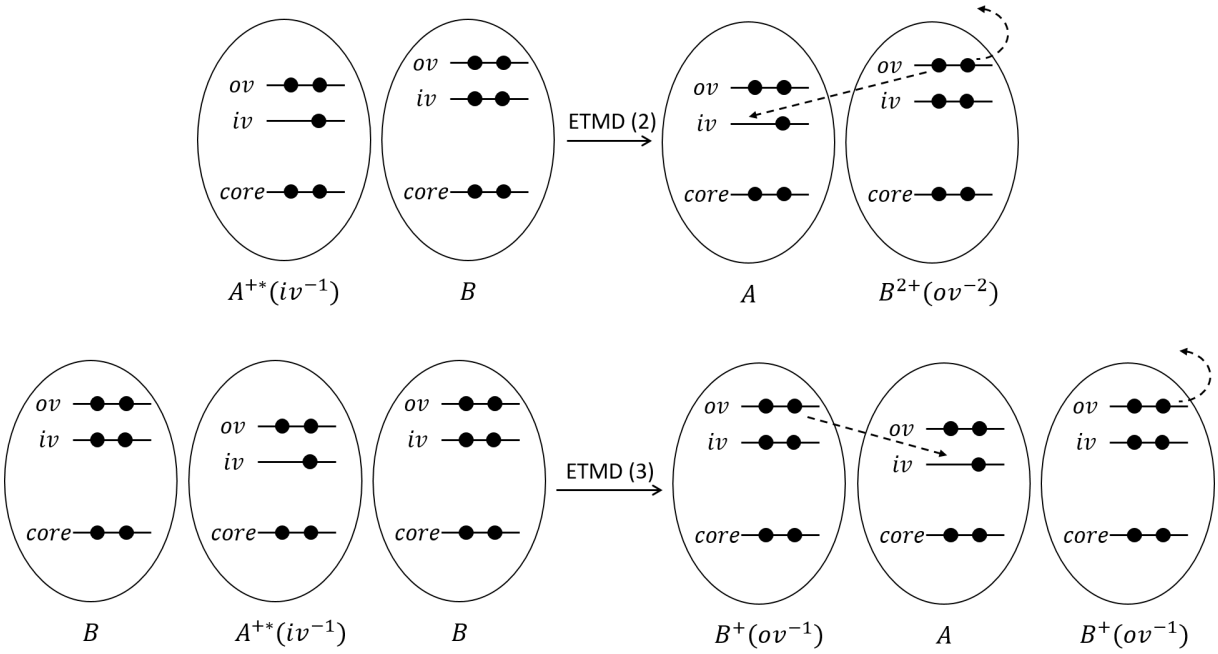

Figure 1.13: Schematic of the electron transfer mediated decay (ETMD) in heterogeneous cluster. The inner valence vacancy (iv^{-1}) of the initially ionized constituent (A) is filled by an outer valence (ov) electron from the neighbour B, resulting in ionization of another outer valence electron from the same neighbour in ETMD(2) and from the adjacent neighbour in ETMD(3).

Both these processes are schematically shown in Fig. 1.13. The internal energy of the final state from ETMD(3) (process 1.38) is lower than the same from ETMD(2) (process 1.36), as for the former case two holes are located on two neighbours, while two holes are located on the same neighbour for the later case [64]. Thus, the kinetic energy of the ETMD electron from ETMD(3) will be higher than the same from ETMD(2) and can be used to discern ETMD(2) from ETMD(3). Furthermore, due to the spatially separated locations of two positive holes, the final product-ion in ETMD(3) undergoes Coulombic fragmentation. In case of ETMD(2), the product ion can dissociate into charged and neutral fragments depending on the final state. Moreover, ETMD is not limited to emission of only one ETMD electron, *e.g.*, in case of Ne@C_{60} complex, it is also possible that a inner valence $2s$-hole in Ne^{+*} can be neutralized via transfer of one electron from C_{60} and ionization of another two electrons from the same in a double ETMD process [45].

Note that, ETMD can also proceed from outer valence ionization in one of the constituents in heterogeneous cluster, if the neutralization energy of the outer valence vacancy is higher than the double ionization energy of the neighbour(s) [65, 66]. Following core-shell ionization, the system usually relaxes via *intra*-atomic/molecular Auger decay due to strong localization of the core-shell orbital, wherein ETMD from the Auger final state becomes one of the decay channels in loosely-bound cluster [62, 67, 59]. However, ETMD can also be a feasible relaxation pathway due to *inter*-atomic/molecular relaxation of the core-shell vacancy, when a valence electron from the neighbour fills the initially created core-shell vacancy to ionize another valence electron of the neighbour. Such ETMD processes are reported in Li^+ microsolvated small water cluster following Li^+ $1s$ ionization [68], as well as in liquid water upon O $1s$ ionization [54].

1.3 Probing inter-atomic/molecular decay

In *inter*-atomic/molecular decays, discussed in the above section 1.2, the ejected electrons carry characteristic kinetic energies governed by the involved electronic states. Thus, by measuring the kinetic energies of emitted electrons, direct insights into these states and the underlying mechanisms can be achieved. For example, ICD was first experimentally observed in Ne cluster following inner valence ($2s$) photoionization from the electron kinetic energy (eKE) spectrum measured by a hemispherical energy analyser [69]. The

lifetimes of ICD active states at the surface ($\sim$ 30 fs) and interior ($\sim$ 6 fs) of the same were estimated from the widths of eKE peaks associated with ICD electrons [70]. Furthermore, almost 100% efficiency of the ICD process following 2s-photoionization in Ne cluster was estimated by comparing the eKE peak-areas correlated to the ICD electrons and 2s-photoelectrons in the measured eKE spectrum [71]. This high efficiency was later confirmed in electron-electron coincident measurement using a magnetic bottle spectrometer, wherein the ICD electron was detected in coincidence with the photoelectron [72]. Similar electron-electron coincident detection schemes were also implemented to detect ICD processes in inhomogeneous rare gas cluster (NeKr) following Ne 2s-photoionization [73], and to detect ETMD(3) in $ArKr_2$ upon Ar 3s-photoionization for the first time [74].

Furthermore, the measured eKE spectrum revealed resonant ICD processes in Ne cluster, following $2s \rightarrow 3p$ photoexcitation [75], as well as the signatures of ICD and ETMD processes from the core-shell ionized states wherein additional peak structures were observed along with the *intra*-atomic/molecular Auger electron energy spectrum in water cluster [76, 77, 78, 79, 80, 53, 54]. Moreover, measurements of eKE spectra were also helpful in realising ETMD processes from core-ionized $Li^{2+}(1s)$ in aqueous solution, where Auger or ICD processes are forbidden [81, 82].

However, following external perturbation, an atomic or molecular cluster can decay via multiple *intra*- and *inter*- atomic/molecular relaxation channels resulting in different product-ions and electrons. Thus, to unambiguously identify these decay channels, it is necessary to detect the product-ions in coincidence with the ejected electrons. ICD was, therefore, first unambiguously confirmed in Ne_2 upon 2s-photoionization, when two Coulomb exploding Ne^+ ions and a low-energy ICD electron were recorded in coincidence using a cold target recoil ion momentum spectrometer (COLTRIMS) [83]. By measuring the kinetic energies of the ions and electrons in coincidence in this way, different ICD mechanisms, such as ICD via virtual photon transfer and via electron exchange, were discerned in Ne_2 [84]. Moreover, the measured total kinetic energy release (KER) by the product-ions revealed oscillatory structures, which are indicative of the vibrational wave packet dynamics of ICD active states, created by He^{+*} ($n = 2, 3..$) photoexcitation in He_2 [40, 85, 86] and He^* $1s3p$ resonant photoexcitation in HeNe [87]. By implementing similar multi-coincident measurement technique, resonant ICD processes upon inner valence excitations were probed in Ne cluster [88, 89], as well as in rare gas dimers, such as

Ne_2, Ar_2, Kr_2 and Xe_2 [89, 90]. ETMD(2) was first experimentally reported in Ar_2 from a triply ionized state (Ar^{3+}-Ar) with $3s$ vacancy, by detecting two Ar^{2+} ions and the ETMD electron in coincidence with a time of flight based double-sided momentum spectrometer [91]. The recorded eKE spectra correlated to different product-ions, from electron-ion coincident measurements using similar experimental setup, revealed site-selective ETMD processes in mixed ArXe cluster following Ar $2p$-photoionization, which are not active upon resonance photoionization Xe $4d$-electron [92]. Similar coincidence measurements using double-sided velocity map imaging spectrometer unveiled efficient ICD channels in endohedral fullerene ($Ho_3N@C_{80}$) above $4d$-ionization threshold of the holmium (Ho) [93].

Other than the charged particles, detecting (or not detecting) fluorescence from loosely-bound clusters upon electronic excitation or ionization has also proved to be an effective technique to probe *inter*-atomic/molecular decays. For example, radiative charge transfer (RCT) in inner-valence ionized Ne cluster was evident from the wavelength dependent fluorescence measurements [21]. Whereas, following $2p \rightarrow 3s$ electronic excitation of Ne in mixed NeAr cluster, the radiative decay of Ne^* was found to be efficiently quenched by resonant ICD in Ar from fluorescence measurements [94]. Furthermore, detecting the emitted photon, following outer valence ionization of Ne in mixed NeKr cluster, in coincidence with photoelectron confirmed RCT in Ar from Ne^+ ion [20]. Such electron-photon coincidence schemes have been deployed to confirm resonant ICD in Ne cluster upon inner valence excitation [95], as well as ICD from core-ionized states in Ar cluster [96].

Thus, from the above mentioned examples, it is evident that recording the kinetic energy spectra of the ejected electrons and ions as well as the fluorescence is effective for investigating *inter*-atomic/molecular decays, wherein multi-coincidence measurements between the charged particles and the emitted photons aid to clear up the ambiguity between different decay processes. For creating ICD and ETMD active states in loosely-bound clusters, core-shell photoionization, decaying into different inner and outer valence ionized states following Auger decay, has been widely used to experimentally probe these processes [97, 98, 99, 100, 101, 102, 103, 104, 91, 105, 106, 107, 108, 51]. Because of the tunability of photon energy, radiations from synchrotron facilities are particularly suitable for creating localized excitation and ionization in loosely-bound clusters via single photon absorption processes. However, multi-photon absorptions using intense ultrafast photon

pulses, both from table-top laser systems [109], and from free electron lasers [110, 111], are also effective. Note that, laser radiation depending on its intensity can also create multiple excitation sites in the same cluster. Thus, it opens up possibilities to study new types of ICD processes from these multiply excited systems [112, 113, 114, 115]. Ultrafast laser pulses are also used to probe the involved nuclear dynamics in ICD processes, as well as to estimate the lifetime of the ICD active states both theoretically [116, 117] and experimentally [118, 119]. Furthermore, other than irradiating with photons, collisions with ions [120, 121, 122, 123] with electron [124, 125, 126, 127, 128] are also deployed as external sources of perturbations for electronic excitation and ionization in these systems.

The ICD and ETMD processes are widely observed in water clusters [129, 130, 131, 132, 133, 134, 135], making them highly relevant for investigating the radiation damage in biological matter [136, 60, 137, 138, 139, 140, 141]. ICD processes are also observed in small loosely-bound clusters of aromatic hydrocarbon benzene rings [142, 143] and in unbounded pyridine monomers triggered by associative interaction between them following photoexcitation [115] which are pertinent in many biochemical processes, as well as in quantum dots [144, 145] for condensed matter systems. Detailed review of the ICD and ETMD processes can be found in ref.[146, 147, 148]. Therefore, studying these *inter*-atomic/molecular relaxation processes is of fundamental interest.

1.4 The model system - doped helium nanodroplets

In this thesis, *inter*-atomic/molecular relaxation processes are investigated in loosely-bound clusters of He, doped with a few foreign atoms or molecules, upon electronic excitation and ionization of the host He cluster. There are certain advantages for choosing He as the host cluster constituents in these studies:

- The electronic structure of He is very simple with only two electrons. This makes the understanding of underlying electronic excitation and relaxation processes in *inter*-atomic/molecular decays relatively easy. Also the simple electronic structure of He is reflected in relatively simple eKE spectra, and accurate model calculations are feasible at moderate cost due to less number of active electrons.

- Atomic He has the highest ionization energy (24.58 eV) of all the elements, and

even the first electronically excited state has energy of 19.82 eV above the ground state. Thus, following the neutralization of He^+ or relaxation of excited He^*, the released excess energy is sufficient to ionize or excite neighbouring dopant atoms or molecules.

- The electronic orbitals of excited He^* are spatially large enough for efficient *inter*-atomic/molecular correlations, which mediate the electronic decays in the neighbourhood.

- Although, He becomes highly reactive with the environment upon electronic excitation or ionization [149], it is inert in its neutral ground state. Therefore, the dopants inside He cluster do not undergo chemical transformation while preparing the system.

Furthermore, nanometer-sized large clusters of ^{4}He, containing more than 10^4 He atoms per cluster, display superfluidity similar to liquid or bulk ^{4}He [150, 151, 152]. Thus, these superfluid He clusters are also known as He nanodroplets. One of the many interesting properties of He nanodroplets is their extremely low internal temperature ($\sim$ 0.37 K), which can very efficiently cool dopant molecules to their ro-vibrational ground states. Also, owing to high photoexcitation energies of He atoms ($\geq$ 21.21 eV), He nanodroplets are transparent to infrared (IR) radiation. These make He nanodroplets an ideal nano-cryostat for hosting ro-vibrationally cooled molecules for their spectroscopic studies, which are also know as helium nanodroplets isolation (HENDI) infrared (IR) spectroscopy [153, 154, 155, 156, 157]. However, for the current experiments, He nanodroplets are chosen as the host-cluster for following reasons:

- Depending on the interaction between the dopants and the host droplet, the dopants may reside at different locations of the host-droplet [158, 159]. For example, alkali atoms attach to the surface [160, 161], and alkaline-earth metal atoms reside at or near the surface [162], whereas rare gas atoms and most of the molecular dopants are embedded inside the droplets [151, 156].

- Due to the superfluidity of He nanodroplets, the dopants can move freely inside the droplet. This also facilitates frictionless molecular rotations inside the superfluid host-medium [163, 164]. Upon multiple doping, the dopant atoms or molecules can interact with each other inside the droplet to create complex structures. For exam-

ple, due to dipolar-interaction, polar molecules, such as, water aggregates into cyclic hexamer ice crystal [165], while HCN molecules are self-assembled into long linear-chains. Whereas, magnesium atoms create foam-like structure [166], silver atoms concentrate at multiple centres [167] and acetylene molecules form loosely-bound van der Waals oligomers [168]. Furthermore, the dopants inside the droplet can be attracted towards the quantum vortices observed in these superfluid nanoclusters [169, 170], to synthesize nanowires and nanocrystals along the vortices [171, 172].

- Along with the movements of extrinsic dopants, following excitation and ionization of He, movements of the intrinsic He^* and He^+ are also feasible in the host-droplet. Due to repulsive interaction with the droplet environment, He^* migrates to the surface of the droplets presumably due to resonant hopping of excitation or atomic motion within $10-20$ ps [173, 174, 175]. Whereas, due to attractive interaction with the droplet, He^+ migrates to the centre of the droplet on a faster timescale within $60-80$ fs via resonant charge hopping [175, 176, 177, 178]. Both He^* and He^+ can be trapped with a He atom to form vibrationally excited He_2^* excimer and He_2^+ molecular ion, respectively [173]. These He_2^* and He_2^+ are then subject to vibrational relaxations, in which the released energies can evaporate large number of He atoms from the droplet. Thus, ejections of He_2^* and He_2^+ from the droplets are observed. However, since the dopants of different species reside at different sites within the droplet and forms exotic structures, it is very intriguing to investigate how the motions of these extrinsic and intrinsic entities affect different *inter*-atomic/molecular decays and subsequent dynamics.

1.4.1 Outline and motivations

Small weakly-bound clusters have served as test-beds for the detailed characterization of various inter-atomic/molecular electronic decays [146, 147, 148]. However, He nanodroplets doped with a few foreign atoms or molecules, are particularly well-suited for investigating such processes for all the earlier mentioned reasons. For example, resonant ICD processes in the dopants following single-electronic photoexcitation of the droplets have been widely investigated for different kinds of dopants, such as rare gas [179, 180], alkali and alkaline metals [180, 181], as well as inorganic and organic molecules [182, 183, 184]. Upon ionization of the droplets, along with CT processes leading to single ionization

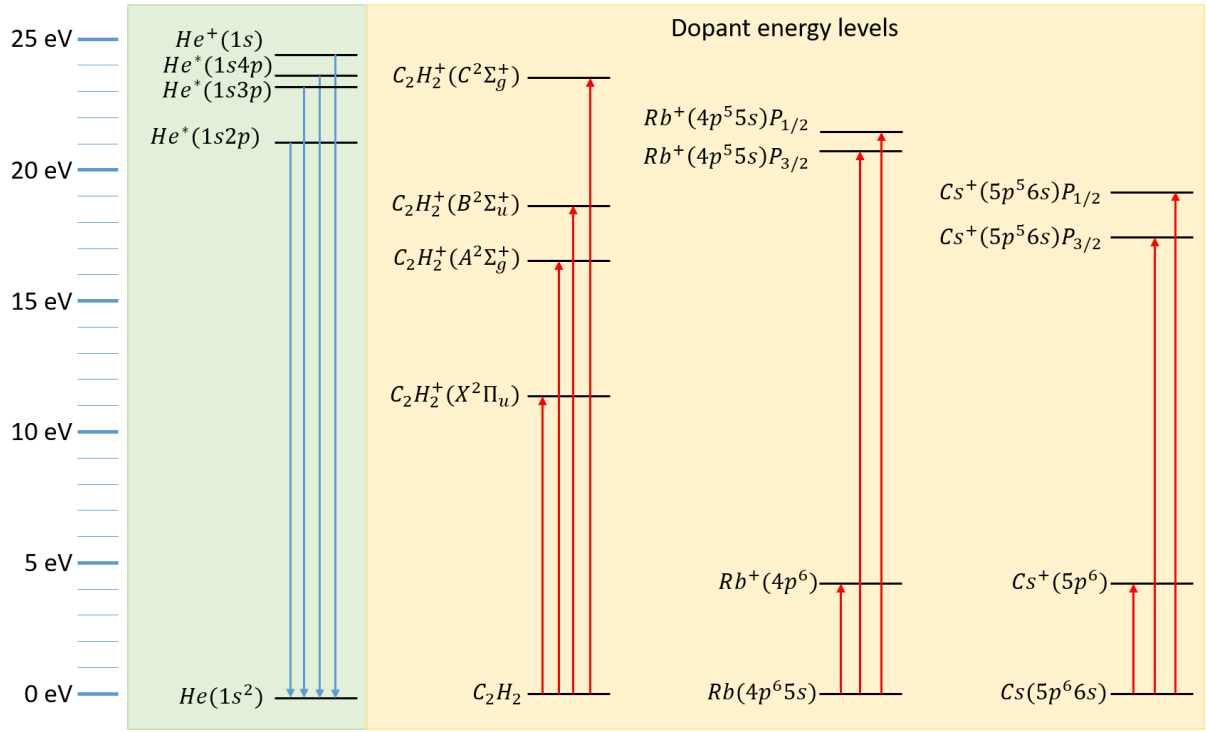

Figure 1.14: Energy levels of atomic He, Rb, Cs and molecular C_2H_2 and possible transitions in C_2H_2, Rb and Cs upon de-excitation of He^* and neutralization of He^+.

of the dopant, double ionization of the same via ETMD(2) for Mg dopants [185] and via ETMD(3) for mixed alkali dopants [186] have been observed. For the later case, even double ionization of the alkali cluster are reported following resonant single-electronic photoexcitation of the host droplet via a new double-ICD mechanism [187]. Furthermore, in case of pure He nanodroplets, ICD processes have been investigated under different experimental conditions, *e.g.*, by creating a singe highly excited $He^{+*}(n = 2, 3, ..)(\geq 65.4$ eV) in the droplet using synchrotron radiation [188], and upon excitations of multiple He atoms in the droplet using highly-intense EUV laser pulses [189, 190, 191, 192].

Thus, research on *inter*-atomic/molecular decay in doped He nanodroplets over the last two decades have resulted in discoveries of many new relaxation processes, and invention of several experimental techniques, making these type investigations an ever-growing active field of research. This thesis specifically concerns with the investigation of *inter*-atomic/molecular decays in the dopants (X_n) following single-electronic resonant-excitation and ionization of the droplet (He_m), see below.

$$He_m{}^* + X_n \rightarrow He_m + X_n{}^{q+} + q\ e^- \tag{1.39}$$

and,

$$\mathrm{He_m}^{+} + \mathrm{X_n} \rightarrow \mathrm{He_m} + \mathrm{X_n}^{q+} + (q-1)\, e^{-} \tag{1.40}$$

where the dopants may undergo different degrees (q) of ionization depending on the participating energy levels of the dopants and the droplets. Two different types of dopants, acetylene (C_2H_2) molecules residing at the interior of the droplet, and heavy alkali metal atoms, rubidium (Rb) and cesium (Cs), which attach to the surface of the droplet are used. Although, the energy levels of dopant- and host- clusters and transitions between them can be quite complex, for simplicity, the energy levels of atomic He, Rb, Cs and molecular C_2H_2 and corresponding transitions are presented in Fig. 1.14. One can see that many cationic states of the dopants are accessible upon decay of the excited or ionized He. Furthermore, some of the energy levels of dopants are very close to the same of He. Thus, specific *inter*-atomic/molecular decay channels can be enhanced, when the host droplet is resonantly excited to a particular energy level by the external perturbation. For this reason, tunable extreme ultraviolet (EUV) radiations having a very high energy resolution ($\Delta E/E \geq 10^{-4}$), available at GasPhase beamline of Elettra Synchrotron Facility, Italy, were used in these experiments to resonantly photoexcite the host to different droplet excitation bands derived from He^* ($1s\ np,\ n \geq 2$) (> 21 eV), and to photoionize above the autoionization threshold (~ 23 eV). Note that, since the double ionization thresholds of C_2H_2, Rb and Cs are $32, 31.45$ and 27.04 eV, respectively, double ionization of monomer dopant in the host-droplet following single-electronic excitation or ionization of the droplet is energetically forbidden. However, double ionization of larger dopant clusters, wherein two single ionization proceed in two neighbouring monomer units, can be observed due to reduction in the double ionization thresholds.

Thus, the following questions are particularly addressed in this thesis:

- What are the pertinent *inter*-atomic/molecular relaxations in the doped He nanodroplets upon photoexcitation and ionization of the host He nanodroplets?
- How do the electronic structures of the dopants, as well as their locations in the host, influence the degree of ionization in the dopants and the corresponding relaxation dynamics?

Electron - multi ion coincident technique using a co-axial time of flight (ToF) and

velocity map imaging (VMI) spectrometer has been implemented for these investigations, wherein correlated kinetic energies of the ejected electrons and ions are measured. In case of alkali dopants, which are weakly-bound to the surface of He nanodroplets, electrons ionized from the dopants due to inter-atomic/molecular decays escape from the host without being massively perturbed by the same. However, for acetylene dopants, which reside at the interior of the droplet, these electrons can undergo inelastic collisions in the droplet environment before the ejection. Thus, the measured electron kinetic energy spectra can be considerably perturbed, from where recovering details about the decay mechanisms and participating electronic states can be challenging [183]. Therefore, the experiment with acetylene dopants is also an attempt to see if electron spectroscopy via inter-atomic/molecular decays can complement the well-established HENDI infrared spectroscopy for structural analysis of the embedded dopants.

Furthermore, the understanding of underlying mechanisms for the simple model-system is beneficial to uncover more intricate decay mechanisms in biological and astrophysical matters in which an entity of interest can be at different locations in the system, and to develop more accurate quantum mechanical description of multi-electron correlation in loosely-bound system.

Details on the experimental setup are presented in chapter 2. Experimental results for acetylene and heavy alkali doping are discussed in chapter 3 and 4, respectively. Finally, in chapter 4.6, the outcomes of this thesis are summarized and future prospects of this research are presented.

Chapter 2

Experimental Methodology

In this chapter, we start by briefly discussing the He nanodroplets generation and doping methodology. Then, the basic principle of the synchrotron radiation and beamline instrumentations to achieve monochromatic radiation to probe the doped He nanodroplets are described. Finally, details about the electron-ion spectrometer as well as the multi-coincidence detection, and data analysis schemes are presented.

2.1 Generating clusters of atoms and molecules

2.1.1 Supersonic expansion in free-jet

One of the most popular ways of creating clusters of atoms or molecules from gaseous state is non-adiabatic expansion of pressurized gas of the corresponding entity through a small orifice or a nozzle into a vacuum chamber. Due to the non-adiabatic nature of the expansion, a collimated beam of atoms or molecules is produced, wherein the three dimensional (3D) velocity distributions of the particles are converted into highly directional velocities with almost near-zero velocity spread. As a consequence, local temperature of the particle beam reduces, and when this local temperature becomes sufficiently low, the particles condense into clusters of atoms or molecules due to the van der Waals forces acting between them.

One can achieve this clusterization by expanding pressurized gas through a nozzle, wherein the gaseous atoms or molecules can attain supersonic velocities following the

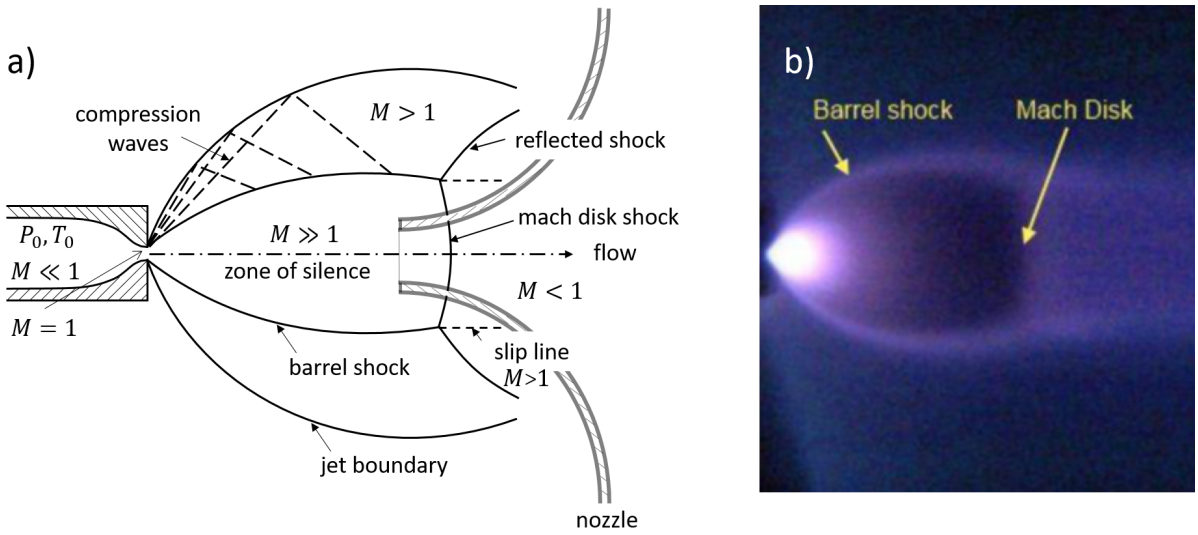

Figure 2.1: a) Schematic of the nozzle-skimmer arrangement for creating supersonic jet, and different expansion regimes. b) Image of the supersonic jet shock-wave and Mach disk structure (adapted with permission from ref.[194]).

expansion [193]. If the backing pressure, commonly known as stagnation pressure, of the gas is P_0, and the pressure on the other side of the nozzle in the vacuum chamber is maintained at P_b (before expansion), then the condition for supersonic expansion is given by,

$$\frac{P_0}{P_b} > 2.1 \tag{2.1}$$

The mean velocity (v) of the atoms or molecules in the supersonic beam is greater than the velocity of sound (v_s) in that medium, i.e., the Mach number, M, which is quantified as v/v_s, is always greater than unity. However, due to interactions with ambient low-pressure gases in the vacuum chamber, the supersonic expansion creates a shock-wave system which separates the supersonic jet from the warm background gases in the vacuum chamber, see Fig. 2.1. Thus, the supersonic beam is only contained in the 'zone of silence', where $M >> 1$. To extract the supersonic beam, therefore, it is required to place a skimmer in the 'zone of silence'. By limiting the transverse jet size, the skimmer prevents the supersonic jet from being destroyed by the interactions with surrounding gases.

2.1.2 Conditions for rare gas clusterization

As the random thermal velocities of the atoms or molecules are converted into highly direction translational velocities in a supersonic free-jet expansion, the local temperature is reduced, which in turn facilitates the cluster formation. Thus, by controlling the local

temperature of the supersonic beam, one can control the cluster formation dynamics. This is experimentally achieved by the changing the stagnation pressure (P_0), the temperature of the gas before expansion, also known as stagnation temperature (T_0), as well as the geometry of the nozzle, such as the diameter of the orifice (d) and the half-angle ($\alpha_{1/2}$) of the nozzle opening. Hagena and co-workers extensively studied rare gas cluster formation by supersonic expansion and proposed a semi-empirical parameter, Γ, also known as Hagena parameter, based on the above mentioned experimental conditions [195], see below.

$$\Gamma = kP_0 \left(\frac{d}{\tan\ \alpha_{1/2}} \right)^{0.85} T_0^{-2.29} \tag{2.2}$$

where, the parameter k depends on the specific gas species. For example, the values of k for He, Ne, Ar, Kr and Xe are 3.85, 185, 1650, 2890 and 5500, respectively. In the above equation, P_0, T_0 and d are expressed in mbar, K and μm, respectively. The cluster formation starts for $\Gamma > 300$ [196], and the estimated average number of atoms per cluster is given by

$$n = 33 \times \left(\frac{\Gamma}{1000} \right)^{q} \tag{2.3}$$

where, the value of q ranges from 2 to 2.5. Usually for $\Gamma \leq 10^4$, one can get an estimate of n by setting $q = 2.35$. However, for $\Gamma \gg 10^4$, Dorchies *et al.* [197], reported a weaker scaling between n and Γ, as shown below.

$$n = 100 \times \left(\frac{\Gamma}{1000} \right)^{1.8} \tag{2.4}$$

2.1.3 Creating helium nanodroplets

As the value of k, used in the Hagena parameter calculation (equation 2.2), is very low for He ($k = 3.85$), compared to other rare gases, creating He clusters is challenging in a standard free-jet expansion. To have Γ greater than 300, required for clusterization, one needs very high stagnation pressure ($P_0 \sim 1 - 100$ bar) and very low stagnation temperature ($T_0 \sim 5 - 30$ K) for typical nozzle diameter of $5 - 100$ μm.

However, due to the large gas throughput resulting from the high stagnation pressure, it is necessary to use ultra-high-vacuum pump with large pumping speed (≥ 1000 L/s) in the source chamber. For unhindered propagation of the cluster beam, a background pressure

of $\sim 10^{-3}$ mbar should be maintained. To manage this background gas pressure in the vacuum chamber, instead of continuous expansion of the He gas, pulsed expansion of the gas has also been implemented using commercial solenoid driven pulsed nozzles, such as, Parker valve [198, 199] and Even Lavie valve [200, 194]. Using these pulsed valves, one can achieve a repetition rate up to 1 KHz with pulse widths between $20 - 100$ μs, which significantly reduces the overall gas load even for higher flux of atoms within a single pulse compared to the continuous mode of operation. Having a pulsed cluster beam is also advantageous for experiments with pulsed laser systems, *e.g.*, table-top femtosecond lasers and free electron lasers (FEL), which have similar repetition rates, since one can synchronize the cluster beam pulses with the light pulses for better probability of light-matter interaction or getting better 'hit-rate'. However, for the current experiments with synchrotron radiation, due to the high repetition rate (500 MHz) of the light pulses, continuous mode of operation with a 5 μm nozzle and a skimmer with 0.4 mm aperture diameter is chosen for obtaining a reasonable data acquisition speed.

The schematic of experimental setup is shown in Fig. 2.2. For producing He clusters, other than having a high stagnation pressure, one also needs low stagnation temperature between $5 - 30$ K. So, the nozzle was first cryogenically cooled to a lower liquid He temperature (4.2 K) using a Sumitomo RDK 415E Cryogenic head connected via high pressure He flex lines with a water-cooled CSW-71D compressor unit [201] from *Sumitomo Heavy Industries Ltd.* Then, the nozzle temperature was raised to a higher value by Joule heating with a resistive heating coil attached to the nozzle holder. To maintain a desired the nozzle temperature, model 325 temperature controller [202] from *Lake Shore Cryotronics Inc.* was used. High purity He gas (99.99999%) (He 6.0) [203] from *Linde Gas & Equipment Inc.*, was delivered from a pressurized gas cylinder (200 bar) to the nozzle for supersonic expansion. For safe delivery of the He gas from the pressurized bottles and monitoring the He backing pressure, high pressure regulators, proportional relief valves, pressure gauges and needle valves from *Swagelok* were installed in the high pressure He gas line as shown schematically in Fig. 2.2. Furthermore, the whole experimental setup consists of four vacuum chambers, housing the mobile He cluster generation machine inside the source chamber, the doping arrangements inside the doping chamber, electron-ion spectrometers inside interaction chamber, and a Langmuir–Taylor detector inside beam dump chamber. In Fig. 2.2, relative distances between different elements are shown above

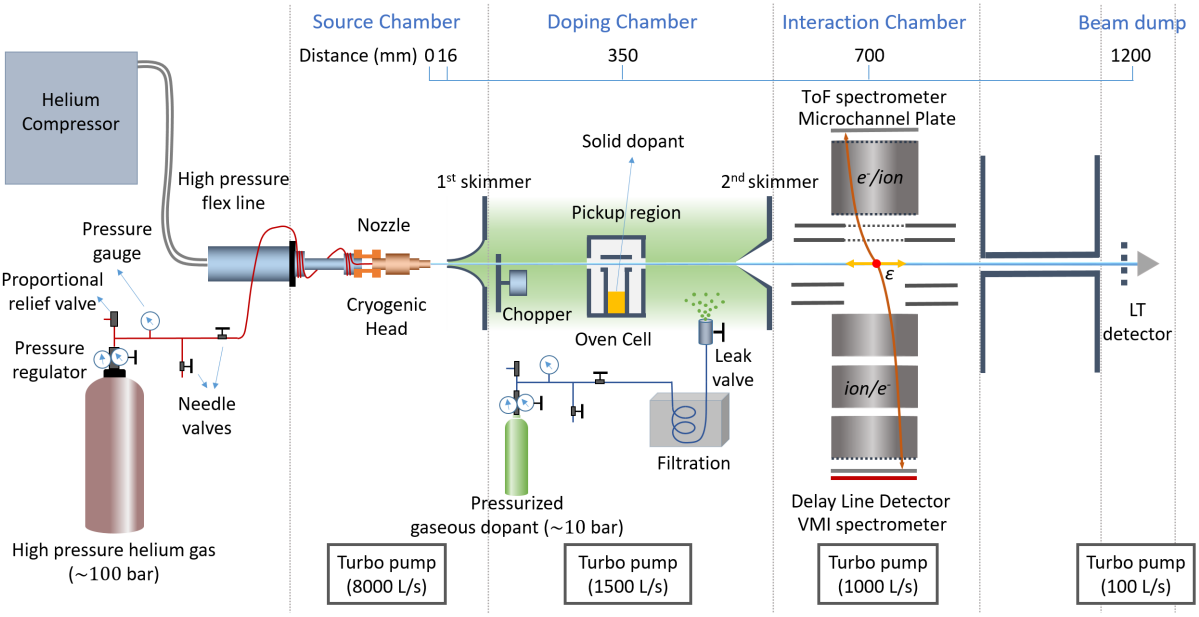

Figure 2.2: Schematic of the experimental setup. Pure He nanodroplets are produced via supersonic expansion of He gas through the cryogenic nozzle and the 1^{st} skimmer in the source chamber. Then, the droplets are doped either with gaseous atoms/molecules which are effused into the doping chamber via a leak valve, or with solid dopants which are evaporated via heating in the oven cell. Subsequently, the doped droplet beam enters the interaction chamber through a 2^{nd} skimmer, wherein the doped droplets are ionized by the linearly polarized EUV light and the resulting ions and electrons are detected by the co-axial ToF and VMI spectrometer. Finally, the droplet beam enters the beam dump chamber, where a Langmuir–Taylor (LT) detector detects to the droplet beam. A mechanical chopper periodically blocks the droplet beam in the doping chamber to enable background subtraction.

and the pumping speeds of the vaccum pumps at each section are shown below. Here, only the source arrangements are discussed, the details on the other parts of the setup are presented in the respective sections, whenever required. However, before going to the doping of He nanodroplets and subsequent probing methods with synchrotron radiation using electron-ion spectrometers, the formation mechanisms of the He clusters at different expansion conditions as well as about their size distributions are presented below.

Fig. 2.3 shows the phase diagram of ^{4}He [204]. Since the temperature in the supersonic jet can reach as low as a few hundred mK [193], one can see that He clusters already reach the superfluid state in the supersonic beam. Furthermore, the generated He clusters in the current experimental conditions have diameters of the order of nanometer. Thus, the He clusters can be referred as He nanodroplets. As discussed in section 2.1.2, the average number of atoms per cluster depends on the stagnation pressure and temperature (P_0, T_0) for a specific nozzle geometry. Therefore, based on the expansion conditions, the cluster

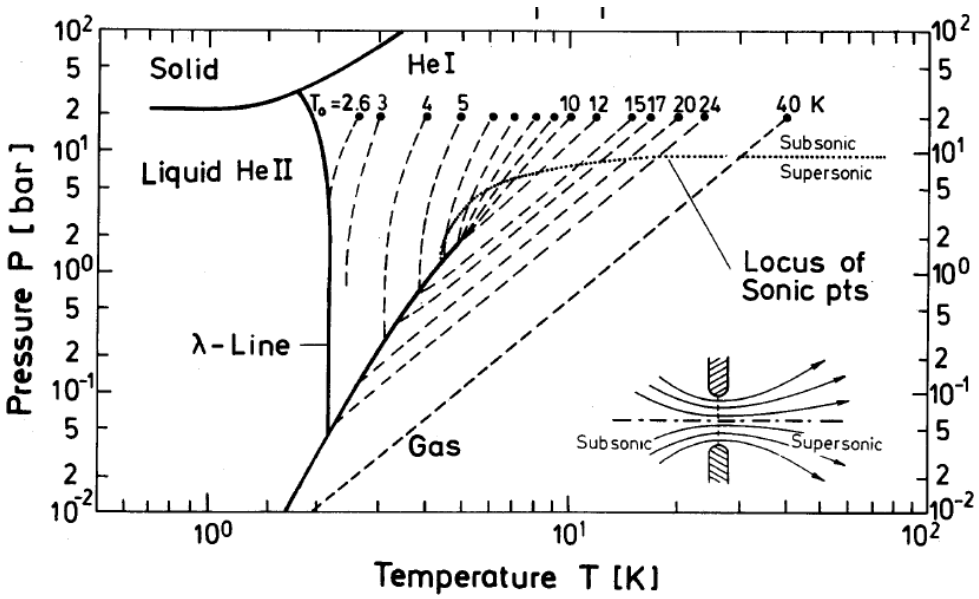

Figure 2.3: Phase diagram of ^{4}He adapted with permission from ref.[204]. The dashed lined shows isentropes for different expansion conditions starting from the stagnation pressure (P_0) of 20 bar at different stagnation temperatures (T_0). The solid lines differentiate between solid, liquid and gas phase of ^{4}He. The solid line between the liquid and gas phase represents the transition from subsonic to supersonic flow of the fluid.

size distributions of He nanodroplets were measured using several techniques, such as, by measuring the fragmented ion time of flights upon electron impact ionization of the droplets [205], by deflecting the droplet beam with a secondary atomic beam and measuring the scattered droplet signal at a specific angle [206], by measuring the attenuated droplet signal upon scattering with rare gases at room temperature [207], or by recent single shot coherent diffraction imaging of individual droplet with X-ray free electron laser pulse [208].

Fig. 2.4 a) and b) show the average number of ^{4}He atoms per droplet ($\bar{N}_4$) as a function of T_0 at different P_0 for 5 μm nozzle [151, 209]. Based on the expansion conditions and cluster sizes, the droplet formation dynamics can be divided into two regimes: 1) supercritical, and 2) subcritical. These expansions regimes are depicted in Fig. 2.4 b), where average droplet size with respect to T_0 for a fixed P_0 follows different trends. In supercritical expansion, which occurs at lower stagnation temperature, the droplets are formed due to fragmentation of liquid He, and average number of atoms ($\bar{N}$) per droplet is large ($\bar{N} > 10^5$). Whereas, in the subcritical expansion, smaller droplets ($\bar{N} \leq 10^5$) are formed due to condensation of gaseous He at relatively high stagnation temperature. Furthermore, in the supercritical region, very large droplets ($\bar{N} \sim 10^{10}$) can be formed

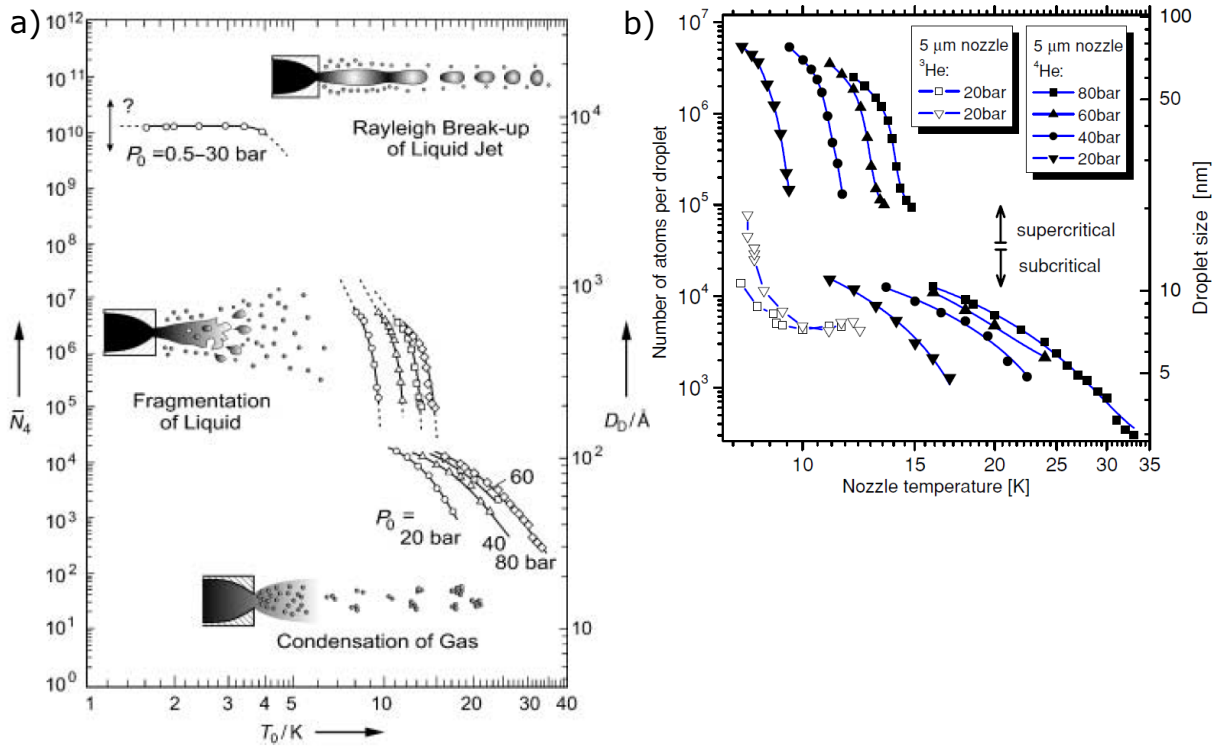

Figure 2.4: a) Average number of ^{4}He atoms per droplet ($\bar{N}_4$) as a function of stagnation temperature (T_0) at different stagnation pressure (P_0) (adapted with permission from ref.[151]). b) Average number of atoms per droplets as a function of nozzle temperature at different stagnation pressures for 5 μm nozzle both for ^{3}He (open symbols) and ^{4}He (adapted with permission from ref.[209]). The vertical axis on the right shows the diameters of the droplets. The data for ^{4}He in panels a) and b) are identical.

from the breakup of liquid He due to Rayleigh instability [210]. These droplet formation mechanisms are schematically shown in the insets of Fig. 2.4 a). Note that, for our experiments, He nanodroplets are generated at $14-16$ K nozzle temperature and 50 bar backing (stagnation) pressure using similar nozzle, which falls under the subcritical regime.

It should be noted that, He nanodroplets produced at this subcritical expansion condition, follows a log-normal size distribution, see below.

$$f(N) = \frac{1}{N}\frac{1}{\sqrt{2\pi\sigma}}\exp\left(-\frac{(\ln(N/N_0))^2}{2\sigma^2}\right) \tag{2.5}$$

where, N, N_0 and σ are the number of the atoms per droplet, most probable cluster size and the standard deviation of the distribution. Fig. 2.5 shows the distribution of number of atoms per droplet produced by a 5 μm nozzle for different nozzle temperatures at 80 bar stagnation pressure [206]. Moreover, assuming the droplets to be spherical with uniform density of atoms, one can estimated the radius of the droplets containing N number of

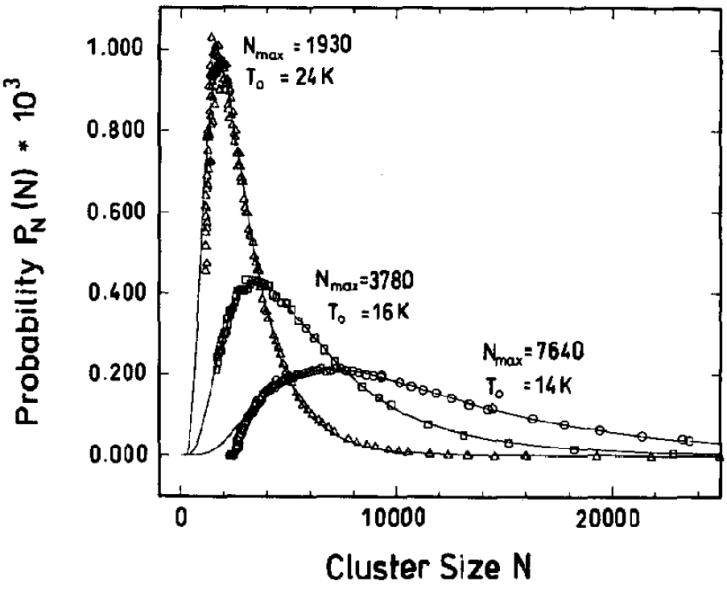

Figure 2.5: Helium cluster size distributions at different nozzle temperatures, for stagnation pressure of 80 bar and 5 μm nozzle diameter (adapted with permission from ref.[206]).

He atoms as follows [151, 211].

$$R = 0.222 \times N^{1/3}[\text{nm}] \tag{2.6}$$

2.2 Doping of foreign atoms and molecules

He nanodroplets can easily pick up foreign atoms and molecules from gas phase by inelastic collisions. Thus, the pure He nanodroplets are doped on their travel path by introducing dopant atoms or molecules of interest in the doping chamber, just after they exit the source chamber (see Fig. 2.2). For gaseous dopants like acetylene, the dopants are usually effused into the doping chamber in a controlled way using an ultra high vacuum variable leak valve from *Leybold*. However, for solid dopants such as alkali metals, the dopants are evaporated by heating the sample in a temperature controlled oven cell, kept on the path of the droplet beam inside the doping chamber. Since the droplets can capture multiple dopants, the number of dopants per droplet is decided by the density of these dopants inside the doping chamber or in the oven cell. Thus, the levels of doping in He nanodroplets are regulated by changing the partial pressure of the dopants. The probability ($p(k)$) of doping k number of dopants follows Poisson distribution [212, 213, 214, 215], which is

given by,

$$p(k) = \frac{K^k}{k!} \exp(-K) \tag{2.7}$$

where, K is the average of number of dopants captured by a droplet of specific size. The value of K is determined by the capture cross section (σ_{cap}) of the droplet, the density (ρ) of the dopants in the pick-up region, and the length (L) of the pick-up region, as shown below.

$$K = \sigma_{cap} \rho L \tag{2.8}$$

Note that, the capture cross section (σ_{cap}) is related to the geometric cross section (σ_{geo}) by a sticking coefficient (ζ) as follows,

$$\sigma_{cap} = \zeta \sigma_{geo} \tag{2.9}$$

where, the value of the sticking coefficient (ζ) varies between 0.5 and 0.9 [212]. Assuming the He droplet to be classical spherical object of radius R, and since the size of the nanometer-sized droplet is much larger than the dopant atom or molecule, the geometric cross section for collisional pick-up of dopant by the droplet can be approximated as $\sigma_{geo} \approx \pi R^2$. For a droplet comprising of N number of He atoms, the radius of the droplet can be calculated from equation 2.6. Thus, the value of σ_{geo} is given by,

$$\sigma_{geo} \approx 0.15 \times N^{2/3} [\text{nm}^2] \tag{2.10}$$

Underlying the above formalism, the capture cross section (σ_{cap}) is assumed to be constant through out pick-up process and the relative velocities of the dopants are neglected. However, this is only true for a very low number of pick-ups. Since the binding energy of a He atom in a droplet is extremely low (~ 0.6 meV), the energy released due to pick-up of several dopants can evaporate a large number of He atoms, resulting in a considerable shrinkage of the droplet size. The total energy released ($E_{pick-up}$) due to the pick-up of the dopants (X) can be estimated as

$$E_{pick-up} = E_{coll} + E_{int}(\text{X}) + E_b(\text{He}-\text{X}) + E_b(\text{X}-\text{X}) \tag{2.11}$$

where, E_{coll} is the collisional kinetic energy release, E_{int} is the internal energy of dopants,

E_b is the binding energy between the dopants (X−X) and between He and dopant (He−X). E_{coll} can be calculated from the random thermal velocities of the dopants and from the velocity of droplet in the jet, as follows.

$$E_{coll} = \frac{3}{2}k_B T + \frac{1}{2}m_{\mathrm{X}} v_{\mathrm{He}}^2 \tag{2.12}$$

where, T in the temperature of the dopant gas, k_B is the Boltzmann constant, m_{X} is the mass of the dopant and v_{He} is the velocity of He droplet ($\sim$ 350 m/s). In case of molecular dopants, E_{int} comprises of the rotational ($\sim$ 1 meV) and the vibrational ($\sim$ 100 meV) energies. For X = Ne, Ar, Kr, and Xe, the binding energies (E_b(X−X)) are 20, 80, 115 and 163 meV, respectively [216], whereas binding energies (E_b(He−X)) are $\sim$ 27 meV [212]. Thus, the number of evaporated He atoms (N_{evap}) for capture of a dopant is given by,

$$N_{evap} = \frac{E_{pick-up}}{0.6 \text{ meV}} \tag{2.13}$$

Considering the shrinkage in droplet size due to evaporation of He atoms, Kuma *et al.* [214] proposed the following formula for the average number of dopants (N) picked up by the droplets in the Poisson distribution (see equation 2.7)

$$K = \frac{N_0}{N_{evap}} \left[1 - \left(1 - \frac{N_{evap} \chi P_{\mathrm{X}}}{3N_0} \right)^3 \right] \tag{2.14}$$

where, N_0 is the number of atoms per droplet before doping, P_{X} is the partial pressure of the dopants, and the parameter χ is given by,

$$\chi = \frac{\sigma_{cap} L}{k_B T} \sqrt{\frac{\langle v_{\mathrm{He}}^2 \rangle + \langle v_{\mathrm{X}}^2 \rangle}{\langle v_{\mathrm{He}}^2 \rangle}} \tag{2.15}$$

The Poissonian distribution of the dopants in He nanodroplets is validated in various studies with molecular dopants such as SF_6 [163], propyne [217], Mg-phthalocyanine [214]. For example, Hartmann *et al.* measured the depletion in the absorption band related to attached $(SF_6)_k$ clustes in the droplets for $k = 1 - 4$ as a function of the density of the dopants or in other words as a function of the dopant pressure in the pick-up cell (see Fig. 2.6). The measured dependences in the depletion signals fit reasonably well with Poisson distributions. However, it should be noted that, for dopants that attach to the

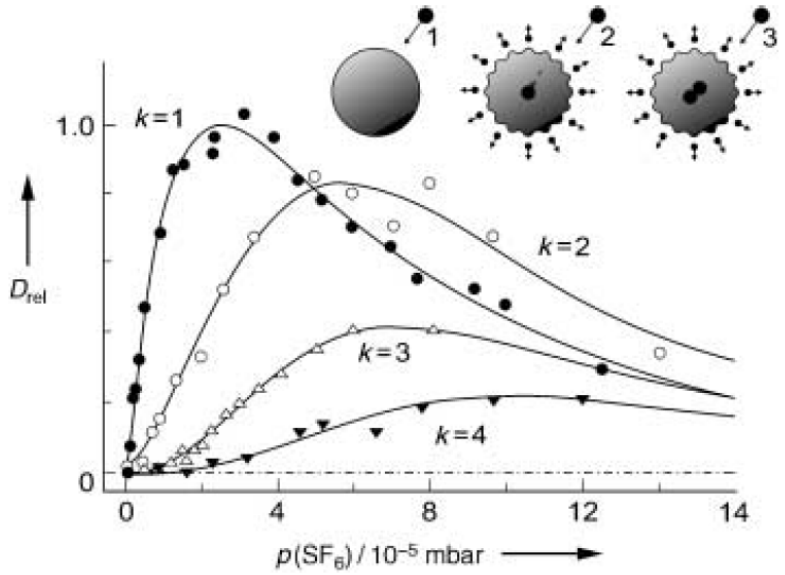

Figure 2.6: Dependence of the depletion signal (D_{rel}) on the SF_6 pressure in the pick-up cell, as measured for the absorption bands for $(SF_6)_k$ complexes with different k values [163]. Solid curves are obtained from fitting Poisson distributions (see equation 2.7). The mean droplet size is $N_0 = 4.1 \times 10^3$ atoms. The insert shows a schematic representation of the pick up, coagulation, and evaporative cooling processes. Adapted with permission from ref.[151].

surface of the droplets such as alkali dopants, considerable deviation from the Poissonian distribution has been reported [218].

2.3 Synchrotron radiation

As a source of perturbation to the doped He nanodroplets, radiation from Elettra Synchrotron Facility, Italy was used in the current set of experiments. In the basis form, charged particles with relativistic energies are accelerated around a circular arc in a synchrotron facility, which leads to emission of radiation. Fig. 2.7 shows schematic of a typical synchrotron facility. First, electrons are usually generated through thermionic emission from a heated filament in an electron gun. Note that, alternative electron generation methods, such as, laser ablation from intense ultrafast laser pulses, are also implemented in modern synchrotron facilities. The generated electrons are then accelerated via a linear accelerator (LINAC) to ~ 100 MeV, and injected into a booster ring where they are further accelerated to a few GeV. Once the electron energy reaches close to the operating energy of the synchrotron ($2 - 2.4$ GeV for Elettra) in the booster ring, they are transported to a storage ring, where bending magnets or insertion devices, such as, wigglers

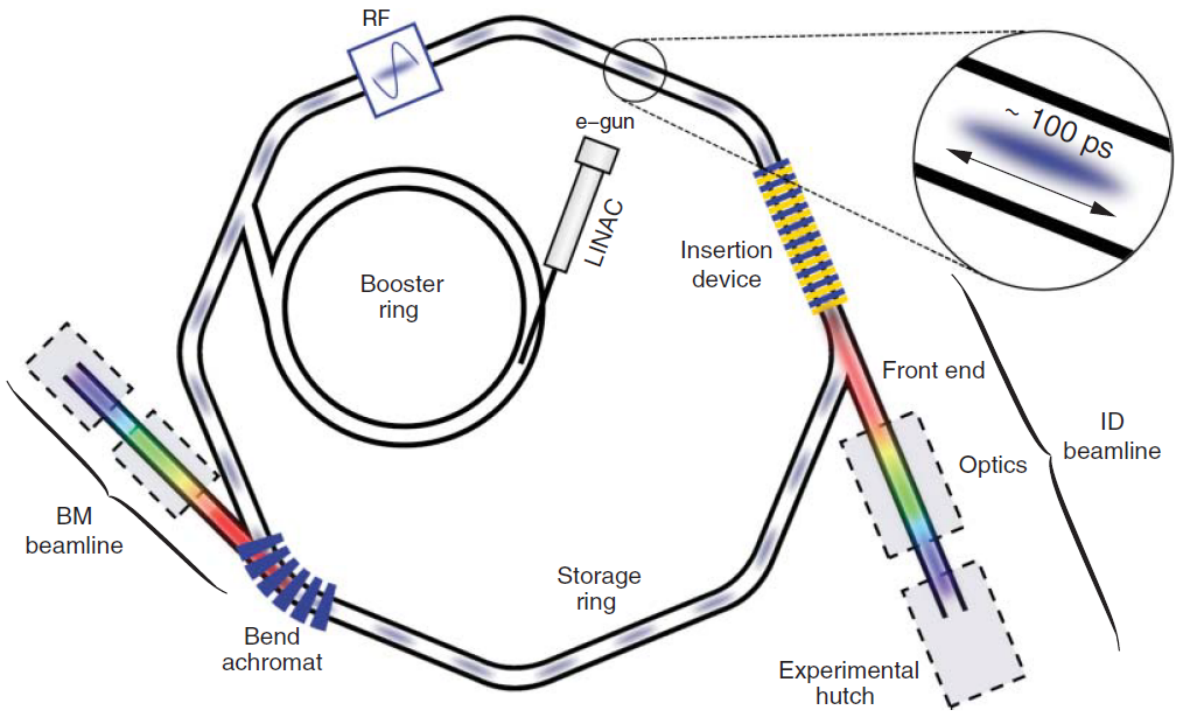

Figure 2.7: Schematic of different components in modern synchrotron radiation facility, adapted with permission from Figure 3.1 of ref.[219].

and undulators, generate radiation by bending the electrons along their paths using magnetic fields. Finally, the generated radiation enters the experimental hutch through a set of beamline optics, wherein the radiation beam is suitably monochromatized and focused for probing the experimental sample.

Note that, the electrons rotate multiple times inside the booster and storage rings, before they decay due to collisions with background gases. Thus, it is important to have a continuous source of electrons, and to periodically 'top up' electrons from the booster ring to the storage ring. Moreover, to keep the electrons in closed paths inside these rings, arrays of magnets, also known as magnetic lattice, are used, wherein bending dipole magnets are used for changing the electron paths so that they follow closed orbits, quadrupole magnets are used to refocus the diverging electron beam, and sextupole magnets are used to correct the chromatic aberrations. To accelerate the electrons and to compensate for the lost power due to radiation, radio frequency (RF) cavities are inserted in the storage ring. These RF cavities also bunch the electrons into pulses which usually have a typical pulse width of hundreds of picoseconds (ps) and repetition time of a few nanoseconds (ns). These repetition time (2 ns for Elettra) and pulse width (130 ps for Elettra) are

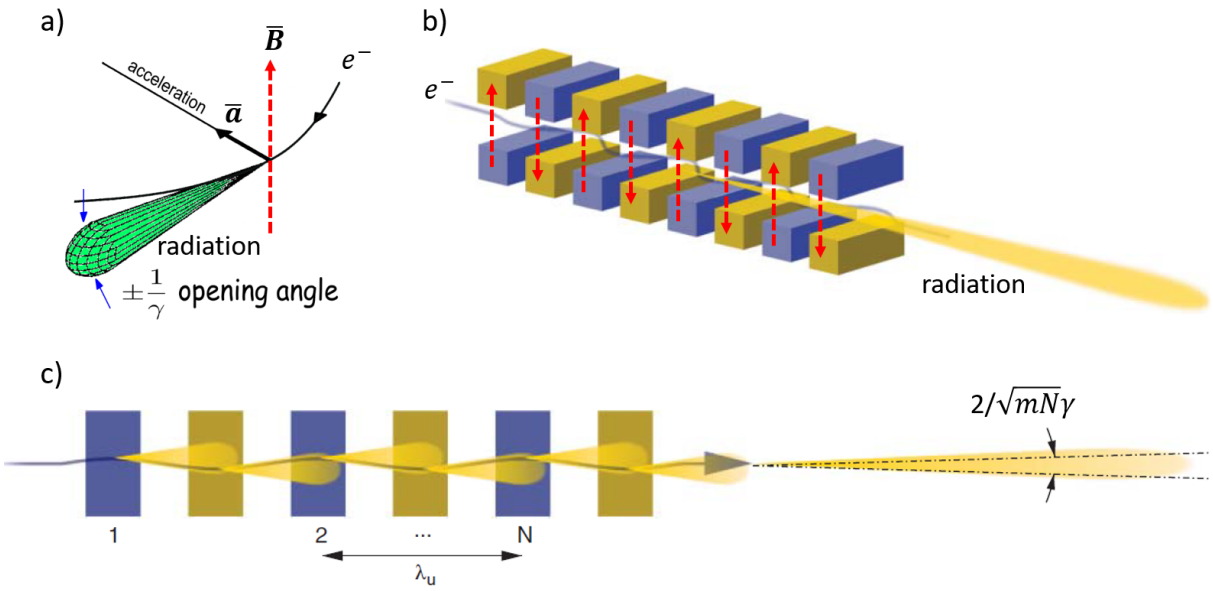

Figure 2.8: a) Schematic of the emitted radiation from a relativistic electron which travels along a circular arc due to the effect of a magnetic field ($\bar{B}$), such as that generated by bending magnet, adapted from ref.[221]. b) Periodic arrangement of magnetic fields in an undulator which generates the radiation, adapted with permission from Figure 3.11 (a) of ref.[219]. c) Interference of radiations generated at each electronic arc in the undulator, adapted with permission from Figure 3.34 of ref.[219].

reflected in the generated synchrotron radiation too. Thus, at Elettra, the obtained radiation pulses have a very high repetition rate of 500 MHz. Details about the Elettra machine parameters can be found in ref.[220].

Fig. 2.8 a) shows the directionality of the emitted radiation, when an electron with relativistic energy is bent across a circular arc under the influence of external magnetic field ($\bar{B}$). The radiative energy-loss (P) of a relativistic electron, due to centripetal acceleration ($\bar{a}$) generated by Lorentz force, is given by,

$$P = \frac{2}{3}\frac{e^2}{c^3}\gamma^4 a^2 \tag{2.16}$$

where, e is charge of the electron and c is velocity of light in vacuum. The Lorentz factor is denoted as γ, which is calculated as $1/\sqrt{1-\beta^2}$, where β is ratio of electron velocity and c. The radiation is emitted tangential to the arc with an opening angle of $\pm(1/\gamma)$. Thus, at relativistic electron energies, the emitted radiation becomes highly directional with a few milliradians (mrad) of beam divergence.

The experiments presented in this thesis were conducted at the GasPhase beamline of

Elettra [222, 223], wherein radiation is obtained from an undulator. An undulator consists of periodic arrangement of permanent magnets, which creates alternating magnetic fields along the electron path as shown in Fig. 2.8 b). Due to this magnetic arrangement, radiations emitted at each electronic arc interfere with each other (see Fig. 2.8 c)), and radiation beam intensity and divergence are greatly improved. The condition for constructive interference is given by,

$$m\lambda_m = \frac{\lambda_u}{\beta}\left[1 + \left(\frac{f}{2\gamma}\right)^2\right] - \lambda_u \tag{2.17}$$

where, λ_m is the wavelength of the m-th harmonic of emitted radiation, λ_u is the undulator period and the parameter, f, is defined as,

$$f = \frac{eB_0\lambda_u}{2\pi m_e c} \tag{2.18}$$

where, B_0 is the maximum magnetic field created in the electron path by the permanent magnets, and m_e is the rest mass of the electron. One can see from the above two equations that the wavelength of the emitted light (λ_m) can be easily tuned by changing B_0 and λ_u. However, since λ_u is a geometrically fixed parameter, in a typical undulator beamline, the wavelengths of emitted radiation is tuned by changing the vertical gap between the permanent magnets, thereby changing the value of B_0. Furthermore, the radiation emitted in the undulator is linearly polarized with the plane of polarization coinciding with the plane of the electron beam undulations.

It should be noted that, the emitted radiation consists of all the harmonics. Thus, in order to obtain radiation of specific wavelength or photon energy, the emitted radiation should be monochromatized. Fig. 2.9 shows the optical arrangements at the GasPhase beamline [222, 224]. First, the synchrotron radiation from the undulator is focused onto a variable angle spherical grating monochromator using a pre-focusing mirror and an entrance slit. The monochromatized beam is then passed through an exit slit and transported to the experimental station at the branch line using a switching mirror. The photon energy resolution and the photon beam flux are controlled by adjusting the slits on the beam path. At the GasPhase beamline, energy resolution ($\Delta E/E$) of 10^{-4} can be achieved over the whole available photon energy range between 13 and 900 eV, wherein

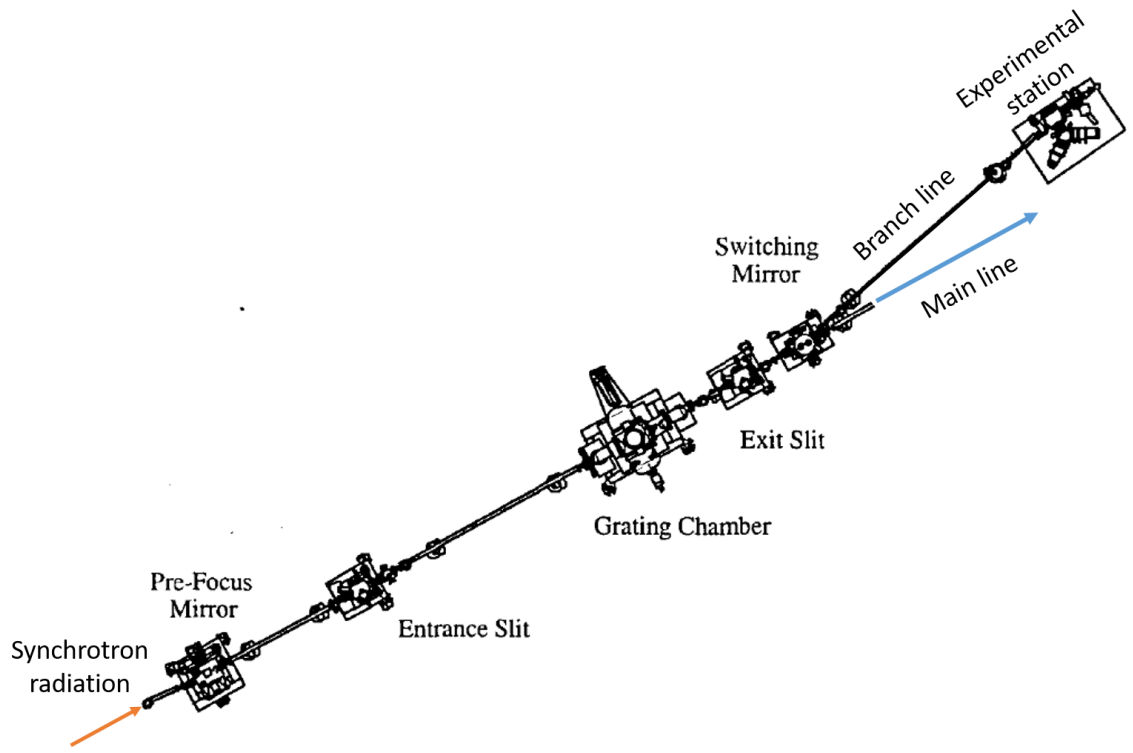

Figure 2.9: Schematic of the optical arrangements implemented to monochromatize the synchrotron radiation at the GasPhase beamline of Elettra, adapted from Figure 1 of ref.[224], permission granted by www.tandfonline.com.

the photon energy of the emitted radiation from the monochromator was calibrated from the photoabsorption and photoionization spectra of rare gas atoms. Note that, for experiments where the host droplets were photoexcited via $19-23$ eV photons, a tin (Sn) filter of 200 nm thickness was used in the beam path to further suppress the higher harmonics, so that the ionization of host He droplets by the incident high harmonic photons can be avoided.

2.4 Co-axial electron and ion spectrometer

As discussed in section 1.3, to investigate the *inter*-atomic/molecular decay processes, it is important to measure the kinetic energies of the electrons in coincidence with the various fragmented ions as well as the total kinetic energy released by the ions in these processes. Thus, a co-axial but opposing pair time of flight (ToF) and velocity map imaging (VMI) spectrometer, capable of detecting ions and electrons in coincidence, is used in these experiments. The spectrometer is kept inside the interaction chamber as shown in Fig. 2.2, wherein the doped droplet clusters as well as the background gases

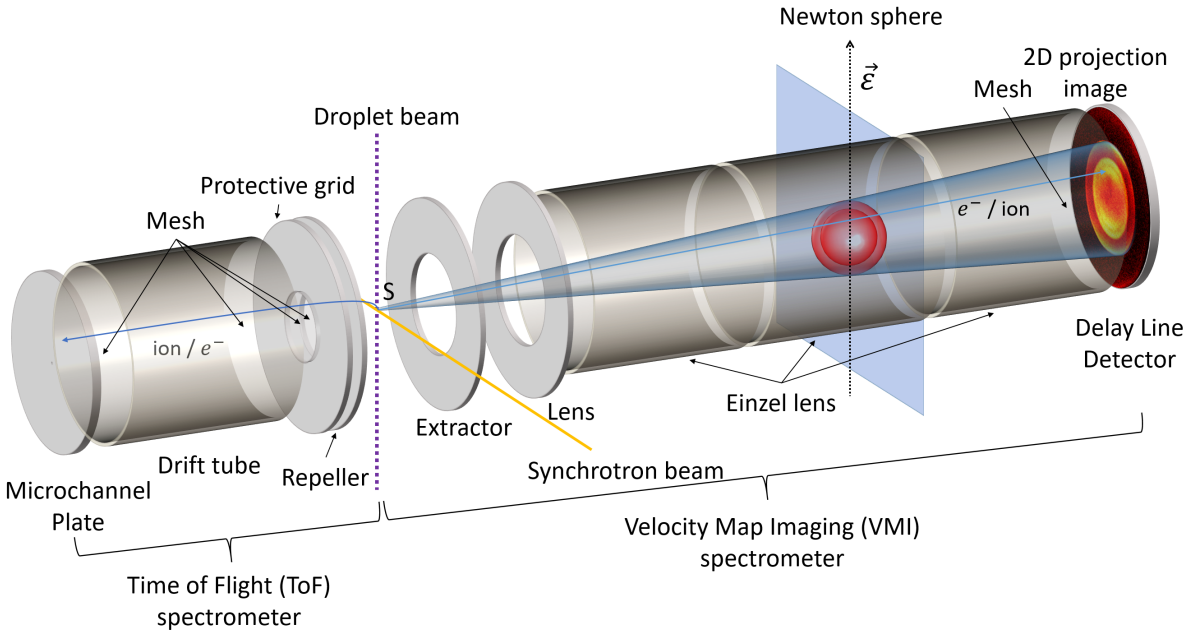

Figure 2.10: Schematic arrangement of the electrodes and detectors of the co-axial time of flight and velocity map imaging spectrometer.

interact with the synchrotron radiation at the middle of the ToF and VMI segments of the spectrometer. However, to get the ionization signals only from droplet ionization, a mechanical chopper is introduced in the doping chamber to periodically block the droplet beam at $\sim$ 60 Hz. When the chopper is 'open', the droplet beam is allowed to enter the interaction chamber, and both the droplet and background ionization signals are recorded. Whereas, only the background ionization signal is recorded when the chopper is closed. Thus, one can properly eliminate the contributions from background ionization by subtracting the chopper 'close' signal from the chopper 'open' signal. Note that, in our experimental configuration, the cluster jet, the photon beam and the spectrometer axis are orthogonal to each other with interaction point residing on the spectrometer axis. Furthermore, the light polarization axis is parallel to the cluster jet direction.

Fig. 2.10 shows the schematic of the spectrometer and geometric arrangement of different electrodes and the detectors. The left side of the spectrometer from the interaction point or source (s) in Fig. 2.10, functions on the principle of a Wiley-McLaren type ToF spectrometer [225], in which the charged particles are detected using a microchannel plate (MCP). This part consists of two accelerating regions and one drift region for enhanced spatial focusing of the source points within the interaction region. In the first accelerating region across the source, static electric field is generated by applying voltage differences

between two electrodes with open apertures (extractor and repeller), to accelerate the charged particles towards the MCP detector. Note that, in the original Wiley-McLaren ToF spectrometer, however, electrode-apertures were covered with meshes for generating homogeneous electric fields at this region. For the current spectrometer, the electrode-apertures are kept open for accommodating the VMI part which requires inhomogeneous electric fields for mapping the velocities of the oppositely charged particles on the other side. Immediately after repeller electrode, a protective grid attached with mesh is placed on the left, so that the electric fields become homogeneous afterwards. Same voltages are applied to the repeller and the grid. The second accelerating region with homogeneous electric field is created between the grid and the drift tube, where on both sides of the drift tube, meshes are attached and same voltages are applied. Note that this voltage is, however, different from that of the grid. After travelling through the accelerating and drift regions, the charged particles hit the MCP detector where appropriate bias voltages between the MCP front and back are applied and the detection signals are collected from the MCP anode.

In Fig. 2.10, the right side of the spectrometer from the source (s) is based on the principle of velocity map imaging [226]. Charged particles with different kinetic energies form three dimensional 'Newton spheres' with different radii, as shown schematically in Fig. 2.10, which are then projected onto a two dimensional position sensitive detector. For mapping particles with same momentum components (parallel to the detector plane) on the same point of the detector, a lens electrode with open aperture and an Einzel lens are placed between the extractor and the position sensitive detector. By referencing the lens electrode to the ground, and voltages are applied to the other electrodes and detectors accordingly using high voltage power supplies from *iseg Spezialelektronik GmbH* and *Elettra – Sincrotrone Trieste S.C.p.A.* [227, 228]. Note that, the Einzel lens is used for mapping very high energy electrons and ions. However, for the current experiments, voltages on all the Einzel lens segments are kept same. This configuration enables detection electrons and ions with kinetic energies up to 30 eV over the entire 4π solid angle, which is sufficient for our current investigation. The end aperture of the Einzel lens is covered with a mesh, after which a cross delay line detector (DLD) [229] from *Elettra – Sincrotrone Trieste S.C.p.A.*, capable of measuring both the two dimensional positions (x,y) and detection times (t) of the particles, is placed. Note that, since the charged par-

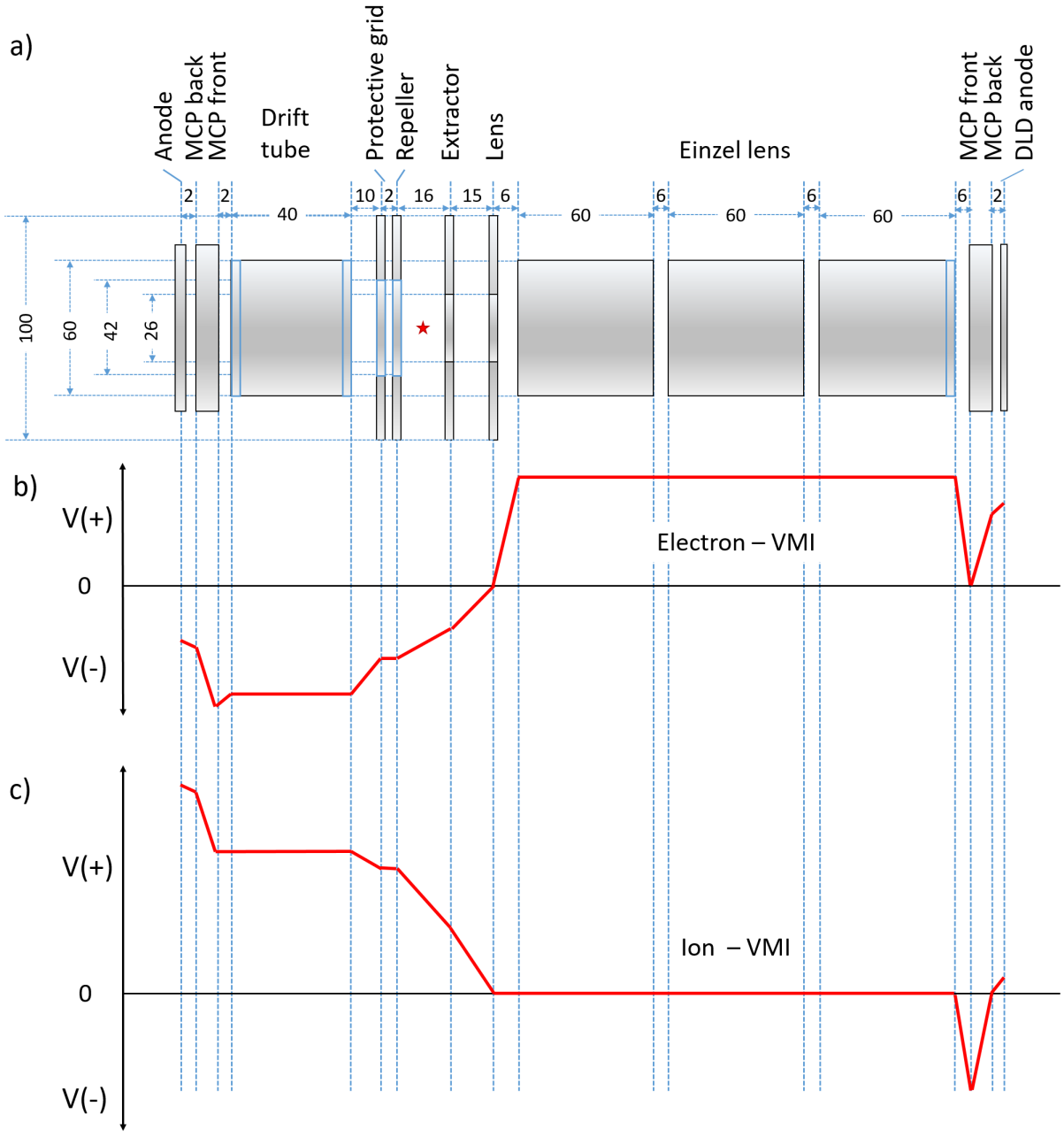

Figure 2.11: a) Schematic of the spectrometer electrodes and detectors along with the relevant dimensions of different elements (in mm) and distances between them (in mm). Schematic of the voltage settings of the spectrometer when operated in b) electron-VMI and c) ion-VMI modes. Adapted with permission from Dr. Robert Richter.

ticle trajectories can be influenced by both the electric and magnetic fields, to eliminate the effect of earth's magnetic field, the whole spectrometer is surrounded by a μ-metal shield of 2 mm thickness. All the mashes attached to the electrode-apertures are gold meshes with a pitch of 70 lines per inch.

The electrons and ions, created at the interaction point, are guided opposite to each other for a particular spectrometer voltage setting. Based on the directions in which the electron and ions are guided, the spectrometer can be operated in two different modes: a) electron-VMI, and b) ion-VMI. In the electron-VMI mode, the electrons are detected on the VMI side while the ions are detected on the ToF side. Whereas, in the ion-VMI mode, the ions on the VMI side and the electrons are detected on the ToF side. Fig. 2.11 a) shows dimensions (in mm) of different electrodes and detectors as well as distances (in mm) between them. Fig. 2.11 b) and c) shows the schematic of voltage settings for the electron-VMI and ion-VMI modes, respectively.

2.4.1 Coincident detection of electrons and ions

In Fig. 2.12, the electronics that enables coincidence detection of the charged particles are schematically presented. The analogue detection signal from the MCP detector on the ToF side, is first fed into a pre-amplifier and then into the constant fraction discriminators (CFD) (from *Elettra – Sincrotrone Trieste S.C.p.A.*). Following which, the signal from the CFD is divided into three routes, where one signal is directly fed into the NIM-TTL converter [230] (from *CAEN S.p.A.*) and other two signals are combined with the chopper 'open' and 'close' signals using AND logic gates [231] (from *Phillips Scientific.*). The chopper 'open' and 'close' signals represent the status of the chopper dictating whether the droplet beam is present or not at the interaction regime when the MCP signal is recorded. Note that, proper delays in these signals before they are fed into the AND logic gates are generated using delay generators [232] (from *Phillips Scientific.*). The outputs of the AND gates are also then fed into the NIM-TTL converter. In this way, three NIM singles are created from the MCP detector that can discriminate between chopper 'open', 'close' and 'all' status. This scheme is useful for subtracting the background from the foreground to get droplet correlated signal, as well as for getting signals out of the MCP detector when the chopper is switched off.

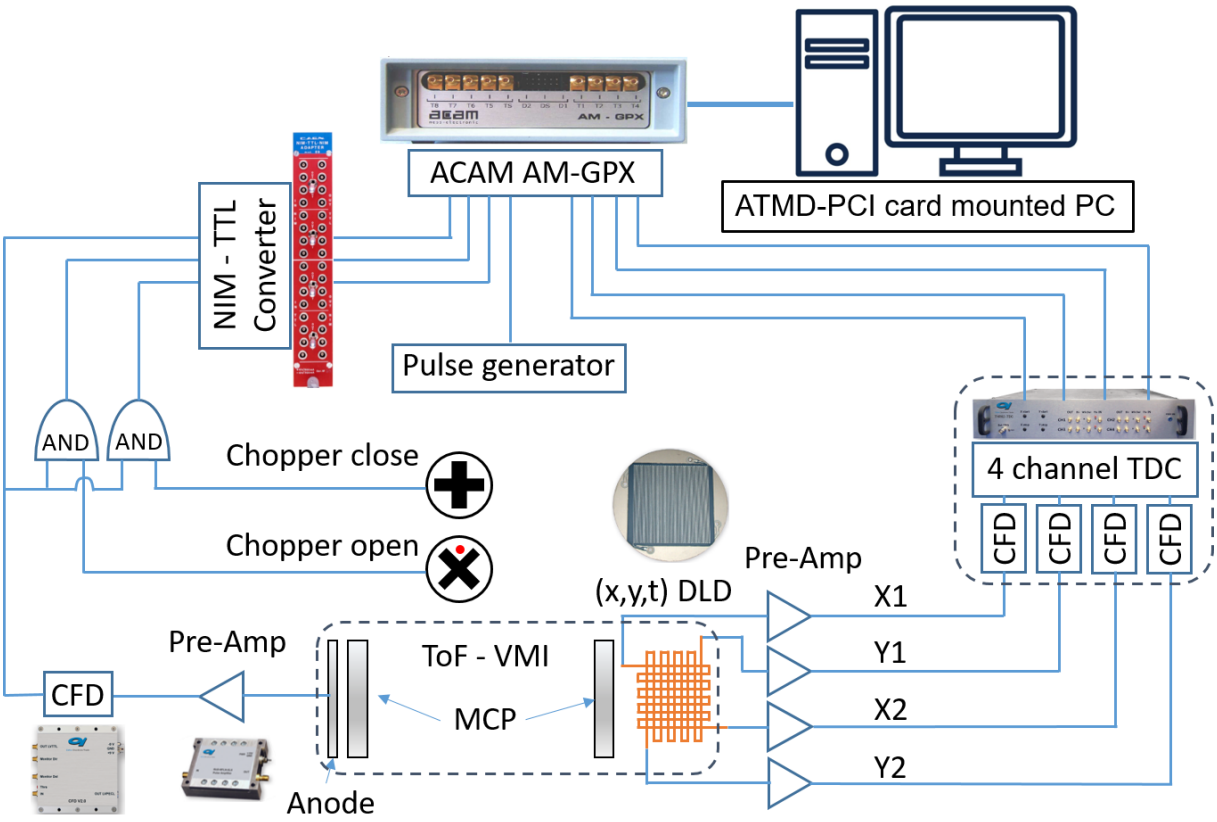

Figure 2.12: Schematic of the electronics for electron - multi ion coincidence measurements using co-axial ToF and VMI spectrometer. Adapted with permission from Dr. Robert Richter.

On the VMI side, four signals (X1, X2, Y1, Y2) are collected from the DLD and fed into four pre-amplifiers. Then, the amplified signals are converted into digital signals, which encode the timing information, using a four-channel THR08-TDC module (from *Elettra – Sincrotrone Trieste S.C.p.A.*). Finally, all the processed signals from the MCP and DLD detectors are fed into the ACAM AM-GPX module [233] (from *acam-messelectronic GmbH.*). An external pulse generator [234] (from *Stanford Research Systems*) is used to trigger the ACAM module at 1 KHz to reset the time counter to zero. After each trigger, an event window is set when all the data is recorded. For the current experiments, it is set at 800 μs, so that even the slowest ion can reach the detector within the event window. The intensity of radiation (typical set at $\sim 15\ W/m^2$) and gas density at the interaction region are also kept low enough such that only one ionization occurs within one event window. However, any false coincidence is eliminated in the post-processing of the data. The output signals from the ACAM AM-GPX, which contains digital time stamps of each detected particle within an event window, are saved on a computer through ATMD-PCI

card (from *acam-messelectronic GmbH.*). Note that, within each event window upto 8 distinguishable-hits can be recorded.

Thus, finally one gets a list mode data for each event of the following: 1) timestamp of each particle detected on the MCP flagged with the chopper status, 2) X1, X2, Y1 and Y2 timestamps of each particle detected on the DLD. From the X1, X2, Y1 and Y2 timestamps, the 2D position of each particle is calculated as follows:

$$x = (t_{X1} - t_{X2}) \times v_{signal} \tag{2.19}$$

$$y = (t_{Y1} - t_{Y2}) \times v_{signal} \tag{2.20}$$

where v_{signal} is the velocity of signal on the delay line. The time of detection (t) of each particle can be calculated from the mean of these timestamps. Due to the very light mass, electrons are detected almost instantaneously after the ionization within a few nanoseconds. In case of multiple electrons produced in the same ionization, the position of only one electron is obtained in the electron-VMI mode, since all the electrons hit the detector virtually at the same time within the time resolution of the TDC ($\sim$ 2 ns). However, the ions are detected on the timescale of microsecond after the ionization. Thus, the electron-detections by the MCP and DLD act as the start signals for measuring flight times of the ions between the source and detector, in the ion- and electron- VMI modes, respectively.

Fig. 2.13 shows the charged particle detection schematic for two sample photoionization events of AB producing A and B^+ in the first event, and A^+ and B^+ in the second. Upon the event trigger at every 1 ms, the TDC starts counting the time, and when the electrons reach the detector, time of ionization is obtained. Depending on their mass and charge, the ions hit the other detector at a later time from which the time of flights (ToFs) are calculated for each detected ion. Fig. 2.13 also shows the processed data that can be calculated from both the electron- and ion- VMI modes. In case of electron-VMI mode, the 2D positions (x,y) of electrons are recorded from the VMI side, while the ion-ToFs and chopper status (ch) are recorded from the ToF side. Whereas, in the ion-VMI mode, the chopper status is known from the electron detection on the ToF side, and 2D position and ToF of each detected ion are recorded from the VMI side. Now, this is obvious

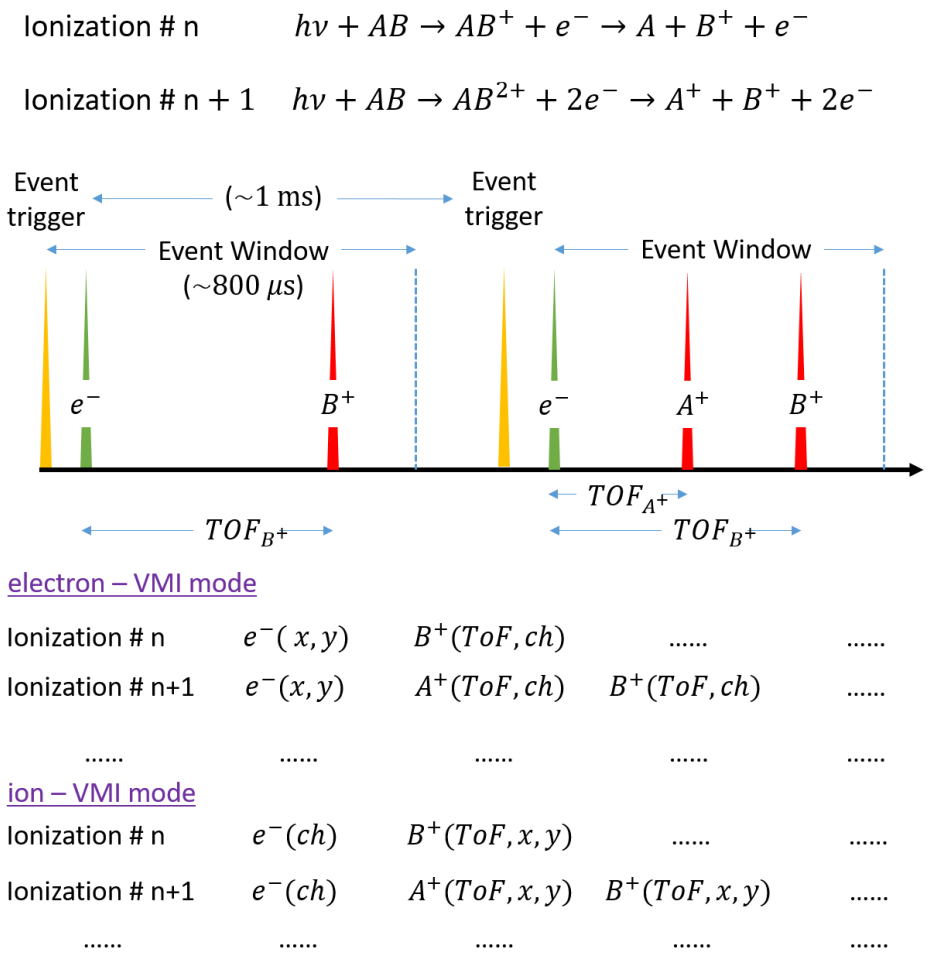

Figure 2.13: Multi-coincidence detection schematic of electrons and ions from different ionization events, as well as processed list mode sample data of the same in electron- and ion- VMI modes.

from the list mode data, presented in Fig. 2.13, that one can get electron and ion- VMI images (2D projections of the velocity distributions) correlated to different ions at different chopper conditions by selecting specific ToF windows and chopper conditions in the post processing.

Furthermore, in ionization where multiple ions are created from the same molecule or cluster, the ion-ToFs will be anti-correlated. This anti-correlation can be easily understood from the second sample photoionization discussed above ($AB^{2+} \rightarrow A^+ + B^+$). When A^+ and B^+ fragment from AB^{2+}, the resultant ions will move opposite to each other with equal and opposite momenta, as the total momentum of the system should be conserved, see Fig. 2.14 a). Now, the fragment-ion (A^+) with a positive momentum component towards the detector will reach the detector slightly earlier than the case when the same ion has zero momentum component towards the detector. Whereas, the fragment-ion (B^+) with

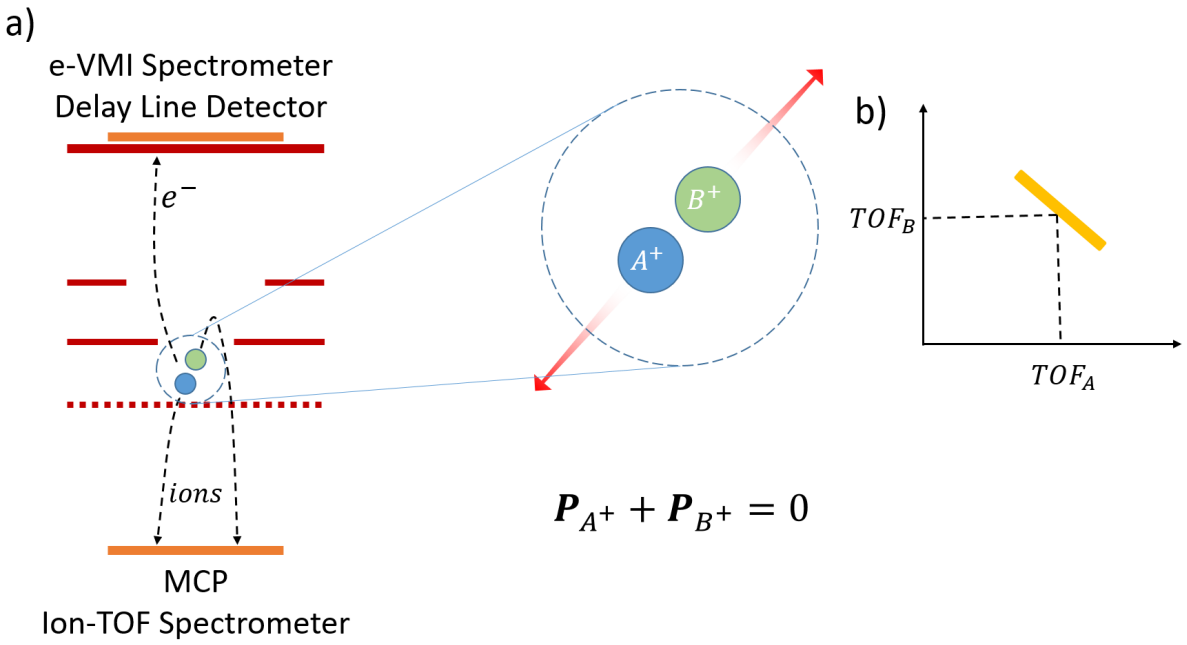

Figure 2.14: a) Schematic of coincident electron - multi ion detection in electron-VMI mode for $AB^{2+} \rightarrow A^+ + B^+$ fragmentation. b) Correlation between the time of flights of A^+ and B^+.

a negative momentum component towards the detector, will reach slightly later than the case when when it has zero momentum component towards the detector. Thus, ToF of A^+ will be reduced while the ToF of B^+ will be increased, making them anti-correlated, see Fig. 2.14 b).

For example, in Fig. 2.15, time of flights of the first two detected ions are plotted against each other from the photoionization of Rb doped He nanodroplets at 21.6 eV using the spectrometer in the electron-VMI mode. One can readily see these anti-correlations from the islands with negative slopes. The magnitudes of these slopes are related to the ratio of corresponding ionic masses in case of two body fragmentation. However, for many body fragmentations, both the slopes and the shapes of these inland will differ [235]. One can also select specific islands and plot the corresponding electron-VMI image (see inset of Fig. 2.15). To gain knowledge about higher order multi-ion fragmentation processes, correlated ToFs of higher order hits (*e.g.,* second and third, third and fourth,...) can also be plotted.

Note that, the electronics of the current spectrometer has been changed over the years according to the experimental requirements, details on the same was, however, published

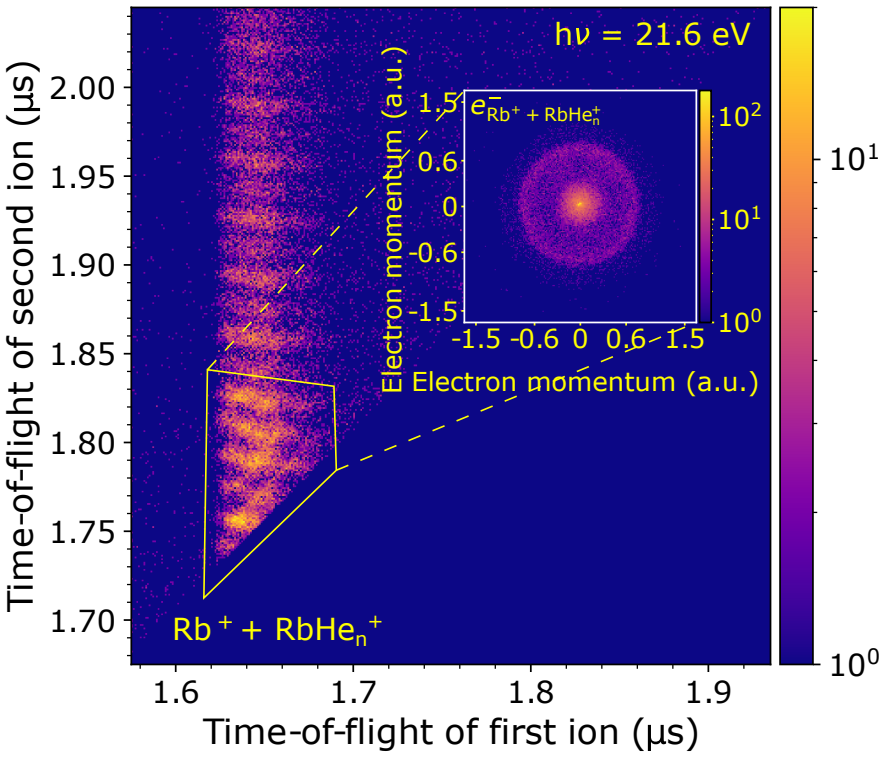

Figure 2.15: Time of flight correlation map between first two detected ions from the photoionization of Rb doped He nanodroplets at 21.6 eV using the spectrometer in the electron-VMI mode. The inset shows the corresponding electron-VMI image from the selected area shown by yellow polygon.

in ref.[236]. The same spectrometer setup had been used in several studies at the Gas-Phase beamline of Elettra Synchrotron Facility to investigate ICD processes in Ar_2, NeAr following resonant Auger decay [107], as well as to investigate ICD and ETMD processes in pure and doped He nanodroplets [180, 185, 188, 183, 187, 181, 186, 184].

2.5 Data analysis

In this section, the methodologies to analyse the experimental data obtained from this spectrometer are presented with some sample examples.

2.5.1 Time of flight data

The time of flights (ToF) of the ions, recorded in the current spectrometer, are proportional to the square root of the mass (M) to charge (q) ratios of the ions. Thus, the ToF can be written as,

$$\text{ToF} = a\sqrt{M/q} + b \tag{2.21}$$

where, parameters, a and b, depend on the geometry and voltage setting of the spectrometer. However, one can obtain these values for particular spectrometer setting, from the time of flights of at least two known ions. For the experiments in this thesis, flight times of H^+, H_2O^+ and N_2^+ ions, created due to photoionization of water and nitrogen in the background, were used.

For example, the histogram of all the recorded ToFs for photoionization of C_2H_2, He and background gases at 26 eV is shown in Fig. 2.16 a). The ToF peaks are associated with different ionic species produced due to the photoionization. Note that, the spread in the ToF peaks correspond to the initial spread in momenta of the ions when they are created. Using equation (2.21), one can convert ToF to M/q and plot the histogram of M/q, as shown in Fig. 2.16 b) to properly identify the all ionic species recorded in the experiment. Thus, upon identification of different fragment-ions, one can easily set ToF limits from a specific ionic fragment from Fig. 2.16 a) to extract the corresponding electron or ion VMI image. Note that, the mass resolution, $\Delta(M/q)/(M/q)$, of the ToF spectrometer, calculated from the M/q peak of the parent atomic or molecular ion, is found to be lower than 2.3 % over the whole spectral range. Analysis procedure of VMI image to get the

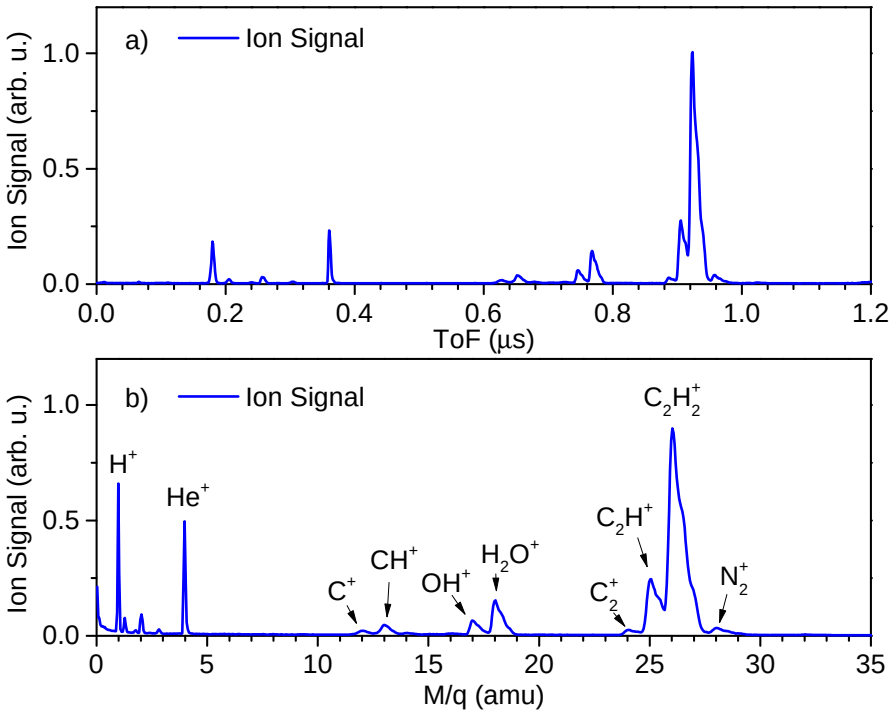

Figure 2.16: a) ToF and b) calibrated M/q spectra upon photoionization of C_2H_2, He, H_2O, and N_2 at 26 eV.

corresponding electron or ion kinetic energy spectrum is presented below.

2.5.2 Velocity map imaging data

The VMI images are projection of the 3D 'Newton spheres' created by the charged particles onto a 2D position sensitive detector upon photoionization. First task of analysing the VMI data, to get the kinetic energy distributions of the charged particles, is to reconstruct the 3D velocity distributions from these 2D projections. Since, the light polarization axis ($\bar{\varepsilon}$) introduces cylindrical symmetry in the 3D 'Newton spheres' (see fig. 2.10), the reconstruction algorithm used here is based on inverse Abel transformation. There are several numerical techniques available to do this inversion, as follows: BASEX, where the 2D projection images are fitted with a set of Gaussian basis functions with known inverse Abel transformations [237]; pBasex, where the same method of fitting is used except the basis set is adapted to the polar symmetry of the photoionization [238]; POP, where the concept of pBasex is combined with polar-onion-peeling algorithm to reconstruct the 2D projections at incremental radius [239]; MEVIR and MEVELER, where the reconstructions are done by iteratively finding out the most likely 3D distributions for which the 2D

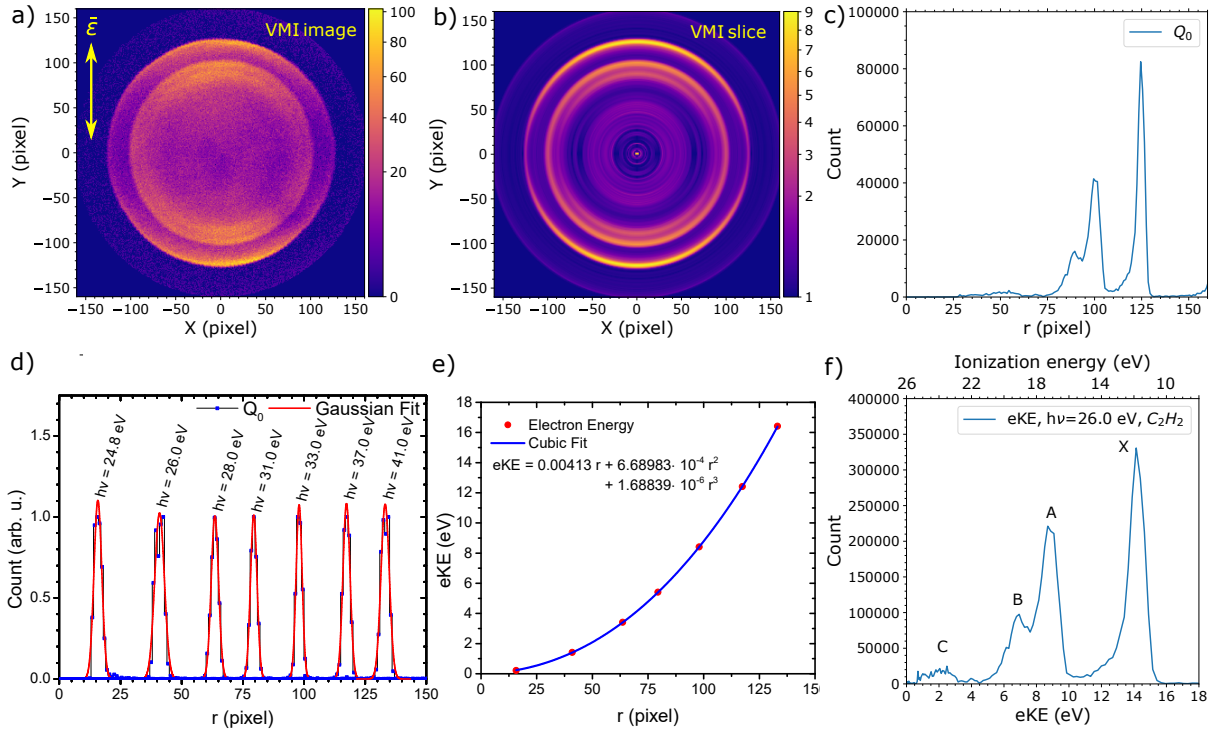

Figure 2.17: a) Electron VMI image from C_2H_2 photoionization at 26 eV. b) Slice of the reconstructed 3D velocity distribution along the polarization axis ($\bar{\varepsilon}$) obtained from MEVELER analysis. c) Radial distributions of $Q_0(v)$ (see equation (2.23)) of C_2H_2 photoelectrons. d) Radial distributions of Q_0 of He photoelectrons at different photon energies. e) Calibration relation between radius (r) and electron kinetic energy (eKE). c) C_2H_2 eKE distribution obtained from corresponding Q_0 distribution using the calibration relation. Ionization energy of C_2H_2 is shown at the top x-axis from which different $C_2H_2^+$ ($X^2\Pi_u$, $A^2\Sigma_g^+$, $B^2\Sigma_u^+$, and $C^2\Sigma_g^+$) states are correctly identified.

projections are obtained using the concept of entropy maximization [240, 241].

For analysing the current data of this thesis, the MEVELER technique is used, where the 3D velocity distribution, $\mathcal{P}(\bar{v})$, is reconstructed as follows:

$$\mathcal{P}(\bar{v}) = \frac{1}{v^2} \sum_l Q_l(v) P_l(\cos\theta) \tag{2.22}$$

where v is magnitude of the velocity ($\bar{v}$), θ is angle between $\bar{v}$ and $\bar{\varepsilon}$, and $P_l(\cos\theta)$ is Legendre polynomial of order l. There is no dependence on the azimuthal angle (ϕ) due to cylindrical symmetry. Under this expansion, the distribution of velocity integrated over all the angle is given by,

$$Q_0(v) = \int_0^\pi \mathcal{P}(v,\theta)\, v^2 \sin\theta \, d\theta \tag{2.23}$$

For example, in Fig. 2.17, panel a) shows a sample electron VMI image recorded from C_2H_2 photoionization at 26 eV, and panel b) shows the 2D slice of the corresponding reconstructed 3D electron velocity distribution along the polarization axis. Since, single-photon ionization of C_2H_2 is done by linearly polarized light, the dipole approximation holds. Thus, the velocity distribution is expanded up to second order Legendre polynomial and odd terms are neglected in equation 2.22. Fig. 2.17 c) shows the distributions of Q_0 as a function of radial distance from the centre of the VMI image, which gives photoelectron velocity distribution integrated over all the angle, see equation 2.23.

Now to convert this radial distribution of Q_0 into the kinetic energy distribution of the photoelectrons, one need to calibrate the radius into kinetic energy of photoelectrons. For this, photoelectrons from the ionization of atomic He at different photon energies are imaged by the VMI at the same spectrometer setting. Since, the ionization energy of He is known, the corresponding kinetic energies of the photoelectrons can be easily mapped to the radial distribution. Fig. 2.17 d) shows the radial distributions of Q_0 corresponding to He photoelectrons recorded at different photon energies. From the peak positions of Gaussian functions fitted to the Q_0 distributions, the relation between the electron kinetic energy (eKE) and radius (r) can be calculated, see Fig. 2.17 e). Now, one can convert $Q_0(r)$ to the eKE distribution, $\mathcal{P}$(eKE), using Jacobian transformation, as follows:

$$\mathcal{P}(\text{eKE}) = \frac{1}{\frac{\partial}{\partial r}\,\text{eKE}}\, Q_0(r) \tag{2.24}$$

In Fig. 2.17, panel f) shows the eKE distribution of C_2H_2 photoionization obtained from Q_0 distribution shown in panel c). From this eKE distribution, $C_2H_2^+$ ($X^2\Pi_u$, $A^2\Sigma_g^+$, $B^2\Sigma_u^+$, and $C^2\Sigma_g^+$) states are identified.

Furthermore, one can estimate the energy resolution of the spectrometer from the full widths at half maxima (FWHM) of He photoelectron kinetic energy peaks obtained at different photon energies, as shown in Fig. 2.18 a). The energy resolution ($\Delta E/E$) of the VMI as a function of measured energy (E) is presented in Fig. 2.18 b). The VMI resolution is improved with the increase in the measured energy, from a quite high value ($\sim$ 42 %) near zero energy to below 7 % at energy greater than $\sim$ 6 eV. Note that, energy resolution functions for different spectrometer settings, calculated in this manner, have been used later to convolute theoretically calculated electron and ion kinetic energy

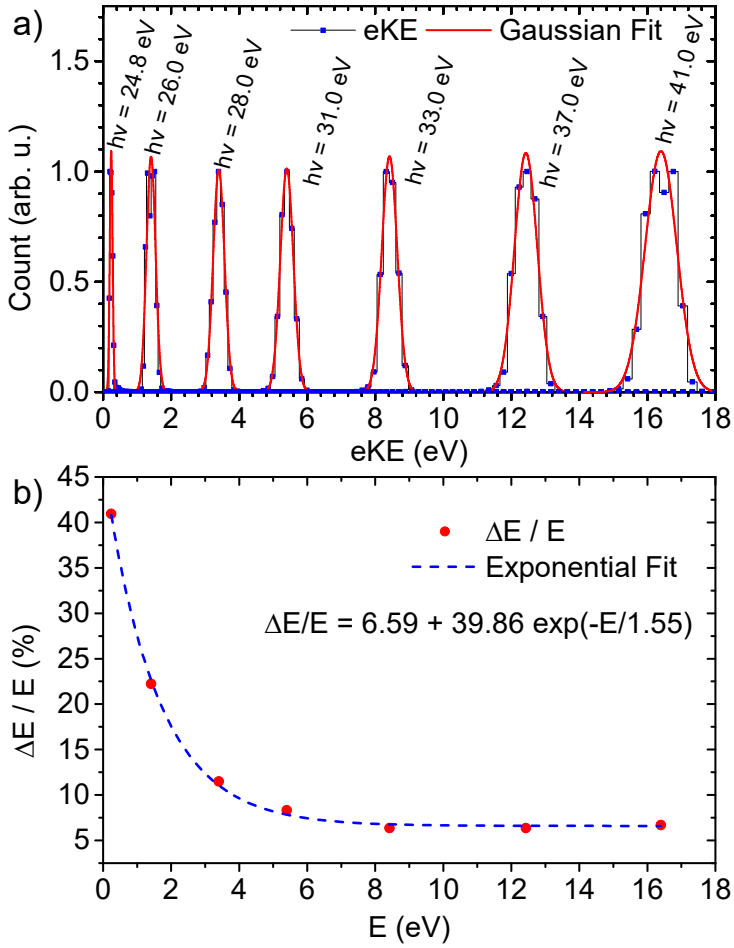

Figure 2.18: a) Electron kinetic energy (eKE) spectra correlated to He photoelectrons at different photon energies. b) Energy resolution ($\Delta E/E$) of the VMI as a function of measure energy (E).

spectra. Furthermore, to eliminate any error introduced by the finite VMI resolution, the convoluted theoretical spectra are always fitted to experimentally measured one.

Thus, one can see that this experimental setup enables the generation He nanodroplets of specific size distribution by controlling the nozzle temperature and He backing pressure, while the number of dopants per droplet can be maintained by changing the dopant gas pressure at the pick up region of the doping chamber. By irradiating tunable synchrotron photons, one can investigate *inter*-atomic/molecular decays in these doped droplets following resonant photoexcitation and ionization of the host. Furthermore, with the help of the co-axial time of flight and velocity map imaging spectrometer, multi-coincident measurements of the product-ions and electrons ejected from the doped droplet as a consequence of different *inter*-atomic/molecular decays become feasible, wherein both the electron and ion kinetic energy spectra correlated to specific product-ion(s) can be mea-

sured in sequence by selecting the relevant charged particle detection scheme (electron- and ion- VMI modes). This measurement methodology allows us to unambiguously identify and study different *inter*-atomic/molecular decay processes in acetylene and heavy alkali doped He nanodroplets following host photoexcitation and ionization, which are discussed in chapter 3 and 4, respectively.

Chapter 3

Acetylene Doped Helium Nanodroplets

In this chapter, the ionization dynamics of acetylene (C_2H_2) doped in He nanodroplets following the photoexcitation and ionization of droplets are discussed. The ionization processes are induced by the EUV photons in the energy range between 20 and 26 eV. The experimental techniques and the results obtained are discussed in detail in the following sections.

3.1 Experimental Methods

Here, only the doping process and the configuration of the electron-ion spectrometer are presented, as rest of the details are already discussed in chapter 2.

3.1.1 Doping process

Fig. 3.1 shows the schematic of the experimental setup, where in the doping chamber C_2H_2 molecules are doped with the beam of pure He nanodroplets via collisional pickup process. Due to safety reasons C_2H_2 gas comes with a mixture of acetone, therefore the acetylene gas was needed to be filtered out from the acetone contamination, before effusing it inside the doping chamber. Thus, the acetylene-acetone gas mixture was passed through a spiral tube emerged inside a slurry of methanol and liquid nitrogen whose temperature was around -100 °C. This process freezes the acetone and thereby filters the C_2H_2 gas.

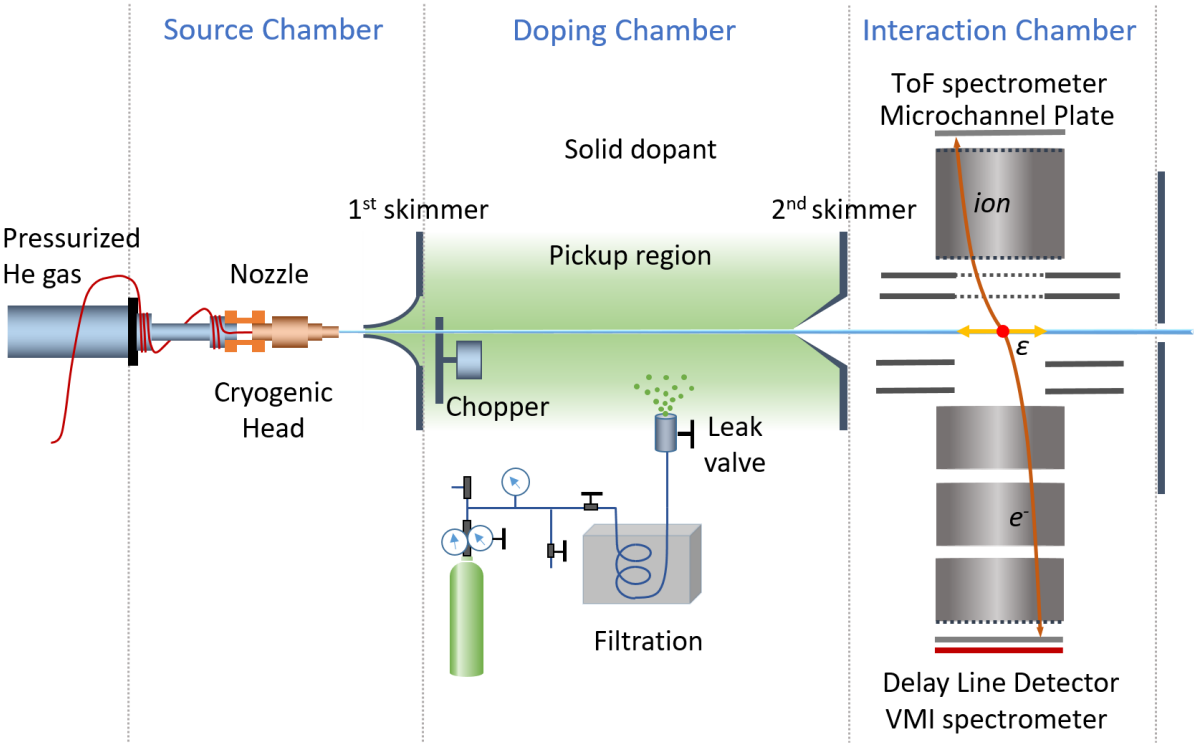

Figure 3.1: Schematic of the experimental setup for C_2H_2 doped He nanodroplets experiments. Pure He nanodroplets are produced via supersonic expansion of He gas through the cryogenic nozzle and the 1^{st} skimmer in the source chamber. Subsequently the droplets are doped with pure C_2H_2 molecules which are effused into the doping chamber via a leak valve to maintain specific doping pressure. Finally, in the interaction chamber, the doped droplet is ionized by the linearly polarized EUV light and the resulting ions and electrons are detected by the ToF and VMI spectrometer, respectively. The C_2H_2 gas is filtered from a mixture of acetone and acetylene by passing them through a slurry of methanol and liquid nitrogen maintained at around -100 °C.

Now this pure acetylene gas was effused inside the doping chamber in a controlled fashion using a ultra high vacuum (UHV) variable leak valve. This gives a control over the level of C_2H_2 doping in the droplets. The gas pressure inside the doping chamber was maintained between 6×10^{-7} and 4×10^{-6} mbar for these experiments to dope only a few C_2H_2 molecules per droplet. The nozzle temperature was kept between 16 and 14 K, while the He backing pressure was maintained at 50 bar. At this experimental condition, He nanodroplets with on average 8800 to 23000 He atoms per were produced [151].

Note that, as discussed in section 2.2, in these experiments at each doping chamber pressure, multiple C_2H_2 molecules can be doped in a single He droplet, wherein the number of dopants per droplet follows a Poissonian distribution depending on the size of the droplet and doping pressure. Thus, not only ionization dynamics of single C_2H_2 molecule

in the droplet is discussed, but also ionization processes in acetylene clusters or oligomers ($[C_2H_2]_n$, n $\geq$ 2) are addressed in this chapter.

3.1.2 Spectrometer configuration

For studying the ionization processes in C_2H_2 doped droplets, we implemented the electron-VMI mode, wherein the ions are detected by the time of flight part, in coincidence with the electron in the velocity map imaging part of the spectrometer. This allows us to measure ion ToF spectra as well as the electron kinetic energy (eKE) spectra correlated to different ions. The insights about the ionization processes gained from the experimental data are presented below.

3.2 Dopant ionization at different photon energies

As the goal of this thesis is to examine the *inter*-atomic/molecular ionization processes induced by EUV radiation in doped He nanodroplets, the yield of the dopant ions coming out of the doped droplets was recorded as a function of the photon energy, when the droplet was being photoexcited or ionized by the incident photons. Fig. 3.2 a) shows the $C_2H_2^+$ ion yield as a function of the photon energy between 20 and 26 eV for nozzle temperature of 16 K and doping chamber pressure of 6.5×10^{-7} mbar. The fluorescence and electron yield from pure droplet photoexcitation and ionization as a function of photon energy are presented in Fig. 3.2 b) by the red and blue lines, respectively.

3.2.1 Inter-atomic/molecular decays

From Fig. 3.2 a), we see very low, almost negligible, ion-yield of $C_2H_2^+$ from the droplet below the threshold ($\sim$ 20.5 eV) for pure droplet excitation to $n = 2$ band, see the onset of fluorescence (red line) in Fig. 3.2 b). Following this, the $C_2H_2^+$ ion yield follows the trend of the fluorescence and total electron yields from the pure droplet, shown by red and blue lines, respectively, in Fig. 3.2 b). These observations suggest indirect ionization of the dopants following droplet excitation or ionization is majorly responsible for the significant increase in the $C_2H_2^+$ ion-yield. The large difference between the ionization cross section of doped C_2H_2 molecules and the effective photoexcitation cross section of the droplet containing $\sim 10^4$ He atoms can be the reason why we do not observe significant direct

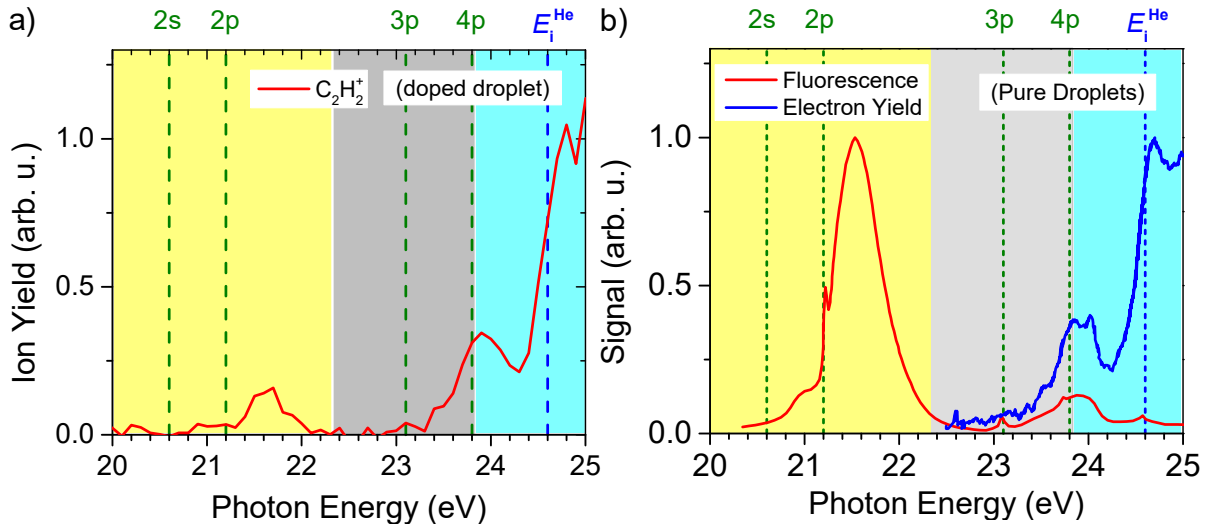

Figure 3.2: a) $C_2H_2^+$ ion-yield spectrum as a function of photon energy from C_2H_2 doped He nanodroplets at 16 K nozzle temperature and 6.5×10^{-7} mbar doping pressure. b) The fluorescence (red line) and total electron yield (blue line) from pure He droplets as a function of photon energy, obtained in previous studies [242, 180]

photoionization of the doped C_2H_2 molecule below the photoexcitation threshold ($\sim$ 20.5 eV) of the droplet, although the ionization energy of gas phase isolated C_2H_2 molecule is 11.4 eV.

However, it should be noted that, to overcome the challenges arising due to this difference in the cross sections, and to observe significant direct dopant ionization signal from the droplets, we performed a similar experiment with coronene ($C_{24}H_{12}$) dopants, having 12 times more C-atoms than that of C_2H_2 and thereby having large photoionization cross section. For comparison, the photoionization cross sections of coronene and acetylene at 18.5 eV are $\sim$ 500 Mb and $\sim$ 50 eV, respectively [243, 244]. At photon energy below the droplet photoexcitation threshold, we observed significant direct photoionization signal from coronene inside the droplets at 19 eV photon energy [184]. Another experiment that we recently conducted was with Xe doped droplets, where we overcame the cross section problem by exciting the system with 90 eV photons at the Xe ($4d$) giant resonance and observed the direct ionization of the dopant inside the droplet [245].

In the current experiment, to know about the degree of ionization, we checked the multi ion coincidences for each ionization event. No double ionization leading to dissociation of the C_2H_2 molecule into two or more ionic fragments was observed at this photon energy range from 20 to 26 eV. Also the double ionization energy of C_2H_2 (32 eV) is much higher

than the incident photon energy range, therefore not doubly ionized $C_2H_2^{2+}$ and their fragment are expected. Therefore, the small ionization peak of C_2H_2 around 21.6 eV, in the shaded yellow region below $\sim$ 22.4 eV of Fig. 3.2 a), suggests single ionization of the dopants through inter-atomic/molecular Coulombic decay (ICD) processes from the excited He^* states following the photoexcitation of the droplet to first excitation band derived from atomic He^* ($1s2p$) state. It is well known that, at this $n = 2$ droplet excitation band, He atom is first excited to He^* ($1s2p\ ^1P$) state, which subsequently undergoes ultrafast internal relaxations to dipole forbidden He^* ($1s2s\ ^{3,1}S$) states inside the droplet [246]. Thus, all these He^* ($^{3,1}S,^1P$) states can participate in the ICD processes for ionizing the dopant $[C_2H_2]_n$ cluster, as shown below.

$$He^*(^{3,1}S,^1P) + [C_2H_2]_n \rightarrow He + [C_2H_2]_n^+ + e^-_{ICD} \tag{3.1}$$

Between 23 eV and the ionization energy of atomic He ($E_i^{He} = 24.58$ eV), we see another peak in the $C_2H_2^+$ ion yield at 23.9 eV. We already know that at this energy range ($23 < h\nu < E_i^{He}$) He atoms are excited to ($n \geq 3$) Rydberg excited states. Thus, relaxation in He^* can proceed in two possible pathways in He nanodroplets: 1) via photoemission, and 2) via autoionization by forming He_n^* excimer which decays to vibrationally excited He_n^+ ion [173, 247]. These two decay processes are evident from the fluorescence and electron yields from pure droplets shown in Fig. 3.2 b) at this energy range (shaded grey region). Thus, there are can be two possible *inter*-atomic/molecular decay mechanisms underlying the ionization of C_2H_2 dopants, as follows:

$$He^* + [C_2H_2]_n \rightarrow He + [C_2H_2]_n^+ + e^-_{ICD} \tag{3.2}$$

and

$$\begin{aligned} He_n^* + [C_2H_2]_n &\rightarrow He_n^+ + [C_2H_2]_n + e^-_{He} \\ &\rightarrow He_n + [C_2H_2]_n^+ + e^-_{He} \end{aligned} \tag{3.3}$$

where, the first process (process 3.2) is similar to the ICD expected at 21.6 eV (process 3.1). At 23 eV $< h\nu < E_i^{He}$, however, higher excited states of both the C_2H_2 and He can participate in the ICD. Whereas, the second process (process 3.3), charge transfer (CT)

following the autoionization of He_n^* is responsible for ionizing the dopants.

Note that, following autoionization of the He droplet, due to very close energy levels of the initial He_n^* state and final vibrationally excited He_n^+ state, near zero kinetic energy electrons are emitted which are independent of the photoexcitation energy. Moreover, the autoionized electron can loose its kinetic energy due to inelastic collisions with the surrounding He atoms and can form electron 'bubble' state in the droplet. Finally, the ionized electron can eject out of the droplet via thermionic emission, leading to detection of near zero electron kinetic energy [247].

Above E_i^{He}, we see that the He atoms in pure droplets are ionized directly by the incident photons, and no photoemission is detected (see Fig. 3.2). Therefore, only possible ionization pathway for C_2H_2 dopants here is charge transfer ionization, see below.

$$\begin{aligned} \mathrm{He} + [\mathrm{C_2H_2}]_n + h\nu &\rightarrow \mathrm{He}^+ + [\mathrm{C_2H_2}]_n + e^-_{He} \\ &\rightarrow \mathrm{He} + [\mathrm{C_2H_2}]_n^+ + e^-_{He} \end{aligned} \tag{3.4}$$

In all these dopant ionization processes described above, we can see that the ejected electrons in coincidence with the dopant ions originate from different relaxation processes involving He^*, He^+ and He_n^+. Thus, the kinetic energy carried by these correlated electron will unravel the ionization dynamics effectively by giving insights about the participating electronic states of the host-droplet and dopants.

3.2.2 Interior localization of acetylene

Furthermore, we observe that the ionization probability of C_2H_2 due to CT above E_i^{He} is much larger than the same following ICD at 21.6 eV photon energy, when the corresponding $C_2H_2^+$ yields are compared in Fig. 3.2 a). The high CT efficiency compared to the ICD efficiency can be due to the higher probability of finding the He^+ ion in the vicinity of C_2H_2 molecules than finding He^* ion near the dopants. As discussed in section 1.4, due to the attractive and repulsive interactions of He^+ and He^* with the droplet, respectively, the He^+ ion submerges to the centre of the droplet [175, 176, 177, 178], while He^* migrates to the surface of the droplet [173, 174]. Thus, the corresponding precursor state for CT ionization is easily formed when He^+ migrates to the centre of the droplet where doped C_2H_2 molecules are likely to be localized. This result complements the already known

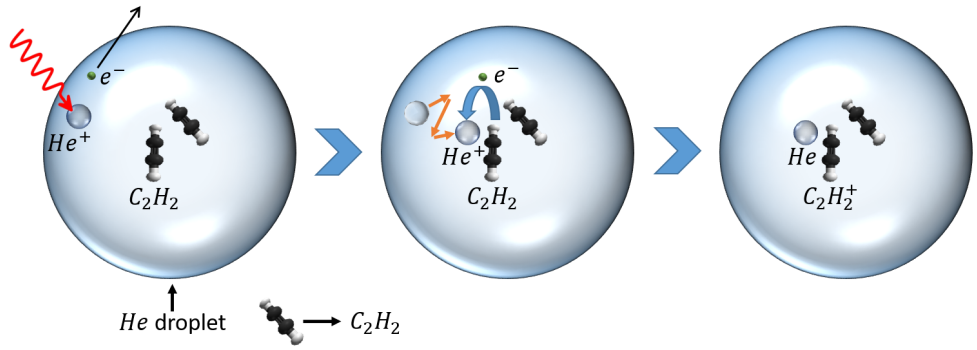

Figure 3.3: Schematic of the charge transfer process. Upon ionization of He, He^+ ion migrates to the interior of the droplet where the doped C_2H_2 molecules reside. The He^+ ion is neutralized by the charge transfer from the dopants, creating $C_2H_2^+$ ion. Here, for illustration purpose only two C_2H_2 molecules are shown inside the droplet, however single to multiple C_2H_2 molecules can be doped in the droplet.

fact about the location of C_2H_2 obtained from He nanodroplets isolation IR spectroscopic studies [248, 249, 250, 168]. Fig. 3.3 schematically shows the migration of He^+ ion and subsequent ionization of C_2H_2 inside the droplet through charge transfer ionization.

3.2.3 Product ions

To get an idea about the ions produced in the C_2H_2 doped droplets by these EUV induced processes, the ion ToF spectra were recorded at different droplet excitation and ionization regimes. Fig. 3.4 shows the calibrated ion mass spectra at a) 21.6, b) 23.9 and c) 26 eV photon energies for $T_{noz} = 14$ K and $P_d = 4.5 \times 10^{-6}$ mbar.

We can readily see that C_2H_2 cluster ions ($[C_2H_2]_n^+$, $n = 1 - 3$) and their fragments are detected at all three photon energies, while the He cluster ions (He_n^+, $n = 1 - 3$) are produced at 23.9 and 26 eV photon energies, following the autoionization and direct ionization of the droplet, see Fig. 3.4 b) and c), respectively. Furthermore, extensive fragmentations of the dopant cluster ions are observed at these higher photon energies, where the CT processes are supposed to be the dominant dopant ionization mechanisms. Similar extensive fragmentations were also reported in thermal collision of He^+ with isolated C_2H_2 molecule, where the underlying charge transfer process is almost identical [252].

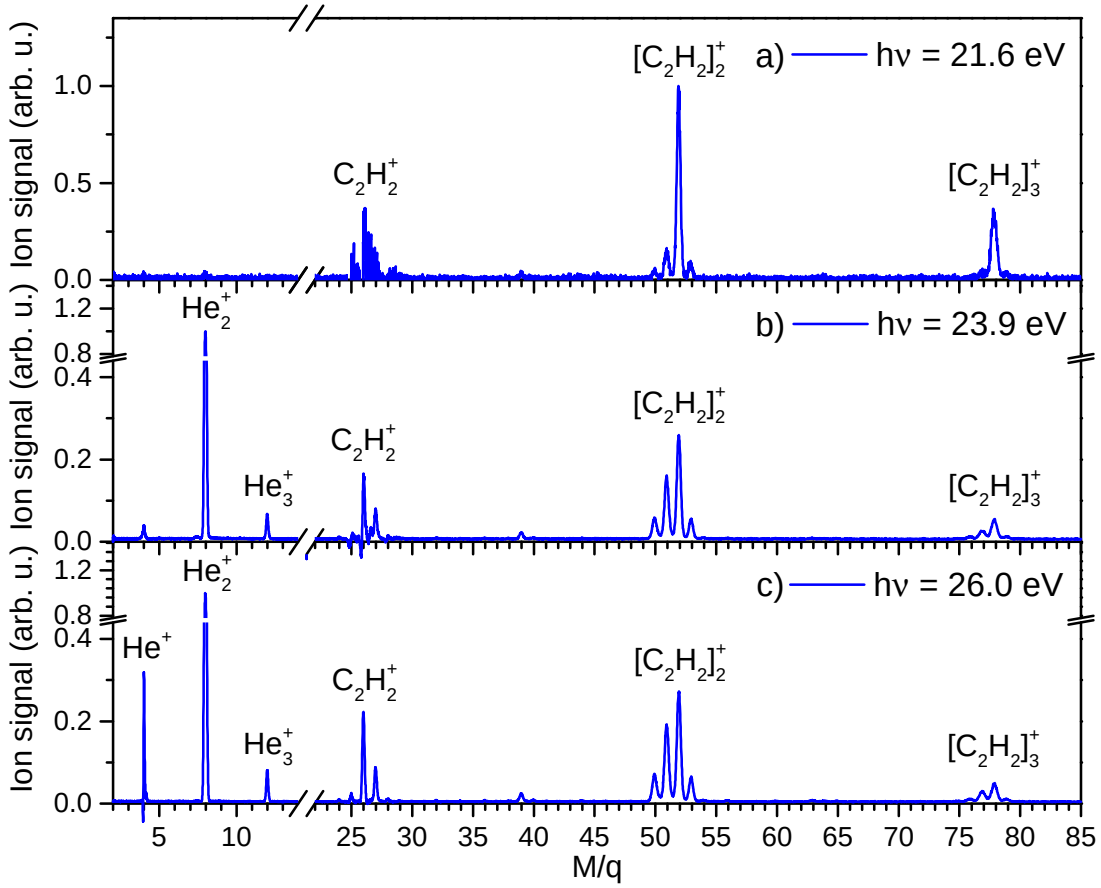

Figure 3.4: Ion mass spectra at photon energies of a) 21.6 eV, b) 23.9 eV and c) 26 eV for T_{noz} = 14 K and $P_d = 4.5 \times 10^{-6}$ mbar. The horizontal axis shows the mass (M) to charge (q) ratio of the ionic fragments. The spectra are normalized with respect to the background N_2^+ ions yields, such that the total N_2^+ ion yields are proportional to the cross sections of producing N_2^+ ion from the photoionization of N_2 at the respective photon energies [251].

3.3 Dopant ionization at $n = 2$ droplet excitation band

Now, we focus on the ionization processes at 21.6 eV photon energy due to $n = 2$ droplets excitation. As discussed earlier in section 3.2.1, ICD between the dopant molecules and the excited He^* ($^{3,1}S, ^1P$) states are expected at this photon energy, as shown by the process 3.1. Since, the eKE spectra of the ICD electrons in coincidence with the detected dopant ions reveal the underlying ionization dynamics, we look into the correlated eKE spectra for the major ionic products, acetylene dimer ions ($[C_2H_2]_2^+$) and acetylene trimer ions ($[C_2H_2]_3^+$) shown in Fig. 3.5 a) and b), respectively.

Owing to low ion yield of the acetylene monomer ions ($C_2H_2^+$) at this experimental condition, we are unable to get a meaningful background subtracted eKE spectrum for $C_2H_2^+$. Initially, it was believed that at the current doping pressure of $P_d = 4.5 \times 10^{-6}$ mbar, multiple C_2H_2 molecules are doped in the droplet which effectively reduces yield of $C_2H_2^+$ ions from the droplet due to the formation of higher order C_2H_2 oligomer ions. Therefore, we decreased the doping pressure of C_2H_2 to achieve a monomer doping condition at the current droplet size. In-spite of that, we were unable to observe considerable statistics in the $C_2H_2^+$ correlated eKE spectrum. There might be two underlying reasons for this observation: 1) the ICD efficiency of C_2H_2 monomer is negligible compared the same for higher order C_2H_2 oligomers, and 2) the probability of ejection of $C_2H_2^+$ ion from the droplet is very low compared to the other higher order oligomer ions.

The first assumption is supported by recent experimental results from acene (anthracene ($C_{14}H_{10}$), tetracene ($C_{18}H_{12}$), pentacene ($C_{22}H_{14}$)) doped He nanodroplets studies at the same photon energy and droplet size [183], where one can see that the normalized yields of these dopant ions at 21.6 eV photon energy systematically decrease for lower mass molecular dopants, suggesting lower ICD efficiency for smaller molecule, see Fig. 1 in ref.[183]. Moreover, since these acene molecules are embedded inside the droplet and He^* tends to migrate to the surface of the droplet from the excitation site, there is always a higher probability of finding He^* in the vicinity of a bigger dopant inside the droplet, allowing the ICD to take place. Furthermore, with the increase in number of available ICD decay channels, the overall ICD decay rate also increases, as stated in section 1.2.4. Since acetylene monomer (C_2H_2) has less number of available degenerate ICD decay channels

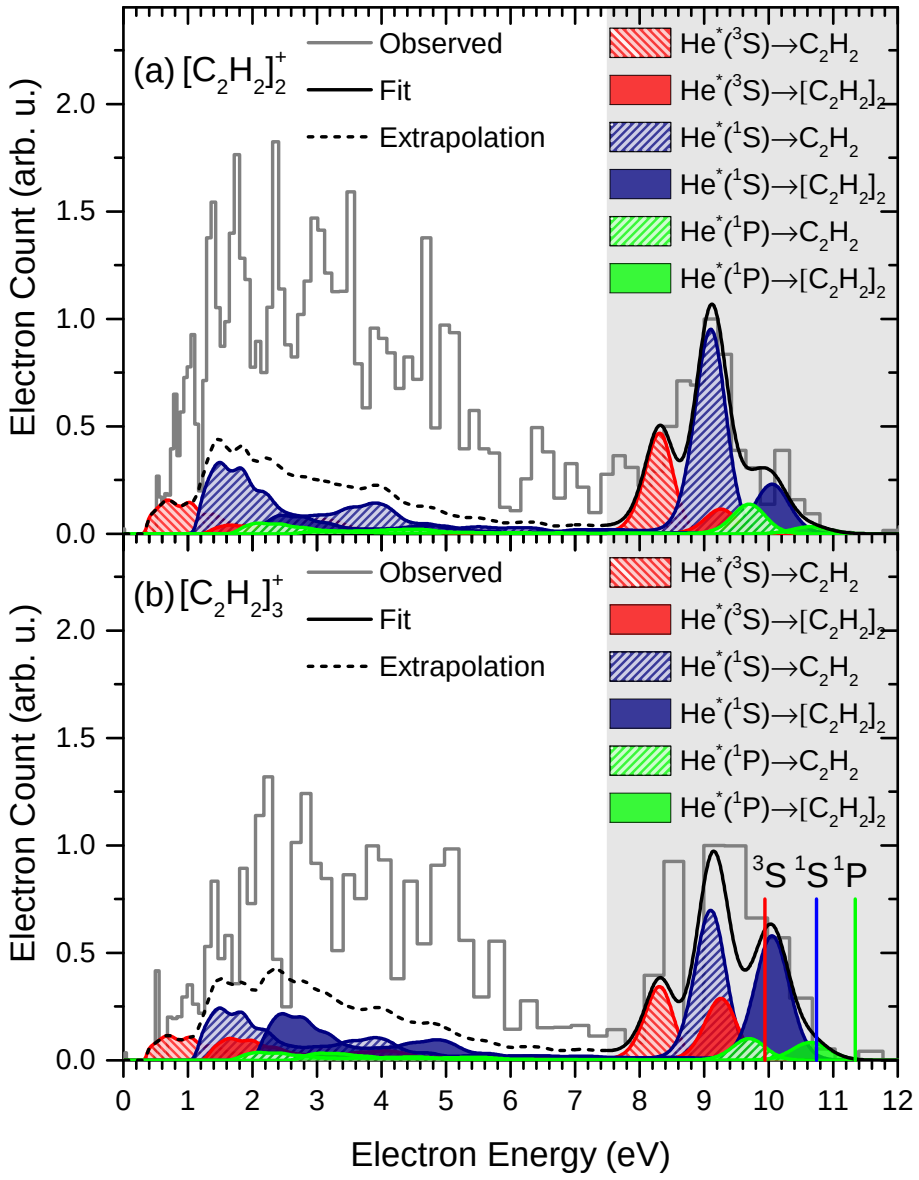

Figure 3.5: PIES correlated to (a) $[C_2H_2]_2^+$ and (b) $[C_2H_2]_3^+$ from acetylene doped He droplet ionization at photon energy of 21.6 eV for $P_{doping} = 4.5 \times 10^{-6}$ mbar and $T_{nozzle} =$ 14 K. The red, blue and green spectra with hatched shading are the convoluted PIES for C_2H_2 monomer from He* ($1s2s\ ^3S$), ($1s2s\ ^1S$) and ($1s2p\ ^1P$) states, respectively, while the convoluted PIES of C_2H_2 dimer from these He* states are represented by the red, blue and green spectra with filled shading, respectively. The solid black line in each panel shows the total fit performed over the high energy feature from 7.5 eV to 11 eV which is arising from the cationic states of C_2H_2 monomer and dimer correlated to $C_2H_2^+$ ($X^2\Pi_u$) state. The parameters for the fit were determined only using experimental data in the region 7.5 eV and beyond. Nonetheless, we extrapolate this using the dashed black line into the region ≤ 7.5 eV considering the corresponding $A^2\Sigma_g^+$ and $B^2\Sigma_u^+$ states. In panel (b), the red, blue and green vertical lines denote the PIES peak positions of C_2H_2 trimer Penning ionization from He* ($1s2s\ ^3S$), ($1s2s\ ^1S$) and ($1s2p\ ^1P$) states, respectively. Note that the width of the bar in the histogram indicates the bin size on the energy scale and does not represent the energy resolution of the VMI spectrometer. Adapted with permission from ref.[253].

compared to that of acetylene oligomer ($[C_2H_2]_n$ ($n \geq 2$)), the ICD decay rate of the monomer can be lower than the same for the oligomers. Whereas, the second assumption of suppression of dopant ion ejection upon monomer ionization can be attributed to the inefficient evaporation of He atoms from the host droplet. In case of multiply doped droplets, upon ionization of one dopant molecule through ICD, the resultant ion can combine with other dopants to form bigger oligomer ion, and the binding energy released in this process can be used to evaporate sufficient number of He atoms, thereby shrinking the host droplet and enhancing the ejection of oligomer ions. In case of monomer doping, the lack of other dopants hinders this process of ejection. Note that, in case of detection of ejected oligomer ion, not only precesses involving ICD in monomer, but also processes involving ICD in oligomers can be responsible.

We can see that the observed eKE spectra in coincidence with C_2H_2 dimer and trimer ions are very similar to each other in Fig. 3.5 a) and b), respectively. The spectra contain two broad peak structures: a) low energy peaks between 0 and 7.5 eV, and b) the high energy peaks between 7.5 and 12 eV (the shaded grey part of Fig. 3.5). In the following section, the origins of both these features are discussed in detail.

3.3.1 Penning ionization electron spectra

The proposed resonant ICD processes leading to single ionization of the dopants are similar to Penning ionization processes where excited metastable atoms or molecules interact with other neutral atoms or molecules in a crossed-beam setup, discussed in section 1.2.2. Only here, the processes are happening inside the droplet between the He^* and $[C_2H_2]_n$, as shown by process 3.1. Thus, we explain the observed eKE spectra in terms of Penning ionization electron spectra (PIES) for different He^* and $[C_2H_2]_n$ states involved.

In Fig. 3.5, the high energy peaks (7.5 to 12 eV) are originating from the ground cationic states of the dopant clusters, derived from $C_2H_2^+$ ($X^2\Pi_u$, 11.4 eV), as the ionization threshold of C_2H_2 monomer, dimer and trimer are 11.4, 10.44 and 9.83 eV, respectively. Thus, upon relaxation of He^* ($1s2s\ ^3S$, 19.82 eV), ($1s2s\ ^1S$, 20.62 eV) and ($1s2p\ ^1P$, 21.21 eV), the resulting Penning ionization peaks should lie in this high energy regime. Whereas, the low energy parts (0 to 7.5 eV) of the measured eKE spectra, result from the Penning ionization of C_2H_2 clusters, leading to excited cationic states, derived from

$C_2H_2^+$ ($A^2\Sigma_g^+$, 16.7 eV) and ($B^2\Sigma_u^+$, 18.8 eV) states [254].

It should be noted that these well separated peak features in the PIES from the dopants embedded inside the droplets are of great significance, for the following reasons. To resolve the structure of embedded molecules or clusters inside the He nanodroplets, high resolution IR spectroscopy has been a long-established method, where IR photons are used to directly perturb the embedded species to gain insights. Whereas in the EUV range above $\sim$ 20.5 eV, the droplets no longer remain transparent to the incident photons and get photoexcited by the EUV radiation. Subsequently, ICD or Penning ionization processes can occur in the dopant - excited droplet system. Now, as discussed earlier, one can gain insights about the structure of the embedded dopants from the PIES. Thus, PIES provides an indirect probe for unravelling the structure of embedded species. However, previous attempts to probe the structure using PIES had failed in case of acene doped droplets [183]. PIES study on rare-gas (Xe, Kr) doped droplets has also been reported [179]. It was observed that in both cases the Penning electrons undergo inelastic scattering with the surrounding He environment and significantly lose energy which lead to broad low-energy features in the PIES. For Xe and Kr doped droplets, the PIES retain some features of unperturbed Penning electrons resulting in ground cationic dopant ions. For acene doped droplets, the reported PIES were massively distorted by the droplet environment and thereby no information about the structure of acene dopants were gained. In our case with C_2H_2 dopant, however, we see relatively unperturbed spectra features at least for the high energy part of the PIES. Therefore, it can provide significant insights about the structure of the embedded cluster and establish this indirect PIES method for probing the same for the first time. However, note that, the exact physical reason behind these contradicting observations in the PIES for acetylene and acene doped droplets, at similar droplet expansion and doping conditions, is not known and requires further explorations beyond the scope of the current thesis.

PIES fitting

Therefore, we fitted the observed eKE spectra correlated to C_2H_2 monomer and dimer ions in Fig. 3.5 with calculated PIES from different He^* states and participating C_2H_2 cluster, in the following way.

The kinetic energies of the ICD or Penning electrons, shown in process 3.1 can be

calculated from

$$\mathrm{eKE}_{n,(i,j)} = E(\mathrm{He}^*_{(i)}) - E([\mathrm{C_2H_2}]_\mathrm{n}^{+}{}_{(j)}) + \Delta E_{n,(i,j)} \tag{3.5}$$

where, $E(\mathrm{He}^*_{(i)})$ are the energies of He^*, wherein i represents He^* $(1s2s^3S)$, $(1s2s^1S)$ and $(1s2p^1P)$ states. $E([\mathrm{C_2H_2}]_\mathrm{n}^{+}{}_{(j)})$ are the energies of $[\mathrm{C_2H_2}]_\mathrm{n}^+$, wherein j represents the different cationic states of $[\mathrm{C_2H_2}]_\mathrm{n}$. $\Delta E_{n,(i,j)}$ are the energy differences between the incoming $\mathrm{He}^*_{(i)} + [\mathrm{C_2H_2}]_\mathrm{n}$ and outgoing $\mathrm{He} + [\mathrm{C_2H_2}]_\mathrm{n}^{+}{}_{(j)} + e^-_{ICD}$ channels [255]. The values of ΔE for interaction with rare gas atoms are usually negligible or less than 0.5 eV. Although experimentally one can determine the values of ΔE by measuring the $\mathrm{eKE}(e^-_{ICD})$ spectra provided the energies of $[\mathrm{C_2H_2}]_\mathrm{n}^+$ are known, while for theoretical evaluation of ΔE, a two-potential-curve model of Penning ionization is presented in ref.[16].

Thus, the PIES for ionization of $[\mathrm{C_2H_2}]_\mathrm{n}$ cluster from all the He^* states can be determined from the following equation:

$$\mathrm{PIES}_n = \sum_{i,j} C_{n,(i,j)}\ \mathrm{eKE}_{n,(i,j)} \tag{3.6}$$

where, $C_{n,(i,j)}$ is the Penning ionization efficiency of the i^{th} state of He^* to ionize $[\mathrm{C_2H_2}]_\mathrm{n}$ to its j^{th} cationic state. Now, if the relative contribution of $[\mathrm{C_2H_2}]_\mathrm{n}$ $(n = 1, 2, 3...)$ oligomer ionization to the measured PIES correlated to a specific dopant cluster ion is ρ_n, one can calculate the total PIES as:

$$\mathrm{PIES} = \sum_n \rho_n\ \mathrm{PIES}_n \tag{3.7}$$

Thus, by fitting the above equation to the measured eKE spectra, one can estimate the values of ρ_n underlying the detection of each correlated dopant ion. This, however, requires that the PIES for Penning ionization from each participating states of He^* and $[\mathrm{C_2H_2}]_\mathrm{n}$ cluster in the droplet are known exactly. Therefore, one need to know all the values of $C_{n,(i,j)}$, $E([\mathrm{C_2H_2}]_\mathrm{n}^{+}{}_{(j)})$ and $\Delta E_{n,(i,j)}$ experimentally or theoretically. Since, the theoretical calculation of these parameters was beyond the scope of the current work, and only the PIES for Penning ionization of gas phase acetylene monomer ($\mathrm{C_2H_2}$) from metastable He^* $1s2s^3S$ state is experimentally known, we developed a simple model to estimate the other PIES, as follows:

First, we consider that the Penning ionization efficiencies ($C_{n,(i,j)}$) for all the involved He^* states and $[\mathrm{C_2H_2}]_\mathrm{n}$ cluster are same as the values obtained from the Penning ionization

of acetylene monomer (C_2H_2) from metastable He* ($1s2s\ ^3S$) state. Thus, equation 3.6 can be rewritten as,

$$\mathrm{PIES}_n = \sum_{i,j} C_{1,(^3S,j)}\ \mathrm{eKE}_{n,(i,j)} \tag{3.8}$$

Now, to calculate the values of the $\mathrm{eKE}_{n,(i,j)}$, one need to known $E([C_2H_2]_n^+{}_{(j)})$ and $\Delta E_{n,(i,j)}$ (see equation 3.5). To estimate $E([C_2H_2]_n^+{}_{(j)})$ for $n \geq 2$, we referred to the reported changes in the ionization energies (ΔIE) between $[C_2H_2]_n$ and C_2H_2, and calculated the values as,

$$E([C_2H_2]_n^+{}_{(j)}) = E([C_2H_2]^+{}_{(j)}) + \Delta IE([C_2H_2]_n) \tag{3.9}$$

Finally, we assumed that the values of $\Delta E_{n,(i,j)}$ are same as the values obtained from the Penning ionization of C_2H_2 from He* ^3S states. Therefore, the equation 3.5 can be rewritten as,

$$\mathrm{eKE}_{n,(i,j)} = E(\mathrm{He}^*_{(i)}) - E(C_2H_2^+{}_{(j)}) + \Delta IE([C_2H_2]_n) + \Delta E_{1,(^3S,j)} \tag{3.10}$$

Thus, the total PIES fitting equation become,

$$\mathrm{PIES} = \sum_{n,(i,j)} \rho_n\ C_{1,(^3S,j)}\ [E(\mathrm{He}^*_{(i)}) - E(C_2H_2^+{}_{(j)}) + \Delta IE([C_2H_2]_n) + \Delta E_{1,(^3S,j)}] \tag{3.11}$$

In the above fitting equation, ρ_n is the fitting parameter, while all the values of $C_{1,(^3S,j)}$, $E(\mathrm{He}^*_{(i)})$, $E(C_2H_2^+|_{(j)})$, $\Delta IE([C_2H_2]_n)$ and $\Delta E_{1,(^3S,j)}$ are known from earlier work [256, 257, 258].

Qualitatively in this model fitting, we referred to the experimental PIES from acetylene monomer due to relaxation of He* ^3S state [258], and calculated the PIES from the other He* ^1S and ^1P states by shifting the reference-PIES by the energy differences between the initial states, *i.e.*, $[E(\mathrm{He}^*\ ^1S) - E(\mathrm{He}^*\ ^3S)]$ and $[E(\mathrm{He}^*\ ^1P) - E(\mathrm{He}^*\ ^3S)]$, respectively. Then, to calculate the PIES from the Penning ionization of acetylene cluster ($[C_2H_2]_n$, $n \geq 2$), due to relaxation of the three He* states, the calculated PIES from the monomer ionization are then further shifted by the change in ionization thresholds of $[C_2H_2]_n$ ($n \geq 2$) compared to the same for monomer C_2H_2. Finally, three sets of PIES for each participating acetylene oligomer are fitted, keeping the same ratios between the three PIES from He*

states.

Note that, the effect of electron scattering in the droplet environment has been accounted for in these simulated PIES by performing a Monte Carlo simulation based on binary electron-He scattering, similar to what was implemented in case of acene doped He nanodroplets [183]. Moreover, each simulated PIES has also been convoluted with the spectrometer resolution factor before the fitting.

Fitting of high energy part

Since the high energy parts ($7.5 - 12$ eV) of the measured PIES in Fig. 3.5 a) and b) show eKE spectral features that are relatively unperturbed by the inelastic scattering of electrons inside the droplet, we fitted the same with our model. The red, blue and green peaks with the hatched shading show the PIES of acetylene monomer from the He^{*} $^{3,1}S$ and ^{1}P states, respectively. Whereas the same with the solid shading show the PIES of acetylene dimer. As the PIES from acetylene monomer and dimer alone can fit the observed PIES correlated to $[C_2H_2]_2^+$ and $[C_2H_2]_3^+$ ions, the PIES from acetylene trimers, which result in PIES peaks at higher electron energies as shown by the vertical red, blue and green line in panel b), are not taken into account. This fitting indicates the following ionization dynamics of the acetylene clusters.

3.3.2 Clusterizations of neutral and ionic dopants

As seen in Fig. 3.5 a), the contribution of acetylene monomer Penning ionization in the PIES in coincidence with $[C_2H_2]_2^+$ ion indicates that the Penning ionized *$C_2H_2^+$ ion combines with a neutral C_2H_2* molecule in the droplet, see below.

$$He^{*} + C_2H_2 \rightarrow He + C_2H_2^{+} + e^{-} \tag{3.12}$$

$$C_2H_2^{+} + C_2H_2 \rightarrow [C_2H_2]_2^{+} \tag{3.13}$$

Whereas the contribution of acetylene dimer Penning ionization in the PIES in coincidence with $[C_2H_2]_2^+$ ion indicates *the formation of neutral $[C_2H_2]_2$* which subsequently

Penning ionized by He^*, see below.

$$C_2H_2 + C_2H_2 \rightarrow [C_2H_2]_2 \tag{3.14}$$

$$He^* + [C_2H_2]_2 \rightarrow He + [C_2H_2]_2^+ + e^- \tag{3.15}$$

The formation of neutral $[C_2H_2]_2$ can also be observed from the acetylene monomer and dimer Penning ionization contributions in the fitted PIES correlated to $[C_2H_2]_3^+$ ion in Fig. 3.5 b), see below.

$$He^* + C_2H_2 \rightarrow He + C_2H_2^+ + e^- \tag{3.16}$$

$$C_2H_2^+ + [C_2H_2]_2 \rightarrow [C_2H_2]_3^+ \tag{3.17}$$

and

$$He^* + [C_2H_2]_2 \rightarrow He + [C_2H_2]_2^+ + e^- \tag{3.18}$$

$$[C_2H_2]_2^+ + C_2H_2 \rightarrow [C_2H_2]_3^+ \tag{3.19}$$

3.3.3 Structures of dopant clusters

The ratio of acetylene monomer to acetylene dimer Penning ionization channels, contributing to the detection of $[C_2H_2]_2^+$ ions is 3.07. Similarly, the ratio of acetylene monomer to acetylene dimer Penning ionization channels, contributing to the detection of $[C_2H_2]_3^+$ ions is 1.09. These values are calculated from the ratio of total area under the fitted PIES from the monomer Penning ionization channels to the total area under the fitted PIES from the dimer Penning ionization channels, contributing to the detection of respective oligomer ion as shown in the previous section. Since the ratios of monomer to dimer Penning ionization channels is greater that one in both the cases, the major contributions to the Penning ionization are from the monomer rather than from larger oligomers. This suggest that, resulting monomer ion ($C_2H_2^+$) combines with one or two dopant molecules in the droplet and the binding energy released in this process evaporates a large number of He atoms from the droplet, leading to shrinkage in the droplet size which aids the detection of $[C_2H_2]_2^+$ or $[C_2H_2]_3^+$ ion. Whereas, the dimer Penning ionization channels contributing to the detections of $[C_2H_2]_2^+$ and $[C_2H_2]_3^+$ ions can be interpreted in terms of Penning ionization of loosely-bound neutral acetylene dimer ($[C_2H_2]_2$) in the droplet,

which subsequently binds into covalently-bound acetylene dimer ion ($[C_2H_2]_2^+$), releasing significant binding energy (> 2 eV) [259]. This again leads to shrinkage in the droplet size through evaporation of He atoms, facilitating the detection of $[C_2H_2]_2^+$ ion. For larger droplets containing three or more C_2H_2 molecules, the resulting covalently-bound $[C_2H_2]_2^+$ ion can associate with another neutral C_2H_2 molecule in the droplet to form $[C_2H_2]_3^+$ ion, which is subsequently detected. However, the absence of C_2H_2 trimer Penning ionization channel leads to the following conclusions: acetylene molecules may not form a weakly-bound trimer in He nanodroplets. Instead the dopant aggregate is very likely loosely bound retaining significant characteristics of the electronic structure of the monomer. This finding is in line with recent results from an IR spectroscopy of acetylene dimers in He nanodroplets [168]. This unusual behaviour of acetylene oligomers in the droplet is reminiscent of the foam-like structure of the dopant aggregate in Mg-doped He nanodroplets and state-specific spatial separation observed in (Cr)-dimers in He nanodroplets [260]. Furthering the analogy, the Mg-foam was also observed to collapse upon photoexcitation forming strongly bound oligomers in the excited state. This motivates further experimental and theoretical investigations of the spatial and electronic structures of similar mesoscopic aggregates formed inside these He quantum fluid host.

Interpretation of fitting in low energy part

In the Fig. 3.5, below 7.5 eV, the black dashed lines show the total PIES when the fitting of the high energy part is extrapolated into the low energy part. As discussed before, in the low energy part we see contributions from 1) Penning ionization leading to excited cationic states, $A^2\Sigma_g^+$ and $B^2\Sigma_u^+$ of C_2H_2, and 2) inelastically scatter Penning electrons. We accounted for the scattering effects on the Penning electrons in the droplet by performing a Monte Carlo simulation based on binary electron-He scattering, similar to the work on acene doped droplet [183]. However, despite incorporating all the features of electron-He scattering in our simulations, we found that even for a large droplet radius of 30 nm (compared to 6.5 nm in our experiments for 14 K nozzle temperature and He expansion pressure of 50 bar) the simulated PIES do not agree with the low-energy part of the electron energy spectra. This indicates that one should take into account possible electron bubble interactions in the simulation. This low energy feature also arises from the higher excited A and B states of $C_2H_2^+$. The large Penning ionization signal involving

the A and B states as compared to that in earlier molecular beam experiments [258] may be related to the steep dependence of the corresponding effective cross-sections on the collision energy [17].

3.4 Dopant ionization upon droplet autoionization

To learn about the ionization mechanisms in the autoionization regime (23 eV $< h\nu <$ E_i^{He}), the doped droplet was photoexcited across the $n = 4$ droplet band corresponding to the atomic He* ($1s4p\ ^1P$) excitation. The electron energy spectra correlated to He_2^+, $C_2H_2^+$ and $[C_2H_2]_2^+$ are presented in Fig. 3.6 at two different photon energies, 23.9 eV where a pronounced ionization maximum was observed, and 24.3 eV which is a minimum that follows in Fig. 3.2 a).

In Fig. 3.6 a1), and a2), the electron energy spectra correlated to He_2^+ at both photon energies reveal very low-energy ($\sim 100 - 500$ meV) electrons which are the signatures of droplet autoionization [180, 247], as also stated in section 3.2.1. Interestingly, the electron energy spectra correlated to $C_2H_2^+$ and $[C_2H_2]_2^+$ at 23.9 and 24.3 eV photon energies also show similar low energy features, see Fig. 3.6 b1), b2), c1), and c2). However, these features are broader with their maxima shifted toward higher energy sides compared to that of He_2^+. This suggests that charge transfer (CT) ionization of the dopant from He_2^+ formed due to autoionization in the droplet (see process 3.3) cannot be the only mechanism responsible for formations of the acetylene oligomer ions. The additional low energy peak around 0.5 eV could therefore be due to Penning ionization of C_2H_2, leading to highly excited $C_2H_2^+$ ion. In Fig. 3.6 d1), and d2), the measured photoelectron spectra (PES) of effusive isolated C_2H_2 at 23.9 and 24.3 eV photon energies energies fit well with the simulated PES from the higher-lying $C^2\Sigma_g^+$ (23.33 eV) and $D^2\Sigma_u^+$ (23.33 eV) states of $C_2H_2^+$ [261].

3.4.1 Competing Penning ionization from $n = 4$ droplet excitation

To confirm the additional Penning processes in the dopant from He* ($1s4p\ ^1P$) state, resulting in $C_2H_2^+$ in $C^2\Sigma_g^+$ and $D^2\Sigma_u^+$ states, the following two-function fitting procedure

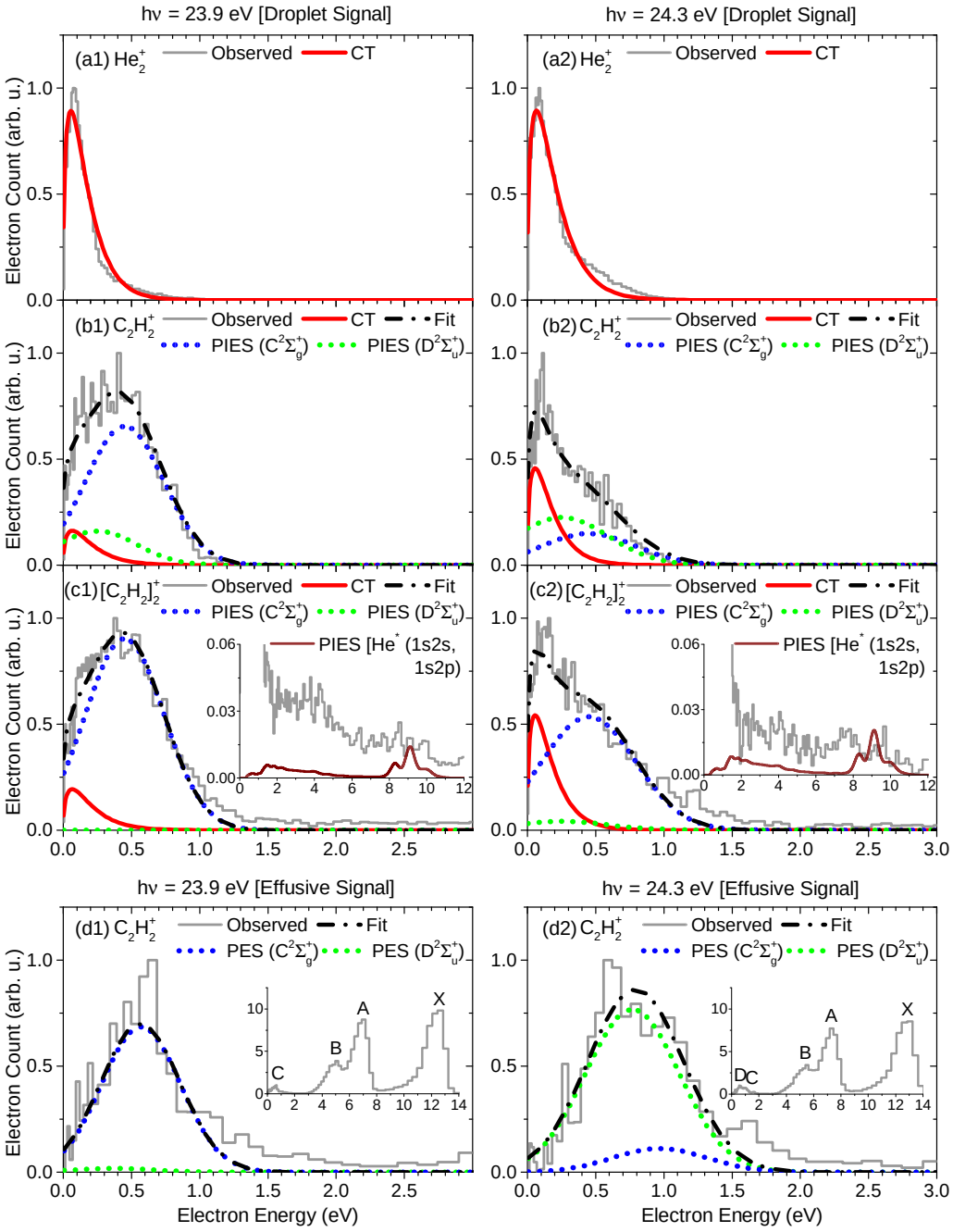

Figure 3.6: Electron energy spectra at 1) 23.9 eV and 2) 24.3 eV photon energies, correlated to different ions a1), a2) He_2^+, b1), b2) $C_2H_2^+$, c1), c2) $[C_2H_2]_2^+$ from the acetylene doped droplet at $P_{doping} = 4.5 \times 10^{-6}$ mbar and $T_{nozzle} = 14$ K. The charge-transfer (CT) ionization processes are shown by red curves whereas the Penning processes via He* ($1s4p$ ^1P) state leading to $C_2H_2^+$ $C^2\Sigma_g^+$ and $D^2\Sigma_u^+$ states are shown by blue and green dotted curves, respectively. Black dashed curves are the sum of CT and Penning processes. The insets in panel c1) and c2) show the zoomed out electron energy spectra correlated to $[C_2H_2]_2^+$ ion at $h\nu = 23.9$ and 24.3 eV, respectively, where one can see the presence of Penning ionization channels from He* ($1s2s, 1s2p$) states, represented by brown lines in c1), c2) observed at 21.6 eV droplet photoexcitation. PES correlated to effusive C_2H_2 photoionization at d1) 23.9 eV and d2) 24.3 eV photon energies. The blue and green dotted curves represent the simulated PES from $C_2H_2^+$ $C^2\Sigma_g^+$ and $D^2\Sigma_u^+$ states, respectively. The insets in panel d1) and d2), PES peaks from $C_2H_2^+$ $X^2\Pi_u$, $A^2\Sigma_g^+$, $B^2\Sigma_u^+$, $C^2\Sigma_g^+$ and $D^2\Sigma_u^+$ states can be observed. Adapted with permission from ref.[253].

is implemented to analyse the electron spectra correlated to $C_2H_2^+$ and $[C_2H_2]_2^+$, see below.

$$F(E) = \frac{C^{MB}}{(k_B T)^{3/2}}\sqrt{E}\exp(-\frac{E}{k_B T}) + \sum_{i=1,2}\frac{C_i^G}{\sigma}\exp(-\frac{(E-E_i^p)^2}{2\sigma^2}) \tag{3.20}$$

where the Maxwell-Boltzmann distribution function (first term) represents the CT ionization and the Gaussian functions (second term) represent the new Penning ionization channels. Using the value of T, obtained from the fitting of the electron spectra correlated to He_2^+, the electron spectra correlated to $C_2H_2^+$ and $[C_2H_2]_2^+$ are fitted by varying the coefficients C^{MB} and C_i^G. Since Penning ionization can proceed from He* ($1s4p\ ^1P$) state, the Gaussian peak positions (E_i^P) are fixed at the energy difference between He* ($1s4p\ ^1P$) and $C_2H_2^+$ ($C^2\Sigma_g^+$, $D^2\Sigma_u^+$) states while the standard deviation (σ) is fixed from the fitting of the effusive acetylene photoelectron energy spectra. As the energy distribution of the autoionized electrons which are detected in coincidence with He_2^+ fits the Maxwell-Boltzmann distribution quite well, the same Maxwell-Boltzmann distributions are used to fit the CT ionization component. Note that, the observed energy distributions of the autoionized electrons are relatively high energy side compared to previously reported spectra due to the finite energy resolution of the VMI [247].

In Fig. 3.6 b1), b2), c1) and c2), the CT components are marked by red curves whereas blue and green dotted lines represent the Penning ionization components from $C_2H_2^+$ $C^2\Sigma_g^+$ and $D^2\Sigma_u^+$ states, respectively. Thus, prominent Penning mechanisms leading to higher-lying $C^2\Sigma_g^+$ and $D^2\Sigma_u^+$ states of $C_2H_2^+$ via relaxation of He* $1s4p\ ^1P$ are identified.

Whereas at $h\nu = 23.9$ eV the Penning channel dominates, at $h\nu = 24.3$ eV CT ionization is more favourable. We notice that the electron spectra correlated to $[C_2H_2]_2^+$ at these energies also have weak long tail, extending up to nearly 11 eV, see insets of Fig. 3.6 c1), c2). This tail is possibly due to Penning ionization from He* $1s2s$ and He* $1s2p$ states arising from internal relaxations in the droplet, as observed in PIES at 21.6 eV photon energy. Earlier femtosecond pump-probe time-resolved studies on pure He nanodroplets reported that upon photoexcitation to the $n = 4$ droplet band, fast internal relaxation to the $n = 2$ droplet band on a time scale of $2 - 3$ ps occurs [262, 263]. The observed strong Penning ionization signal from He* ($1s4s$) compared to the Penning ionization from internally relaxed $n = 2$ states suggests that the Penning ionization from He* ($1s4s$)

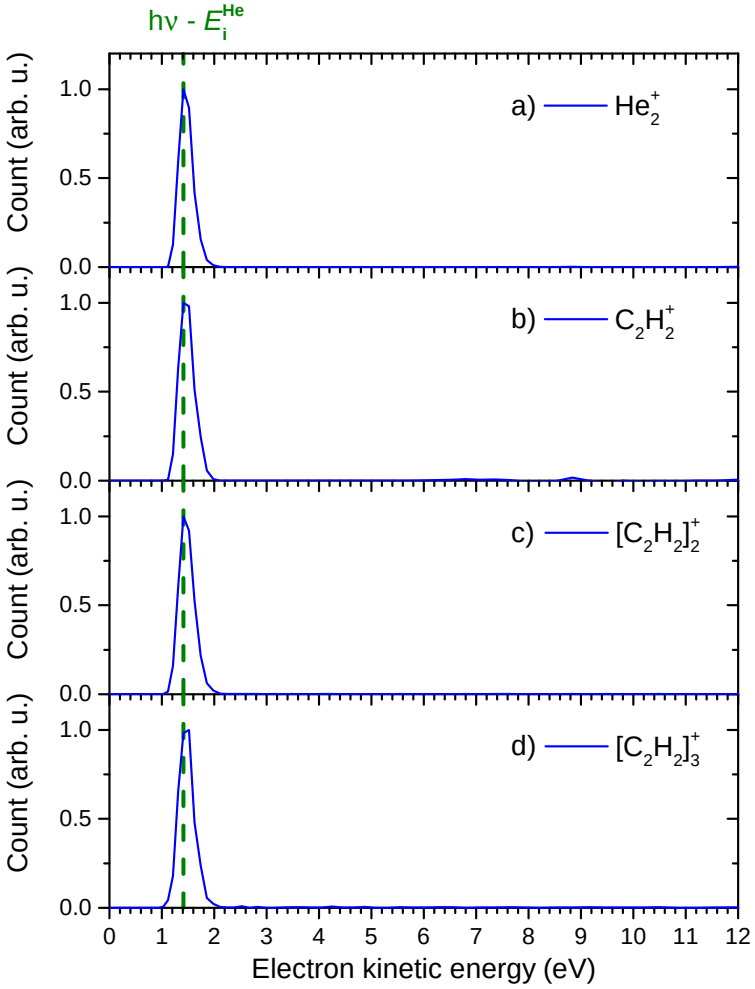

Figure 3.7: Electron kinetic energy spectra correlated to a) He_2^+, b) $C_2H_2^+$, c) $[C_2H_2]_2^+$, and d) $[C_2H_2]_3^+$, at 26 eV photon energy for $T_{noz} = 14$ K and $P_d = 4.5 \times 10^{-6}$ mbar.

occurs on a faster time scale than the internal relaxation time of the $n = 4$ droplet excitation.

Upon resonant excitation to the $n = 2$ droplet excitation band at 21.6 eV, we observed Penning ionization of acetylene clusters leading to $C_2H_2^+$ in X, A, and B states. However, when the droplet is photoexcited to even higher $1s4p$ state, Penning ionization channels leading to higher-lying $C_2H_2^+$ states such as C and D states become energetically accessible and are observed here in this autoionization regime along with Penning ionization leading to lower-lying $C_2H_2^+$ states (X, A, B). The enhanced Penning ionization cross-section leading to C and D states by He^* $(1s4p\ ^1P)$ could be related to the near degeneracy of these C and D states with the $1s4p\ ^1P$ state.

This interpretation is further supported by PIES recorded for He nanodroplets doped

with Li atoms presented previously by Ltaief *et al.* [181]. The spectrum recorded at 21.6 eV photon energy is dominated by electrons emitted by Penning ionization of Li interacting with excited He in the $1s2s\ ^1S$ and ^3S states. In the coincident electron energy spectra recorded above the droplet ionization threshold (23 eV), the peaks between 13 and 16 eV reflects Penning ionization of Li after electronic relaxation of the excited He droplet into the $1s2s\ ^1S$ and ^3S states, and the low-intensity feature around 18 eV is due to Penning ionization involving the $1s3s$; $1s3p$ and $1s4s$; $1s4p$ states of He^*. The fact that the contributions to the Li Penning ionization arising from these higher excited states are significantly lower than in the case of acetylene can be due to the differing location of the dopants in the droplet: Li atoms are on the surface, whereas C_2H_2 molecules are expected to be located in the He droplet interior. Consequently, a He^* excitation initially localized within the He droplet migrates over a significant distance until it reaches the Li dopant which affords the relaxation into the metastable $1s2s\ ^1S$ and ^3S states before Penning ionization takes place. In comparison, the distance between the He^* and the acetylene dopant is shorter on average thereby facilitating direct Penning ionization prior to He^* relaxation.

3.5 Dopant ionization upon droplet direct ionization

At 26 eV photon energy, above the photoionization threshold of atomic He (24.58 eV), the electron kinetic energy spectra correlated to He_2^+ ions, along with the dopant-ions, $C_2H_2^+$, $[C_2H_2]_2^+$ and $[C_2H_2]_3^+$, are presented in Fig. 3.7 a), b), c), and d), respectively. One can readily see that all these electron kinetic energy spectra are identical and the peak positions match with the kinetic energy of He photoelectrons at 26 eV. Thus, it is evident that the dopants C_2H_2 oligomer ions are formed due to charge transfer to the directly ionized droplet above atomic He photoionization threshold, as predicted previously section 3.2.1 (see process 3.4). The obtained He photoelectrons in coincidence with the C_2H_2 oligomer ions confirm the mentioned charge transfer ionization mechanism in the dopants.

3.6 Summary

Inelastic scattering of Penning electron with the host-He nanodroplet environment was thought to obscure the information about the electronic structure of the embedded dopants in the dopant-ion correlated PIES, as demonstrated earlier for acene dopants [183]. However, in the current experiments with C_2H_2 as dopants, we demonstrate that this is not always the case. Penning ionization can indeed be used as spectroscopic tool to study atomic and molecular quantum aggregates formed in He nanodroplets by exciting the host matrix. By studying the electrons and ions for the host and dopant in coincidence, one can identify relevant excited states of the host and dopants. Moreover, it is shown that Penning ionization electron spectroscopy is not only limited to the $n = 2$ droplet excitation, but can also be extended to perform spectroscopy employing higher droplet excitation bands such as $n = 4$ to probe higher lying excited states of the dopants which are not accessible via $n = 2$ droplet excitation. By implementing this dopant-ion correlated PIES, we are able to uncovered the structure of embedded acetylene clusters inside nanodroplets. These C_2H_2 molecules coalesce in the form of loosely bound van der Waals aggregates, similar to a foam-like structures observed for magnesium dopants. However, these structure collapses into a composite oligomer ions following Penning ionization from He^*. Thus, theses results motivate further time-resolved study of C_2H_2 aggregates in He nanodroplets. Furthermore, Penning ionization electron spectroscopy has been established as a widely applicable technique to probe mesoscopic quantum aggregates in He nanodroplets.

Chapter 4

Heavy Alkali Doped Helium Nanodroplets

In this chapter, the experimental methods and results obtained from the investigation of *inter*-atomic/molecular decays in He nanodroplets doped with heavy alkali (Ak) atoms, rubidium (Rb) and cesium (Cs), when irradiated with EUV radiations in the photon energy range from 20 to 60 eV, are presented. This photon energy range covers both, the $n = 2$ droplet excitation band at 21.6 eV and direct ionization of the He droplet above $E_i^{He} = 24.58$ eV. Note that, these photon energies are below the double ionization energy of atomic He (79 eV). Therefore, the expected dynamics is mainly initiated by the single electronic excitation or ionization of droplet up to 58.31 eV photon energy, beyond which doubly-excited He can also influence the ionization processes.

4.1 Experimental Methods

Here, only the doping process and the configuration of the electron-ion spectrometer are presented, as rest of the details are already discussed in chapter 2.

4.1.1 Doping process

As shown in the schematic diagram of the experimental setup, in Fig. 4.1, inside the oven cell at the doping chamber, a small amount of the alkali metal ($\sim$ 1 g) was kept and heated to $70-100$°C. This evaporates the Ak atoms inside the oven cell. The He droplets

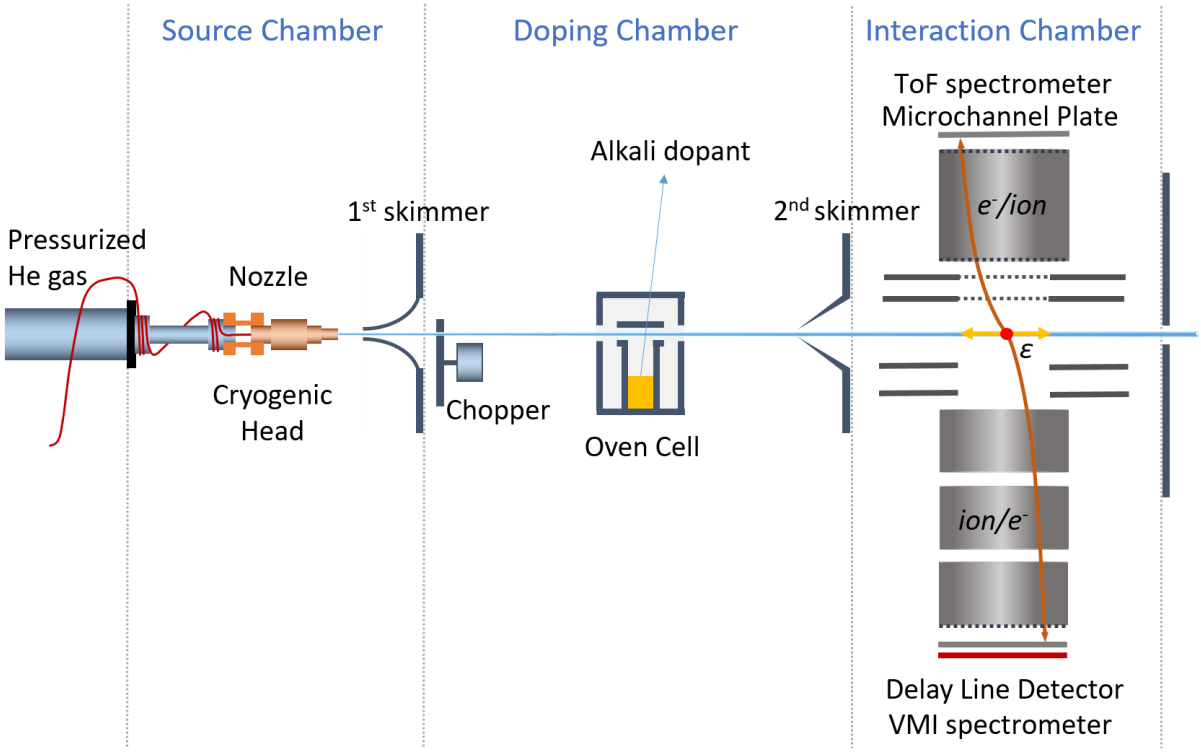

Figure 4.1: Schematic of the experimental setup for Ak doped He nanodroplets experiment. Pure He nanodroplets are produced via supersonic expansion of He gas through the cryogenic nozzle and the 1^{st} skimmer in the source chamber. In the doping chamber, the droplets are doped with Ak dopants inside the oven cell where the Ak metals are evaporated from the solid sample by heating. Finally, in the interaction chamber, the doped droplet is ionized by the linearly polarized EUV light and the resulting ions and electrons are detected by the ToF and VMI spectrometer in both the electron- and ion-VMI configurations.

then pick up a few dopant atoms on their travel paths through the oven cell via collisional pickup process. We kept the nozzle temperature at 14 K and the He backing pressure at 50 bar, thereby producing an average droplet size of $\sim$ 23000 He atoms per droplet [151].

4.1.2 Spectrometer configurations

To get more information about the ionization processes in Ak doped He nanodroplets at different photon energies, unlike the previous experiments with C_2H_2 dopants wherein only electron-VMI mode was implemented, here we performed the experiments in both the electron- and ion- VMI modes. In the electron-VMI mode, we recorded the mass to charge correlated ion-yield spectra as a function of photon energy, electron kinetic energy (eKE) spectra correlated to single and multiple ions as well as the total electron kinetic energy spectra. Whereas, the ion-VMI mode enables us to record the kinetic energies

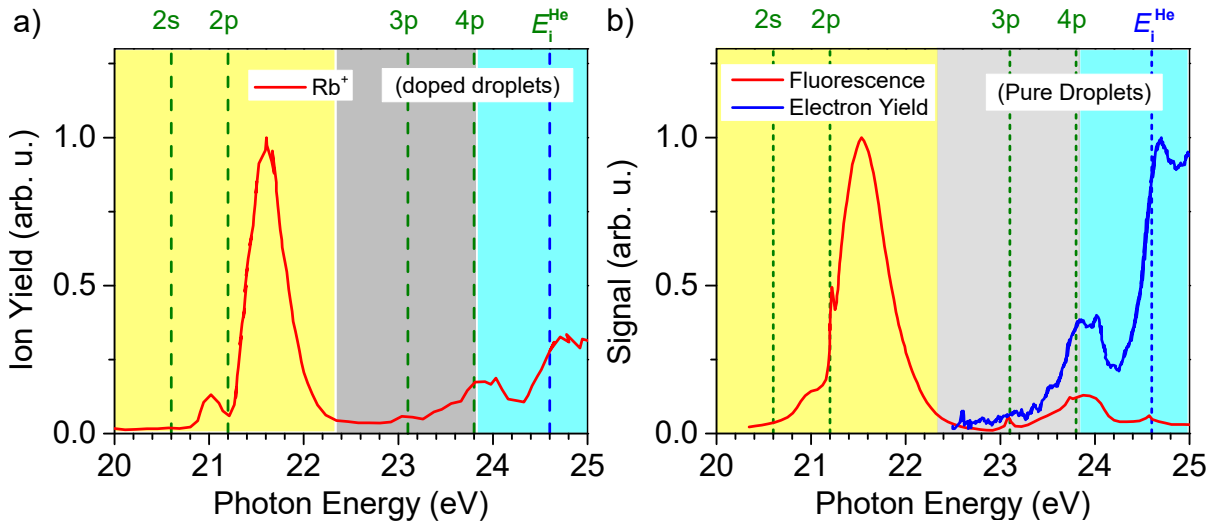

Figure 4.2: a) Rb^+ ion-yield spectrum as a function of photon energy for Rb doped He nanodroplets at 14 K nozzle and 90°C oven temperatures. b) The fluorescence (red line) and total electron yield (blue line) as a function of photon energy due to photoexcitation and ionization of pure He droplets, reported in earlier studies [242, 180]

of the detected ions, from where one can derive the total kinetic energy release (KER) spectra of the product-ions.

4.2 Dopant ionization at different photon energies

To monitor the dopant ionization in the droplet, the yields of alkali ions originating from droplet excitation or ionization are measured as a function of photon energy from 20 to 26 eV in case of the Rb doping. Fig. 4.2 a) shows the measured ion-yield spectrum of Rb^+ ions as a function of photon energy for Rb doped He nanodroplets at 14 K nozzle and 90°C oven temperatures. For reference, Fig. 4.2 b) shows the fluorescence (red line) and total electron yield (blue line) due to photoexcitation and ionization of pure He droplets obtained in earlier studies [242, 264].

4.2.1 Inter-atomic/molecular decays

One can see from the Fig. 4.2 a), Rb^+ ions are significantly detected from the droplets above $\sim$ 20.8 eV photon energy, which is around the threshold for pure droplet photoexcitation, see the onset in fluorescence yield (red line) in Fig. 4.2 b). Above this photoexcitation threshold, the Rb^+ ion yield curve follows both the fluorescence and total electron signals from the droplet. Therefore, one can argue that the Ak dopants are

significantly ionized through *inter*-atomic/molecular decay via excited or ionized droplet. Negligible detection of Ak^+ ion below the droplet photoexcitation threshold suggests that at this experimental condition only a few Rb atoms are doped in relative large He droplets, leading to large difference in photoexcitation yield of the droplet compared to the direct photoionization yield of the dopants in the droplets.

One can directly see that below 23 eV photon energy (yellow shaded region) the Rb^+ ion yield follows the pure droplet fluorescence spectra and shows a large ionization peak around 21.6 eV photon energy. This indicates that at this energy range the Rb dopants are significantly indirectly ionized via photoexcitation of the He droplet to the first droplet excitation band ($n = 2$). Similarly, above 23 eV photon energy where the host droplet is either autoionized ($23 < h\nu < E_i^{\mathrm{He}}$) (grey shaded region) or directly ionized ($h\nu \geq E_i^{\mathrm{He}}$) (cyan shaded region) by the incident photon, the Rb^+ ion-yield spectrum follows the total electron-yield spectrum of pure droplet ionization. This indicates indirect ionization of the dopants following ionization of the host.

4.2.2 Surface localization of alkali

The large relative intensity of the peak around 21.6 eV in the Rb^+ ion-yield compared to the peaks at the droplet autoionization ($23 < h\nu < E_i^{\mathrm{He}}$) and direct ionization ($h\nu \geq E_i^{\mathrm{He}}$) regimes gives an indication of the position of these dopants on the surface of the droplet. Since the dopant ionization process is *inter*-atomic/molecular in nature, as seen above, and the photoexcited He^* tends to migrate to the surface of the droplet [173, 174] as opposed the He^+ ion which migrates to the centre of the droplet [175, 176, 177, 178], dopants attached to the surface of the droplet preferably undergo *inter*-atomic/molecular ionization through droplet de-excitation rather than via charge transfer to the ionized droplet [180]. The shape of the Rb^+ ion-yield curve confirms the surface localization of these heavy alkali metal (Rb) dopants. This finding complements the earlier studies done with light alkali metal (Li) dopant [180], and the ultrafast laser experiments done with Na [265], K [266], Rb [267] and Cs [268] doped He droplets, indicating that small Ak dopant clusters are generally bound to the surface of the droplet. Fig. 4.3 schematically shows the migration of He^* from the photoexcitation site to the droplet surface where subsequent ionization of Ak dopant takes place through interatomic Coulombic decay (ICD) from the de-excitation of He^*.

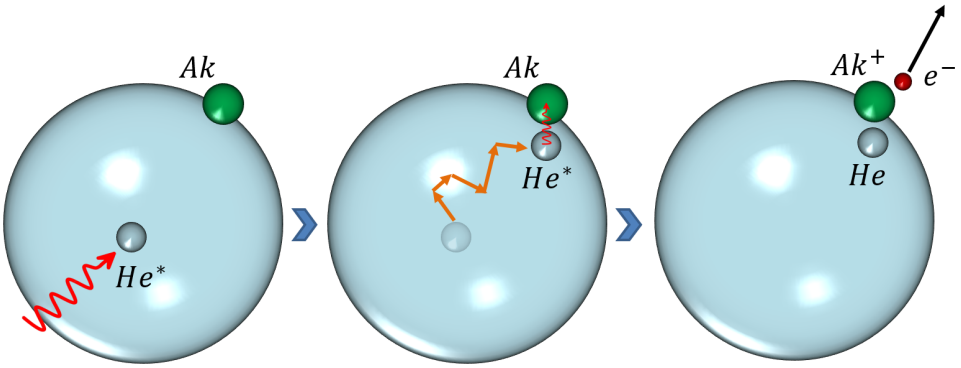

Figure 4.3: Schematic of the *inter*-atomic decay following droplet photoexcitation. Upon excitation of He in the droplet, He* migrates to the droplet surface where the doped Ak atoms are located, and He* relaxes via interatomic Coulombic decay (ICD) leading to ionization of the dopant.

Selected photon energies

Now, to gain detailed insight into the *inter*-atomic/molecular decays following both the droplet photoexcitation and photoionization, we focused our study on two different photon energies; 1) at 21.6 eV ($n = 2$ droplet excitation band) and 2) at photon energy higher than the droplet direct ionization threshold ($E_i^{He} = 24.58$ eV); 26 eV for Rb and 60 eV for Cs dopants. The ion mass spectra, multi-ion coincidence maps, correlated electron and ion kinetic energy spectra at these two photon energy ranges are presented in the following sections.

4.2.3 Product ions

Fig. 4.4 shows the measured ion mass spectra at a) 21.6 eV and at b) 26.0 eV photon energies from Rb doped He nanodroplets at 14 K nozzle and 90°C oven temperatures. Both Rb_n^+ cluster ions as well as $RbHe_n^+$ snowball ions are detected at these photon energies. Additionally at 26.0 eV, one can observe the He_n^+ ions generated from the direct droplet ionization. Formation of $RbHe_n^+$ snowball ion has been observed in earlier experiments following femtosecond laser photoionization of alkali doped droplets [269] as well as upon resonant two photon ionization of Rb dopants attached to the surface of the droplet [270]. The attractive potential between the positively charged ion and the droplet is mainly responsible for such aggregation. Interestingly, the abundance of $RbHe_n^+$ snowball ions relative to the bare Rb^+ ions is greater for dopant ionization following droplet direct ionization at 26.0 eV as compared to the same for ionization upon droplet photoexcitation

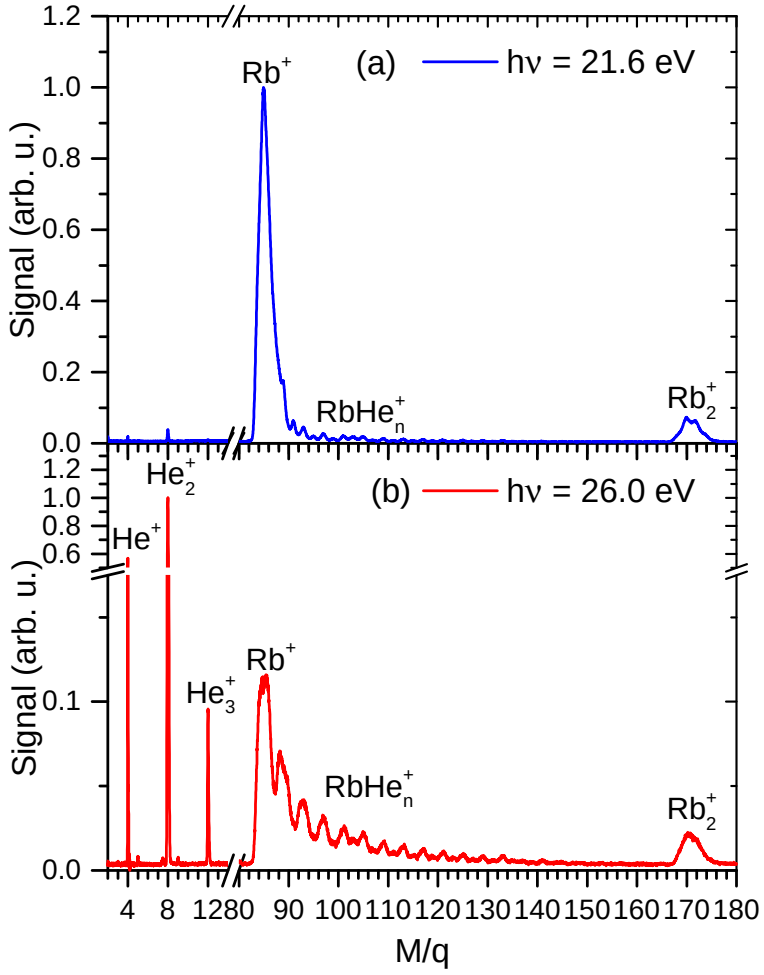

Figure 4.4: Ion mass spectrum at a) 21.6 eV and at b) 26.0 eV photon energies from Rb doped He nanodroplets at 14 K nozzle and 90°C oven temperatures. The horizontal axis shows the mass in amu. (M) to charge (q) ratios of the ions.

at 21.6 eV. This observation motivates further investigations into the snowball formation dynamics specific to these photon energies. However, this is beyond the scope of the current thesis work.

4.2.4 Degree of ionization of the dopants

Although we get the information about the He_n^+, Rb_n^+ and $RbHe_n^+$ ions formed in these photon energies from the ion mass spectra, to know the degree of ionization of the dopants, we plotted the ion-ion coincidence maps. Ion-ion coincidence maps for Rb doping at 21.6 eV and 26 eV photon energies are presented in Fig. 4.5 a) and b), while the same for Cs doping, at 21.6 eV and 60 eV photon energies are shown in Fig. 4.5 c) and d), respectively.

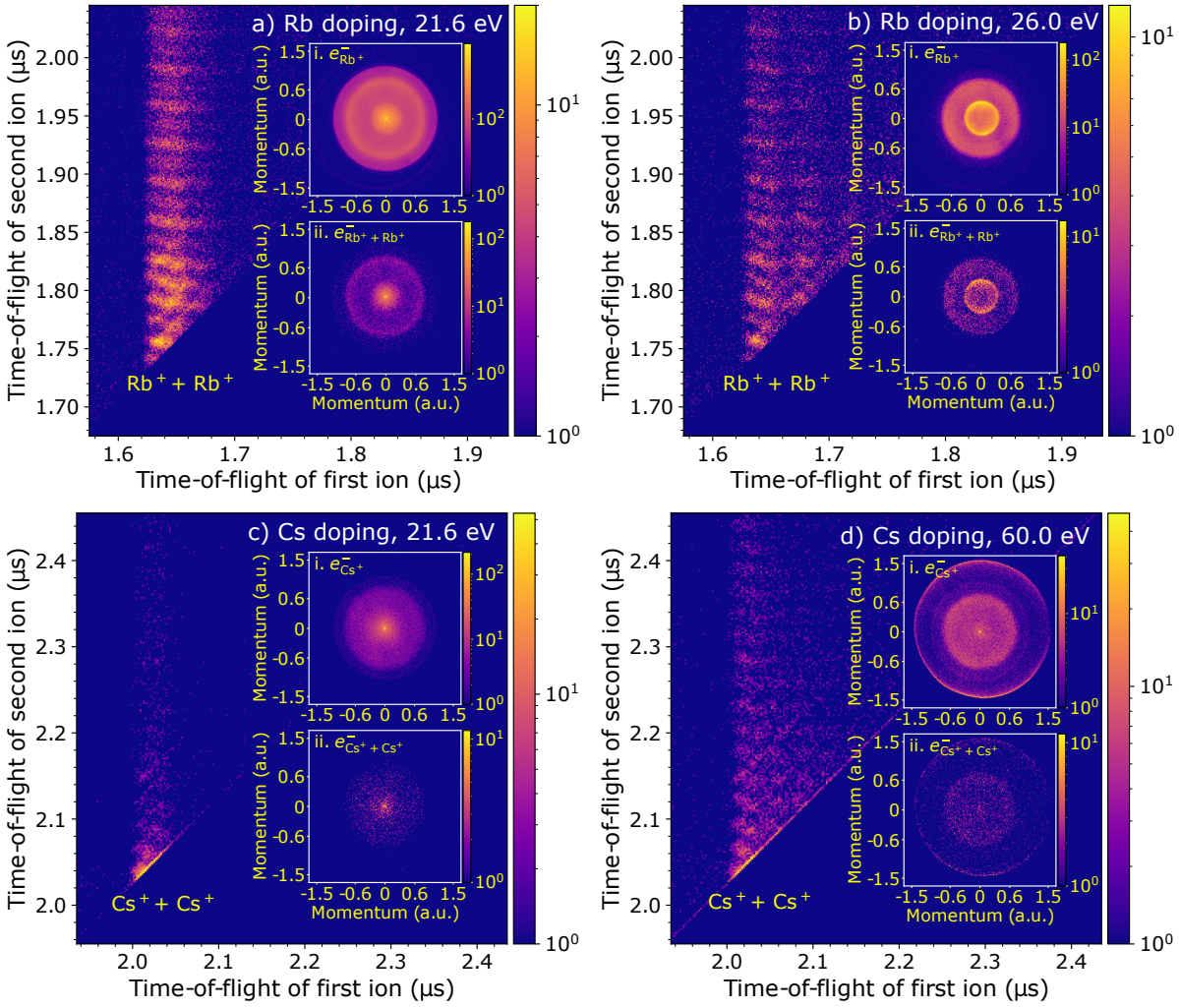

Figure 4.5: Ion-ion ToF coincidence maps at a) 21.6 eV and at b) 26 eV for Rb doped droplets. Ion-ion ToF coincidence maps at c) 21.6 eV and at d) 60 eV for Cs doped droplets. The correlated electron VMI images in coincidence with single and double Rb^+ and Cs^+ ions are shown in the insets i. and ii. respectively for these the photon energies. Note that, the off-centred outer ring structures in the electron VMI images, prominently seen in case of Cs doping at 60 eV photon energy, originate from the focusing of scattered electrons in the spectrometer. Hence, these outer structures, which are artefact in these VMI images, are not considered for electron kinetic energy (eKE) spectrum calculations. The smaller central region of the VMI image ($|\mathbf{p}| < 1.2$) corresponds to electrons ejected from doped droplets, and only that region is used for extracting eKE spectra.

One can observe that the time of flights of the first two dopant cluster ions (Rb^+ and $RbHe_n^+$, and, Cs^+ and $CsHe_n^+$) are strongly anti-correlated, evident from negative slopes for the coincidence islands. The slopes of these ToF coincidence islands vary with the ratio of masses of the involved ions, consistent with the fact that the total momentum of these ions is conserved. No higher order coincidences, *e.g.*, time of flight correlation between second and third detected ions for each detected ionization event, were observed for these dopants. Therefore, one can argue that for these dopants, Rb and Cs, the dopant clusters undergo only up to double ionization upon droplet photoexcitation and ionization, wherein the created positive charges reside on separate atomic constituents of the Ak_2 leading to subsequent Coulomb explosion of the dication (Ak_2^{2+}). Note that, direct double ionization of atomic Rb and Cs is unlikely since their double ionization energies are 31.45 and 27.04 eV, respectively, which are beyond the energy available after single photon excitation and ionization of the doped droplet. These observations are contrary to the previous experiments with C_2H_2 dopants, where only single ionization of the C_2H_2 cluster was observed in the droplet following photoexcitation and ionization of the droplet.

4.2.5 Identifying single and double ionization processes

The correlated electron VMI images in coincidence with single and double Ak^+ ion are shown in the insets i. and ii., respectively, in Fig. 4.5 a), b), c) and d) for the corresponding dopants and photon energies. Note that, the electron VMI images corresponding to single Ak^+ ions which are obtained by selecting different ion peaks in the corresponding ToF spectra are insensitive to the degree of ionization as the ToF spectra contain all the detected ions. Therefore, they include electrons from both the single and double ionization events. To separate the single ionization processes from the double ionization events, we obtained the electron VMI images correlated to double alkali ions in coincidence by selecting the corresponding ToF coincidence islands on the ToF coincidence map and compared the same with the electron VMI images corresponding to single ions. Since the former only includes electrons from double ionization events, any structure that is unique to the later will indicate single ionization of the dopants, and one can assign the common structures purely to double ionization events.

Note that, the off-centred outer ring structures in the electron VMI images originate

from the focusing of scattered electrons in the spectrometer onto the VMI detector. Hence, these artefact are not considered further in the discussion. Only the relevant concentric VMI structures correlated to the unperturbed electrons, which are ejected out of the doped droplets and detected in the smaller central region of the VMI detector, are discussed here.

At 21.6 eV, from Fig. 4.5 a) and c), insets i. and ii., one can see that there are three ring structures in the electron VMI images, in which the central and inner rings are common to both the cases, whereas the outer ring is unique to the VMI image corresponding to single Ak^+ ions in coincidence. Therefore, this structure arises only due to single ionization of the dopants, whereas the other two are from double ionization of the dopants. Likewise at 26.0 and 60.0 eV, in Fig. 4.5 b) and d), insets i. and ii., we can observe similar structures in all the VMI images, which indicates double ionization of the dopants. These processes are discussed in the following sections by presenting the corresponding eKE and ion-KER spectra, first for 21.6 eV photon energy upon droplet excitation and later for photon energy above E_i^{He} upon droplet direct ionization.

4.3 Dopant ionization upon droplet excitation

Fig. 4.6 a) and b) show the eKE spectra corresponding to single Ak^+ ion (grey line), double Ak^+ ions (red line) in coincidence and total electrons (green line) for Rb and Cs doped droplets at 21.6 eV photon energy, respectively. By looking at the eKE spectra, the obtained spectra can be divided into three different regimes, as follows: 1) low energy peaks ($0-4.5$eV), 2) mid energy peaks ($4.5-12$ eV), and 3) high energy peaks ($13-20$ eV). From the previous discussion, we can directly assign the high energy peaks to the processes that lead to the single ionization of the dopants and the rest of the peak structures to the processes that lead to double ionization. Here, the single ionization processes are presented first, and then the double ionization processes are discussed.

Single ionization processes

It is well known that upon photoexcitation at 21.6 eV, the droplet is excited to $n = 2$ droplet excitation band, and He atom inside the droplet is photoexcited to He* $1s2p\ ^1P$ state. Subsequently, ultrafast internal relaxation in He* $1s2p\ ^1P$ state allows for some of the initially excited He* to be populated in dipole forbidden $1s2s\ ^{3,1}S$ states in the

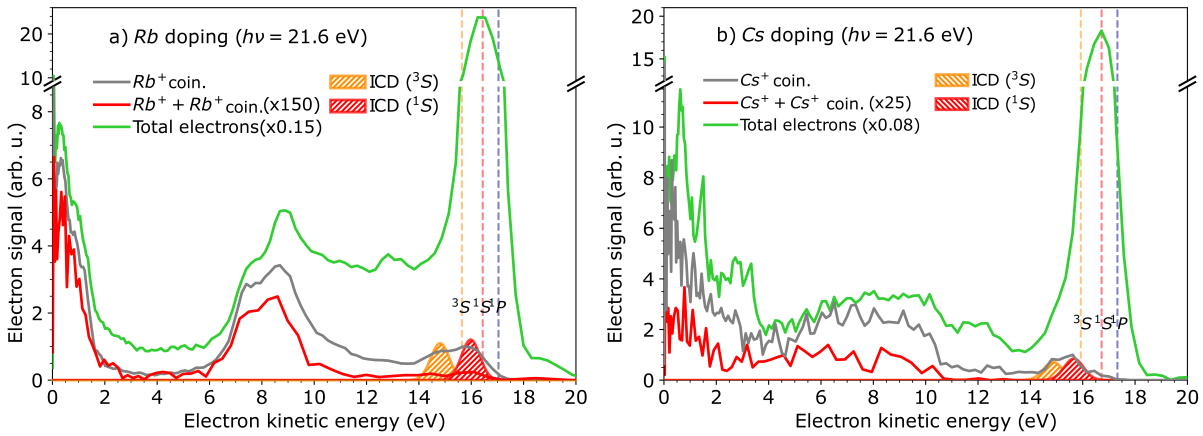

Figure 4.6: Electron kinetic energy (eKE) spectra corresponding to single Ak^+ ion (grey line), double Ak^+ ions (red line) ions in coincidence, and total electrons (green line) for a) Rb and b) Cs doped droplets at 21.6 eV photon energy. The orange, red and blue vertical dashed lines represent the expected electron energies for single ionization of the Ak dopant due to long-range ICD from He^* $1s2s$ $^{3,1}S$ and $1s2p$ ^1P states, respectively, whereas the orange and red peaks with hatched shading are the simulated eKE spectra due to short-range ICD from He^* $1s2s$ $^{3,1}S$ states, respectively.

droplet [246]. Finally, all these He^* $^{3,1}S$, ^1P states relax to the ground He $1s^2$ ^1S state by ionizing the neighbouring dopant via resonant interatomic Coulombic decay (ICD). Now, if this ICD leads to ionization of the outer shell (ns) electron in the Ak dopants ($n = 5$ for Rb, and $n = 6$ for Cs), the expected ICD electron energy will be in the range from 14 to 18 eV as the ionization threshold for Rb and Cs are 4.17 and 3.89 eV, respectively. Since the observed high energy peaks are in the same range, one can argue that the single ionization of Ak proceeds via the ionization of outer valence electron through ICD from He^* states in the droplet.

However, the distance between the He^* and Rb or Cs plays an important role in determining the ICD electron energy and subsequent emission of the ions from the droplet as evidenced in our recent publication [181]. These ionization processes occur at two interatomic distances, thus they are named as follows: 1) long-range ICD and 2) short-range ICD.

4.3.1 Long-range interatomic Coulombic decay

In case of long-range ICD, ionization occurs at large interatomic distance such that the internal energy of the He^*-Ak complex remains equal to the energy of He^* states. Therefore, the emitted ICD electron (e^-_{ICD}) kinetic energy in this process (shown below) will

be equal to $eKE(e^-_{ICD}) = E(\mathrm{He}^*) - E_i^{Ak}$, where $E(\mathrm{He}^*)$ and E_i^{Ak} are the energy He* and ionization energy of Ak atom, respectively. The orange, red and blue dashed vertical lines in Fig. 4.6 a) and b) show the calculated long-range ICD eKE for both the Rb and Cs doping due to relaxation of He* $^{3,1}S$,^1P states, respectively.

$$\mathrm{He}^* - \mathrm{Ak} \rightarrow \mathrm{He} + \mathrm{Ak}^+ + e^-_{ICD} \tag{4.1}$$

The estimated long-range ICD eKEs match with the total electron signal which also includes electrons for which no ions are detected in coincidence. This signifies that the this process produces Ak^+ ions with very low kinetic energy release (KER) which are not able to eject out of the host He nanodroplets.

4.3.2 Short-range interatomic Coulombic decay

In case of short-range ICD process, He*Ak molecule is formed following the photoexcitation of He droplet at the droplet surface. Subsequently, ICD occurs from the equilibrium interatomic distance of potential energy curve of the same (see fig.2 of ref. [181]). Due to this, the internal energy of the He*Ak reduces from that of a long-distance He*-Ak complex, leading to a decrease in ICD eKE for this short-range process shown below:

$$\mathrm{He}^*\mathrm{Ak} \rightarrow \mathrm{He} + \mathrm{Ak}^+ + e^-_{ICD} \tag{4.2}$$

This process is equivalent to gas phase Penning ionization processes where ionization occurs through charge-transfer between the outer shell electron of the ground state constituent and the low energy hole created in the excited constituent, eventually leading to the ionization of initially excited electron [16]. Since the efficiency of the charge-transfer process highly depends on the interatomic distance, Penning ionization is known to occur at lower interatomic separation. Therefore, we referred to the gas phase Penning ionization electron spectra (PIES) of Rb and Cs by He* $^{3,1}S$ states from earlier experiments [271]. First, the PIES of Rb and Cs due to the relaxations of He* $^{3,1}S$ states are extracted from ref.[271]. Then, the extracted PIES are convoluted with our VMI resolution factor. Finally, the corresponding convoluted PIES from He* $^{3,1}S$ states are fitted to the high energy part of the eKE spectra measured in coincidence with Rb^+ and Cs^+ ions, where to

get best possible fitting the peak positions of the convoluted PIES from He* $^{3,1}S$ states are varied along with their relative intensities both for Rb and Cs doping. The orange and red lines with hatched shading in Fig. 4.6 a) and b) show the fitted energy-shifted convoluted PIES from He* $^{3,1}S$ states, for Rb and Cs atoms, respectively. In case of doped He nanodroplets, the shifts in energy in the fitted convoluted PIES compared to the same from gas phase Penning ionization study are -0.65 and -0.33 eV for Rb, and -0.73 and -0.87 eV for Cs, following ICD from He* ^3S and ^1S states, respectively. The high energy peaks of the eKE spectra in coincidence with single alkali ions (grey line) fit quite well with the simulated PIES, thereby evidencing the short-range ICD process in Ak doped droplet at 21.6 eV. The further decrease in the short-range ICD electron kinetic energy for doped droplets, compared to the same from gas phase Penning ionization, suggests that the internal energy difference between the initial and final states for the former case is lower than that from the latter case.

Moreover, the fact that the short range ICD process is only visible in the eKE spectra for which dopant ions (Ak^+) are detected in coincidence, indicates that the initial He*Ak complex is likely to be created on an attractive potential energy curve at a larger interatomic distance than the same where short-range ICD takes place. Thus, before the short-range ICD proceeds, the initially created He*Ak complex gains kinetic energy at the expense of potential energy while its interatomic distance reduces. Following the short-range ICD, this kinetic energy acquired by the system, enables the Ak^+ ion to bounce back off the He atom and escape the droplet-surface. In contrast, the kinetic energy acquired by the initial He*Ak complex, before long-range ICD takes place, is minimal. Thus, the product ion ($HeAk^+$) is created with almost negligible kinetic energy at the droplet surface. Subsequently, due to the attractive interaction of He droplet with positive ion, $HeAk^+$ ion created from long-range ICD is most-likely to sink into the droplet, inhibiting the detection of the same out of the droplet [181].

Between the short-range and long-range ICD processes, the long-range ICD is more dominant one as seen from the corresponding huge total electron peaks compared to the same for coincident electron peaks. The long-range ICD process (high energy peaks in total electron spectra) also dominates over the double ionization processes indicated by the low and mid energy peaks. This observation is in contrast with the recent suggestion that double ionization process dominates over the single ionization process for alkali doped

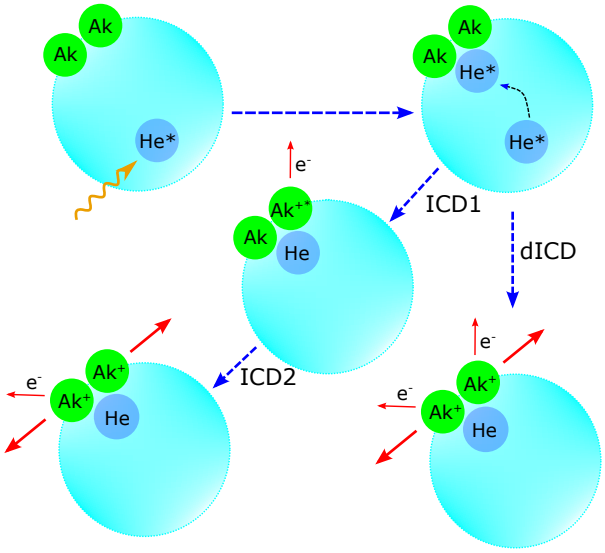

Figure 4.7: Schematic representation of the dICD and cICD processes. In dICD, following the photoexcitation of the droplets, He* migrates to the surface of the droplets and doubly ionize the attached Ak_2 in the vicinity by dICD process, wherein total two electrons are ionized simultaneously from both the alkali constituents and the resulting Ak_2^{2+} ion undergoes Coulomb explosion. Whereas in cICD, following the relaxation of He* one of the constituent Ak atoms of the attached Ak_2 is ionized from the inner valence p-shell in a ICD process (ICD1). The resultant excited Ak_2^* ions then decays via another ICD (ICD2), leading to charge separated Ak_2^{2+} ion which undergoes the Coulomb explosion.

droplets upon photoexcitation to the $n = 2$ droplet band [187].

Double ionization processes

Let us now look into the double ionization processes indicated by the low and mid energy peaks in Fig. 4.6 a) and b). The double ionization of mixed-alkali dimer attached to the surface of the He nanodroplets upon photoexcitation to the $n = 2$ droplet band at 21.6 eV was recently reported by LaForge *et al.* [187]. They proposed a novel *inter*-atomic/molecular decay mechanism known as double-ICD (dICD) underlying the observed process, schematically shown in Fig. 4.7. In this dICD, upon relaxation He* following the photoexcitation, the neighbouring alkali dimer undergoes double ionization, wherein both the alkali atoms are ionized simultaneously and two electrons are emitted. Due to spatially separated localization of two positive holes on both the nuclei, the product-Ak_2^{2+} ion undergo Coulomb explosion. We calculated the corresponding eKE and ion-KER spectra resulting from the dICD processes in Rb_2 and Cs_2 upon relaxation of He* $^{3,1}S, ^1P$ states to fit the observed eKE peaks between 0 and 12 eV (see Fig. 4.6).

In case of single ionization of the Ak upon relaxation of He*, we observed that the ICD proceeds via ionization from the valence shell (ns) of the Ak atoms, resulting in the high energy peaks between 14 and 18 eV in Fig. 4.6. However, it is energetically allowed to ionize the inner valence $(n-1)p$-shells of Rb and Cs through ICD from He* states, creating an excited Ak^{+*} ions which decay via another ICD with the neighbouring Ak atom. Therefore we propose a new novel step-wise ionization scheme in Ak_2 involving the inner $(n-1)p$-shell ionization of the alkali atoms. This new process involves two ICD steps, thereby calling this a cascaded-ICD (cICD) process. As shown schematically in Fig. 4.7, the first cICD step (cICD1) results in an excited Ak_2^{+*} ion in which one of the Ak atoms of Ak_2 is ionized from the $(n-1)p$-shell following the relaxation of He* in the droplet. Subsequently, the newly created Ak_2^{+*} undergoes the second cICD step (cICD2), wherein the inner p-shell vacancy is filled by a valence s-shell electron and the other alkali atom of Ak_2 is ionized in an ICD process, resulting in Ak_2^{2+} ion which eventually undergoes Coulomb explosion. Detailed discussions on these processes are in the following sections.

4.3.3 Double inter-atomic/molecular Coulombic decay

Since the energy levels of He* $^{3,1}S,^1P$ states reside above the repulsive Coulombic dicationic state of Ak_2 both for Rb and Cs, the dICD processes are expected to occur for both these cases. In the dICD process, upon relaxation He* states, the attached Ak_2 in He nanodroplets undergoes double ionization and simultaneously two electrons are ionized. In the final state of the alkali dimer dication, two positive holes are created on each of the dimer constituents, thereby it results in Coulomb explosion, releasing high kinetic energy alkali ions from the droplets, see below.

$$He^* + Ak_2 \rightarrow He + Ak_2^{2+} + 2e^-_{dICD} \rightarrow He + [Ak^+ + Ak^+] + 2\ e^-_{dICD} \tag{4.3}$$

The excess energy are released in terms of eKE and ion-KER in this process, in which interestingly both the emitted electrons share asymmetric kinetic energy distributions, where one electron carries almost all the energy leaving the other one with negligible kinetic energy. This energy sharing is similar to the shake-off processes observed in the double Auger decay and single photon double ionization processes [272, 273].

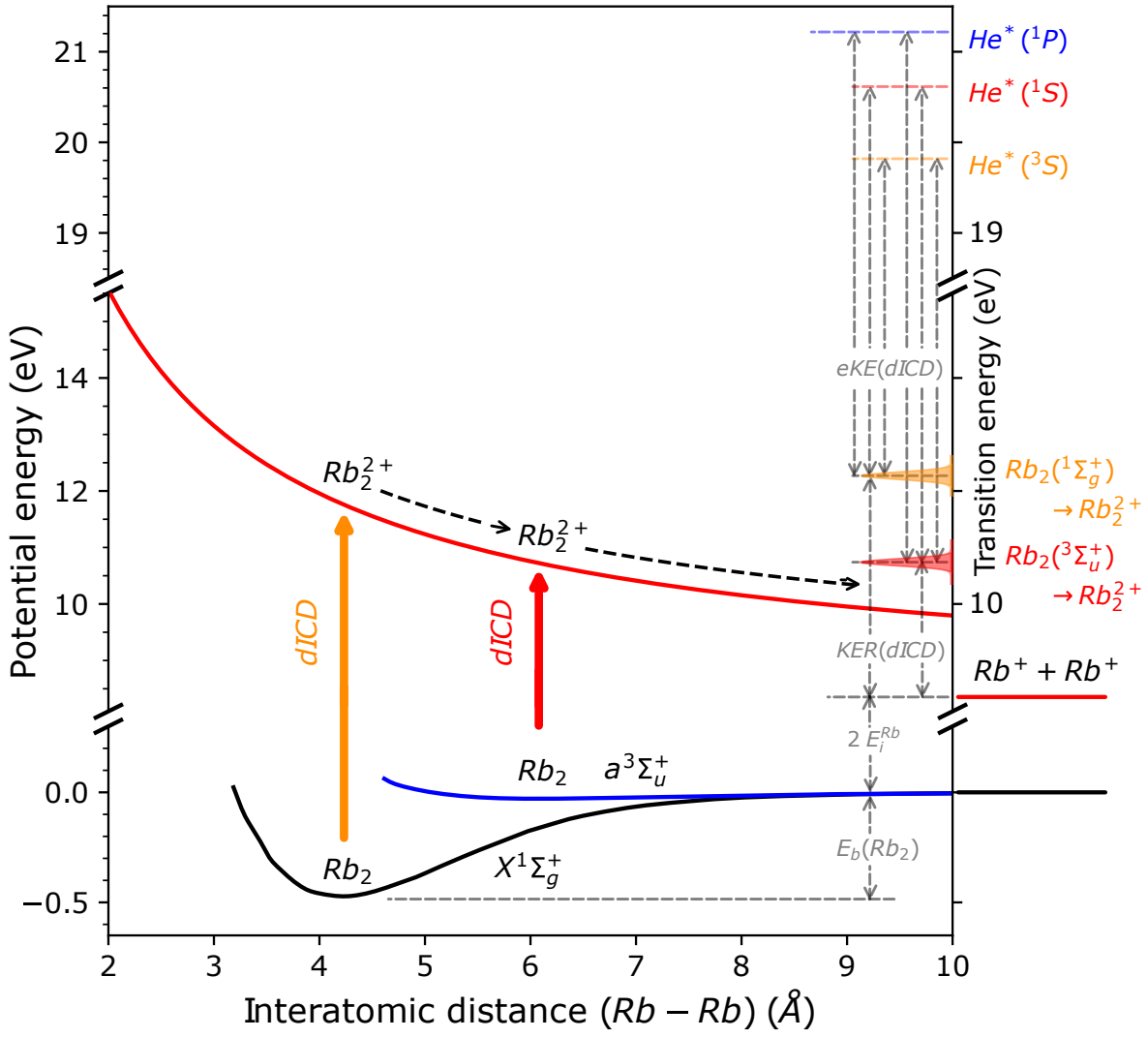

Figure 4.8: Black and blue curves represent the potential energy of Rb_2 $X^1\Sigma_g^+$ and $a^3\Sigma_u^+$ states, respectively [274]. The red curve shows the Coulombic potential energy of Rb_2^{2+}, which is calculated from $V(R) = 14.4/R + 2E_i^{Rb}$, where V is in eV, R is the interatomic distance of Rb_2 in Å and E_i^{Rb} is the ionization energy of Rb. The dICD process from $X^1\Sigma_g^+$ and $a^3\Sigma_u^+$ states are presented by the orange and red vertical arrows, respectively. On the right vertical axis, transition energy profiles from the $X^1\Sigma_g^+$ and $a^3\Sigma_u^+$ states to the Coulombic Rb_2^{2+} state are shown respectively by orange and red shaded peaks. The schemes to calculate the eKE and KER for relaxation of He* are also shown.

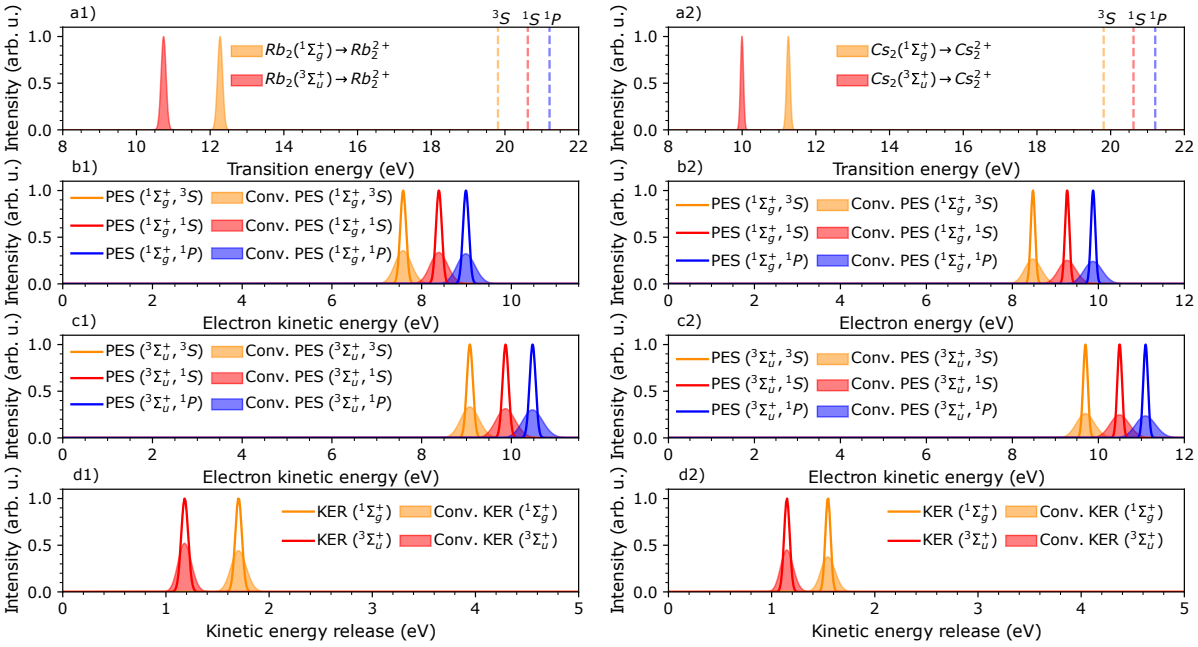

Figure 4.9: (a1,a2) The orange and red shaded peaks show the transition energy intensity profiles calculated from $(F[V - E(\Psi_{X,v=0})])$ for (Rb_2 and Cs_2) $X^1\Sigma_g^+$ and $a^3\Sigma_u^+$ states, respectively. The vertical dashed orange, red and blue lines in (a1, a2) are the energy levels of He* $^{3,1}S$,^1P states, respectively. (b1,b2) The orange, red and blue lines show the calculated eKE from the (Rb_2 and Cs_2) $X^1\Sigma_g^+$ due to relaxation from He* $^{3,1}S$,^1P states, respectively. Similarly, (c1,c2) shows the corresponding calculated eKE from the (Rb_2 and Cs_2) $a^3\Sigma_u^+$ state. (d1,d2) The orange and red lines show the KER of single Ak^+ ion from (Rb_2 and Cs_2) $X^1\Sigma_g^+$ and $a^3\Sigma_u^+$ states, respectively. The peaks with the solid shading in (b1,b2,c1,c2,d1,d2) show the corresponding spectra convoluted with the VMI spectrometer resolution function. The peak heights of the unconvoluted spectra are normalized to unity for better visualization, although for fitting the observed eKE and KER spectra with these calculated convoluted spectra, their amplitudes are varied.

Since it is well known that both the Rb_2 and Cs_2 are populated in the ground $X^1\Sigma_g^+$ and first excited $a^3\Sigma_u^+$ states on He nanodroplets [268], one can argue that the dICD process occurs at the equilibrium interatomic distances of these states. Fig. 4.8 b) shows the schematic of these dICD processes with the potential energy curves (PEC) of Rb_2. The black and blue lines represent the PEC of $X^1\Sigma_g^+$ and $a^3\Sigma_u^+$ states, respectively, while the red curve shows the repulsive Coulombic states of Rb_2 where the positive charges are located on both the Rb constituents. The vertical bound-continuum transitions in the dICD processes from $X^1\Sigma_g^+$ and $a^3\Sigma_u^+$ states are presented by the vertical orange and red arrows, respectively.

Now, to calculate the eKE and ion KER from these processes, we first calculated the Frank-Condon factors (F) for the vertical transitions from the initial neutral states to the

repulsive Coulombic state as follows:

$$F = \left| \int_0^\infty \Psi_{X,v=0}(R)\ \Psi_{[Ak_2]^{2+}}(R)\ dR \right|^2 \tag{4.4}$$

where, $\Psi_{X,v=0}$ and $\Psi_{[Ak_2]^{2+}}$ are the initial ground vibrational wavefunction of the Ak_2 and the continuum wavefunction of the repulsive dissociative state of Ak_2^{2+} at the potential energy V, and R is the interatomic distance of the Ak_2. Due to the sub-Kelvin (~ 0.37 K) temperature of the host-He nanodroplets [151], one can assume that the attached alkali dimers are in their ground vibrational states. We used the numerical program, BCONT 2.2 [275], to calculate F. In Fig. 4.9 (a1,a2), the orange and red shaded peaks show the transition energy intensity profiles calculated from ($F[(E(\Psi_{X,v=0}) - V)]$) for (Rb_2 and Cs_2) $X^1\Sigma_g^+$ and $a^3\Sigma_u^+$ states, respectively.

The eKE of the dICD electrons are calculated from the following equation:

$$eKE(2\ e^-_{dICD}) = F[E(\mathrm{He}^*) - (V - E(\Psi_{X,v=0}))] \tag{4.5}$$

where $E(\mathrm{He}^*)$ is the energy of the excited He^*. [$E(\Psi_{X,v=0})$ is the energy of the initial ground state of Ak_2. Since in the proposed dICD process the eKE is distributed asymmetrically between the dICD electrons, we assume that entire electron kinetic energy is carried away by one dICD electron with the other one having negligible kinetic energy. In Fig. 4.9 (b1,b2), the orange, red and blue lines show the calculated eKE from the (Rb_2 and Cs_2) $X^1\Sigma_g^+$ due to relaxation from $\mathrm{He}^*\ ^{3,1}S,^1P$ states, respectively. Similarly, Fig. 4.9 (c1,c2) shows the corresponding calculated eKE from the (Rb_2 and Cs_2) $a^3\Sigma_u^+$ state. The peaks with the solid shading in Fig. 4.9 (b1,b2,c1,c2), show the eKE spectra convoluted with the VMI spectrometer resolution function, which are expected from the measurements. These convoluted spectra are later used to fit the observed eKE spectra presented in Fig. 4.6.

Now, the total KER of the Coloumb exploding product-Ak^+ ions is calculated from the following equation:

$$KER([\mathrm{Ak}^+ + \mathrm{Ak}^+]) = F[V - 2 \times (E_i^{Ak}) + E_b(\mathrm{Ak}_2)] \tag{4.6}$$

where E_i^{Ak} and $E_b(\mathrm{Ak}_2)$ are the ionization energy of the Ak atom and the binding energy

of the Ak_2, respectively. Since, both the ions have equal masses, this total KER is divided equally to both the fragmented ions. In Fig. 4.9 (d1,d2), the orange and red lines show the KER of single Ak^+ ion calculated from the above equation for (Rb_2 and Cs_2) $X^1\Sigma_g^+$ and $a^3\Sigma_u^+$ states, respectively. Likewise, the peaks with the solid shading show the convoluted KER spectra, expected from the VMI spectrometer in ion-imaging mode.

4.3.4 Cascaded inter-atomic/molecular Coulombic decay

As discussed earlier, in cascaded-ICD processes, first ionization occurs in the inner valence ($(n-1)p$)-shell of one of the alkali atoms in the Ak_2 following the relaxation of He^* via an ICD process (cICD1), leaving the alkali dimer in excited cationic state (Ak_2^{+*}). Subsequently, the Ak_2^{+*} goes through another ICD (cICD2), wherein two charge separated Ak^+ ions are formed, which eventually undergoes Coulomb explosion, see below:

$$\begin{aligned} \mathrm{He}^* + \mathrm{Ak}_2 &\rightarrow \mathrm{He} + \mathrm{Ak}^{+*}((n-1)p^-1).\mathrm{Ak} + e^-_{cICD1} \\ &\rightarrow \mathrm{He} + \mathrm{Ak}^+(ns^{-1}).\mathrm{Ak}^+(ns^{-1}) + e^-_{cICD1} + e^-_{cICD2} \\ &\rightarrow \mathrm{He} + [\mathrm{Ak}^+ + \mathrm{Ak}^+] + e^-_{cICD1} + e^-_{cICD2} \end{aligned} \tag{4.7}$$

Since the ionization energies of the inner valence $(n-1)p$-shell of Rb and Cs are lower than the energy of He^* states, the relaxations of the later allow for ionization from the inner valence p-shell. Therefore, both the dopants are expected to show the cICD process.

The cICD process is schematically shown using the potential energy diagram of Rb_2 in Fig. 4.10. The first-step of cICD (cICD1) is shown by the cyan vertical arrows, wherein the relaxation of He^* leads to ionization of Rb $4p$-shell from both the $X^1\Sigma_g^+$ (black line) and $a^3\Sigma_u^+$ (blue line) states. As a result, excited Rb_2^{+*} ion is formed at a higher potential energy, which is shown by the green-dashed line in Fig. 4.10. Due to unavailability of theoretical PEC for Rb_2^{+*} in literature, the shown green PEC is an hypothetical one whose asymptotic limit matches with the energy of $Rb^{+*}(4p^{-1})$. Now in the next step of the cICD process (cICD2), the Rb_2^{+*} undergoes another ICD to create a Rb_2^{2+} ion on the repulsive Coulombic state (red line). This cICD2 step is shown by the purple arrows and involves considerable nuclear-dynamics where the interatomic distance of Rb_2^+ reduces to facilitate the ICD process. As a result of this, the second ICD takes place at a lower interatomic separation than that of the dICD processes, thereby increasing the KER

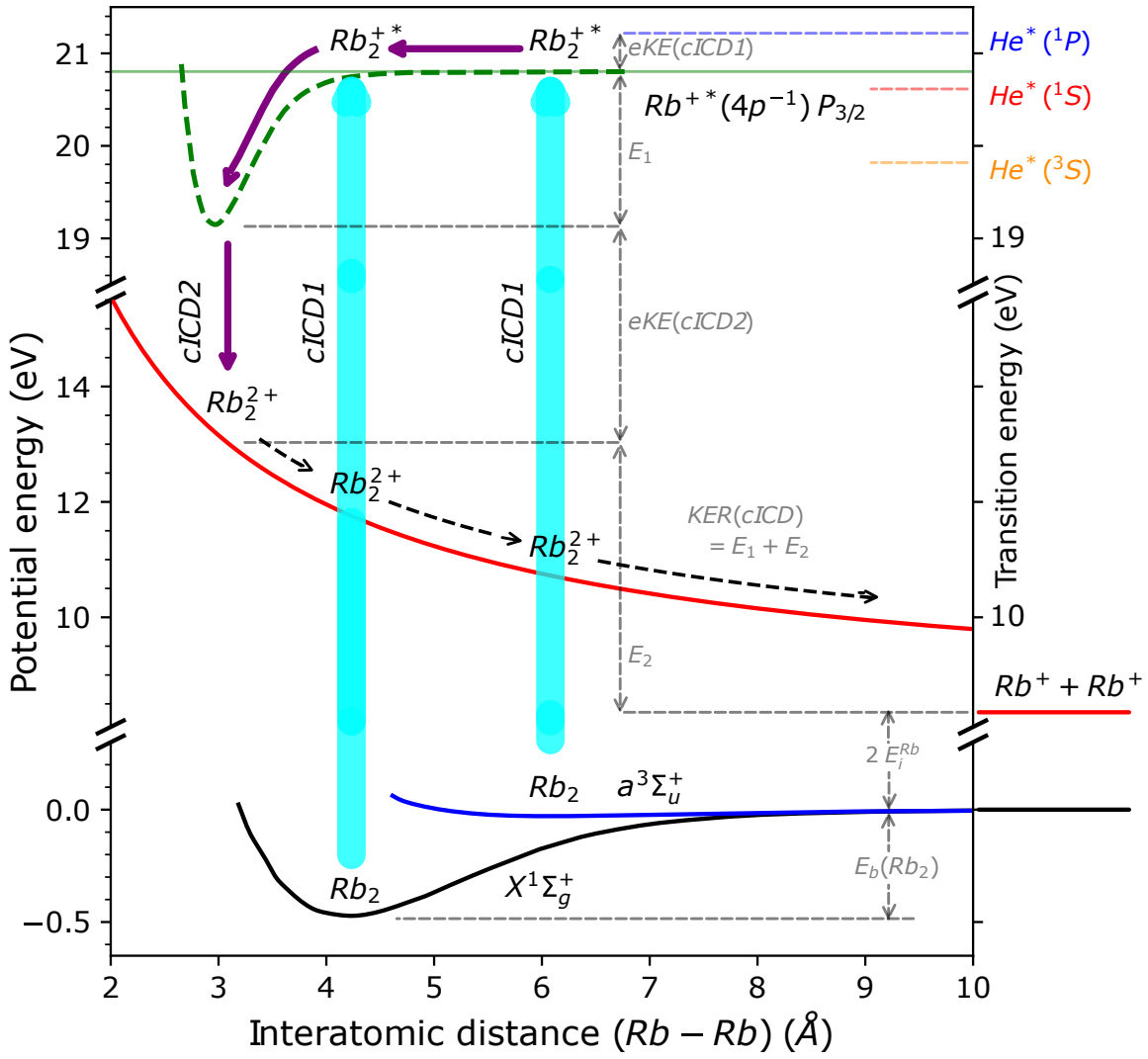

Figure 4.10: Schematic of the cICD process using the potential energy diagram of Rb_2. Black and blue curves represent the potential energy of Rb_2 $X^1\Sigma_g^+$ and $a^3\Sigma_u^+$ states, respectively [274]. The red curve shows the Coulombic potential energy of Rb_2^{2+}, which is calculated from $V(R) = 14.4/R + 2E_i^{Rb}$, where V is in eV, R is the interatomic distance of Rb_2 in Å and E_i^{Rb} is the ionization energy of Rb. The cICD process consists of two ICD steps: cICD1 and cICD2. The first cICD1 process from $X^1\Sigma_g^+$ and $a^3\Sigma_u^+$ states are presented by the vertical cyan arrows, whereas the second cICD2 step from Rb_2^{+*} state (dashed-green line) to the Rb_2^{2+} Coulombic state is shown by the purple arrows. Note that the dashed-green line is a hypothetical potential energy curve with asymptotic energy of Rb^{+*} $4p^{-1}$ level. The schemes to calculate the eKE and KER for relaxation of He^* are also shown.

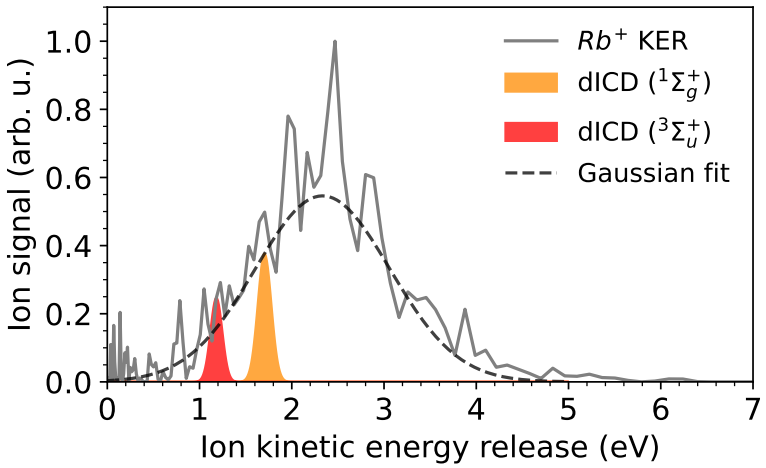

Figure 4.11: Ion kinetic energy release (KER) spectra correlated to Rb^+ ions (grey line) at 21.6 eV photon energy for Rb doped droplets. The orange and red shaded peaks show the calculated KER corresponding to Rb^+ ions for dICD in Rb_2 from $^1\Sigma_g^+$ and $^3\Sigma_u^+$ states, respectively. The black dashed line shows the Gaussian fit of the observed KER spectra.

gained by the ions. This assumption is validated in terms of the observed Rb^+ KER spectra in Fig. 4.11. As we can see that the measured peak of KER spectra of the Rb^+ ions at 21.6 eV photon energy is higher than the calculated KER peaks arising due to the dICD processes from Rb_2 $X^1\Sigma_g^+$ and $a^3\Sigma_u^+$ states, orange and red shaded peaks, respectively.

From Fig. 4.10, the total KER of two product-ions in cICD process is the summation of energies E_1 and E_2, where E_1 is the energy gained in expense of potential energy due to the reduction of interatomic distance of Rb_2^* and E_2 is the difference between the potential energy of Rb_2^{2+} when the cICD2 takes place and its asymptotic limit. Since the exact internuclear distance where the cICD2 proceeds is unknown, one can only experimentally assign this KER for the cICD process, based on an approximate form for the upper PE curve. We assigned observed KER peak of the Ak^+ ions to the newly proposed cICD process. Thus, we can calculate the eKE of e^-_{cICD1} and e^-_{cICD2} from the following equations:

$$\mathrm{eKE}(e^-_{cICD1}) = E(\mathrm{He}^*) - E(\mathrm{Ak}^{+*}((n-1)p^{-1})) \tag{4.8}$$

$$\mathrm{eKE}(e^-_{cICD2}) = E(\mathrm{Ak}^{+*}((n-1)p^{-1})) - 2\,E_i^{Ak} - \mathrm{KER}([\mathrm{Ak}^+ + \mathrm{Ak}^+]) \tag{4.9}$$

where, $E(\mathrm{He}^*)$ and $E(\mathrm{Ak}^{+*}((n-1)p^{-1}))$ are energies of He^* and $\mathrm{Ak}^{+*}((n-1)p^{-1})$ states, respectively. Whereas, E_i^{Ak} and $\mathrm{KER}([\mathrm{Ak}^+ + \mathrm{Ak}^+])$ are the ionization energies of the alkali

atoms and the total KER of the fragmented ions from the cICD processes, respectively.

Fitting of eKE spectra

Now, to explain the double ionization process at 21.6 eV photon energy which results into low energy peak structures between 0 and 12 eV in the eKE spectra correlated to Rb^+ and Cs^+, we fitted the calculated eKE peaks from both the dICD and cICD processes in Fig. 4.12. Note that, assuming the dICD efficiencies of He* $^{3,1}S$,^1P states are identical both for $X^1\Sigma_g^+$ and $a^3\Sigma_u^+$ states, the ratios between peak amplitudes arising due to He* states were kept constant both for the X and a states. Whereas, the total intensity of these peaks from X and a states were varied assuming the difference in population of Ak_2 in the droplet environment. For fitting of eKE from cICD processes, multiple Gaussian peaks centred at the calculated eKE energy from eq.4.8 and eq.4.9 were fitted, keeping their amplitudes and widths variable.

One can see that for both the cases of Rb and Cs doping, the calculated eKE can explain the existences of both these processes. The low energy peak structures between 0 and 4 eV broadly cover all the cICD1 peaks shown by purple and magenta shaded peaks, where the purple and magenta peaks represent ionization to $Ak^{+*}((n-1)p^{-1}\ P_{1/2})$ and $Ak^{+*}((n-1)p^{-1}\ P_{3/2})$ states, respectively. Note that, for Rb doping, only one magenta shaded peak is shown, since the energy of $Rb^{+*}(4p^{-1}\ P_{3/2})$ state ($\sim$ 20.80 eV) is lower than the same of He$^*(1s2p\ ^1P)$ state (21.21 eV), making ionization to $Rb^{+*}(4p^{-1}\ P_{3/2})$ following relaxation of He$^*(1s2p\ ^1P)$ state the only cICD1 channel. The energy of the other inner valence ionized state, $Rb^{+*}(4p^{-1}\ P_{1/2})$, ($\sim$ 21.50 eV) is higher than that of all He$^*(1s2s\ ^{3,1}S, 1s2p\ ^1P)$ states. For Cs doping, however, both the inner valence ionized $Cs^{+*}(5p^{-1}\ P_{3/2})$ ($\sim$ 17.43 eV) and $Cs^{+*}(5p^{-1}\ P_{1/2})$ ($\sim$ 19.09 eV) states are energetically accessible following relaxation of He*($^{3,1}S$,^1P) states. Thus, both magenta and purple peaks, denoted with the He* state, are presented in case of Cs doping. The mid energy peak structures between 4 and 12 eV originate from both the cICD2 and dICD processes. The purple and magenta lines show cICD2 following the relaxation of $Ak^{+*}((n-1)p^{-1}\ P_{1/2})$ and $Ak^{+*}((n-1)p^{-1}\ P_{3/2})$ states, respectively. Here, for Rb doping, the purple line is missing, since the precursor state ($Rb^{+*}(4p^{-1}\ P_{1/2})$) for the subsequent cICD2 is energetically forbidden via cICD1. The orange, red and blue peaks correlate to dICD in Ak_2 from He* $^{3,1}S$ and ^1P states, respectively, wherein the peaks with and

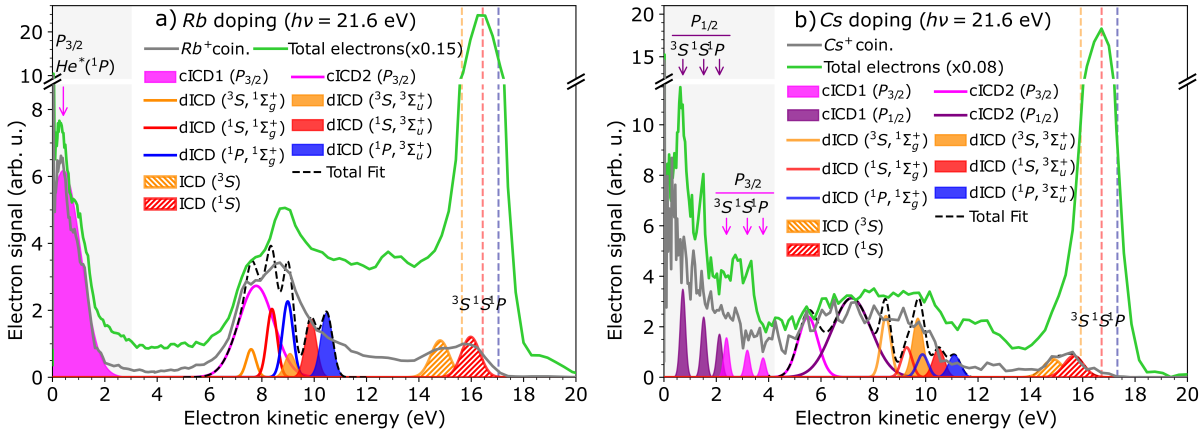

Figure 4.12: eKE spectra correlated to a) Rb^+ and b) Cs^+ (grey lines), and total electrons (green lines) at 21.6 eV for Rb and Cs doping, respectively. The orange, red and blue peaks correlate to eKE due to dICD in Ak_2 from He^* $^{3,1}S$ and ^1P states, respectively, wherein the peaks with and without shading correspond to dICD from Ak_2 $a^3\Sigma_u^+$ and $X^1\Sigma_g^+$ states, respectively. The shaded purple and magenta peaks are the calculated eKE from first cascaded-ICD step (cICD1) due to inner $(n-1)p$-shell ionization (n being the valence shell of the alkali atoms) upon relaxation of He^* $^{3,1}S$ and ^1P, while purple and magenta lines are the same from the second cascaded-ICD step (cICD2) in Ak_2^{+*} due to decay of the p-shell vacancy. The downward arrows on the cICD1 peaks show the He^* state that relaxes, resulting in the cICD1, whereas the purple and magenta colours indicate one of the Ak_2 constituent being populated to Ak^+ $(n-1)p^{-1}ns$ $P_{3/2}$ and $(n-1)p^{-1}ns$ $P_{1/2}$ states following cICD1, respectively. For Rb doping, the purple shaded peaks and purple lines are missing, since ionization to $Rb^{+*}(4p^{-1}$ $P_{1/2})$ state is energetically inaccessible via cICD1, thereby also inhibiting the cICD2 from the same precursor state. The orange, red and blue vertical dashed lines are the expected eKE for single ionization of Ak due to long-range ICD from He^* $^{3,1}S$ and ^1P states, respectively, whereas the orange and red peaks with hatched shading show the calculated eKE due to short-range ICD from He^* $^{3,1}S$ states, respectively. The black dashed lines between 4 and 12 eV shows the total fit of the measured spectra.

without shading correspond to dICD from Ak_2 $a^3\Sigma_u^+$ and $X^1\Sigma_g^+$ states, respectively.

As we can see, while the low energy peaks of the measured eKE spectra indicate the cICD1 for Rb doping, the peaks due to subsequent cICD2 process overlaps with the peaks due to dICD processes in the mid energy part. Therefore, for Rb doping, these two competing processes are not completely discernable. Although for the case of Cs doping, these processes can be unambiguously identified. We see that the cICD1 peak positions are very close to the observed fine peak structures of the low energy part of total eKE spectra (green line), and for the mid energy part the cICD2 peaks are well separated from the dICD peaks, explaining the entire mid energy structure.

Thus, we have identified a new two-step cICD process competing with the single step dICD process leading to double ionization in heavy alkali dimer attached to He nanodroplets following the photoexcitation of $n = 2$ droplet band at 21.6 eV.

4.4 Dopant ionization following droplet direct ionization

Now lets look into the processes occurring in the attached alkali dopants upon direct photoionization of the host-droplets. Fig. 4.13 a) and b) show the electron kinetic energy (eKE) spectra corresponding to single Ak^+ ion (grey line), double Ak^+ ions (red line) ions and total electrons (green line) for Rb and Cs doped droplets at 26 and 60 eV photon energies, respectively. By comparing the eKE spectra in coincidence with double Ak^+ ions with the rest of the spectra, one can argue that at photon energy beyond the ionization energy of atomic He, attached Ak_2 undergoes double ionization. In Fig. 4.13 a) and b), the peaks at $h\nu - E_i^{He}$ and $h\nu - E_i^{He} - E(\mathrm{He}^*\ 1s2p^1P)$ (shown by vertical grey dashed lines) indicate indirect ionization of Rb and Cs dopants, respectively, as follows:

For Rb doped droplets, at 26 eV photon energy, the host-droplets are directly photoionized and the attached Rb dopants are ionized through charge transfer (CT) processes, see below.

$$\mathrm{He_m} + \mathrm{Rb_n} + h\nu \rightarrow \mathrm{He_m^+} + \mathrm{Rb_n} + e^-_{\mathrm{He}} \rightarrow \mathrm{He_m} + \mathrm{Rb_n^+} + e^-_{\mathrm{He}} + \Delta E \qquad (4.10)$$

where, ΔE is the energy difference between the incoming ($\mathrm{He_m^+}$ + $\mathrm{Rb_n}$) and outgoing

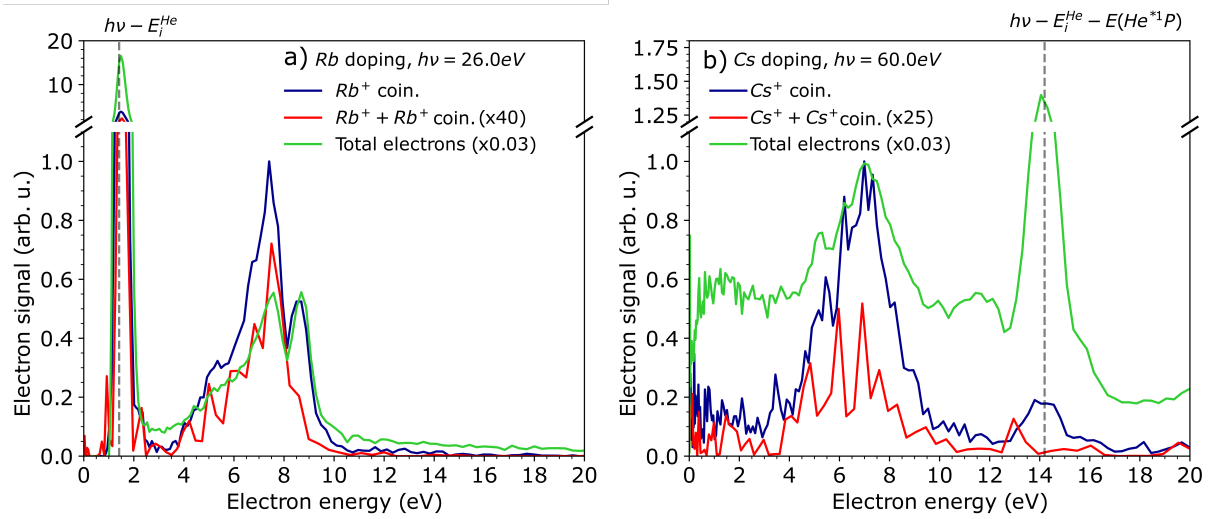

Figure 4.13: Electron kinetic energy (eKE) spectra corresponding to single Ak^+ ion (blue line), double Ak^+ ions (red line) ions and total electrons (green line) for a) Rb and b) Cs doped droplets at 26 and 60 eV photon energies, respectively. The vertical grey dashed line in panel a) at $h\nu - E_i^{He}$ shows the He photoelectron energy originating from the direct ionization of the droplet. Whereas, the grey dashed lines in panel b) at $h\nu - E_i^{He} - E(\mathrm{He}^*\ ^1P)$ shows the inelastically scattered He photoelectron energy leading to excitation of an another He atom to $1s2p^1P$ state. Both the corresponding peaks indicate the charge transfer ionization of the dopants following direct photoionization of the droplet.

$(\mathrm{He_m} + \mathrm{Rb_n^+})$ channels, which can be released either radiatively via photoemission or non-radiatively via potential energy curve crossing.

Therefore, the same He photoelectron (e^-_{He}) is observed in coincidence with the $\mathrm{Rb_n^+}$ ions. Although, in case of Cs doping at 60 eV photon energy, the eKE of the e^-_{He} is beyond the detection limit of our VMI spectrometer, the inelastically scattered e^-_{He} which excites another He atom to $1s2p^1P$ states inside the droplets was captured in coincidence with $\mathrm{Cs^+}$ ions, due to its reduction in kinetic energy. In this case the CT process is shown below:

$$\mathrm{He_m} + \mathrm{Cs_n} + h\nu \rightarrow \mathrm{He_m^+} + \mathrm{Cs_n} + e^-_{\mathrm{He}} \rightarrow \mathrm{He_{m-1}.He^*} + \mathrm{Cs_n^+} + e^-_{\mathrm{He}} + \Delta E \qquad (4.11)$$

where, ΔE is the energy difference between the incoming $(\mathrm{He_m^+} + \mathrm{Cs_n})$ and outgoing $(\mathrm{He_m} + \mathrm{Cs_n^+})$ channels.

Since at this energy regime the alkali dopants are doubly ionized following the direct ionization of the droplets, to explain the mid-energy eKE peaks between 4 and 12 eV in Fig. 4.13, we propose and discuss two different double ionization processes: a) electron

transfer mediated decay (ETMD) and b) CT followed by ICD process (CT-ICD) in the following sections.

4.4.1 Electron transfer mediated decay

Ltaief *et al.* [186] recently reported similar double ionization phenomena for mixed alkali dimers attached to He nanodroplets through ETMD process at the same photon energy range. They proposed that He^+ ion following the direct ionization of the droplet inside the droplet gets trapped with another He atom to produce He_2^+ ion, which then participates in ETMD with the attached alkali dimer as follows.

$$\begin{aligned} He^+ + He + Ak_2 &\rightarrow He_2^+ + Ak_2 \\ &\rightarrow He_2 + Ak_2^{2+} + e^-_{ETMD} \\ &\rightarrow He_2 + [Ak^+ + Ak^+] + e^-_{ETMD} \end{aligned} \tag{4.12}$$

In this ETMD process, the He_2^+ is neutralized by an electron transfer from the on of the constituent Ak atoms of neighbouring Ak_2 and the excess is utilized to ionize the othe Ak atom, thus producing Ak_2^{2+} ion. Eventually, this charge-separated Ak_2^{2+} undergoes Coulomb explosion. This process is schematically shown in Fig. 4.14 a). This ETMD process is equivalent to the dICD prosess discussed earlier, as the Ak_2 gets doubly ionized in a single step, only here the ionization dynamics proceeds from the neutralization of He_2^+ instead of the relaxation of He^*. Fig. 4.14 b) shows these ETMD processes from the initially populated Ak_2 $X^1\Sigma_g^+$ and $a^3\Sigma_u^+$ states with the vertical orange and red arrows, respectively with the help of the potential energy diagram of Cs_2. The resultant Cs_2^{2+} dissociated in the final repulsive Coulombic state shown by the red lines.

Now the eKE and ion-KER spectra from these ETMD processes are calculated from the following equation:

$$\text{eKE}(e^-_{ETMD}) = F_{He_2^+ \rightarrow He_2} F_{Ak_2 \rightarrow Ak_2^{2+}} [(E(He_2^+) - E(He_2)) - (E(Ak_2^{2+}) - E(Ak_2))] \tag{4.13}$$

where, $F_{He_2^+ \rightarrow He_2}$ and $F_{Ak_2 \rightarrow Ak_2^+}$ are the Frank-Condon factors calculated for vertical transitions from He_2^+ to He_2 states and from Ak_2 ($X^1\Sigma_g^+$ and $a^3\Sigma_u^+$) to Ak_2^{2+} states at their respective equilibrium interatomic distances, using the BCONT 2.2 numerical program

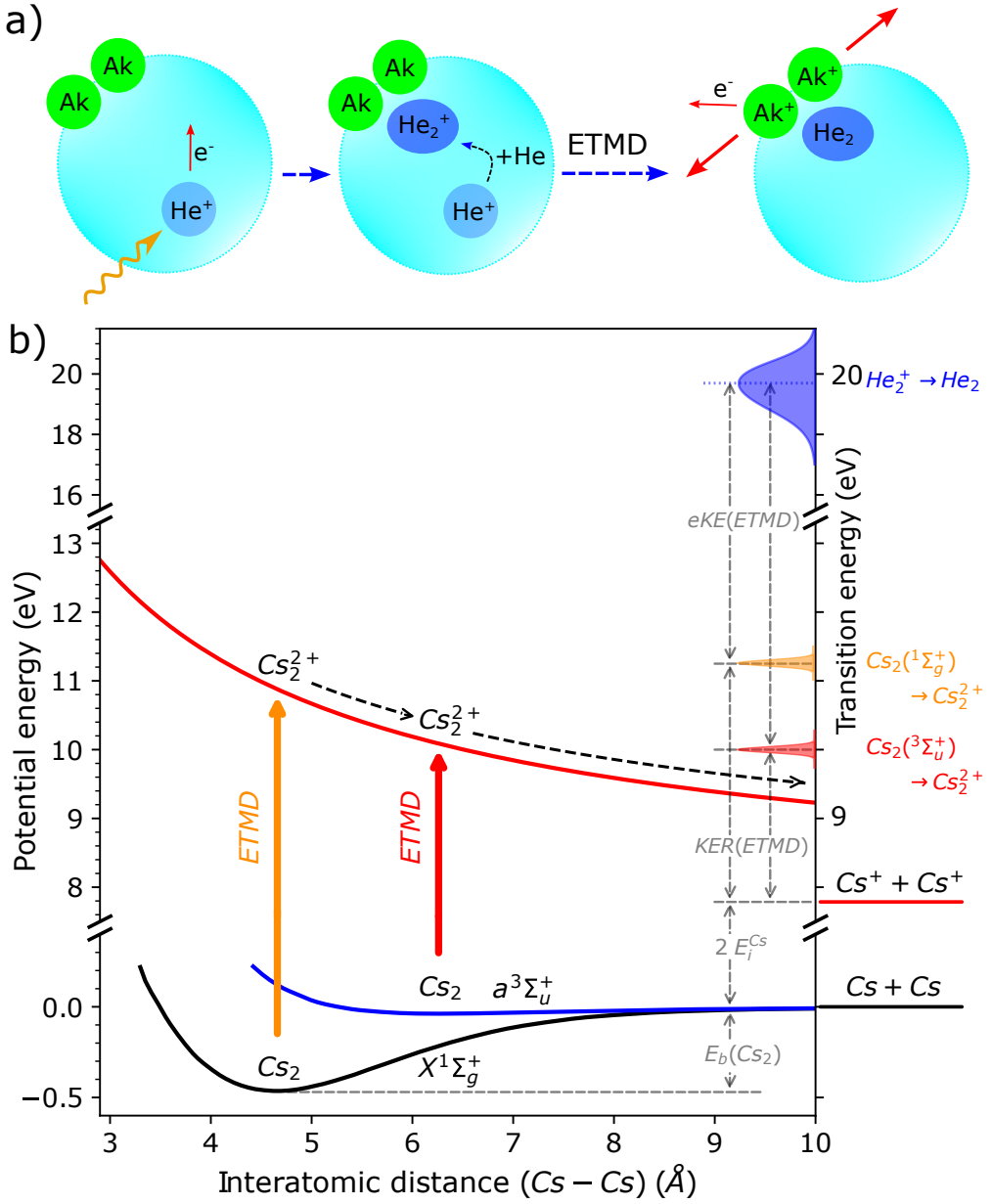

Figure 4.14: a) Schematic of the ETMD processes in Ak_2 attached to the He nanodroplets. Following the photoionization of the droplets, He_2^+ ion is formed which is then neutralized in an ETMD process via electron transfer from the Ak_2, leaving a doubly ionized Ak_2 and an ETMD e^-. As both the alkali constituents are ionized simultaneously, the Ak_2^+ undergoes Coulomb explosion. b) Black and blue curves represent the potential energy of Cs_2 $X^1\Sigma_g^+$ and $a^3\Sigma_u^+$ states, respectively [276]. The red curve shows the Coulombic potential energy of Cs_2^{2+}, which is calculated from $V(R) = 14.4/R + 2E_i^{Cs}$, where V is in eV, R is the interatomic distance of Cs_2 in Å and E_i^{Cs} is the ionization energy of Cs. The ETMD process from $X^1\Sigma_g^+$ and $a^3\Sigma_u^+$ states are presented by the orange and red vertical arrows, respectively. On the right vertical axis, transition energy profiles from the $X^1\Sigma_g^+$ and $a^3\Sigma_u^+$ states to the Coulombic Cs_2^{2+} state are shown respectively by orange and red shaded peaks, while the same for He_2^+ to He_2 decay is shown by the blue curve. The schemes to calculate the eKE and KER due to neutralization of He_2^+.

[275], respectively. Whereas, $E(He_2^+)$, $E(He_2)$, ($E(Ak_2^{2+})$ and $E(Ak_2)$ are the energies of He_2^+, He_2, Ak_2^{2+} and E(Ak_2) states, respectively. The corresponding potential energy diagrams and the transition energy profile for He_2^+ to He_2 decay is shown in Fig. 4.15. In Fig. 4.16 a1) and a2), the orange and red shaded peaks show the transition energy intensity profiles calculated from ($F[(E(\Psi_{X,v=0}) - V)]$) for (Rb_2 and Cs_2) $X^1\Sigma_g^+$ and $a^3\Sigma_u^+$ states, respectively, while the blue shaded peak shows the transition energy profile for He_2^+ to He_2 transition. In Fig. 4.16 b1) and b2), the calculated eKE spectra of the ETMD electrons are shown by the orange and red lines for X and a states of Rb_2 and Cs_2, respectively, while the solid-shaded peak shows the corresponding convoluted eKE spectra expected from the VMI spectrometer.

Similar to the dICD processes (shown in Fig. 4.8), in case of ETMD the KER spectra of the Coulomb exploded ions (Ak^+) will be the same, as in both the cases of dICD and ETMD, the dissociations occur from the same interatomic distances of Ak_2^{2+}. The calculated and convoluted KER spectra are shown by orange and red lines without and with solid-shading from X and a states of Rb_2 and Cs_2, respectively.

4.4.2 Charge transfer followed by interatomic Coulombic decay

Since the neutralization of He_2^+ allows for ionization of the alkali atom from the inner p-shell, similar to the cICD1 process discussed earlier, here we propose a new charge transfer followed by interatomic Coulombic decay (CT-ICD) process in Ak_2 attached to He nanodroplets following the direct ionization of the droplet, leading to doubly ionized Ak_2. In this two step CT-ICD process, first CT occurs from the inner valence $(n-1)p$-shell of one of the alkali dimer constituents, which produces the an excited Ak_2^{+*} ion, see below:

$$He_2^+ + Ak_2 \rightarrow He_2 + Ak^{+*}((n-1)p^{-1}).Ak \tag{4.14}$$

Following that, an ICD takes place in which the inner p-shell gets filled by a valence s-shell electron and another valence electron from the other alkali atom is ionized and Coulomb explosion occur in the resulting Ak_2^{2+} ion as follows:

$$Ak^{+*}((n-1)p^{-1}).Ak \rightarrow Ak^+(ns^{-1}).Ak^+(ns^{-1}) + e^-_{ICD} \rightarrow [Ak^+ + Ak^+] + e^-_{ICD} \tag{4.15}$$

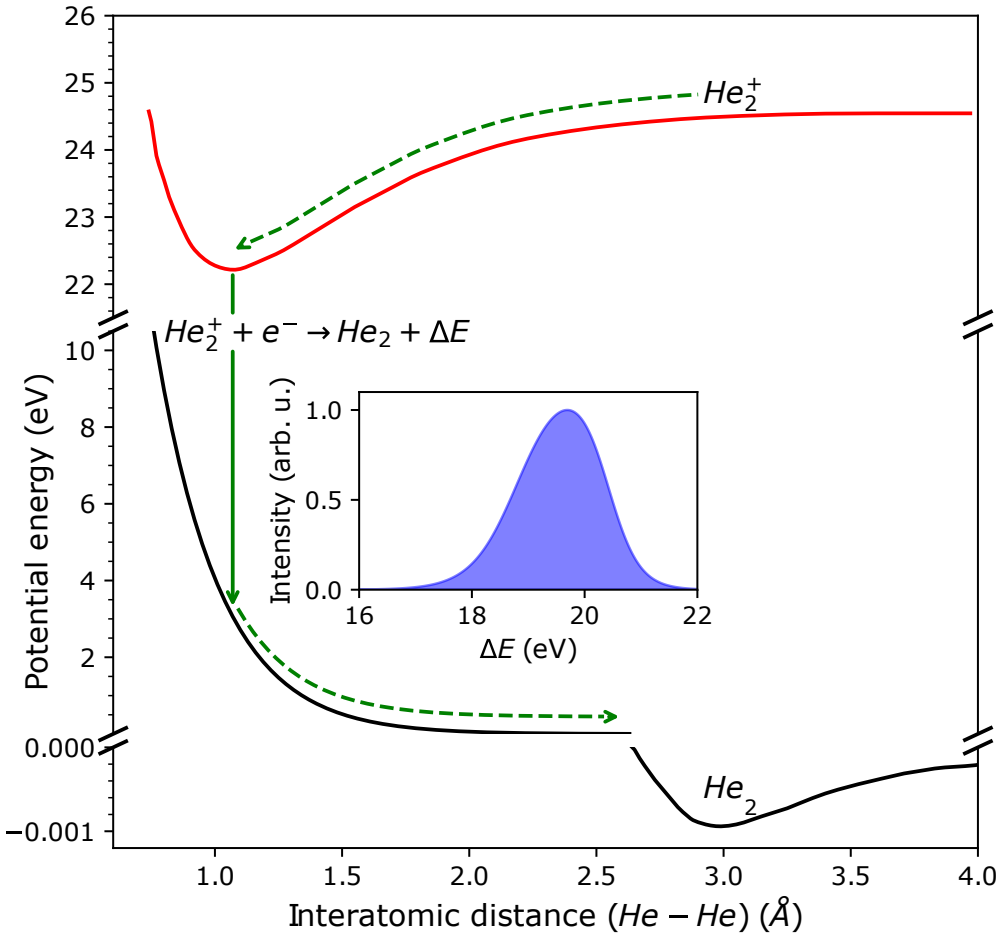

Figure 4.15: Schematic of the neutralization process of He_2^+ in terms of the molecular potential energy diagram. The black and the red lines show the potential energies of He_2 [277] and He_2^+ [173], respectively. The He_2^+ is formed inside the droplet due to trapping of He^+ with a neutral He at a large interatomic distance. Due the attractive potential of He_2^+, the interatomic distance of the same is reduced, and He_2^+ de-excite to the ground vibrational state by releasing the excess energy into the environment. At the interatomic distance of potential minimum of He_2^+, neutralization of He_2^+ takes place, shown by the downward vertical green arrow. The inset shows the normalized intensity profile of the released neutralization energy (ΔE).

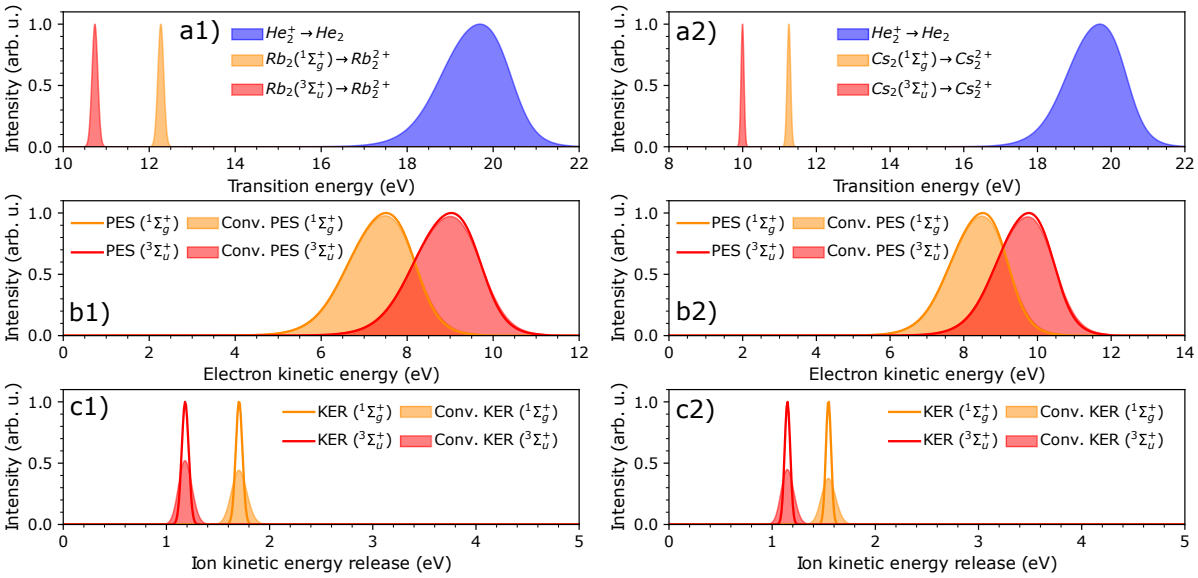

Figure 4.16: (a1,a2) The orange and red shaded peaks show the transition energy intensity profiles calculated from $(F[(V - E(\Psi_{X,v=0}))])$ for (Rb_2 and Cs_2) $X^1\Sigma_g^+$ and $a^3\Sigma_u^+$ states, respectively. The blue shaded peaks shows the intensity distribution of the transition energy due to neutralization of He_2^+. (b1,b2) The orange and red lines show the calculated eKE from the (Rb_2 and Cs_2) $X^1\Sigma_g^+$ and $a^3\Sigma_u^+$ stats due to ETMD, respectively. (d1,d2) The orange and red lines show the KER of single Ak^+ ion from (Rb_2 and Cs_2) $X^1\Sigma_g^+$ and $a^3\Sigma_u^+$ states, respectively. The peaks with the solid shading in (b1,b2,c1,c2) show the corresponding spectra convoluted with the VMI spectrometer resolution function. The peak heights of the unconvoluted spectra are normalized to unity for better visualization, although for fitting the observed eKE and KER spectra with these calculated convoluted spectra, their amplitudes were varied.

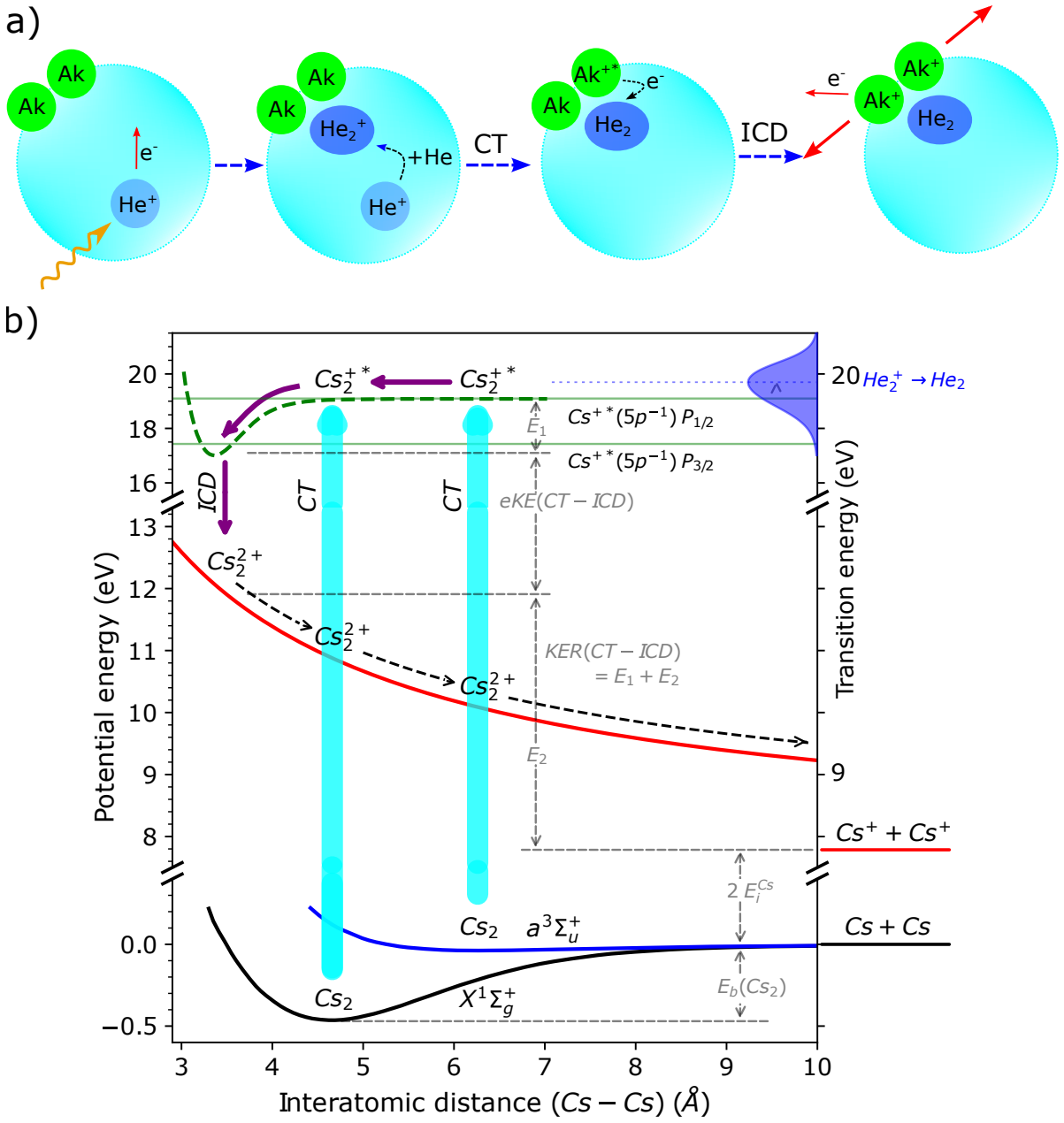

Figure 4.17: Schematic of the CT-ICD process using the potential energy diagram of Cs_2. Black and blue curves represent the potential energy of Cs_2 $X^1\Sigma_g^+$ and $a^3\Sigma_u^+$ states, respectively [276]. The red curve shows the Coulombic potential energy of Cs_2^{2+}, which is calculated from $V(R) = 14.4/R + 2E_i^{Cs}$, where V is in eV, R is the interatomic distance of Cs_2 in Å and E_i^{Cs} is the ionization energy of Cs. The CT-ICD process consists of two steps: CT and ICD. The first CT processes from $X^1\Sigma_g^+$ and $a^3\Sigma_u^+$ states are presented by the vertical cyan arrows, whereas the second ICD step from Cs_2^{+*} state (dashed-green line) to the Cs_2^{2+} Coulombic state is shown by the purple arrows. Note that the dashed-green line is a hypothetical potential energy curve with asymptotic energy of Cs^{+*} $5p^{-1}$ level. The schemes to calculate the eKE and KER for this CT-ICD are also shown.

This second ICD process is exactly same as the cICD2 process, since the product ions of the previous CT and the cICD1 process are the same. Therefore the same eKE spectra are expected from both the CT-ICD and cICD2 processes. The CT-ICD process is schematically shown in Fig. 4.17 a), while in Fig. 4.17 b), the cyan vertical arrows show the CT process from the X and a states (black and red lines) of Cs_2 to the potential energy curve of Cs_2^{+*} (hypothetically shown by the green dashed line). Following this, ICD (shown by the vertical purple arrow) takes place in the Cs_2^* state, where the reduction in the interatomic distance aides the decay, similar to the cICD2 step.

The assumption of the reduction in the interatomic distance is justified by the observed ion-KER spectra, shown in Fig. 4.18. Clearly the calculated KER peaks from the ETMD processes, taking place at the equilibrium interatomic distances of the X and a states (shown by orange and red shaded peaks), are lower in energy than the observed KER peak (shown by the Gaussian fit, black dashed line). Therefore, one can argue that there are contributions from other processes taking place at lower interatomic distances, in our case these are the ICD processes discussed above. Again in this case due to lack of knowledge about the exact interatomic distance where the ICD processes occur, we attributed the KER of each product-Cs^+ ions to the experimentally observed ion-KER peak shown in Fig. 4.18.

Thus the eKE of the emitted electron in this ICD process, can be calculated from the following equation:

$$\mathrm{eKE}(e^-_{ICD}) = E(\mathrm{Ak}^{+*}((n-1)p^{-1})) - 2\,E_i^{Ak} - \mathrm{KER}([\mathrm{Ak}^+ + \mathrm{Ak}^+]) \tag{4.16}$$

where, E_i^{Ak} and KER([Ak^++Ak^+]) are the ionization energies of the alkali atoms and the total KER of the fragmented ions from the ICD processes following the CT, respectively.

Fitting of eKE spectra

Now, to explain the double ionization process at 26 and 60 eV photon energies respectively for Rb and Cs doping, the corresponding eKE spectra correlated to Rb^+ and Cs^+ are fitted with the calculated eKE peaks from both the ETMD and CT-ICD processes in Fig. 4.19. The orange and red shaded peaks show the calculated eKE peaks corresponding to Ak^+ upon ETMD in Ak_2 from $X^1\Sigma_g^+$ and $a^3\Sigma_u^+$ states, respectively. Whereas, the magenta

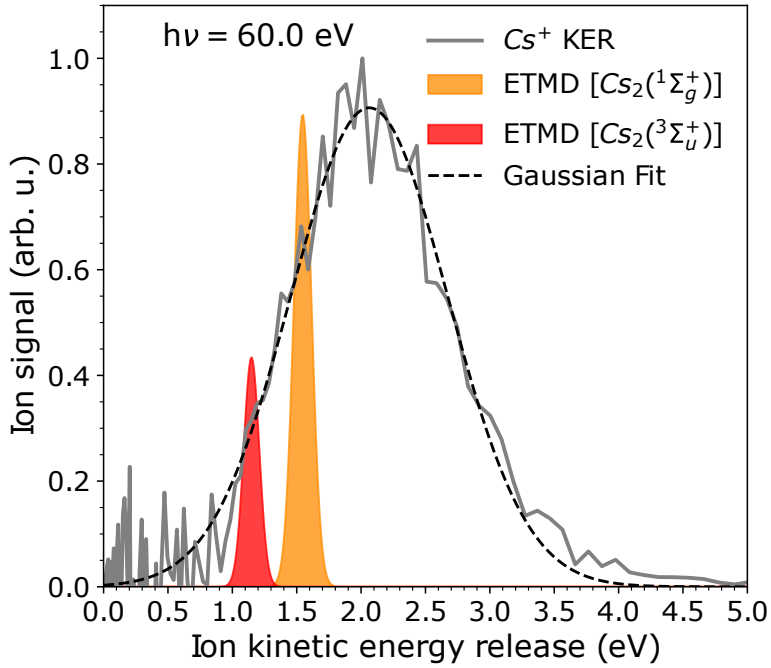

Figure 4.18: Ion kinetic energy release (KER) spectra correlated to Cs^+ ions (grey line) at 60 eV photon energy for Cs doped droplets. The orange and red shaded peaks show the calculated KER corresponding to Cs^+ ions for ETMD in Cs_2 from $^1\Sigma_g^+$ and $^3\Sigma_u^+$ states, respectively. The black dashed line shows the Gaussian fit of the observed KER spectra.

and purple lines show the calculated eKE from CT-ICD in Ak_2 where ICD proceeds from Ak^{+*} ($(n-1)p^{-1}$) $P_{3/2}$ and $P_{1/2}$ states upon CT to He_2^+, respectively. Note that, for Rb doping, the CT-ICD peak from the ionization of Rb^{+*} ($4p^{-1}$) $P_{1/2}$ state is missing, since the mentioned state in energetically inaccessible via CT from He_2^+. The existence of both the processes is clearly visible in the fitted eKE spectra. Although in case of Rb doping, the eKE peaks due to ETMD (orange and red shaded peaks) and CT-ICD (purple line) overlapped, this is not the case for Cs doping as the calculated corresponding eKE peaks (orange and red shaded peaks for ETMD, and magenta and purple lines for CT-ICD) are well separated and especially the newly proposed CT-ICD process dominates over the known ETMD processes.

4.5 Discussion on dopant double ionization

From the above analysis on the electron and ion kinetic energy spectra in coincidence with single and double alkali ions, we observe that due to photoexcitation of He $1s$ electron both to the $n = 2$ droplets excitation band at 21.6 eV and to the continuum above

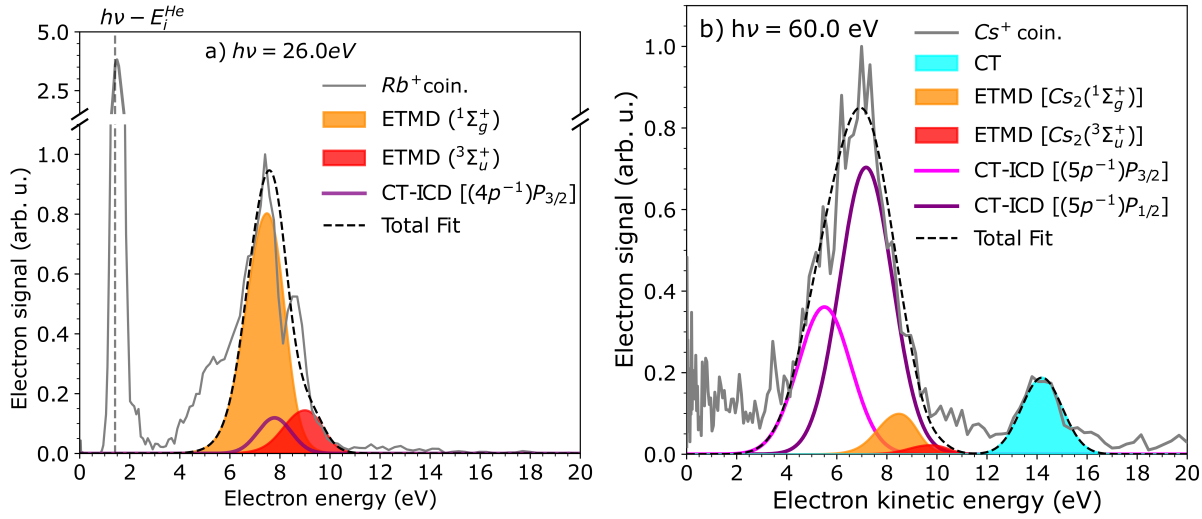

Figure 4.19: The eKE spectra correlated to a) Rb^+ and b) Cs^+ ions (grey lines) at 26 and 60 eV photon energies for Rb and Cs doping, respectively. The orange and red shaded peaks show the calculated eKE peaks corresponding to Ak^+ upon ETMD in Ak_2 from $X^1\Sigma_g^+$ and $a^3\Sigma_u^+$ states, respectively. Whereas, the magenta and purple lines show the calculated eKE from CT-ICD in Ak_2 where ICD proceeds from Ak^{+*} $((n-1)p^{-1})$ $P_{3/2}$ and $P_{1/2}$ states upon CT to He_2^+, respectively. For Rb doping, the magenta line is missing, since ionization to Rb^{+*} $(4p^{-1})$ $P_{1/2}$ state is energetically inaccessible via CT from He_2^+. The shaded cyan Gaussian peak shows the inelastically scattered eKE leading to $He^*(1s2p^1P)$ excitation following direct photoionization of the droplet and subsequent charge transfer ionization of Cs_2 in panel b). The black dashed lines show the total fit of the measured eKE spectra.

the ionization energy of the atomic He (E_i^{He}), the Ak_2 attached to the He nanodroplets undergoes double ionization. At 21.6 eV, two competing processes, dICD and cICD are present, whereas above E_i^{He} the competing processes are ETMD and CT-ICD. In the dICD and ETMD processes, both the alkali atoms are ionized simultaneously, while in cases of cICD and CT-ICD, step-wise double ionization in the Ak_2 proceeds via inner p-shell ionization of one of the Ak through ICD and CT from excited and ionized He, respectively, in the first step.

Usually ICD process leads to ionization from the valence orbital, therefore the proposed double ionization pathway in cICD is not very obvious. However, due to the large number (6) of electrons in the inner valence $(n-1)p$-shell compared the single electron present in the valence ns-shell of an alkali atom and due to the relatively large orbital size of the p-shell for heavy alkali atoms, ICD efficiency of p-shall can be considerable. In fact Woratschek *et al.* [278] experimentally reported ionization from the Cs 5p-shell due to interaction of He* with monolayer of Cs, and Ruf *et al.* [271] reported the same in an atomic beam Penning ionization experiments. These observations confirm our claim of having an ICD from the inner p-shell. Furthermore, theoretical calculations[1] were carried out to estimate the decay widths (which are inversely proportion to the ICD timescales) for ICD from the 5p-shell and from the 6s-shell of Cs due to relaxation of the He* $1s2s^3S$ and $1s2s^1S$ states at varying interatomic distance for the following processes:

$$\mathrm{He}^*(^{3,1}S) + \mathrm{Cs} \rightarrow \mathrm{He} + \mathrm{Cs}^+(6s^{-1}) + e^-_{ICD} \tag{4.17}$$

$$\mathrm{He}^*(^{3,1}S) + \mathrm{Cs} \rightarrow \mathrm{He} + \mathrm{Cs}^{+*}(5p^{-1}) + e^-_{ICD} \tag{4.18}$$

In Fig. 4.20 a), the decay widths as a function of interatomic distance for processes (4.17) and (4.18) are shown by (red and green) and (orange and blue) points for He* ($^{3,1}S$) states, respectively. Clearly, at interatomic distance lower than $\sim$ 4 Å, ICD processes leading to inner p-shell ionization dominate over the same from the outer valence s-shell. This indicates that the first ICD step in cICD process occurs when the distance between the He* and Ak is low, which allows for sufficient overlap between the He* $1s2s,p$ and Ak

[1]These calculations were performed by Dr. Nicolas Sisourat, Sorbonne Université, CNRS, Laboratoire de Chimie Physique Matière et Rayonnement, 75005 Paris, France, and the results were privately communicated.

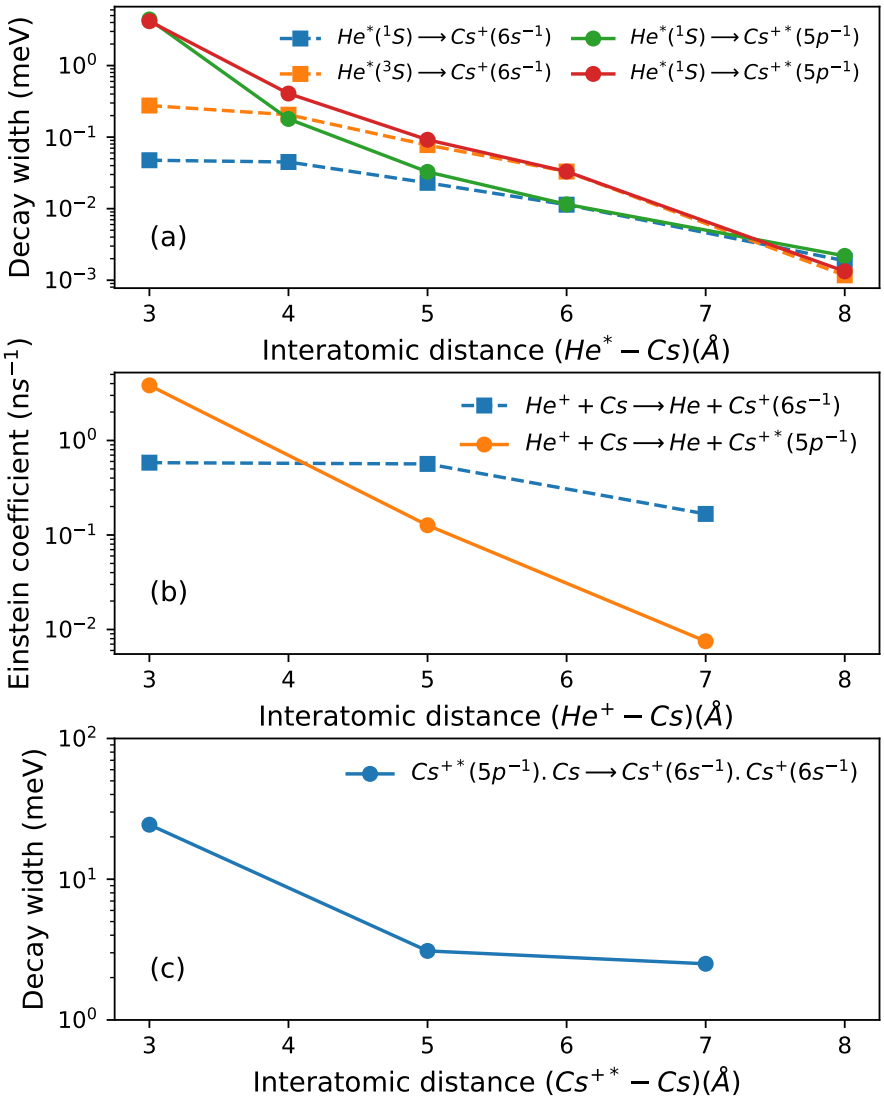

Figure 4.20: a) Decay width as function of interatomic distance between He* ($^{3,1}S$) and Cs both for $5p$ and $6s$ ionization channels. b) Einstein coefficients as function of the interatomic distance between He^+ and Cs both for charge transfer ionization from Cs $5p$ and $6s$ orbitals. c) Decay width as a function of interatomic distance between Cs^{+*} ($5p^{-1}$) and Cs leading to doubly ionized Cs_2^{2+} ion.

$(n-1)p$, aiding the ICD process.

Now the proposed CT-ICD process also requires charge transfer (CT) from the $(n-1)p$-shell of the Ak atom to the He_2^+ ion to initiate the subsequent ICD step. The former CT process is most likely an non-radiative CT process through curve crossing between the initial He_2^+Ak and final $He_2Ak^{+*}((n-1)p^-)$ potential energy curves. Theoretical validation of such curve crossing phenomena is computationally expensive, due to large number of participating electrons in the p-shell of the Ak, therefore was not pursued in the current work. However, the assumption of non-radiative CT is valid because the potential energy of curve of He_2^+ (shown by the red line in Fig. 4.15) lies very close to the energy of the Ak^{+*} $((n-1)p^{-1})$. Note that, the energies of Ak^{+*} $((n-1)p^{-1})$ $P_{3/2}$ and $P_{1/2}$ states are 20.803 and 21.497 eV for Rb and 17.430 and 19.097 eV for Cs, respectively. Whereas the asymptotic limit and the minimum of He_2^+ potential energy are 24.587 and 22.220 eV, respectively. Moreover, recently Ruchti *et al.* [279] showed that Xe atoms doped in He nanodroplets are more efficiently ionized upon electron impact ionization of the droplet than other rare gas dopants (Ne and Ar). The underlying mechanism responsible for this highly efficient indirect ionization process derives from non-radiative charge transfer process through potential energy curve crossing between the initial and final states (see fig.6 in [279]). This non-radiative CT process produces Xe^+ ion in excited $^2S_{1/2}$ state, whose energy is 20.95 eV, very close to the ionization energy of He (24.587 eV). They also reported an radiative CT process, producing Xe^+ ion in its ground state ($E_i^{Xe} = 13.436$ eV), wherein the excess energy is released by a vacuum ultraviolet (VUV) photoemission. Although the later process is comparatively very slow that the former non-radiative process. These observations also validates our efficient CT ionization process from the inner p-shell of the Ak atoms to the He_2^+ ion, producing excited Ak^{+*} ions which then participate in another ICD process.

Furthermore, the CT efficiencies were theoretically estimated [2] in terms of the Einstein coefficients, which indicate the rate of transition between two quantum levels, for the CT processes producing $Cs^+(6s^{-1})$ and $Cs^{+*}(5p^{-1})$ ions as a function of interatomic distance

[2]These calculations were also carried out by Dr. Nicolas Sisourat, Sorbonne Université, CNRS, Laboratoire de Chimie Physique Matière et Rayonnement, 75005 Paris, France, and the results were privately communicated.

between He^+ and Cs, see below:

$$He^+ + Cs \rightarrow He + Cs^+(6s^{-1}) + e^-_{ICD} \tag{4.19}$$

$$He^+ + Cs \rightarrow He + Cs^{+*}(5p^{-1}) + e^-_{ICD} \tag{4.20}$$

In Fig. 4.20 b) the blue and orange points show the Einstein coefficients from processes (4.19) and (4.20) as a function of the interatomic distance, respectively. It is clearly seen that the CT rate for ionization to from the inner valence $5p$-shell dominates over the same from the valence $6s$-shell at a lower interatomic distance below 4 Å.

Now, we also calculated the decay widths for the second ICD steps (see process (4.21) below) in both cICD and CT-ICD processes in case of Cs_2 as a function of interatomic distance.

$$Cs^{+*}(5p^{-1}).Cs \rightarrow Cs^+(6s^{-1}) + Cs^+(6s^{-1}) + e^-_{ICD} \tag{4.21}$$

In Fig. 4.20 c) the blue points show the decay width as a function of the interatomic distance, wherein we observe that there is a certain increase in the decay width below 5 Å. This confirms our assumption that this ICD process occurs at a reduced interatomic distance of Cs_2, and also explains the observed high KER of the product ions.

4.6 Summary

In these experiments with heavy alkali doped He nanodroplets, the *inter*-atomic/molecular ionization of Rb and Cs, following both the photoexcitation at 21.6 eV and ionization of the droplets above E_i^{He} are first observed by monitoring the Rb^+ and Cs^+ ion yields originating from the droplet as a function of photon energy, wherein the surface localizations of these dopant atoms are indicated from the difference in these ion-yield intensities at the droplet excitation and ionization regimes. We see double ionization of the dopant cluster and their subsequent Coulombic fragmentations from the multi-ion ToF coincidence measurements following both the excitation and ionization of the droplets. By analysing the eKE spectra in coincidence with both single and double alkali ions, both the single and double ionization processes are identified.

Upon photoexcitation to the $n = 2$ droplet band at 21.6 eV, the observed single ion-

ization processes in the alkali dopants occur at different interatomic distances between the He^* and Ak in long-range and short-range ICD processes. Due to the difference in the KER of the product-Ak^+ ions from these processes and their ability to emerge out of the droplet overcoming the strong attractive droplet-potential, these two processes are differentiated by measuring the electron kinetic energy spectra in coincidence with the alkali ions and the total electron kinetic energy spectra. To explain eKE spectral features and ion-KER arising due to the double ionization, we proposed a novel two-step double ionization process called cascaded-ICD (cICD) which competes with the known one-step double-ICD (dICD) process. In the cICD process, first ICD step ionizes the inner-valence p-shell of the alkali atoms due to relaxation of He^*. Then the resulting Ak^{+*} ions de-excite via another ICD which ionizes the neighbouring Ak atom.

Above E_i^{He} following droplet photoionization, CT ionization of the dopants which leads to double ionization in alkali dimer is observed. For our heavy alkali dopants, we proposed ETMD and CT-ICD processes underlying the double ionization. While the ETMD is a one-step process, the CT-ICD involves two ionizing steps, in which similar to the cascaded-ICD, inner-valence p-shell of the Ak atom first gets ionized due to CT to the ionized droplet, leaving an excited Ak^{+*} ion for another ICD with the neighbouring Ak atom.

Summary and Future Prospects

4.7 Summary

Inter-atomic/molecular decays in acetylene (C_2H_2) and heavy alkali (Rb and Cs) doped He nanodroplets are studied by implementing electron - multi ion coincidence spectroscopy, where EUV radiations are used to resonantly excite or ionize the droplets. Upon photoexcitation of the host He droplet to the $n = 2$ droplet band by 21.6 eV photon, interatomic/molecular Coulombic decay (ICD) processes are observed in C_2H_2 dopants leading to only single ionization, and in Rb and Cs dopants leading to both single and double ionization. Here, electronic relaxations in He* ($1s2s/p$) induce ionization in the dopants, and the kinetic energies of emitted electrons and ions carry the information about ionization dynamics, *i.e.*, insights into the participating electronic states of the host and dopants as well as the corresponding nuclear dynamics. For C_2H_2 doped He nanodroplets, we conclude that the C_2H_2 clusters in the droplet are singly ionized via Penning-like resonant ICD process to all the available cationic states below the droplet de-excitation energy from He* $1s2s\ ^{3,1}S$, and $1s2p\ ^1P$ states, whereas for alkali dopants, both single and double ionization of dopant cluster occur as a result of the same relaxations in excited host. Model calculations are carried out to get insights into the surprisingly efficient double ionization processes in alkali dimer attached to the droplet surface. Two mechanisms are proposed: double-ICD (dICD) and cascaded-ICD (cICD). In the dICD process, two electrons are ionized simultaneously from the alkali dimer upon de-excitation of He*, while in the cICD process two electrons are emitted from two cascaded ICD steps. First ICD occurs in the inner valence p-shell in one of the alkali dimer constituents upon de-excitation of He* leaving the alkali dimer in an excited ionized state. In the second ICD, the p-shell vacancy is filled by an outer s-shell electron which leads to ionization in the other alkali

atom. Thereby, this cICD creates spatially separated two positive holes in two neighbouring alkali atoms which eventually undergo Coulomb explosion. Single ionization of alkali dopant occurs when outer s-shell electron is ejected from the alkali atom upon de-excitation of He^*, resulting in emission of electron with high kinetic energy and leaving inadequate internal energy in the dopant ion for further ionization.

Decays initiated by single ionization in the host droplet are studied by irradiating photons with energy higher than the autoionization threshold ($\sim$ 23 eV) of He nanodroplets. The doped C_2H_2 cluster in the droplet is efficiently singly ionized upon autoionization below ionization threshold of atomic He ($E_i^{\mathrm{He}} = 24.6$ eV), and upon direct ionization of the droplet above E_i^{He}, via electron transfer from the C_2H_2 cluster to the initially created hole in the droplet. This process is known as charge transfer (CT) ionization and confirmed by detecting the ionized host electron in coincidence with C_2H_2 cluster ions. However, upon photoexcitation to $n = 4$ droplet excitation band below E_i^{He}, competing resonant ICD or Penning ionization channels that lead to excited $C_2H_2^+$ $C^2\Sigma_g^+$ and $D^2\Sigma_g^+$ states due to relaxation of higher lying He^* $1s4p\ ^1P$ state are discovered, along with the dominant CT ionization channel following the autoionization.

Following direct photoionization of the host above E_i^{He}, for alkali doping, both single and double ionization of the dopant clusters are detected. Charge transfer from the outer valence s-orbital of alkali atom to He_2^+ is responsible for single ionization in the dopant, while the double ionization in the attached alkali dimer occurs due to two distinct ionization mechanisms; electron transfer mediated decay (ETMD) and CT followed by ICD. The ETMD process is equivalent to the dICD process, previously seen upon $n = 2$ droplet band excitation, wherein an outer valence electron from the alkali dimer gets transferred to the vacancy of He_2^+ in the droplet and simultaneously another outer valence electron from the neighbouring dimer constituent is ejected, creating doubly ionized alkali dimer. Likewise, the CT followed by ICD process is similar to the cICD process. Charge transfer occurs between the inner valence p-shell of one of the alkali dimer constituents and He_2^+. This initial CT creates neutral He_2 and an excited inner valence ionized alkali dimer cation where a subsequent ICD takes place. In the later step, the p-shell vacancy of the excited alkali dimer cation is filled by an outer valence s-shell electron, and another outer s-electron is ionized from the other alkali dimer constituent. Finally, both these ETMD and CT followed by ICD processes lead to doubly ionized alkali dimers which

Coulomb explode to produce same product ions. Theoretical calculations are performed to simulate and compare the electron and ion kinetic energy spectra which confirm the proposed mechanisms.

We are able to unambiguously identify various correlated *inter*-atomic/molecular decay processes upon excitation and ionization of host He environment for two different types of dopant with distinct electronic structure, by coincident measurements of electron and ion kinetic energy spectra using co-axial time of flight and velocity map imaging spectrometer working in tandem. We find that the decay processes indeed depend on the dopant electronic configurations. We propose that a correlated electronic decay involving an excited intermediate state with p-shell vacancy which subsequently decays through anther ICD process is responsible for higher degree of ionisation. We show that C_2H_2 and alkali dopants behave differently in response to decay processes, owing to their locations in the droplet. Furthermore, from experiments with C_2H_2 doping, we demonstrate that Penning ionization electron spectroscopy (PIES) can be used to uncover the structure of molecular cluster formed inside He nanodroplets by exciting the host matrix. One can even gain knowledge about the dynamics of the dopants post Penning ionization from the PIES correlated to different dopant oligomer ions.

4.8 Future Prospects

The newly-proposed cICD and CT followed ICD processes provide the first experimental evidence for higher order ionization mechanisms through intermediate excited cations created by the ICD and CT processes in case of heavy alkali doping. Earlier theoretical studies on aqueous lithium (Li^+) and magnesium (Mg^{2+}) ionic clusters predicted cascades of ETMD and ICD processes producing multiple water ions (H_2O^+) through transient excited H_2O^{+*} and Mg_4^{+*} ions, respectively, upon initial $1s$ ionization of these metal ions [68, 59]. Previous attempts to experimentally observe such phenomena in LiCl doped water cluster upon Li ($1s$) ionization were not successful, possibly due to the competition between the subsequent ICD within H_2O^{+*} and H_2O and Coulombic fragmentation within Li^+ and H_2O^{+*} [81, 82]. We are able to overcome such challenges arising from Coulombic fragmentation which can inhibit the subsequent *inter*-atomic/molecular decays in our current study by exploring these higher-order ionization processes where only a single

transient excited ion is created in the intermediate step. Thus, this work motivates further time-resolved studies on such higher order processes using ultrafast pump-probe techniques to map the dynamics of the participating transient states.

Furthermore, upon resonant photoexcitation of the droplet to specific droplet bands derived from He* $1s2p\ ^1P$ and $1s4p\ ^1P$ states, we have seen that the droplet first undergoes ultrafast internal relaxations into lower lying excited states, He* $1s2s\ ^{3,1}S$ [190, 191, 192], then from these internally relaxed states *inter*-atomic/molecular decay proceeds in the dopants. Thus, it will be intriguing to find out the time scales of these multi-step processes by implementing pump-probe photoelectron spectroscopy. Ultrafast EUV-pump and IR-probe available at free electron lasers or high harmonic generation lasers can be used for these time-resolved investigations as recently done in case of Na doped He nanodroplets [280].

In these experiments, the main focus was on studying *inter*-atomic/molecular decays that lead to dopant ionization following single-electronic excitation or ionization of the droplets. However, many radiative decay processes can be active following the external perturbation and even from the final states that are discussed in this work. But, we were not sensitive to these radiative decays because of the electron - multi ion coincident technique used. Thus, one can also integrate coincident detection of photons into these experiment to gain a more complete picture about the relaxation dynamics. Another direction regarding the study of *inter*-atomic/molecular decays in doped He nanodroplets is to investigate these processes upon double electronic-excitation of He where more complex interplay with *intra*-atomic relaxations, such as, autoionization in doubly excited He**, are expected [281].

Publications

Publications related to the thesis

1. *Penning spectroscopy and structure of acetylene oligomers in He nanodroplets*, **S. Mandal**, R. Gopal, M. Shcherbinin, A. D'Elia, H. Srinivas, R. Richter, M. Coreno, B. Bapat, M. Mudrich, S. R. Krishnan, and V. Sharma.
   Physical Chemistry Chemical Physics, **22**, 1014-10157 (2020)

2. *Photoionization of Acetylene Doped in Helium Nanodroplets by EUV Synchrotron Radiation*, **S. Mandal**, R. Gopal, S. R. Krishnan, R. Richter, M. Coreno, M. Mudrich, H. Srinivas, A. D'Elia, B. Bapat, and V. Sharma.
   Springer Proceedings in Physics, **230**, 130-138 (2019)

3. *Cascaded interatomic double ionization via decay of intermediate excited states in heavy alkali dimers upon photoexcitation of host helium nanodroplets*, **S. Mandal**, L. Ben Ltaief, M. Shcherbinin, R. Gopal, V. Sharma, H. Srinivas, A. D'Elia, R. Richter, M. Coreno, B. Bapat, P. Kolorenc, N. Sisourat, M. Mudrich, A. C. LaForge, and S. R. Krishnan [*under preparation*]

Other publications

4. *Fragmentation dynamics of doubly charged camphor molecule following C* 1*s Auger decay*, Sanket Sen, **S. Mandal**, Arnab Sen, R. Gopal, L. Ben Ltaief, S. Turchini, D. Catone, N. Zema, M. Coreno, R. Richter, M. Mudrich, S. R. Krishnan, and V. Sharma.
   Physical Chemistry Chemical Physics, **24**, 2944-2957 (2022)

5. *Dissociation dynamics of multiply charged CH_3I in moderately intense laser fields*, Arnab Sen, **S. Mandal**, Sanket Sen, Bhas Bapat, R. Gopal, and V. Sharma.
   Physical Review A, **103**, 043107 (2021)

6. *Coincident angle-resolved state-selective EUV photoelectron spectroscopy of acetylene molecules: a candidate system for time-resolved dynamics*, **S. Mandal**, R. Gopal, H. Srinivas, A. D'Elia, A. Sen, S. Sen, R. Richter, M. Coreno, B. Bapat, M. Mudrich, V. Sharma, and S. R. Krishnan.
   Faraday Discussions, **228**, 242-265 (2021)

7. *Photoelectron Spectroscopy of Coronene Molecules Embedded in Helium Nanodroplets*, L. Ben Ltaief, M. Shcherbinin, **S. Mandal**, S. R. Krishnan, R. Richter, S. Turchini, N. Zema, and M. Mudrich.
   Journal of Low Temperature Physics, **202**, 444–455 (2021)

8. *Direct inner-shell photoionization of Xe atoms embedded in helium nanodroplets*, L. Ben Ltaief, M. Shcherbinin, **S. Mandal**, S. R. Krishnan, R. Richter, T. Pfeifer, and M. Mudrich.
   Journal of Physics B: Atomic, Molecular and Optical Physics, **53**, 204001 (2020)

9. *Electron transfer mediated decay of alkali dimers attached to He nanodroplets*, L. Ben Ltaief, M. Shcherbinin, **S. Mandal**, S. R. Krishnan, R. Richter, T. Pfeifer, M. Bauer, A. Ghosh, M. Mudrich, K. Gokhberg, and A. C. LaForge.
   Physical Chemistry Chemical Physics, **22**, 8557-8564 (2020)

10. *Charge Exchange Dominates Long-Range Interatomic Coulombic Decay of Excited Metal-Doped Helium Nanodroplets*, L. Ben Ltaief, M. Shcherbinin, **S. Mandal**, S. R. Krishnan, A. C. LaForge, R. Richter, S. Turchini, N. Zema, T. Pfeifer, E. Fasshauer, N. Sisourat, and M. Mudrich.
    The Journal of Physical Chemistry Letters, **10**(21), 6904-6909 (2019)

11. *Intriguing Single Photon Induced Processes in Helium Nanodroplets*, S. R. Krishnan, **S. Mandal**, B. Bapat, R. Gopal, A. D'Elia, H. Srinivas, R. Richter, M. Coreno, M. Mudrich, and V. Sharma.
    Springer Proceedings in Physics, **230**, 121-129 (2019)

12. *Ignition of a helium nanoplasma by x-ray multiple ionization of a heavy rare-gas core*, D. Schomas, C. Medina, L. Ben Ltaief, R. B. Fink, **S. Mandal**, S. R. Krishnan, R. Michiels, M. Debatin, F. Stienkemeier, S. Toleikis, C. Passow, N. Ekanayake, C. Ott, R. Moshammer, T. Pfeifer, A. Heidenreich, and M. Mudrich.
arXiv:2005.02944 (2020)

Conference presentations

1. *"Ionic motion of photofragments in EUV excited doped He nanodroplets"* at QFS 2021 - Quantum Fluids and Solids (10-14 and 16-19 August, 2021) held virtually at Indian Institute of Science, Bangalore, India

2. *"Structure of acetylene clusters in helium nanodroplets probed by Penning ionization electron spectroscopy"* at Virtual International Conference on Photonic Electronic and Atomic Collisions (20-24 July, 2021) held virtually in Ottawa, Canada

3. *"Penning spectroscopy and structure of acetylene oligomers in He nanodroplets probed by EUV photons"* at DESY Photon Science Users' Meeting 2021 (25-29 January, 2021) held virtually at DESY, Germany

4. *"Penning Spectroscopy of Ionic Molecular Cluster in He Nanodroplets"* at 8th Topical Conference on Atomic and Molecular Collisions for Plasma Applications (3-5 March, 2020) held at Indian Institute of Technology Roorkee, India

5. *"Role of Helium Nanodroplet Environment on the Ionization Dynamics of Acetylene Under EUV Synchrotron Radiation"* at 22nd National Conference on Atomic Molecular Physics (25 -28 March, 2019) held at Indian Institute of Technology Kanpur, India

6. *"Acetylene Cluster Photoionization Dynamics in He Nanodroplets"* at 13th Asian International Seminar on Atomic and Molecular Physics (3 – 8 December, 2018) held at Indian Institute of Technology Bombay and Tata Institute of Fundamental Research Mumbai, India

7. *"Isomerization of Acetylene doped in He nanodroplets by EUV synchrotron radiation"* at 7th Topical Conference of the Indian Society of Atomic and Molecular Physics (6 – 8 January, 2018) held at Indian Institute of Science Education and Research Tirupati and Indian Institute Technology Tirupati, India

Bibliography

[1] Klaus Ruedenberg. The physical nature of the chemical bond. *Rev. Mod. Phys.*, 34: 326–376, Apr 1962. doi: 10.1103/RevModPhys.34.326. URL https://link.aps.org/doi/10.1103/RevModPhys.34.326.

[2] Linus Pauling. The nature of the chemical bond. iii. the transition from one extreme bond type to another. *Journal of the American Chemical Society*, 54(3):988–1003, Mar 1932. ISSN 0002-7863. doi: 10.1021/ja01342a022. URL https://doi.org/10.1021/ja01342a022.

[3] Linus Pauling. The nature of the chemical bond. iv. the energy of single bonds and the relative electronegativity of atoms. *Journal of the American Chemical Society*, 54(9):3570–3582, Sep 1932. ISSN 0002-7863. doi: 10.1021/ja01348a011. URL https://doi.org/10.1021/ja01348a011.

[4] Peter W. Atkins and Ronald S. Friedman. *Molecular Quantum Mechanics*. Oxford University Press, November 2010. ISBN 9780199541423. URL https://global.oup.com/academic/product/molecular-quantum-mechanics-9780199541423?cc=in&lang=en&#.

[5] Lise Meitner. Über dieβ-strahl-spektra und ihren zusammenhang mit der γ-strahlung. *Zeitschrift für Physik*, 11(1):35–54, Dec 1922. ISSN 0044-3328. doi: 10.1007/BF01328399. URL https://doi.org/10.1007/BF01328399.

[6] Auger, Pierre. Sur l'effet photoélectrique composé. *J. Phys. Radium*, 6(6):205–208, 1925. doi: 10.1051/jphysrad:0192500606020500. URL https://doi.org/10.1051/jphysrad:0192500606020500.

[7] Vor allem P. Debye. *Physik. Zeits.*, 21:178, 1920.

[8] Vor allem P. Debye. *Physik. Zeits.*, 22:302, 1921.

[9] W. H. Keesom. *Physik. Zeits.*, 22:129, 1921.

[10] F. London. Zur theorie und systematik der molekularkräfte. *Zeitschrift für Physik*, 63(3):245–279, Mar 1930. ISSN 0044-3328. doi: 10.1007/BF01421741. URL https://doi.org/10.1007/BF01421741.

[11] Th. Förster. Zwischenmolekulare energiewanderung und fluoreszenz. *Annalen der Physik*, 437(1-2):55–75, 1948. doi: https://doi.org/10.1002/andp.19484370105. URL https://onlinelibrary.wiley.com/doi/abs/10.1002/andp.19484370105.

[12] Gregory D. Scholes. Long-range resonance energy transfer in molecular systems. *Annual Review of Physical Chemistry*, 54(1):57–87, 2003. doi: 10.1146/annurev.physchem.54.011002.103746. URL https://doi.org/10.1146/annurev.physchem.54.011002.103746. PMID: 12471171.

[13] Garth A. Jones and David S. Bradshaw. Resonance energy transfer: From fundamental theory to recent applications. *Frontiers in Physics*, 7:100, 2019. ISSN 2296-424X. doi: 10.3389/fphy.2019.00100. URL https://www.frontiersin.org/article/10.3389/fphy.2019.00100.

[14] D. L. Dexter. A theory of sensitized luminescence in solids. *The Journal of Chemical Physics*, 21(5):836–850, 1953. doi: 10.1063/1.1699044. URL https://doi.org/10.1063/1.1699044.

[15] F. M. Penning. Über ionisation durch metastabile atome. *Naturwissenschaften*, 15 (40):818–818, Oct 1927. ISSN 1432-1904. doi: 10.1007/BF01505431. URL https://doi.org/10.1007/BF01505431.

[16] P. E. Siska. Molecular-beam studies of penning ionization. *Rev. Mod. Phys.*, 65: 337–412, Apr 1993. doi: 10.1103/RevModPhys.65.337. URL https://link.aps.org/doi/10.1103/RevModPhys.65.337.

[17] Takuya Horio, Takuro Hatamoto, Satoshi Maeda, Naoki Kishimoto, and Koichi Ohno. Probing anisotropic interaction potentials of unsaturated hydrocarbons with he*(2s3) metastable atom: Attractive-site preference of σ-direction in c2h2 and π-

direction in c2h4. *The Journal of Chemical Physics*, 124(10):104308, 2006. doi: 10.1063/1.2178298. URL https://doi.org/10.1063/1.2178298.

[18] Rainer Johnsen and Manfred A. Biondi. Measurements of radiative charge-transfer reactions of doubly and singly charged rare-gas ions with rare-gas atoms at thermal energies. *Phys. Rev. A*, 18:996–1003, Sep 1978. doi: 10.1103/PhysRevA.18.996. URL https://link.aps.org/doi/10.1103/PhysRevA.18.996.

[19] N. Saito, Y. Morishita, I.H. Suzuki, S.D. Stoychev, A.I. Kuleff, L.S. Cederbaum, X.-J. Liu, H. Fukuzawa, G. Prümper, and K. Ueda. Evidence of radiative charge transfer in argon dimers. *Chemical Physics Letters*, 441(1):16–19, 2007. ISSN 0009-2614. doi: https://doi.org/10.1016/j.cplett.2007.04.077. URL https://www.sciencedirect.com/science/article/pii/S0009261407005404.

[20] Andreas Hans, Tsveta Miteva, Xaver Holzapfel, Christian Ozga, Philipp Schmidt, Huda Otto, Gregor Hartmann, Clemens Richter, Nicolas Sisourat, Arno Ehresmann, Kirill Gokhberg, Uwe Hergenhahn, and André Knie. Electronic decay of singly charged ground-state ions by charge transfer via van der waals bonds. *Phys. Rev. Lett.*, 123:213001, Nov 2019. doi: 10.1103/PhysRevLett.123.213001. URL https://link.aps.org/doi/10.1103/PhysRevLett.123.213001.

[21] Andreas Hans, Vasili Stumpf, Xaver Holzapfel, Florian Wiegandt, Philipp Schmidt, Christian Ozga, Philipp Reiß, Ltaief Ben Ltaief, Catmarna KÃ¼stner-Wetekam, Till Jahnke, Arno Ehresmann, Philipp V Demekhin, Kirill Gokhberg, and AndrÃ© Knie. Direct evidence for radiative charge transfer after inner-shell excitation and ionization of large clusters. *New Journal of Physics*, 20(1):012001, apr 2018. doi: 10.1088/1367-2630/aaa4af. URL https://doi.org/10.1088/1367-2630/aaa4af.

[22] L. S. Cederbaum, J. Zobeley, and F. Tarantelli. Giant intermolecular decay and fragmentation of clusters. *Physical Review Letters*, 79:4778–4781, 1997. doi: 10.1103/PhysRevLett.79.4778. URL https://link.aps.org/doi/10.1103/PhysRevLett.79.4778.

[23] J. Zobeley, L. S. Cederbaum, and F. Tarantelli. Highly excited electronic states of molecular clusters and their decay. *The Journal of Chemical Physics*, 108(23):9737–9750, 1998. doi: 10.1063/1.476448. URL https://doi.org/10.1063/1.476448.

[24] Nayana Vaval and Lorenz S. Cederbaum. Ab initio lifetimes in the interatomic coulombic decay of neon clusters computed with propagators. *The Journal of Chemical Physics*, 126(16):164110, 2007. doi: 10.1063/1.2723117. URL https://doi.org/10.1063/1.2723117.

[25] Elke Fasshauer, Markus Pernpointner, and Kirill Gokhberg. Interatomic decay of inner-valence ionized states in arxe clusters: Relativistic approach. *The Journal of Chemical Physics*, 138(1):014305, 2013. doi: 10.1063/1.4772654. URL https://doi.org/10.1063/1.4772654.

[26] Robin Santra and Lorenz S. Cederbaum. Non-hermitian electronic theory and applications to clusters. *Physics Reports*, 368(1):1 – 117, 2002. ISSN 0370-1573. doi: https://doi.org/10.1016/S0370-1573(02)00143-6. URL http://www.sciencedirect.com/science/article/pii/S0370157302001436.

[27] Vitali Averbukh, Imke B. Müller, and Lorenz S. Cederbaum. Mechanism of interatomic coulombic decay in clusters. *Physical Review Letters*, 93:263002, 2004. doi: 10.1103/PhysRevLett.93.263002. URL https://link.aps.org/doi/10.1103/PhysRevLett.93.263002.

[28] Robin Santra, Jürgen Zobeley, and Lorenz S. Cederbaum. Electronic decay of valence holes in clusters and condensed matter. *Phys. Rev. B*, 64:245104, Nov 2001. doi: 10.1103/PhysRevB.64.245104. URL https://link.aps.org/doi/10.1103/PhysRevB.64.245104.

[29] Vitali Averbukh and Lorenz S. Cederbaum. Ab initio calculation of interatomic decay rates by a combination of the fano ansatz, green's-function methods, and the stieltjes imaging technique. *The Journal of Chemical Physics*, 123(20):204107, 2005. doi: 10.1063/1.2126976. URL https://doi.org/10.1063/1.2126976.

[30] Vitali Averbukh and Lorenz S. Cederbaum. Calculation of interatomic decay widths of vacancy states delocalized due to inversion symmetry. *The Journal of Chemical Physics*, 125(9):094107, 2006. doi: 10.1063/1.2244567. URL https://doi.org/10.1063/1.2244567.

[31] Přemysl Kolorenč, Vitali Averbukh, Kirill Gokhberg, and Lorenz S. Cederbaum. Ab initio calculation of interatomic decay rates of excited doubly ionized states in

clusters. *The Journal of Chemical Physics*, 129(24):244102, 2008. doi: 10.1063/1.3043437. URL https://doi.org/10.1063/1.3043437.

[32] Aryya Ghosh, Sourav Pal, and Nayana Vaval. Study of interatomic coulombic decay of ne(h2o)n (n = 1,3) clusters using equation-of-motion coupled-cluster method. *The Journal of Chemical Physics*, 139(6):064112, 2013. doi: 10.1063/1.4817966. URL https://doi.org/10.1063/1.4817966.

[33] V. Stumpf, C. Brunken, and K. Gokhberg. Impact of metal ion's charge on the interatomic coulombic decay widths in microsolvated clusters. *The Journal of Chemical Physics*, 145(10):104306, 2016. doi: 10.1063/1.4962353. URL https://doi.org/10.1063/1.4962353.

[34] Ghazal Jabbari, Keyvan Sadri, Lorenz S. Cederbaum, and Kirill Gokhberg. Strong enhancement of cage effects in water photolysis caused by interatomic coulombic decay. *The Journal of Chemical Physics*, 144(16):164307, 2016. doi: 10.1063/1.4947238. URL https://doi.org/10.1063/1.4947238.

[35] Tsveta Miteva, Sévan Kazandjian, P řemysl Kolorenč, Petra Votavová, and Nicolas Sisourat. Interatomic coulombic decay mediated by ultrafast superexchange energy transfer. *Phys. Rev. Lett.*, 119:083403, Aug 2017. doi: 10.1103/PhysRevLett.119.083403. URL https://link.aps.org/doi/10.1103/PhysRevLett.119.083403.

[36] Petra Votavová, Tsveta Miteva, Selma Engin, Sévan Kazandjian, P řemysl Kolorenč, and Nicolas Sisourat. Mechanism of superexchange interatomic coulombic decay in rare-gas clusters. *Phys. Rev. A*, 100:022706, Aug 2019. doi: 10.1103/PhysRevA.100.022706. URL https://link.aps.org/doi/10.1103/PhysRevA.100.022706.

[37] Robert Bennett, Petra Votavová, P řemysl Kolorenč, Tsveta Miteva, Nicolas Sisourat, and Stefan Yoshi Buhmann. Virtual photon approximation for three-body interatomic coulombic decay. *Phys. Rev. Lett.*, 122:153401, Apr 2019. doi: 10.1103/PhysRevLett.122.153401. URL https://link.aps.org/doi/10.1103/PhysRevLett.122.153401.

[38] Nimrod Moiseyev, Robin Santra, Jürgen Zobeley, and Lorenz S. Cederbaum. Fingerprints of the nodal structure of autoionizing vibrational wave functions in clusters: Interatomic coulombic decay in ne dimer. *The Journal of Chemical Physics*, 114

(17):7351–7360, 2001. doi: 10.1063/1.1361070. URL https://doi.org/10.1063/1.1361070.

[39] Nicolas Sisourat, Nikolai V. Kryzhevoi, P řemysl Kolorenč, Simona Scheit, and Lorenz S. Cederbaum. Impact of nuclear dynamics on interatomic coulombic decay in a he dimer. *Phys. Rev. A*, 82:053401, Nov 2010. doi: 10.1103/PhysRevA.82.053401. URL https://link.aps.org/doi/10.1103/PhysRevA.82.053401.

[40] Nicolas Sisourat, Nikolai V. Kryzhevoi, Přemysl Kolorenč, Simona Scheit, Till Jahnke, and Lorenz S. Cederbaum. Ultralong-range energy transfer by interatomic coulombic decay in an extreme quantum system. *Nature Physics*, 6(7):508–511, Jul 2010. ISSN 1745-2481. doi: 10.1038/nphys1685. URL https://doi.org/10.1038/nphys1685.

[41] Simona Scheit, Vitali Averbukh, Hans-Dieter Meyer, Jürgen Zobeley, and Lorenz S. Cederbaum. Interatomic coulombic decay in a heteroatomic rare gas cluster. *The Journal of Chemical Physics*, 124(15):154305, 2006. doi: 10.1063/1.2185637. URL https://doi.org/10.1063/1.2185637.

[42] Kirill Gokhberg, Vitali Averbukh, and Lorenz S. Cederbaum. Interatomic decay of inner-valence-excited states in clusters. *The Journal of Chemical Physics*, 124(14):144315, 2006. doi: 10.1063/1.2187472. URL https://doi.org/10.1063/1.2187472.

[43] Anael Ben-Asher, Arie Landau, Lorenz S. Cederbaum, and Nimrod Moiseyev. Quantum effects dominating the interatomic coulombic decay of an extreme system. *The Journal of Physical Chemistry Letters*, 11(16):6600–6605, 2020. doi: 10.1021/acs.jpclett.0c01974. URL https://doi.org/10.1021/acs.jpclett.0c01974. PMID: 32706968.

[44] Lorenz S. Cederbaum. Ultrafast intermolecular energy transfer from vibrations to electronic motion. *Phys. Rev. Lett.*, 121:223001, Nov 2018. doi: 10.1103/PhysRevLett.121.223001. URL https://link.aps.org/doi/10.1103/PhysRevLett.121.223001.

[45] Vitali Averbukh and Lorenz S. Cederbaum. Interatomic electronic decay in endohe-

dral fullerenes. *Phys. Rev. Lett.*, 96:053401, Feb 2006. doi: 10.1103/PhysRevLett.96.053401. URL https://link.aps.org/doi/10.1103/PhysRevLett.96.053401.

[46] Robin Santra and Lorenz S. Cederbaum. Coulombic energy transfer and triple ionization in clusters. *Phys. Rev. Lett.*, 90:153401, Apr 2003. doi: 10.1103/PhysRevLett.90.153401. URL https://link.aps.org/doi/10.1103/PhysRevLett.90.153401.

[47] Spas D. Stoychev, Alexander I. Kuleff, Francesco Tarantelli, and Lorenz S. Cederbaum. On the interatomic electronic processes following auger decay in neon dimer. *The Journal of Chemical Physics*, 129(7):074307, 2008. doi: 10.1063/1.2960593. URL https://doi.org/10.1063/1.2960593.

[48] Spas D. Stoychev, Alexander I. Kuleff, Francesco Tarantelli, and Lorenz S. Cederbaum. On the doubly ionized states of ar2 and their intra- and interatomic decay to ar23+. *The Journal of Chemical Physics*, 128(1):014307, 2008. doi: 10.1063/1.2814241. URL https://doi.org/10.1063/1.2814241.

[49] Ph. V. Demekhin, S. Scheit, S. D. Stoychev, and L. S. Cederbaum. Dynamics of interatomic coulombic decay in a ne dimer following the $k{-}L_1L_{2,3}(^1p)$ auger transition in the ne atom. *Phys. Rev. A*, 78:043421, Oct 2008. doi: 10.1103/PhysRevA.78.043421. URL https://link.aps.org/doi/10.1103/PhysRevA.78.043421.

[50] V. Averbukh, Ph.V. Demekhin, P. Kolorenč, S. Scheit, S.D. Stoychev, A.I. Kuleff, Y.-C. Chiang, K. Gokhberg, S. Kopelke, N. Sisourat, and L.S. Cederbaum. Interatomic electronic decay processes in singly and multiply ionized clusters. *Journal of Electron Spectroscopy and Related Phenomena*, 183(1):36–47, 2011. ISSN 0368-2048. doi: https://doi.org/10.1016/j.elspec.2010.03.003. URL https://www.sciencedirect.com/science/article/pii/S0368204810000484. Electron Spectroscopy Kai Siegbahn Memorial Volume.

[51] Kirill Gokhberg, Přemysl Kolorenč, Alexander I. Kuleff, and Lorenz S. Cederbaum. Site- and energy-selective slow-electron production through intermolecular coulombic decay. *Nature*, 505(7485):661–663, Jan 2014. ISSN 1476-4687. doi: 10.1038/nature12936. URL https://doi.org/10.1038/nature12936.

[52] Craig P. Schwartz, Shervin Fatehi, Richard J. Saykally, and David Prendergast. Importance of electronic relaxation for inter-coulombic decay in aqueous systems. *Phys. Rev. Lett.*, 105:198102, Nov 2010. doi: 10.1103/PhysRevLett.105.198102. URL https://link.aps.org/doi/10.1103/PhysRevLett.105.198102.

[53] Stephan Thürmer, Milan Ončák, Niklas Ottosson, Robert Seidel, Uwe Hergenhahn, Stephen E. Bradforth, Petr Slavíček, and Bernd Winter. On the nature and origin of dicationic, charge-separated species formed in liquid water on x-ray irradiation. *Nature Chemistry*, 5(7):590–596, Jul 2013. ISSN 1755-4349. doi: 10.1038/nchem.1680. URL https://doi.org/10.1038/nchem.1680.

[54] Petr Slavíček, Bernd Winter, Lorenz S. Cederbaum, and Nikolai V. Kryzhevoi. Proton-transfer mediated enhancement of nonlocal electronic relaxation processes in x-ray irradiated liquid water. *Journal of the American Chemical Society*, 136(52):18170–18176, Dec 2014. ISSN 0002-7863. doi: 10.1021/ja5117588. URL https://doi.org/10.1021/ja5117588.

[55] Petr Slavíček, Nikolai V. Kryzhevoi, Emad F. Aziz, and Bernd Winter. Relaxation processes in aqueous systems upon x-ray ionization: Entanglement of electronic and nuclear dynamics. *The Journal of Physical Chemistry Letters*, 7(2):234–243, 2016. doi: 10.1021/acs.jpclett.5b02665. URL https://doi.org/10.1021/acs.jpclett.5b02665. PMID: 26712083.

[56] Nikolai V. Kryzhevoi. Microhydration of lioh: Insight from electronic decays of core-ionized states. *The Journal of Chemical Physics*, 144(24):244302, 2016. doi: 10.1063/1.4954661. URL https://doi.org/10.1063/1.4954661.

[57] Nikolai V. Kryzhevoi and Lorenz S. Cederbaum. Nonlocal effects in the core ionization and auger spectra of small ammonia clusters. *The Journal of Physical Chemistry B*, 115(18):5441–5447, May 2011. ISSN 1520-6106. doi: 10.1021/jp109920p. URL https://doi.org/10.1021/jp109920p.

[58] Nikolai V. Kryzhevoi and Lorenz S. Cederbaum. Exploring protonation and deprotonation effects with auger electron spectroscopy. *The Journal of Physical Chemistry Letters*, 3(18):2733–2737, Sep 2012. doi: 10.1021/jz301130t. URL https://doi.org/10.1021/jz301130t.

[59] V. Stumpf, K. Gokhberg, and L. S. Cederbaum. The role of metal ions in x-ray-induced photochemistry. *Nature Chemistry*, 8(3):237–241, Mar 2016. ISSN 1755-4349. doi: 10.1038/nchem.2429. URL https://doi.org/10.1038/nchem.2429.

[60] Oliviero Carugo and Kristina Djinović Carugo. When x-rays modify the protein structure: radiation damage at work. *Trends in Biochemical Sciences*, 30(4):213–219, 2005. ISSN 0968-0004. doi: https://doi.org/10.1016/j.tibs.2005.02.009. URL https://www.sciencedirect.com/science/article/pii/S0968000405000575.

[61] Jürgen Zobeley, Robin Santra, and Lorenz S. Cederbaum. Electronic decay in weakly bound heteroclusters: Energy transfer versus electron transfer. *The Journal of Chemical Physics*, 115(11):5076–5088, 2001. doi: 10.1063/1.1395555. URL https://doi.org/10.1063/1.1395555.

[62] V. Stumpf, P. Kolorenč, K. Gokhberg, and L. S. Cederbaum. Efficient pathway to neutralization of multiply charged ions produced in auger processes. *Phys. Rev. Lett.*, 110:258302, Jun 2013. doi: 10.1103/PhysRevLett.110.258302. URL https://link.aps.org/doi/10.1103/PhysRevLett.110.258302.

[63] Christian Buth, Robin Santra, and Lorenz S. Cederbaum. Impact of interatomic electronic decay processes on xe 4d hole decay in the xenon fluorides. *The Journal of Chemical Physics*, 119(20):10575–10584, 2003. doi: 10.1063/1.1620502. URL https://doi.org/10.1063/1.1620502.

[64] Elke Faßhauer, Nikolai V. Kryzhevoi, and Markus Pernpointner. Possible electronic decay channels in the ionization spectra of small clusters composed of ar and xe: A four-component relativistic treatment. *The Journal of Chemical Physics*, 133 (1):014303, 2010. doi: 10.1063/1.3462246. URL https://doi.org/10.1063/1.3462246.

[65] V. Stumpf, N. V. Kryzhevoi, K. Gokhberg, and L. S. Cederbaum. Enhanced one-photon double ionization of atoms and molecules in an environment of different species. *Phys. Rev. Lett.*, 112:193001, May 2014. doi: 10.1103/PhysRevLett.112.193001. URL https://link.aps.org/doi/10.1103/PhysRevLett.112.193001.

[66] Aryya Ghosh, Lorenz S. Cederbaum, and Kirill Gokhberg. Electron transfer mediated decay in heli2 cluster: Potential energy surfaces and decay widths. *The*

Journal of Chemical Physics, 150(16):164309, 2019. doi: 10.1063/1.5082952. URL https://doi.org/10.1063/1.5082952.

[67] Vasili Stumpf, Simona Scheit, Přemysl Kolorenč, and Kirill Gokhberg. Electron transfer mediated decay in nexe triggered by k-ll auger decay of ne. *Chemical Physics*, 482:192–200, 2017. ISSN 0301-0104. doi: https://doi.org/10.1016/j.chemphys.2016.08.018. URL https://www.sciencedirect.com/science/article/pii/S0301010416305213. Electrons and nuclei in motion - correlation and dynamics in molecules (on the occasion of the 70th birthday of Lorenz S. Cederbaum).

[68] Imke B. Müller and Lorenz S. Cederbaum. Electronic decay following ionization of aqueous li+ microsolvation clusters. *The Journal of Chemical Physics*, 122 (9):094305, 2005. doi: 10.1063/1.1854118. URL https://doi.org/10.1063/1.1854118.

[69] S. Marburger, O. Kugeler, U. Hergenhahn, and T. Möller. Experimental evidence for interatomic coulombic decay in ne clusters. *Phys. Rev. Lett.*, 90:203401, May 2003. doi: 10.1103/PhysRevLett.90.203401. URL https://link.aps.org/doi/10.1103/PhysRevLett.90.203401.

[70] G. Öhrwall, M. Tchaplyguine, M. Lundwall, R. Feifel, H. Bergersen, T. Rander, A. Lindblad, J. Schulz, S. Peredkov, S. Barth, S. Marburger, U. Hergenhahn, S. Svensson, and O. Björneholm. Femtosecond interatomic coulombic decay in free neon clusters: Large lifetime differences between surface and bulk. *Phys. Rev. Lett.*, 93:173401, Oct 2004. doi: 10.1103/PhysRevLett.93.173401. URL https://link.aps.org/doi/10.1103/PhysRevLett.93.173401.

[71] S. Barth, S. Marburger, O. Kugeler, V. Ulrich, S. Joshi, A.M. Bradshaw, and U. Hergenhahn. The efficiency of interatomic coulombic decay in ne clusters. *Chemical Physics*, 329(1):246–250, 2006. ISSN 0301-0104. doi: https://doi.org/10.1016/j.chemphys.2006.06.035. URL https://www.sciencedirect.com/science/article/pii/S0301010406003636. Electron Correlation and Multimode Dynamics in Molecules.

[72] M. Förstel, T. Arion, and U. Hergenhahn. Measuring the efficiency of inter-

atomic coulombic decay in ne clusters. *Journal of Electron Spectroscopy and Related Phenomena*, 191:16–19, 2013. ISSN 0368-2048. doi: https://doi.org/10.1016/j.elspec.2013.11.002. URL https://www.sciencedirect.com/science/article/pii/S0368204813002065.

[73] Tiberiu Arion, Melanie Mucke, Marko Förstel, Alex M. Bradshaw, and Uwe Hergenhahn. Interatomic coulombic decay in mixed nekr clusters. *The Journal of Chemical Physics*, 134(7):074306, 2011. doi: 10.1063/1.3552082. URL https://doi.org/10.1063/1.3552082.

[74] Marko Förstel, Melanie Mucke, Tiberiu Arion, Alex M. Bradshaw, and Uwe Hergenhahn. Autoionization mediated by electron transfer. *Phys. Rev. Lett.*, 106:033402, Jan 2011. doi: 10.1103/PhysRevLett.106.033402. URL https://link.aps.org/doi/10.1103/PhysRevLett.106.033402.

[75] S. Barth, S. Joshi, S. Marburger, V. Ulrich, A. Lindblad, G. Öhrwall, O. Björneholm, and U. Hergenhahn. Observation of resonant interatomic coulombic decay in ne clusters. *The Journal of Chemical Physics*, 122(24):241102, 2005. doi: 10.1063/1.1937395. URL https://doi.org/10.1063/1.1937395.

[76] Emad F. Aziz, Niklas Ottosson, Manfred Faubel, Ingolf V. Hertel, and Bernd Winter. Interaction between liquid water and hydroxide revealed by core-hole de-excitation. *Nature*, 455(7209):89–91, Sep 2008. ISSN 1476-4687. doi: 10.1038/nature07252. URL https://doi.org/10.1038/nature07252.

[77] Wandared Pokapanich, Henrik Bergersen, Ioana L. Bradeanu, Ricardo R. T. Marinho, Andreas Lindblad, Sebastien Legendre, Aldana Rosso, Svante Svensson, Olle Björneholm , Maxim Tchaplyguine, Gunnar Öhrwall , Nikolai V. Kryzhevoi, and Lorenz S. Cederbaum. Auger electron spectroscopy as a probe of the solution of aqueous ions. *Journal of the American Chemical Society*, 131(21):7264–7271, 2009. doi: 10.1021/ja8096866. URL https://doi.org/10.1021/ja8096866.

[78] Matthew A. Brown, Manfred Faubel, and Bernd Winter. X-ray photo- and resonant auger-electron spectroscopy studies of liquid water and aqueous solutions. *Annu. Rep. Prog. Chem., Sect. C: Phys. Chem.*, 105:174–212, 2009. doi: 10.1039/B803023P. URL http://dx.doi.org/10.1039/B803023P.

[79] Wandared Pokapanich, Nikolai V. Kryzhevoi, Niklas Ottosson, Svante Svensson, Lorenz S. Cederbaum, Gunnar Öhrwall, and Olle Björneholm. Ionic-charge dependence of the intermolecular coulombic decay time scale for aqueous ions probed by the core-hole clock. *Journal of the American Chemical Society*, 133(34):13430–13436, 2011. doi: 10.1021/ja203430s. URL https://doi.org/10.1021/ja203430s. PMID: 21797195.

[80] Robert Seidel, Stephan Thürmer, and Bernd Winter. Photoelectron spectroscopy meets aqueous solution: Studies from a vacuum liquid microjet. *The Journal of Physical Chemistry Letters*, 2(6):633–641, Mar 2011. doi: 10.1021/jz101636y. URL https://doi.org/10.1021/jz101636y.

[81] Isaak Unger, Robert Seidel, Stephan Thürmer, Marvin N. Pohl, Emad F. Aziz, Lorenz S. Cederbaum, Eva Muchová, Petr Slavíček, Bernd Winter, and Nikolai V. Kryzhevoi. Observation of electron-transfer-mediated decay in aqueous solution. *Nature Chemistry*, 9(7):708–714, Jul 2017. ISSN 1755-4349. doi: 10.1038/nchem.2727. URL https://doi.org/10.1038/nchem.2727.

[82] Marvin N. Pohl, Clemens Richter, Evgeny Lugovoy, Robert Seidel, Petr Slavíček, Emad F. Aziz, Bernd Abel, Bernd Winter, and Uwe Hergenhahn. Sensitivity of electron transfer mediated decay to ion pairing. *The Journal of Physical Chemistry B*, 121(32):7709–7714, 2017. doi: 10.1021/acs.jpcb.7b06061. URL https://doi.org/10.1021/acs.jpcb.7b06061. PMID: 28696722.

[83] T. Jahnke, A. Czasch, M. S. Schöffler, S. Schössler, A. Knapp, M. Käsz, J. Titze, C. Wimmer, K. Kreidi, R. E. Grisenti, A. Staudte, O. Jagutzki, U. Hergenhahn, H. Schmidt-Böcking, and R. Dörner. Experimental observation of interatomic coulombic decay in neon dimers. *Phys. Rev. Lett.*, 93:163401, Oct 2004. doi: 10.1103/PhysRevLett.93.163401. URL https://link.aps.org/doi/10.1103/PhysRevLett.93.163401.

[84] T. Jahnke, A. Czasch, M. Schöffler, S. Schössler, M. Käsz, J. Titze, K. Kreidi, R. E. Grisenti, A. Staudte, O. Jagutzki, L. Ph. H. Schmidt, Th. Weber, H. Schmidt-Böcking, K. Ueda, and R. Dörner. Experimental separation of virtual photon exchange and electron transfer in interatomic coulombic decay of neon dimers.

Phys. Rev. Lett., 99:153401, Oct 2007. doi: 10.1103/PhysRevLett.99.153401. URL https://link.aps.org/doi/10.1103/PhysRevLett.99.153401.

[85] T. Havermeier, T. Jahnke, K. Kreidi, R. Wallauer, S. Voss, M. Schöffler, S. Schössler, L. Foucar, N. Neumann, J. Titze, H. Sann, M. Kühnel, J. Voigtsberger, J. H. Morilla, W. Schöllkopf, H. Schmidt-Böcking, R. E. Grisenti, and R. Dörner. Interatomic coulombic decay following photoionization of the helium dimer: Observation of vibrational structure. *Phys. Rev. Lett.*, 104:133401, Mar 2010. doi: 10.1103/PhysRevLett.104.133401. URL https://link.aps.org/doi/10.1103/PhysRevLett.104.133401.

[86] F. Trinter, J. B. Williams, M. Weller, M. Waitz, M. Pitzer, J. Voigtsberger, C. Schober, G. Kastirke, C. Müller, C. Goihl, P. Burzynski, F. Wiegandt, T. Bauer, R. Wallauer, H. Sann, A. Kalinin, L. Ph. H. Schmidt, M. Schöffler, N. Sisourat, and T. Jahnke. Evolution of interatomic coulombic decay in the time domain. *Phys. Rev. Lett.*, 111:093401, Aug 2013. doi: 10.1103/PhysRevLett.111.093401. URL https://link.aps.org/doi/10.1103/PhysRevLett.111.093401.

[87] F. Trinter, J. B. Williams, M. Weller, M. Waitz, M. Pitzer, J. Voigtsberger, C. Schober, G. Kastirke, C. Müller, C. Goihl, P. Burzynski, F. Wiegandt, R. Wallauer, A. Kalinin, L. Ph. H. Schmidt, M. S. Schöffler, Y.-C. Chiang, K. Gokhberg, T. Jahnke, and R. Dörner. Vibrationally resolved decay width of interatomic coulombic decay in hene. *Phys. Rev. Lett.*, 111:233004, Dec 2013. doi: 10.1103/PhysRevLett.111.233004. URL https://link.aps.org/doi/10.1103/PhysRevLett.111.233004.

[88] T. Aoto, K. Ito, Y. Hikosaka, E. Shigemasa, F. Penent, and P. Lablanquie. Properties of resonant interatomic coulombic decay in ne dimers. *Phys. Rev. Lett.*, 97:243401, Dec 2006. doi: 10.1103/PhysRevLett.97.243401. URL https://link.aps.org/doi/10.1103/PhysRevLett.97.243401.

[89] A. Mhamdi, J. Rist, D. Aslitürk, M. Weller, N. Melzer, D. Trabert, M. Kircher, I. Vela-Pérez, J. Siebert, S. Eckart, S. Grundmann, G. Kastirke, M. Waitz, A. Khan, M. S. Schöffler, F. Trinter, R. Dörner, T. Jahnke, and Ph. V. Demekhin. Breakdown of the spectator concept in low-electron-energy resonant decay processes. *Phys.*

Rev. Lett., 121:243002, Dec 2018. doi: 10.1103/PhysRevLett.121.243002. URL https://link.aps.org/doi/10.1103/PhysRevLett.121.243002.

[90] P. Lablanquie, T. Aoto, Y. Hikosaka, Y. Morioka, F. Penent, and K. Ito. Appearance of interatomic coulombic decay in ar, kr, and xe homonuclear dimers. *The Journal of Chemical Physics*, 127(15):154323, 2007. doi: 10.1063/1.2778430. URL https://doi.org/10.1063/1.2778430.

[91] K. Sakai, S. Stoychev, T. Ouchi, I. Higuchi, M. Schöffler, T. Mazza, H. , K. Nagaya, M. Yao, Y. Tamenori, A. I. Kuleff, N. Saito, and K. Ueda. Electron-transfer-mediated decay and interatomic coulombic decay from the triply ionized states in argon dimers. *Phys. Rev. Lett.*, 106:033401, Jan 2011. doi: 10.1103/PhysRevLett.106.033401. URL https://link.aps.org/doi/10.1103/PhysRevLett.106.033401.

[92] M. Hoener, D. Rolles, A. Aguilar, R. C. Bilodeau, D. Esteves, P. Olalde Velasco, Z. D. Pešić, E. Red, and N. Berrah. Site-selective ionization and relaxation dynamics in heterogeneous nanosystems. *Phys. Rev. A*, 81:021201, Feb 2010. doi: 10.1103/PhysRevA.81.021201. URL https://link.aps.org/doi/10.1103/PhysRevA.81.021201.

[93] Razib Obaid, Hui Xiong, Sven Augustin, Kirsten Schnorr, Utuq Ablikim, Andrea Battistoni, Thomas J. A. Wolf, René C. Bilodeau, Timur Osipov, Kirill Gokhberg, Daniel Rolles, Aaron C. LaForge, and Nora Berrah. Intermolecular coulombic decay in endohedral fullerene at the $4d \rightarrow 4f$ resonance. *Phys. Rev. Lett.*, 124:113002, Mar 2020. doi: 10.1103/PhysRevLett.124.113002. URL https://link.aps.org/doi/10.1103/PhysRevLett.124.113002.

[94] Andreas Hans, Philipp Schmidt, Christian Ozga, Clemens Richter, Huda Otto, Xaver Holzapfel, Gregor Hartmann, Arno Ehresmann, Uwe Hergenhahn, and André Knie. Efficient fluorescence quenching by distant production of a free electron. *The Journal of Physical Chemistry Letters*, 10(5):1078–1082, Mar 2019. doi: 10.1021/acs.jpclett.9b00124. URL https://doi.org/10.1021/acs.jpclett.9b00124.

[95] André Knie, Andreas Hans, Marko Förstel, Uwe Hergenhahn, Philipp Schmidt, Philipp Reiß, Christian Ozga, Benjamin Kambs, Florian Trinter, Jörg Voigtsberger, Daniel Metz, Till Jahnke, Reinhard Dörner, Alexander I Kuleff, Lorenz S Ceder-

baum, Philipp V Demekhin, and Arno Ehresmann. Detecting ultrafast interatomic electronic processes in media by fluorescence. *New Journal of Physics*, 16(10):102002, oct 2014. doi: 10.1088/1367-2630/16/10/102002. URL https://doi.org/10.1088/1367-2630/16/10/102002.

[96] Andreas Hans, Catmarna Küstner-Wetekam, Philipp Schmidt, Christian Ozga, Xaver Holzapfel, Huda Otto, Christina Zindel, Clemens Richter, Lorenz S. Cederbaum, Arno Ehresmann, Uwe Hergenhahn, Nikolai V. Kryzhevoi, and André Knie. Core-level interatomic coulombic decay in van der waals clusters. *Phys. Rev. Research*, 2:012022, Jan 2020. doi: 10.1103/PhysRevResearch.2.012022. URL https://link.aps.org/doi/10.1103/PhysRevResearch.2.012022.

[97] Y. Morishita, X.-J. Liu, N. Saito, T. Lischke, M. Kato, G. Prümper, M. Oura, H. Yamaoka, Y. Tamenori, I. H. Suzuki, and K. Ueda. Experimental evidence of interatomic coulombic decay from the auger final states in argon dimers. *Phys. Rev. Lett.*, 96:243402, Jun 2006. doi: 10.1103/PhysRevLett.96.243402. URL https://link.aps.org/doi/10.1103/PhysRevLett.96.243402.

[98] K. Ueda, X.-J. Liu, G. Prümper, H. Fukuzawa, Y. Morishita, and N. Saito. Electron–ion coincidence momentum spectroscopy: Its application to ar dimer interatomic decay. *Journal of Electron Spectroscopy and Related Phenomena*, 155(1):113 – 118, 2007. ISSN 0368-2048. doi: https://doi.org/10.1016/j.elspec.2006.10.007. URL http://www.sciencedirect.com/science/article/pii/S0368204806001228. Scattering, Coincidence and Absorption Studies of Molecules.

[99] Norio Saito, Xiao Jing Liu, Yuichiro Morishita, Isao H. Suzuki, and Kiyoshi Ueda. Electron–ion multiple coincidence spectroscopy for small molecules and clusters. *Journal of Electron Spectroscopy and Related Phenomena*, 156-158:68–72, 2007. ISSN 0368-2048. doi: https://doi.org/10.1016/j.elspec.2006.11.048. URL https://www.sciencedirect.com/science/article/pii/S0368204806001964. Electronic Spectroscopy and Structure: ICESS-10.

[100] K. Ueda, H. Fukuzawa, X.-J. Liu, K. Sakai, G. Prümper, Y. Morishita, N. Saito, I.H. Suzuki, K. Nagaya, H. Iwayama, M. Yao, K. Kreidi, M. Schöffler, T. Jahnke, S. Schössler, R. Dörner, Th. Weber, J. Harries, and Y. Tamenori.

Interatomic coulombic decay following the auger decay: Experimental evidence in rare-gas dimers. *Journal of Electron Spectroscopy and Related Phenomena*, 166-167:3–10, 2008. ISSN 0368-2048. doi: https://doi.org/10.1016/j.elspec.2008.03.002. URL https://www.sciencedirect.com/science/article/pii/S0368204808000236. Clusters and Nanoparticles Studied by Short-Wavelength Radiation.

[101] Y Morishita, N Saito, I H Suzuki, H Fukuzawa, X-J Liu, K Sakai, G Prümper, K Ueda, H Iwayama, K Nagaya, M Yao, K Kreidi, M Schöffler, T Jahnke, S Schössler, R Dörner, T Weber, J Harries, and Y Tamenori. Evidence of interatomic coulombic decay in ArKr after ar 2p auger decay. *Journal of Physics B: Atomic, Molecular and Optical Physics*, 41(2):025101, jan 2008. doi: 10.1088/0953-4075/41/2/025101. URL https://doi.org/10.1088/0953-4075/41/2/025101.

[102] Kiyoshi Ueda. Photoemission and coincidence studies on gas-phase molecules. *Applied Physics A*, 92(3):487–494, Aug 2008. ISSN 1432-0630. doi: 10.1007/s00339-008-4552-9. URL https://doi.org/10.1007/s00339-008-4552-9.

[103] K. Kreidi, T. Jahnke, Th. Weber, T. Havermeier, X. Liu, Y. Morisita, S. Schössler, L. Ph. H. Schmidt, M. Schöffler, M. Odenweller, N. Neumann, L. Foucar, J. Titze, B. Ulrich, F. Sturm, C. Stuck, R. Wallauer, S. Voss, I. Lauter, H. K. Kim, M. Rudloff, H. Fukuzawa, G. Prümper, N. Saito, K. Ueda, A. Czasch, O. Jagutzki, H. Schmidt-Böcking, S. Stoychev, Ph. V. Demekhin, and R. Dörner. Relaxation processes following 1s photoionization and auger decay in ne_2. *Phys. Rev. A*, 78:043422, Oct 2008. doi: 10.1103/PhysRevA.78.043422. URL https://link.aps.org/doi/10.1103/PhysRevA.78.043422.

[104] T. Ouchi, K. Sakai, H. Fukuzawa, I. Higuchi, Ph. V. Demekhin, Y.-C. Chiang, S. D. Stoychev, A. I. Kuleff, T. Mazza, M. Schöffler, K. Nagaya, M. Yao, Y. Tamenori, N. Saito, and K. Ueda. Interatomic coulombic decay following ne 1s auger decay in near. *Phys. Rev. A*, 83:053415, May 2011. doi: 10.1103/PhysRevA.83.053415. URL https://link.aps.org/doi/10.1103/PhysRevA.83.053415.

[105] R. W. Dunford, S. H. Southworth, D. Ray, E. P. Kanter, B. Krässig, L. Young, D. A. Arms, E. M. Dufresne, D. A. Walko, O. Vendrell, S.-K. Son, and R. Santra. Evidence for interatomic coulombic decay in xe k-shell-vacancy decay of xef_2. *Phys.*

Rev. A, 86:033401, Sep 2012. doi: 10.1103/PhysRevA.86.033401. URL https://link.aps.org/doi/10.1103/PhysRevA.86.033401.

[106] Miku Kimura, Hironobu Fukuzawa, Tetsuya Tachibana, Yuta Ito, Subhendu Mondal, Misaki Okunishi, Markus Schöffler, Joshua Williams, Yuhai Jiang, Yusuke Tamenori, Norio Saito, and Kiyoshi Ueda. Controlling low-energy electron emission via resonant-auger-induced interatomic coulombic decay. *The Journal of Physical Chemistry Letters*, 4(11):1838–1842, Jun 2013. doi: 10.1021/jz4006674. URL https://doi.org/10.1021/jz4006674.

[107] Patrick O'Keeffe, Enrico Ripani, Paola Bolognesi, Marcello Coreno, Michele Devetta, Carlo Callegari, Michele Di Fraia, Kevin Charles Prince, Robert Richter, Michele Alagia, Antti Kivimäki, and Lorenzo Avaldi. The role of the partner atom and resonant excitation energy in interatomic coulombic decay in rare gas dimers. *The Journal of Physical Chemistry Letters*, 4(11):1797–1801, Jun 2013. doi: 10.1021/jz400671h. URL https://doi.org/10.1021/jz400671h.

[108] F. Trinter, M. S. Schöffler, H.-K. Kim, F. P. Sturm, K. Cole, N. Neumann, A. Vredenborg, J. Williams, I. Bocharova, R. Guillemin, M. Simon, A. Belkacem, A. L. Landers, Th. Weber, H. Schmidt-Böcking, R. Dörner, and T. Jahnke. Resonant auger decay driving intermolecular coulombic decay in molecular dimers. *Nature*, 505(7485):664–666, Jan 2014. ISSN 1476-4687. doi: 10.1038/nature12927. URL https://doi.org/10.1038/nature12927.

[109] B. Ulrich, A. Vredenborg, A. Malakzadeh, M. Meckel, K. Cole, M. Smolarski, Z. Chang, T. Jahnke, and R. Dörner. Double-ionization mechanisms of the argon dimer in intense laser fields. *Phys. Rev. A*, 82:013412, Jul 2010. doi: 10.1103/PhysRevA.82.013412. URL https://link.aps.org/doi/10.1103/PhysRevA.82.013412.

[110] Philipp V. Demekhin, Spas D. Stoychev, Alexander I. Kuleff, and Lorenz S. Cederbaum. Exploring interatomic coulombic decay by free electron lasers. *Phys. Rev. Lett.*, 107:273002, Dec 2011. doi: 10.1103/PhysRevLett.107.273002. URL https://link.aps.org/doi/10.1103/PhysRevLett.107.273002.

[111] A Dubrouil, M Reduzzi, M Devetta, C Feng, J Hummert, P Finetti, O Plekan,

C Grazioli, M Di Fraia, V Lyamayev, A La Forge, R Katzy, F Stienkemeier, Y Ovcharenko, M Coreno, N Berrah, K Motomura, S Mondal, K Ueda, K C Prince, C Callegari, A I Kuleff, Ph V Demekhin, and G Sansone. Two-photon resonant excitation of interatomic coulombic decay in neon dimers. *Journal of Physics B: Atomic, Molecular and Optical Physics*, 48(20):204005, sep 2015. doi: 10.1088/0953-4075/48/20/204005. URL `https://doi.org/10.1088/0953-4075/48/20/204005`.

[112] Alexander I. Kuleff, Kirill Gokhberg, Sören Kopelke, and Lorenz S. Cederbaum. Ultrafast interatomic electronic decay in multiply excited clusters. *Phys. Rev. Lett.*, 105:043004, Jul 2010. doi: 10.1103/PhysRevLett.105.043004. URL `https://link.aps.org/doi/10.1103/PhysRevLett.105.043004`.

[113] D. Iablonskyi, K. Nagaya, H. Fukuzawa, K. Motomura, Y. Kumagai, S. Mondal, T. Tachibana, T. Takanashi, T. Nishiyama, K. Matsunami, P. Johnsson, P. Piseri, G. Sansone, A. Dubrouil, M. Reduzzi, P. Carpeggiani, C. Vozzi, M. Devetta, M. Negro, F. Calegari, A. Trabattoni, M. C. Castrovilli, D. Faccialà, Y. Ovcharenko, T. Möller, M. Mudrich, F. Stienkemeier, M. Coreno, M. Alagia, B. Schütte, N. Berrah, A. I. Kuleff, G. Jabbari, C. Callegari, O. Plekan, P. Finetti, C. Spezzani, E. Ferrari, E. Allaria, G. Penco, C. Serpico, G. De Ninno, I. Nikolov, B. Diviacco, S. Di Mitri, L. Giannessi, K. C. Prince, and K. Ueda. Slow interatomic coulombic decay of multiply excited neon clusters. *Phys. Rev. Lett.*, 117:276806, Dec 2016. doi: 10.1103/PhysRevLett.117.276806. URL `https://link.aps.org/doi/10.1103/PhysRevLett.117.276806`.

[114] T. Takanashi, N. V. Golubev, C. Callegari, H. Fukuzawa, K. Motomura, D. Iablonskyi, Y. Kumagai, S. Mondal, T. Tachibana, K. Nagaya, T. Nishiyama, K. Matsunami, P. Johnsson, P. Piseri, G. Sansone, A. Dubrouil, M. Reduzzi, P. Carpeggiani, C. Vozzi, M. Devetta, M. Negro, D. Faccialà, F. Calegari, A. Trabattoni, M. C. Castrovilli, Y. Ovcharenko, M. Mudrich, F. Stienkemeier, M. Coreno, M. Alagia, B. Schütte, N. Berrah, O. Plekan, P. Finetti, C. Spezzani, E. Ferrari, E. Allaria, G. Penco, C. Serpico, G. De Ninno, B. Diviacco, S. Di Mitri, L. Giannessi, G. Jabbari, K. C. Prince, L. S. Cederbaum, Ph. V. Demekhin, A. I. Kuleff, and K. Ueda. Time-resolved measurement of interatomic coulombic decay induced by two-photon double excitation of ne_2. *Phys. Rev. Lett.*, 118:033202, Jan

2017. doi: 10.1103/PhysRevLett.118.033202. URL https://link.aps.org/doi/10.1103/PhysRevLett.118.033202.

[115] Saroj Barik, Saurav Dutta, Nihar Ranjan Behera, Rajesh Kumar Kushawaha, Y. Sajeev, and G. Aravind. Ambient-light-induced intermolecular coulombic decay in unbound pyridine monomers. *Nature Chemistry*, Jul 2022. ISSN 1755-4349. doi: 10.1038/s41557-022-01002-2. URL https://doi.org/10.1038/s41557-022-01002-2.

[116] Alexander I. Kuleff and Lorenz S. Cederbaum. Tracing ultrafast interatomic electronic decay processes in real time and space. *Phys. Rev. Lett.*, 98:083201, Feb 2007. doi: 10.1103/PhysRevLett.98.083201. URL https://link.aps.org/doi/10.1103/PhysRevLett.98.083201.

[117] Qingli Jing and Lars Bojer Madsen. Dynamics of interatomic coulombic decay in neon dimers by xuv-pump–xuv-probe spectroscopy. *Phys. Rev. A*, 99:013409, Jan 2019. doi: 10.1103/PhysRevA.99.013409. URL https://link.aps.org/doi/10.1103/PhysRevA.99.013409.

[118] K. Schnorr, A. Senftleben, M. Kurka, A. Rudenko, L. Foucar, G. Schmid, A. Broska, T. Pfeifer, K. Meyer, D. Anielski, R. Boll, D. Rolles, M. Kübel, M. F. Kling, Y. H. Jiang, S. Mondal, T. Tachibana, K. Ueda, T. Marchenko, M. Simon, G. Brenner, R. Treusch, S. Scheit, V. Averbukh, J. Ullrich, C. D. Schröter, and R. Moshammer. Time-resolved measurement of interatomic coulombic decay in ne_2. *Phys. Rev. Lett.*, 111:093402, Aug 2013. doi: 10.1103/PhysRevLett.111.093402. URL https://link.aps.org/doi/10.1103/PhysRevLett.111.093402.

[119] U. Frühling, F. Trinter, F. Karimi, J.B. Williams, and T. Jahnke. Time-resolved studies of interatomic coulombic decay. *Journal of Electron Spectroscopy and Related Phenomena*, 204:237–244, 2015. ISSN 0368-2048. doi: https://doi.org/10.1016/j.elspec.2015.06.012. URL https://www.sciencedirect.com/science/article/pii/S0368204815001425. Gas phase spectroscopic and dynamical studies at Free-Electron Lasers and other short wavelength sources.

[120] J. Titze, M. S. Schöffler, H.-K. Kim, F. Trinter, M. Waitz, J. Voigtsberger, N. Neumann, B. Ulrich, K. Kreidi, R. Wallauer, M. Odenweller, T. Havermeier,

S. Schössler, M. Meckel, L. Foucar, T. Jahnke, A. Czasch, L. Ph. H. Schmidt, O. Jagutzki, R. E. Grisenti, H. Schmidt-Böcking, H. J. Lüdde, and R. Dörner. Ionization dynamics of helium dimers in fast collisions with he^{++}. *Phys. Rev. Lett.*, 106:033201, Jan 2011. doi: 10.1103/PhysRevLett.106.033201. URL `https://link.aps.org/doi/10.1103/PhysRevLett.106.033201`.

[121] H.-K. Kim, H. Gassert, M. S. Schöffler, J. N. Titze, M. Waitz, J. Voigtsberger, F. Trinter, J. Becht, A. Kalinin, N. Neumann, C. Zhou, L. Ph. H. Schmidt, O. Jagutzki, A. Czasch, H. Merabet, H. Schmidt-Böcking, T. Jahnke, A. Cassimi, and R. Dörner. Ion-impact-induced interatomic coulombic decay in neon and argon dimers. *Phys. Rev. A*, 88:042707, Oct 2013. doi: 10.1103/PhysRevA.88.042707. URL `https://link.aps.org/doi/10.1103/PhysRevA.88.042707`.

[122] W. Iskandar, J. Matsumoto, A. Leredde, X. Fléchard, B. Gervais, S. Guillous, D. Hennecart, A. Méry, J. Rangama, C. L. Zhou, H. Shiromaru, and A. Cassimi. Interatomic coulombic decay as a new source of low energy electrons in slow ion-dimer collisions. *Phys. Rev. Lett.*, 114:033201, Jan 2015. doi: 10.1103/PhysRevLett.114.033201. URL `https://link.aps.org/doi/10.1103/PhysRevLett.114.033201`.

[123] Dyuman Bhattacharya and Tom Kirchner. Strengthening the case for interatomic coulomb decay as a subdominant reaction channel in slow $o^{3+}-ne_2$ collisions with independent-atom-model coupled-channel calculations. *Phys. Rev. A*, 102:062816, Dec 2020. doi: 10.1103/PhysRevA.102.062816. URL `https://link.aps.org/doi/10.1103/PhysRevA.102.062816`.

[124] S. Yan, P. Zhang, X. Ma, S. Xu, B. Li, X. L. Zhu, W. T. Feng, S. F. Zhang, D. M. Zhao, R. T. Zhang, D. L. Guo, and H. P. Liu. Observation of interatomic coulombic decay and electron-transfer-mediated decay in high-energy electron-impact ionization of ar_2. *Phys. Rev. A*, 88:042712, Oct 2013. doi: 10.1103/PhysRevA.88.042712. URL `https://link.aps.org/doi/10.1103/PhysRevA.88.042712`.

[125] Xueguang Ren, Elias Jabbour Al Maalouf, Alexander Dorn, and Stephan Denifl. Direct evidence of two interatomic relaxation mechanisms in argon dimers ionized by electron impact. *Nature Communications*, 7(1):11093, Mar 2016. ISSN 2041-1723. doi: 10.1038/ncomms11093. URL `https://doi.org/10.1038/ncomms11093`.

[126] Xueguang Ren, Tsveta Miteva, P řemysl Kolorenč, Kirill Gokhberg, Alexander I. Kuleff, Lorenz S. Cederbaum, and Alexander Dorn. Observation of fast and slow interatomic coulombic decay in argon dimers induced by electron-impact ionization. *Phys. Rev. A*, 96:032715, Sep 2017. doi: 10.1103/PhysRevA.96.032715. URL https://link.aps.org/doi/10.1103/PhysRevA.96.032715.

[127] S. Yan, P. Zhang, V. Stumpf, K. Gokhberg, X. C. Zhang, S. Xu, B. Li, L. L. Shen, X. L. Zhu, W. T. Feng, S. F. Zhang, D. M. Zhao, and X. Ma. Interatomic relaxation processes induced in neon dimers by electron-impact ionization. *Phys. Rev. A*, 97:010701, Jan 2018. doi: 10.1103/PhysRevA.97.010701. URL https://link.aps.org/doi/10.1103/PhysRevA.97.010701.

[128] S. Yan, X. L. Zhu, S. F. Zhang, D. M. Zhao, P. Zhang, B. Wei, and X. Ma. Enhanced damage induced by secondary high-energy electrons. *Phys. Rev. A*, 102:032809, Sep 2020. doi: 10.1103/PhysRevA.102.032809. URL https://link.aps.org/doi/10.1103/PhysRevA.102.032809.

[129] Spas D. Stoychev, Alexander I. Kuleff, and Lorenz S. Cederbaum. On the intermolecular coulombic decay of singly and doubly ionized states of water dimer. *The Journal of Chemical Physics*, 133(15):154307, 2010. doi: 10.1063/1.3499317. URL https://doi.org/10.1063/1.3499317.

[130] Oriol Vendrell, Spas D. Stoychev, and Lorenz S. Cederbaum. Generation of highly damaging h2o+ radicals by inner valence shell ionization of water. *ChemPhysChem*, 11(5):1006–1009, 2010. doi: 10.1002/cphc.201000034. URL https://chemistry-europe.onlinelibrary.wiley.com/doi/abs/10.1002/cphc.201000034.

[131] Spas D. Stoychev, Alexander I. Kuleff, and Lorenz S. Cederbaum. Intermolecular coulombic decay in small biochemically relevant hydrogen-bonded systems. *Journal of the American Chemical Society*, 133(17):6817–6824, 2011. doi: 10.1021/ja200963y. URL https://doi.org/10.1021/ja200963y. PMID: 21486035.

[132] Ondřej Svoboda, Daniel Hollas, Milan Ončák, and Petr Slavíček. Reaction selectivity in an ionized water dimer: nonadiabatic ab initio dynamics simulations.

Phys. Chem. Chem. Phys., 15:11531–11542, 2013. doi: 10.1039/C3CP51440D. URL http://dx.doi.org/10.1039/C3CP51440D.

[133] T. Jahnke, H. Sann, T. Havermeier, K. Kreidi, C. Stuck, M. Meckel, M. Schöffler, N. Neumann, R. Wallauer, S. Voss, A. Czasch, O. Jagutzki, A. Malakzadeh, F. Afaneh, Th. Weber, H. Schmidt-Böcking, and R. Dörner. Ultrafast energy transfer between water molecules. *Nature Physics*, 6(2):139–142, Feb 2010. ISSN 1745-2481. doi: 10.1038/nphys1498. URL https://doi.org/10.1038/nphys1498.

[134] Melanie Mucke, Markus Braune, Silko Barth, Marko Förstel, Toralf Lischke, Volker Ulrich, Tiberiu Arion, Uwe Becker, Alex Bradshaw, and Uwe Hergenhahn. A hitherto unrecognized source of low-energy electrons in water. *Nature Physics*, 6 (2):143–146, Feb 2010. ISSN 1745-2481. doi: 10.1038/nphys1500. URL https://doi.org/10.1038/nphys1500.

[135] Pengju Zhang, Conaill Perry, Tran Trung Luu, Danylo Matselyukh, and Hans Jakob Wörner. Intermolecular coulombic decay in liquid water. *Phys. Rev. Lett.*, 128: 133001, Apr 2022. doi: 10.1103/PhysRevLett.128.133001. URL https://link.aps.org/doi/10.1103/PhysRevLett.128.133001.

[136] Badia Boudaıffa, Pierre Cloutier, Darel Hunting, Michael A. Huels, and Léon Sanche. Resonant formation of dna strand breaks by low-energy (3 to 20 ev) electrons. *Science*, 287(5458):1658–1660, 2000. ISSN 0036-8075. doi: 10.1126/science.287.5458.1658. URL https://science.sciencemag.org/content/287/5458/1658.

[137] Hong-Keun Kim, Jasmin Titze, Markus Schöffler, Florian Trinter, Markus Waitz, Jörg Voigtsberger, Hendrik Sann, Moritz Meckel, Christian Stuck, Ute Lenz, Matthias Odenweller, Nadine Neumann, Sven Schössler, Klaus Ullmann-Pfleger, Birte Ulrich, Rui Costa Fraga, Nikos Petridis, Daniel Metz, Annika Jung, Robert Grisenti, Achim Czasch, Ottmar Jagutzki, Lothar Schmidt, Till Jahnke, Horst Schmidt-Böcking, and Reinhard Dörner. Enhanced production of low energy electrons by alpha particle impact. *Proceedings of the National Academy of Sciences*, 108(29):11821–11824, 2011. ISSN 0027-8424. doi: 10.1073/pnas.1104382108. URL https://www.pnas.org/content/108/29/11821.

[138] Philipp H. P. Harbach, Matthias Schneider, Shirin Faraji, and Andreas Dreuw. Intermolecular coulombic decay in biology: The initial electron detachment from fadh– in dna photolyases. *The Journal of Physical Chemistry Letters*, 4(6):943–949, 2013. doi: 10.1021/jz400104h. URL https://doi.org/10.1021/jz400104h. PMID: 26291360.

[139] Shirin Faraji and Andreas Dreuw. Physicochemical mechanism of light-driven dna repair by (6-4) photolyases. *Annual Review of Physical Chemistry*, 65(1):275–292, 2014. doi: 10.1146/annurev-physchem-040513-103626. URL https://doi.org/10.1146/annurev-physchem-040513-103626. PMID: 24364918.

[140] Elahe Alizadeh, Thomas M. Orlando, and Léon Sanche. Biomolecular damage induced by ionizing radiation: The direct and indirect effects of low-energy electrons on dna. *Annual Review of Physical Chemistry*, 66(1):379–398, 2015. doi: 10.1146/annurev-physchem-040513-103605. URL https://doi.org/10.1146/annurev-physchem-040513-103605. PMID: 25580626.

[141] Xueguang Ren, Enliang Wang, Anna D. Skitnevskaya, Alexander B. Trofimov, Kirill Gokhberg, and Alexander Dorn. Experimental evidence for ultrafast intermolecular relaxation processes in hydrated biomolecules. *Nature Physics*, 14(10):1062–1066, Oct 2018. ISSN 1745-2481. doi: 10.1038/s41567-018-0214-9. URL https://doi.org/10.1038/s41567-018-0214-9.

[142] Xueguang Ren, Jiaqi Zhou, Enliang Wang, Tao Yang, Zhongfeng Xu, Nicolas Sisourat, Thomas Pfeifer, and Alexander Dorn. Ultrafast energy transfer between π-stacked aromatic rings upon inner-valence ionization. *Nature Chemistry*, 14(2):232–238, Feb 2022. ISSN 1755-4349. doi: 10.1038/s41557-021-00838-4. URL https://doi.org/10.1038/s41557-021-00838-4.

[143] Jiaqi Zhou, Xitao Yu, Sizuo Luo, Xiaorui Xue, Shaokui Jia, Xinyu Zhang, Yongtao Zhao, Xintai Hao, Lanhai He, Chuncheng Wang, Dajun Ding, and Xueguang Ren. Triple ionization and fragmentation of benzene trimers following ultrafast intermolecular coulombic decay. *Nature Communications*, 13(1):5335, Sep 2022. ISSN 2041-1723. doi: 10.1038/s41467-022-33032-2. URL https://doi.org/10.1038/s41467-022-33032-2.

[144] Annika Bande, Kirill Gokhberg, and Lorenz S. Cederbaum. Dynamics of interatomic coulombic decay in quantum dots. *The Journal of Chemical Physics*, 135 (14):144112, 2011. doi: 10.1063/1.3646205. URL https://doi.org/10.1063/1.3646205.

[145] Tamar Goldzak, Liron Gantz, Ido Gilary, Gad Bahir, and Nimrod Moiseyev. Interatomic coulombic decay in two coupled quantum wells. *Phys. Rev. B*, 91:165312, Apr 2015. doi: 10.1103/PhysRevB.91.165312. URL https://link.aps.org/doi/10.1103/PhysRevB.91.165312.

[146] U. Hergenhahn. Interatomic and intermolecular coulombic decay: The early years. *Journal of Electron Spectroscopy and Related Phenomena*, 184(3):78 – 90, 2011. ISSN 0368-2048. doi: https://doi.org/10.1016/j.elspec.2010.12.020. URL http://www.sciencedirect.com/science/article/pii/S0368204810002914.

[147] T Jahnke. Interatomic and intermolecular coulombic decay: the coming of age story. *Journal of Physics B: Atomic, Molecular and Optical Physics*, 48(8):082001, 2015. doi: 10.1088/0953-4075/48/8/082001. URL https://doi.org/10.1088%2F0953-4075%2F48%2F8%2F082001.

[148] Till Jahnke, Uwe Hergenhahn, Bernd Winter, Reinhard Dörner, Ulrike Frühling, Philipp V. Demekhin, Kirill Gokhberg, Lorenz S. Cederbaum, Arno Ehresmann, André Knie, and Andreas Dreuw. Interatomic and intermolecular coulombic decay. *Chemical Reviews*, 120(20):11295–11369, 2020. doi: 10.1021/acs.chemrev.0c00106. URL https://doi.org/10.1021/acs.chemrev.0c00106.

[149] A. Mauracher, O. Echt, A.M. Ellis, S. Yang, D.K. Bohme, J. Postler, A. Kaiser, S. Denifl, and P. Scheier. Cold physics and chemistry: Collisions, ionization and reactions inside helium nanodroplets close to zero k. *Physics Reports*, 751:1–90, 2018. ISSN 0370-1573. doi: https://doi.org/10.1016/j.physrep.2018.05.001. URL https://www.sciencedirect.com/science/article/pii/S0370157318301182.

[150] Slava Grebenev, J. Peter Toennies, and Andrei F. Vilesov. Superfluidity within a small helium-4 cluster: The microscopic andronikashvili experiment. *Science*, 279 (5359):2083–2086, 1998. doi: 10.1126/science.279.5359.2083. URL https://www.science.org/doi/abs/10.1126/science.279.5359.2083.

[151] J. Peter Toennies and Andrey F. Vilesov. Superfluid helium droplets: A uniquely cold nanomatrix for molecules and molecular complexes. *Angewandte Chemie International Edition*, 43(20):2622–2648. doi: 10.1002/anie.200300611. URL https://onlinelibrary.wiley.com/doi/abs/10.1002/anie.200300611.

[152] J. Peter Toennies. *Helium Nanodroplets: Formation, Physical Properties and Superfluidity*, pages 1–40. Springer International Publishing, Cham, 2022. ISBN 978-3-030-94896-2. doi: 10.1007/978-3-030-94896-2_1. URL https://doi.org/10.1007/978-3-030-94896-2_1.

[153] Frank Stienkemeier and Andrey F. Vilesov. Electronic spectroscopy in he droplets. *The Journal of Chemical Physics*, 115(22):10119–10137, 2001. doi: 10.1063/1.1415433. URL https://aip.scitation.org/doi/abs/10.1063/1.1415433.

[154] Carlo Callegari, Kevin K. Lehmann, Roman Schmied, and Giacinto Scoles. Helium nanodroplet isolation rovibrational spectroscopy: Methods and recent results. *The Journal of Chemical Physics*, 115(22):10090–10110, 2001. doi: 10.1063/1.1418746. URL https://aip.scitation.org/doi/abs/10.1063/1.1418746.

[155] M. Y. Choi, G. E. Douberly, T. M. Falconer, W. K. Lewis, C. M. Lindsay, J. M. Merritt, P. L. Stiles, and R. E. Miller. Infrared spectroscopy of helium nanodroplets: novel methods for physics and chemistry. *International Reviews in Physical Chemistry*, 25(1-2):15–75, 2006. doi: 10.1080/01442350600625092. URL https://doi.org/10.1080/01442350600625092.

[156] Deepak Verma, Rico Mayro P. Tanyag, Sean M. O. O'Connell, and Andrey F. Vilesov. Infrared spectroscopy in superfluid helium droplets. *Advances in Physics: X*, 4(1):1553569, 2019. doi: 10.1080/23746149.2018.1553569. URL https://doi.org/10.1080/23746149.2018.1553569.

[157] Marc Briant, Jean-Michel Mestdagh, Marc-André Gaveau, and Lionel Poisson. Reaction dynamics within a cluster environment. *Phys. Chem. Chem. Phys.*, 24: 9807–9835, 2022. doi: 10.1039/D1CP05783A. URL http://dx.doi.org/10.1039/D1CP05783A.

[158] Francesco Ancilotto, Peter B. Lerner, and Milton W. Cole. Physics of solvation.

Journal of Low Temperature Physics, 101(5):1123–1146, Dec 1995. ISSN 1573-7357. doi: 10.1007/BF00754527. URL https://doi.org/10.1007/BF00754527.

[159] Francesco Ancilotto, Manuel Barranco, François Coppens, Jussi Eloranta, Nadine Halberstadt, Alberto Hernando, David Mateo, and Martí Pi. Density functional theory of doped superfluid liquid helium and nanodroplets. *International Reviews in Physical Chemistry*, 36(4):621–707, 2017. doi: 10.1080/0144235X.2017.1351672. URL https://doi.org/10.1080/0144235X.2017.1351672.

[160] F. Ancilotto, E. Cheng, M. W. Cole, and F. Toigo. The binding of alkali atoms to the surfaces of liquid helium and hydrogen. *Zeitschrift für Physik B Condensed Matter*, 98(3):323–329, Sep 1995. ISSN 1431-584X. doi: 10.1007/BF01338398. URL https://doi.org/10.1007/BF01338398.

[161] F. Stienkemeier, J. Higgins, C. Callegari, S. I. Kanorsky, W. E. Ernst, and G. Scoles. Spectroscopy of alkali atoms (li, na, k) attached to large helium clusters. *Zeitschrift für Physik D Atoms, Molecules and Clusters*, 38(3):253–263, Sep 1996. ISSN 1431-5866. doi: 10.1007/s004600050090. URL https://doi.org/10.1007/s004600050090.

[162] Yanfei Ren and Vitaly V. Kresin. Surface location of alkaline-earth-metal-atom impurities on helium nanodroplets. *Phys. Rev. A*, 76:043204, Oct 2007. doi: 10.1103/PhysRevA.76.043204. URL https://link.aps.org/doi/10.1103/PhysRevA.76.043204.

[163] Matthias Hartmann, Roger E. Miller, J. Peter Toennies, and Andrej F. Vilesov. High-resolution molecular spectroscopy of van der waals clusters in liquid helium droplets. *Science*, 272(5268):1631–1634, 1996. doi: 10.1126/science.272.5268.1631. URL https://www.science.org/doi/abs/10.1126/science.272.5268.1631.

[164] Slava Grebenev, Matthias Hartmann, Martina Havenith, Boris Sartakov, J. Peter Toennies, and Andrei F. Vilesov. The rotational spectrum of single ocs molecules in liquid 4he droplets. *The Journal of Chemical Physics*, 112(10):4485–4495, 2000. doi: 10.1063/1.481011. URL https://doi.org/10.1063/1.481011.

[165] K. Nauta and R. E. Miller. Formation of cyclic water hexamer in liquid helium: The smallest piece of ice. *Science*, 287(5451):293–295, 2000. doi: 10.1126/science.

287.5451.293. URL https://www.science.org/doi/abs/10.1126/science.287.5451.293.

[166] Andreas Przystawik, Sebastian Göde, Tilo Döppner, Josef Tiggesbäumker, and Karl-Heinz Meiwes-Broer. Light-induced collapse of metastable magnesium complexes formed in helium nanodroplets. *Phys. Rev. A*, 78:021202, Aug 2008. doi: 10.1103/PhysRevA.78.021202. URL https://link.aps.org/doi/10.1103/PhysRevA.78.021202.

[167] Evgeny Loginov, Luis F. Gomez, Naihao Chiang, Avik Halder, Nicholas Guggemos, Vitaly V. Kresin, and Andrey F. Vilesov. Photoabsorption of $ag_N(n \sim 6 - -6000)$ nanoclusters formed in helium droplets: Transition from compact to multicenter aggregation. *Phys. Rev. Lett.*, 106:233401, Jun 2011. doi: 10.1103/PhysRevLett.106.233401. URL https://link.aps.org/doi/10.1103/PhysRevLett.106.233401.

[168] M. Briant, E. Mengesha, M.-A. Gaveau, B. Soep, J.-M. Mestdagh, and L. Poisson. Dynamics of acetylene dimers hosted in helium droplets. *Phys. Chem. Chem. Phys.*, 20:2597–2605, 2018. doi: 10.1039/C7CP07741F. URL http://dx.doi.org/10.1039/C7CP07741F.

[169] Luis F. Gomez, Ken R. Ferguson, James P. Cryan, Camila Bacellar, Rico Mayro P. Tanyag, Curtis Jones, Sebastian Schorb, Denis Anielski, Ali Belkacem, Charles Bernando, Rebecca Boll, John Bozek, Sebastian Carron, Gang Chen, Tjark Delmas, Lars Englert, Sascha W. Epp, Benjamin Erk, Lutz Foucar, Robert Hartmann, Alexander Hexemer, Martin Huth, Justin Kwok, Stephen R. Leone, Jonathan H. S. Ma, Filipe R. N. C. Maia, Erik Malmerberg, Stefano Marchesini, Daniel M. Neumark, Billy Poon, James Prell, Daniel Rolles, Benedikt Rudek, Artem Rudenko, Martin Seifrid, Katrin R. Siefermann, Felix P. Sturm, Michele Swiggers, Joachim Ullrich, Fabian Weise, Petrus Zwart, Christoph Bostedt, Oliver Gessner, and Andrey F. Vilesov. Shapes and vorticities of superfluid helium nanodroplets. *Science*, 345(6199):906–909, 2014. doi: 10.1126/science.1252395. URL https://www.science.org/doi/abs/10.1126/science.1252395.

[170] Curtis F. Jones, Charles Bernando, Rico Mayro P. Tanyag, Camila Bacellar, Ken R. Ferguson, Luis F. Gomez, Denis Anielski, Ali Belkacem, Rebecca Boll, John Bozek, Sebastian Carron, James Cryan, Lars Englert, Sascha W. Epp, Benjamin Erk, Lutz

Foucar, Robert Hartmann, Daniel M. Neumark, Daniel Rolles, Artem Rudenko, Katrin R. Siefermann, Fabian Weise, Benedikt Rudek, Felix P. Sturm, Joachim Ullrich, Christoph Bostedt, Oliver Gessner, and Andrey F. Vilesov. Coupled motion of xe clusters and quantum vortices in he nanodroplets. *Phys. Rev. B*, 93:180510, May 2016. doi: 10.1103/PhysRevB.93.180510. URL https://link.aps.org/doi/10.1103/PhysRevB.93.180510.

[171] Philipp Thaler, Alexander Volk, Florian Lackner, Johannes Steurer, Daniel Knez, Werner Grogger, Ferdinand Hofer, and Wolfgang E. Ernst. Formation of bimetallic core-shell nanowires along vortices in superfluid he nanodroplets. *Phys. Rev. B*, 90: 155442, Oct 2014. doi: 10.1103/PhysRevB.90.155442. URL https://link.aps.org/doi/10.1103/PhysRevB.90.155442.

[172] Florian Lackner. *Synthesis of Metallic Nanoparticles in Helium Droplets*, pages 513–560. Springer International Publishing, Cham, 2022. ISBN 978-3-030-94896-2. doi: 10.1007/978-3-030-94896-2_11. URL https://doi.org/10.1007/978-3-030-94896-2_11.

[173] H. Buchenau, J. P. Toennies, and J. A. Northby. Excitation and ionization of 4he clusters by electrons. *The Journal of Chemical Physics*, 95(11):8134–8148, 1991. doi: 10.1063/1.461294. URL https://doi.org/10.1063/1.461294.

[174] Oliver Bünermann, Oleg Kornilov, Daniel J. Haxton, Stephen R. Leone, Daniel M. Neumark, and Oliver Gessner. Ultrafast probing of ejection dynamics of rydberg atoms and molecular fragments from electronically excited helium nanodroplets. *The Journal of Chemical Physics*, 137(21):214302, 2012. doi: 10.1063/1.4768422. URL https://doi.org/10.1063/1.4768422.

[175] A. Scheidemann, B. Schilling, and J. Peter Toennies. Anomalies in the reactions of helium(1+) with sulfur hexafluoride embedded in large helium-4 clusters. *The Journal of Physical Chemistry*, 97(10):2128–2138, Mar 1993. ISSN 0022-3654. doi: 10.1021/j100112a012. URL https://doi.org/10.1021/j100112a012.

[176] Nadine Halberstadt and Kenneth C Janda. The resonant charge hopping rate in positively charged helium clusters. *Chemical Physics Letters*, 282(5):409–412,

1998. ISSN 0009-2614. doi: https://doi.org/10.1016/S0009-2614(97)01276-1. URL https://www.sciencedirect.com/science/article/pii/S0009261497012761.

[177] JAN A. NORTHBY K. K. LEHMANN. Potential of an ionic impurity in a large 4he cluster. *Molecular Physics*, 97(5):639–644, 1999. doi: 10.1080/002689799163488. URL https://doi.org/10.1080/002689799163488.

[178] William K. Lewis, C. Michael Lindsay, Raymond J. Bemish, and Roger E. Miller. Probing charge-transfer processes in helium nanodroplets by optically selected mass spectrometry (osms): charge steering by long-range interactions. *Journal of the American Chemical Society*, 127(19):7235–7242, May 2005. ISSN 0002-7863. doi: 10.1021/ja042489s. URL https://doi.org/10.1021/ja042489s.

[179] Chia C. Wang, Oleg Kornilov, Oliver Gessner, Jeong Hyun Kim, Darcy S. Peterka, and Daniel M. Neumark. Photoelectron imaging of helium droplets doped with xe and kr atoms. *The Journal of Physical Chemistry A*, 112(39):9356–9365, 2008. doi: 10.1021/jp802332f. URL https://doi.org/10.1021/jp802332f. PMID: 18690675.

[180] Dominic Buchta, Siva R. Krishnan, Nils B. Brauer, Marcel Drabbels, Patrick O'Keeffe, Michele Devetta, Michele Di Fraia, Carlo Callegari, Robert Richter, Marcello Coreno, Kevin C. Prince, Frank Stienkemeier, Robert Moshammer, and Marcel Mudrich. Charge transfer and penning ionization of dopants in or on helium nanodroplets exposed to euv radiation. *The Journal of Physical Chemistry A*, 117 (21):4394–4403, 2013. doi: 10.1021/jp401424w. URL https://doi.org/10.1021/jp401424w. PMID: 23638683.

[181] L. Ben Ltaief, M. Shcherbinin, S. Mandal, S. R. Krishnan, A. C. LaForge, R. Richter, S. Turchini, N. Zema, T. Pfeifer, E. Fasshauer, N. Sisourat, and M. Mudrich. Charge exchange dominates long-range interatomic coulombic decay of excited metal-doped helium nanodroplets. *The Journal of Physical Chemistry Letters*, 10(21):6904–6909, 2019. doi: 10.1021/acs.jpclett.9b02726. URL https://doi.org/10.1021/acs.jpclett.9b02726. PMID: 31625747.

[182] Darcy S. Peterka, Jeong Hyun Kim, Chia C. Wang, and Daniel M. Neumark. Photoionization and photofragmentation of sf6 in helium nanodroplets. *The Journal of*

Physical Chemistry B, 110(40):19945–19955, 2006. doi: 10.1021/jp062195o. URL https://doi.org/10.1021/jp062195o. PMID: 17020381.

[183] M. Shcherbinin, A. C. LaForge, M. Hanif, R. Richter, and M. Mudrich. Penning ionization of acene molecules by helium nanodroplets. *The Journal of Physical Chemistry A*, 122(7):1855–1860, 2018. doi: 10.1021/acs.jpca.7b12506. URL https://doi.org/10.1021/acs.jpca.7b12506. PMID: 29376655.

[184] L. Ben Ltaief, M. Shcherbinin, S. Mandal, S. R. Krishnan, R. Richter, S. Turchini, N. Zema, and M. Mudrich. Photoelectron spectroscopy of coronene molecules embedded in helium nanodroplets. *Journal of Low Temperature Physics*, 202(5): 444–455, Mar 2021. ISSN 1573-7357. doi: 10.1007/s10909-020-02553-9. URL https://doi.org/10.1007/s10909-020-02553-9.

[185] A. C. LaForge, V. Stumpf, K. Gokhberg, J. von Vangerow, F. Stienkemeier, N. V. Kryzhevoi, P. O'Keeffe, A. Ciavardini, S. R. Krishnan, M. Coreno, K. C. Prince, R. Richter, R. Moshammer, T. Pfeifer, L. S. Cederbaum, and M. Mudrich. Enhanced ionization of embedded clusters by electron-transfer-mediated decay in helium nanodroplets. *Phys. Rev. Lett.*, 116:203001, May 2016. doi: 10.1103/PhysRevLett.116.203001. URL https://link.aps.org/doi/10.1103/PhysRevLett.116.203001.

[186] L. Ben Ltaief, M. Shcherbinin, S. Mandal, S. R. Krishnan, R. Richter, T. Pfeifer, M. Bauer, A. Ghosh, M. Mudrich, K. Gokhberg, and A. C. LaForge. Electron transfer mediated decay of alkali dimers attached to he nanodroplets. *Phys. Chem. Chem. Phys.*, 22:8557–8564, 2020. doi: 10.1039/D0CP00256A. URL http://dx.doi.org/10.1039/D0CP00256A.

[187] A. C. LaForge, M. Shcherbinin, F. Stienkemeier, R. Richter, R. Moshammer, T. Pfeifer, and M. Mudrich. Highly efficient double ionization of mixed alkali dimers by intermolecular coulombic decay. *Nature Physics*, 15(3):247–250, 2019. ISSN 1745-2481. doi: 10.1038/s41567-018-0376-5. URL https://doi.org/10.1038/s41567-018-0376-5.

[188] M. Shcherbinin, A. C. LaForge, V. Sharma, M. Devetta, R. Richter, R. Moshammer, T. Pfeifer, and M. Mudrich. Interatomic coulombic decay in helium nanodroplets.

Phys. Rev. A, 96:013407, Jul 2017. doi: 10.1103/PhysRevA.96.013407. URL https://link.aps.org/doi/10.1103/PhysRevA.96.013407.

[189] Y Ovcharenko, A C LaForge, B Langbehn, O Plekan, R Cucini, P Finetti, P O'Keeffe, D Iablonskyi, T Nishiyama, K Ueda, P Piseri, M Di Fraia, R Richter, M Coreno, C Callegari, K C Prince, F Stienkemeier, T Möller, and M Mudrich. Autoionization dynamics of helium nanodroplets resonantly excited by intense XUV laser pulses. *New Journal of Physics*, 22(8):083043, aug 2020. doi: 10.1088/1367-2630/ab9554. URL https://doi.org/10.1088/1367-2630/ab9554.

[190] M. Mudrich, A. C. LaForge, A. Ciavardini, P. O'Keeffe, C. Callegari, M. Coreno, A. Demidovich, M. Devetta, M. Di Fraia, M. Drabbels, P. Finetti, O. Gessner, C. Grazioli, A. Hernando, D. M. Neumark, Y. Ovcharenko, P. Piseri, O. Plekan, K. C. Prince, R. Richter, M. P. Ziemkiewicz, T. Möller, J. Eloranta, M. Pi, M. Barranco, and F. Stienkemeier. Ultrafast relaxation of photoexcited superfluid he nanodroplets. *Nature Communications*, 11(1):112, Jan 2020. ISSN 2041-1723. doi: 10.1038/s41467-019-13681-6. URL https://doi.org/10.1038/s41467-019-13681-6.

[191] Jakob D. Asmussen, Rupert Michiels, Katrin Dulitz, Aaron Ngai, Ulrich Bangert, Manuel Barranco, Marcel Binz, Lukas Bruder, Miltcho Danailov, Michele Di Fraia, Jussi Eloranta, Raimund Feifel, Luca Giannessi, Marti Pi, Oksana Plekan, Kevin C. Prince, Richard J. Squibb, Daniel Uhl, Andreas Wituschek, Marco Zangrando, Carlo Callegari, Frank Stienkemeier, and Marcel Mudrich. Unravelling the full relaxation dynamics of superexcited helium nanodroplets. *Phys. Chem. Chem. Phys.*, 23:15138–15149, 2021. doi: 10.1039/D1CP01041G. URL http://dx.doi.org/10.1039/D1CP01041G.

[192] A. C. LaForge, R. Michiels, Y. Ovcharenko, A. Ngai, J. M. Escartín, N. Berrah, C. Callegari, A. Clark, M. Coreno, R. Cucini, M. Di Fraia, M. Drabbels, E. Fasshauer, P. Finetti, L. Giannessi, C. Grazioli, D. Iablonskyi, B. Langbehn, T. Nishiyama, V. Oliver, P. Piseri, O. Plekan, K. C. Prince, D. Rupp, S. Stranges, K. Ueda, N. Sisourat, J. Eloranta, M. Pi, M. Barranco, F. Stienkemeier, T. Möller, and M. Mudrich. Ultrafast resonant interatomic coulombic decay induced by quantum fluid dynamics. *Phys. Rev. X*, 11:021011, Apr 2021. doi: 10.1103/PhysRevX.

11.021011. URL https://link.aps.org/doi/10.1103/PhysRevX.11.021011.

[193] U. Buck G. Scoles, D. Bassi and D. C. Lainé (eds.). *Atomic and Molecular Beam Methods*. Oxford University Press, USA, 1988.

[194] U. Even. "the even-lavie valve as a source for high intensity supersonic beam". *EPJ Techniques and Instrumentation*, 2(1):17, Dec 2015. ISSN 2195-7045. doi: 10.1140/epjti/s40485-015-0027-5. URL https://doi.org/10.1140/epjti/s40485-015-0027-5.

[195] O. F. Hagena and W. Obert. Cluster formation in expanding supersonic jets: Effect of pressure, temperature, nozzle size, and test gas. *The Journal of Chemical Physics*, 56(5):1793–1802, 1972. doi: 10.1063/1.1677455. URL https://doi.org/10.1063/1.1677455.

[196] R. A. Smith, T. Ditmire, and J. W. G. Tisch. Characterization of a cryogenically cooled high-pressure gas jet for laser/cluster interaction experiments. *Review of Scientific Instruments*, 69(11):3798–3804, 1998. doi: 10.1063/1.1149181. URL https://doi.org/10.1063/1.1149181.

[197] F. Dorchies, F. Blasco, T. Caillaud, J. Stevefelt, C. Stenz, A. S. Boldarev, and V. A. Gasilov. Spatial distribution of cluster size and density in supersonic jets as targets for intense laser pulses. *Phys. Rev. A*, 68:023201, Aug 2003. doi: 10.1103/PhysRevA.68.023201. URL https://link.aps.org/doi/10.1103/PhysRevA.68.023201.

[198] Susumu Kuma and Toshiyuki Azuma. Pulsed beam of extremely large helium droplets. *Cryogenics*, 88:78–80, Dec 2017. ISSN 0011-2275. URL https://www.sciencedirect.com/science/article/pii/S0011227517302631.

[199] Deepak Verma and Andrey F. Vilesov. Pulsed helium droplet beams. *Chemical Physics Letters*, 694:129–134, 2018. ISSN 0009-2614. doi: https://doi.org/10.1016/j.cplett.2018.01.035. URL https://www.sciencedirect.com/science/article/pii/S0009261418300447.

[200] Dominik Pentlehner, Ricarda Riechers, Bernhard Dick, Alkwin Slenczka, Uzi Even, Nachum Lavie, Raviv Brown, and Kfir Luria. Rapidly pulsed helium droplet source. *Review of Scientific Instruments*, 80(4):043302, 2009. doi: 10.1063/1.3117196. URL https://doi.org/10.1063/1.3117196.

[201] Csw-71d compressor unit, sumitomo heavy industries, ltd. www.chem.cmu.edu/groups/bier/procedure_files/lit/CSW-71D%20-%20CD32ZZ-208B.pdf.

[202] Model 325 temperature controller, lake shore cryotronics inc. www.lakeshore.com/docs/default-source/product-downloads/catalog/lstc_325_l.pdf?sfvrsn=a88645a_3.

[203] Hiq helium 6.0, linde gases division. hiq.linde-gas.com/en/images/HiQ%20Helium_tcm899-89982.pdf.

[204] H. Buchenau, E. L. Knuth, J. Northby, J. P. Toennies, and C. Winkler. Mass spectra and time-of-flight distributions of helium cluster beams. *The Journal of Chemical Physics*, 92(11):6875–6889, 1990. doi: 10.1063/1.458275. URL https://doi.org/10.1063/1.458275.

[205] T. Jiang and J. A. Northby. Fragmentation clusters formed in supercritical expansions of ^{4}He. *Phys. Rev. Lett.*, 68:2620–2623, Apr 1992. doi: 10.1103/PhysRevLett.68.2620. URL https://link.aps.org/doi/10.1103/PhysRevLett.68.2620.

[206] M. Lewerenz, B. Schilling, and J.P. Toennies. A new scattering deflection method for determining and selecting the sizes of large liquid clusters of 4he. *Chemical Physics Letters*, 206(1):381–387, 1993. ISSN 0009-2614. doi: https://doi.org/10.1016/0009-2614(93)85569-A. URL https://www.sciencedirect.com/science/article/pii/000926149385569A.

[207] Luis F. Gomez, Evgeny Loginov, Russell Sliter, and Andrey F. Vilesov. Sizes of large he droplets. *The Journal of Chemical Physics*, 135(15):154201, 2011. doi: 10.1063/1.3650235. URL https://doi.org/10.1063/1.3650235.

[208] Rico Mayro P. Tanyag, Camila Bacellar, Weiwu Pang, Charles Bernando, Luis F. Gomez, Curtis F. Jones, Ken R. Ferguson, Justin Kwok, Denis Anielski, Ali Belkacem, Rebecca Boll, John Bozek, Sebastian Carron, Gang Chen, Tjark Delmas, Lars Englert, Sascha W. Epp, Benjamin Erk, Lutz Foucar, Robert Hartmann, Alexander Hexemer, Martin Huth, Stephen R. Leone, Jonathan H. Ma, Stefano Marchesini, Daniel M. Neumark, Billy K. Poon, James Prell, Daniel Rolles, Benedikt Rudek, Artem Rudenko, Martin Seifrid, Michele Swiggers, Joachim Ullrich, Fabian Weise, Petrus Zwart, Christoph Bostedt, Oliver Gessner, and Andrey F. Vilesov.

Sizes of pure and doped helium droplets from single shot x-ray imaging. *The Journal of Chemical Physics*, 156(4):041102, 2022. doi: 10.1063/5.0080342. URL https://doi.org/10.1063/5.0080342.

[209] Frank Stienkemeier and Kevin K Lehmann. Spectroscopy and dynamics in helium nanodroplets. *Journal of Physics B: Atomic, Molecular and Optical Physics*, 39(8): R127, 2006. URL http://stacks.iop.org/0953-4075/39/i=8/a=R01.

[210] Lord Rayleigh. On the instability of jets. *Proceedings of the London Mathematical Society*, s1-10(1):4–13, 1878. doi: https://doi.org/10.1112/plms/s1-10.1.4. URL https://londmathsoc.onlinelibrary.wiley.com/doi/abs/10.1112/plms/s1-10.1.4.

[211] D. M. Brink and S. Stringari. Density of states and evaporation rate of helium clusters. *Zeitschrift für Physik D Atoms, Molecules and Clusters*, 15(3):257–263, Sep 1990. ISSN 1431-5866. doi: 10.1007/BF01437187. URL https://doi.org/10.1007/BF01437187.

[212] M. Lewerenz, B. Schilling, and J. P. Toennies. Successive capture and coagulation of atoms and molecules to small clusters in large liquid helium clusters. *The Journal of Chemical Physics*, 102(20):8191–8207, 1995. doi: 10.1063/1.469231. URL https://doi.org/10.1063/1.469231.

[213] K. Nauta and R. E. Miller. The hydrogen fluoride dimer in liquid helium: A prototype system for studying solvent effects on hydrogen bonding. *The Journal of Chemical Physics*, 113(22):10158–10168, 2000. doi: 10.1063/1.1289824. URL https://doi.org/10.1063/1.1289824.

[214] Susumu Kuma, Haruka Goto, Mikhail N. Slipchenko, Andrey F. Vilesov, Alexander Khramov, and Takamasa Momose. Laser induced fluorescence of mg-phthalocyanine in he droplets: Evidence for fluxionality of large h2 clusters at 0.38k. *The Journal of Chemical Physics*, 127(21):214301, 2007. doi: 10.1063/1.2802303. URL https://doi.org/10.1063/1.2802303.

[215] Josef Tiggesbäumker and Frank Stienkemeier. Formation and properties of metal clusters isolated in helium droplets. *Phys. Chem. Chem. Phys.*, 9:4748–4770, 2007. doi: 10.1039/B703575F. URL http://dx.doi.org/10.1039/B703575F.

[216] Andreas Hermann and Peter Schwerdtfeger. Complete basis set limit second-order møller–plesset calculations for the fcc lattices of neon, argon, krypton, and xenon. *The Journal of Chemical Physics*, 131(24):244508, 2009. doi: 10.1063/1.3279303. URL https://doi.org/10.1063/1.3279303.

[217] Vadim Mozhayskiy, Mikhail N. Slipchenko, Vera K. Adamchuk, and Andrey F. Vilesov. Use of helium nanodroplets for assembly, transport, and surface deposition of large molecular and atomic clusters. *The Journal of Chemical Physics*, 127 (9):094701, 2007. doi: 10.1063/1.2759927. URL https://doi.org/10.1063/1.2759927.

[218] Sascha Vongehr and Vitaly V. Kresin. Unusual pickup statistics of high-spin alkali agglomerates on helium nanodroplets. *The Journal of Chemical Physics*, 119(21): 11124–11129, 2003. doi: 10.1063/1.1622930. URL https://doi.org/10.1063/1.1622930.

[219] Philip Willmott. *Synchrotron Physics*, chapter 3, pages 51–106. 2019. doi: https://doi.org/10.1002/9781119280453.ch3. URL https://onlinelibrary.wiley.com/doi/abs/10.1002/9781119280453.ch3.

[220] Machine parameters, elettra sincrotrone trieste, italy. https://www.elettra.trieste.it/lightsources/elettra/odac/elettra-parameters.html.

[221] photon-science.desy.de. https://photon-science.desy.de/research/students__teaching/primers/synchrotron_radiation/index_eng.html.

[222] R.R Blyth, R Delaunay, M Zitnik, J Krempasky, R Krempaska, J Slezak, K.C Prince, R Richter, M Vondracek, R Camilloni, L Avaldi, M Coreno, G Stefani, C Furlani, M de Simone, S Stranges, and M.-Y Adam. The high resolution gas phase photoemission beamline, elettra. *Journal of Electron Spectroscopy and Related Phenomena*, 101-103:959–964, 1999. ISSN 0368-2048. doi: https://doi.org/10.1016/S0368-2048(98)00381-8. URL https://www.sciencedirect.com/science/article/pii/S0368204898003818.

[223] Gasphase beamline, elettra sincrotrone trieste, italy. https://www.elettra.trieste.it/lightsources/elettra/elettra-beamlines/gas-phase/bl-description.html.

[224] M. Alagia, L. Avaldi, M. Coreno, R. Camilloni, C. Furlani, K. C. Prince, R. Richter, M. de Simone, G. Stefani, and S. Stranges. The gas phase photoemission beamline at elettra. *Synchrotron Radiation News*, 16(2):19–27, 2003. doi: 10.1080/08940880308603010. URL https://doi.org/10.1080/08940880308603010.

[225] W. C. Wiley and I. H. McLaren. Time-of-flight mass spectrometer with improved resolution. *Review of Scientific Instruments*, 26(12):1150–1157, 1955. doi: 10.1063/1.1715212. URL https://doi.org/10.1063/1.1715212.

[226] D. H. Parker and A. T. J. B. Eppink. Photoelectron and photofragment velocity map imaging of state-selected molecular oxygen dissociation/ionization dynamics. *The Journal of Chemical Physics*, 107(7):2357–2362, 1997. doi: 10.1063/1.474624. URL https://doi.org/10.1063/1.474624.

[227] Nhq high voltage power supplies, high voltage.exactly. iseg spezialelektronik gmbh. iseg-hv.com/files/media/iseg_datasheet_NHQ_en_20210329082518.pdf.

[228] Hv flex, elettra – sincrotrone trieste s.c.p.a. www.elettra.trieste.it/images/Documents/ILO/Strumenti%20Scientifici/06_Elettra_HV%20FLEX.pdf.

[229] 3d (x,y,t) cross delay-line detector, elettra – sincrotrone trieste s.c.p.a. www.elettra.trieste.it/images/Documents/ILO/Strumenti%20Scientifici/01_Elettra_3D%20Cross%20Delay-Line%20Detector.pdf.

[230] Mod. n89 nim - ttl - nim adapter, caen s.p.a. www.caen.it/products/n89/.

[231] Model 754 quad four-fold logic unit, phillips scientific. hallcweb.jlab.org/experiments/hks/datasheets/754ds.pdf, .

[232] Model 794 quad gate/delay generator, phillips scientific. groups.nscl.msu.edu/nscl_library/manuals/phillips/794.pdf, .

[233] Acam atmd-gpx, acam-messelectronic gmbh. www.pmt-fl.com/uploads/2017/09/precision-measurement-db-amgpx-e.pdf.

[234] Dg535 digital delay generator, stanford research systems. www.thinksrs.com/products/dg535.html.

[235] J. H. D. Eland. Dynamics of fragmentation reactions from peak shapes in mul-

tiparticle coincidence experiments. *Laser Chemistry*, 11:717149, Jan 1991. ISSN 0278-6273. doi: 10.1155/LC.11.259. URL https://doi.org/10.1155/LC.11.259.

[236] P. O'Keeffe, P. Bolognesi, M. Coreno, A. Moise, R. Richter, G. Cautero, L. Stebel, R. Sergo, L. Pravica, Y. Ovcharenko, and L. Avaldi. A photoelectron velocity map imaging spectrometer for experiments combining synchrotron and laser radiations. *Review of Scientific Instruments*, 82(3):033109, 2011. doi: 10.1063/1.3563723. URL https://doi.org/10.1063/1.3563723.

[237] Vladimir Dribinski, Alexei Ossadtchi, Vladimir A. Mandelshtam, and Hanna Reisler. Reconstruction of abel-transformable images: The gaussian basis-set expansion abel transform method. *Review of Scientific Instruments*, 73(7):2634–2642, 2002. doi: 10.1063/1.1482156. URL https://doi.org/10.1063/1.1482156.

[238] Gustavo A. Garcia, Laurent Nahon, and Ivan Powis. Two-dimensional charged particle image inversion using a polar basis function expansion. *Review of Scientific Instruments*, 75(11):4989–4996, 2004. doi: 10.1063/1.1807578. URL https://doi.org/10.1063/1.1807578.

[239] G. M. Roberts, J. L. Nixon, J. Lecointre, E. Wrede, and J. R. R. Verlet. Toward real-time charged-particle image reconstruction using polar onion-peeling. *Review of Scientific Instruments*, 80(5):053104, 2009. doi: 10.1063/1.3126527. URL https://doi.org/10.1063/1.3126527.

[240] Bernhard Dick. Inverting ion images without abel inversion: maximum entropy reconstruction of velocity maps. *Physical Chemistry Chemical Physics*, 16:570–580, 2014. doi: 10.1039/C3CP53673D. URL http://dx.doi.org/10.1039/C3CP53673D.

[241] Bernhard Dick. Melexir: maximum entropy legendre expanded image reconstruction. a fast and efficient method for the analysis of velocity map imaging or photoelectron imaging data. *Phys. Chem. Chem. Phys.*, 21:19499–19512, 2019. doi: 10.1039/C9CP03353J. URL http://dx.doi.org/10.1039/C9CP03353J.

[242] M. Joppien, R. Karnbach, and T. Möller. Electronic excitations in liquid helium: The evolution from small clusters to large droplets. *Phys. Rev. Lett.*, 71:2654–2657,

Oct 1993. doi: 10.1103/PhysRevLett.71.2654. URL https://link.aps.org/doi/10.1103/PhysRevLett.71.2654.

[243] M. A. Khakoo, J. M. Ratliff, and S. Trajmar. Electron impact excitation of coronene. *The Journal of Chemical Physics*, 93(12):8616–8619, 1990. doi: 10.1063/1.459248. URL https://doi.org/10.1063/1.459248.

[244] M. Ruberti, R. Yun, K. Gokhberg, S. Kopelke, L. S. Cederbaum, F. Tarantelli, and V. Averbukh. Total molecular photoionization cross-sections by algebraic diagrammatic construction-stieltjes-lanczos method: Benchmark calculations. *The Journal of Chemical Physics*, 139(14):144107, 2013. doi: 10.1063/1.4824431. URL https://doi.org/10.1063/1.4824431.

[245] L Ben Ltaief, M Shcherbinin, S Mandal, S R Krishnan, R Richter, T Pfeifer, and M Mudrich. Direct inner-shell photoionization of xe atoms embedded in helium nanodroplets. *Journal of Physics B: Atomic, Molecular and Optical Physics*, 53 (20):204001, sep 2020. doi: 10.1088/1361-6455/abaafb. URL https://doi.org/10.1088/1361-6455/abaafb.

[246] M. Mudrich, A. C. LaForge, A. Ciavardini, P. O'Keeffe, C. Callegari, M. Coreno, A. Demidovich, M. Devetta, M. Di Fraia, M. Drabbels, P. Finetti, O. Gessner, C. Grazioli, A. Hernando, D. M. Neumark, Y. Ovcharenko, P. Piseri, O. Plekan, K. C. Prince, R. Richter, M. P. Ziemkiewicz, T. Möller, J. Eloranta, M. Pi, M. Barranco, and F. Stienkemeier. Ultrafast relaxation of photoexcited superfluid he nanodroplets. *Nature Communications*, 11(1):112, Jan 2020. ISSN 2041-1723. doi: 10.1038/s41467-019-13681-6. URL https://doi.org/10.1038/s41467-019-13681-6.

[247] Darcy S. Peterka, Albrecht Lindinger, Lionel Poisson, Musahid Ahmed, and Daniel M. Neumark. Photoelectron imaging of helium droplets. *Physical Review Letters*, 91:043401, Jul 2003. doi: 10.1103/PhysRevLett.91.043401. URL https://link.aps.org/doi/10.1103/PhysRevLett.91.043401.

[248] K. Nauta and R. E. Miller. The vibrational and rotational dynamics of acetylene solvated in superfluid helium nanodroplets. *The Journal of Chemical Physics*, 115

(18):8384–8392, 2001. doi: 10.1063/1.1412257. URL https://doi.org/10.1063/1.1412257.

[249] Anja Metzelthin, Özgür Birer, Elsa Sánchez-García, and Martina Havenith. High resolution ir spectroscopy of acetylene-furan in ultracold helium nanodroplets. *The Journal of Chemical Physics*, 129(11):114307, 2008. doi: 10.1063/1.2976772. URL https://doi.org/10.1063/1.2976772.

[250] M. Briant, E. Mengesha, P. de Pujo, M.-A. Gaveau, B. Soep, J.-M. Mestdagh, and L. Poisson. Large amplitude motion of the acetylene molecule within acetylene–neon complexes hosted in helium droplets. *Phys. Chem. Chem. Phys.*, 18: 16414–16422, 2016. doi: 10.1039/C6CP02989B. URL http://dx.doi.org/10.1039/C6CP02989B.

[251] J.A. Fennelly and D.G. Torr. Photoionization and photoabsorption cross sections of o, n2, o2, and n for aeronomic calculations. *Atomic Data and Nuclear Data Tables*, 51(2):321 – 363, 1992. ISSN 0092-640X. doi: https://doi.org/10.1016/0092-640X(92)90004-2. URL http://www.sciencedirect.com/science/article/pii/0092640X92900042.

[252] J.K. Kim and W.T. Huntress. Product distributions and rate constants for the reactions of thermal energy he÷ ions with some neutral hydrides and hydrocarbons. *International Journal of Mass Spectrometry and Ion Physics*, 16(4):451 – 454, 1975. ISSN 0020-7381. doi: https://doi.org/10.1016/0020-7381(75)85034-0. URL http://www.sciencedirect.com/science/article/pii/0020738175850340.

[253] S. Mandal, R. Gopal, M. Shcherbinin, A. D'Elia, H. Srinivas, R. Richter, M. Coreno, B. Bapat, M. Mudrich, S. R. Krishnan, and V. Sharma. Penning spectroscopy and structure of acetylene oligomers in he nanodroplets. *Phys. Chem. Chem. Phys.*, 22:10149–10157, 2020. doi: 10.1039/D0CP00689K. URL http://dx.doi.org/10.1039/D0CP00689K.

[254] Patrick Duffy, S.A.C. Clark, C.E. Brion, Mark.E. Casida, D.P. Chong, E.R. Davidson, and C. Maxwell. Electron momentum spectroscopy of the valence orbitals of acetylene: Quantitative comparisons using near hartree-fock limit and correlated wavefunctions. *Chemical Physics*, 165(2):183–199, 1992. ISSN 0301-

0104. doi: https://doi.org/10.1016/0301-0104(92)87036-9. URL https://www.sciencedirect.com/science/article/pii/0301010492870369.

[255] Ryo Maruyama, Hideyasu Tanaka, Yoshihiro Yamakita, Fuminori Misaizu, and Koichi Ohno. Penning ionization electron spectroscopy of co2 clusters in collision with metastable rare gas atoms. *Chemical Physics Letters*, 327(1):104–110, 2000. ISSN 0009-2614. doi: https://doi.org/10.1016/S0009-2614(00)00848-4. URL https://www.sciencedirect.com/science/article/pii/S0009261400008484.

[256] Y. Ono and C. Y. Ng. A study of the unimolecular decomposition of the (c2h2)2+ complex. *The Journal of Chemical Physics*, 77(6):2947–2955, 1982. doi: 10.1063/1.444216. URL https://doi.org/10.1063/1.444216.

[257] Y. Ono and C. Y. Ng. A study of the unimolecular decomposition of the (c2h2)3+ complex. *Journal of the American Chemical Society*, 104(18):4752–4758, 1982. doi: 10.1021/ja00382a003. URL https://doi.org/10.1021/ja00382a003.

[258] Koichi Ohno, Hideki Mutoh, and Yoshiya Harada. Study of electron distributions of molecular orbitals by penning ionization electron spectroscopy. *Journal of the American Chemical Society*, 105(14):4555–4561, 1983. doi: 10.1021/ja00352a009. URL https://doi.org/10.1021/ja00352a009.

[259] Tamar Stein, Biswajit Bandyopadhyay, Tyler P. Troy, Yigang Fang, Oleg Kostko, Musahid Ahmed, and Martin Head-Gordon. Ab initio dynamics and photoionization mass spectrometry reveal ion–molecule pathways from ionized acetylene clusters to benzene cation. *Proceedings of the National Academy of Sciences*, 114(21):E4125–E4133, 2017. ISSN 0027-8424. doi: 10.1073/pnas.1616464114. URL https://www.pnas.org/content/114/21/E4125.

[260] Andreas Kautsch, Markus Koch, and Wolfgang E. Ernst. Photoinduced molecular dissociation and photoinduced recombination mediated by superfluid helium nanodroplets. *Physical Chemistry Chemical Physics*, 17:12310–12316, 2015. doi: 10.1039/C5CP01009H. URL http://dx.doi.org/10.1039/C5CP01009H.

[261] M. C. Wells and Robert R. Lucchese. The outer valence photoionization of acetylene. *The Journal of Chemical Physics*, 111(14):6290–6299, 1999. doi: 10.1063/1.479963. URL https://doi.org/10.1063/1.479963.

[262] Oleg Kornilov, Chia C. Wang, Oliver Bünermann, Andrew T. Healy, Mathew Leonard, Chunte Peng, Stephen R. Leone, Daniel M. Neumark, and Oliver Gessner. Ultrafast dynamics in helium nanodroplets probed by femtosecond time-resolved euv photoelectron imaging. *The Journal of Physical Chemistry A*, 114(21):6350–6350, 2010. doi: 10.1021/jp103774z. URL https://doi.org/10.1021/jp103774z.

[263] O. Bünermann, O. Kornilov, S. R. Leone, D. M. Neumark, and O. Gessner. Femtosecond extreme ultraviolet ion imaging of ultrafast dynamics in electronically excited helium nanodroplets. *IEEE Journal of Selected Topics in Quantum Electronics*, 18(1):308–317, 2012.

[264] D. Buchta, S. R. Krishnan, N. B. Brauer, M. Drabbels, P. O'Keeffe, M. Devetta, M. Di Fraia, C. Callegari, R. Richter, M. Coreno, K. C. Prince, F. Stienkemeier, J. Ullrich, R. Moshammer, and M. Mudrich. Extreme ultraviolet ionization of pure he nanodroplets: Mass-correlated photoelectron imaging, penning ionization, and electron energy-loss spectra. *The Journal of Chemical Physics*, 139(8):084301, 2013. doi: 10.1063/1.4818531. URL https://doi.org/10.1063/1.4818531.

[265] Evgeniy Loginov and Marcel Drabbels. Dynamics of excited sodium atoms attached to helium nanodroplets. *The Journal of Physical Chemistry A*, 118(15):2738–2748, Apr 2014. ISSN 1089-5639. doi: 10.1021/jp4121996. URL https://doi.org/10.1021/jp4121996.

[266] P Claas, G Droppelmann, C P Schulz, M Mudrich, and F Stienkemeier. Wave packet dynamics of k2attached to helium nanodroplets. *Journal of Physics B: Atomic, Molecular and Optical Physics*, 39(19):S1151–S1168, sep 2006. doi: 10.1088/0953-4075/39/19/s23. URL https://doi.org/10.1088/0953-4075/39/19/s23.

[267] Johannes von Vangerow, François Coppens, Antonio Leal, Martí Pi, Manuel Barranco, Nadine Halberstadt, Frank Stienkemeier, and Marcel Mudrich. Imaging excited-state dynamics of doped he nanodroplets in real-time. *The Journal of Physical Chemistry Letters*, 8(1):307–312, Jan 2017. doi: 10.1021/acs.jpclett.6b02598. URL https://doi.org/10.1021/acs.jpclett.6b02598.

[268] J. von Vangerow, A. Sieg, F. Stienkemeier, M. Mudrich, A. Leal, D. Mateo, A. Hernando, M. Barranco, and M. Pi. Desorption dynamics of heavy alkali metal atoms

(rb, cs) off the surface of helium nanodroplets. *The Journal of Physical Chemistry A*, 118(33):6604–6614, Aug 2014. ISSN 1089-5639. doi: 10.1021/jp503308w. URL https://doi.org/10.1021/jp503308w.

[269] S. Müller, M. Mudrich, and F. Stienkemeier. Alkali-helium snowball complexes formed on helium nanodroplets. *The Journal of Chemical Physics*, 131(4):044319, 2009. doi: 10.1063/1.3180819. URL https://doi.org/10.1063/1.3180819.

[270] Moritz Theisen, Florian Lackner, and Wolfgang E. Ernst. Forming rb+ snowballs in the center of he nanodroplets. *Phys. Chem. Chem. Phys.*, 12:14861–14863, 2010. doi: 10.1039/C0CP01283A. URL http://dx.doi.org/10.1039/C0CP01283A.

[271] M.-W. Ruf, A. J. Yencha, and H. Hotop. The interaction of metastable helium atoms with alkali atoms. *Zeitschrift für Physik D Atoms, Molecules and Clusters*, 5(1):9–20, 1987. ISSN 1431-5866. doi: 10.1007/BF01436569. URL https://doi.org/10.1007/BF01436569.

[272] Thomas A. Carlson. Double electron ejection resulting from photo-ionization in the outermost shell of he, ne, and ar, and its relationship to electron correlation. *Phys. Rev.*, 156:142–149, Apr 1967. doi: 10.1103/PhysRev.156.142. URL https://link.aps.org/doi/10.1103/PhysRev.156.142.

[273] Tobias Schneider, Peter Leszek Chocian, and Jan-Michael Rost. Separation and identification of dominant mechanisms in double photoionization. *Phys. Rev. Lett.*, 89:073002, Jul 2002. doi: 10.1103/PhysRevLett.89.073002. URL https://link.aps.org/doi/10.1103/PhysRevLett.89.073002.

[274] J. Lozeille, A. Fioretti, C. Gabbanini, Y. Huang, H. K. Pechkis, D. Wang, P. L. Gould, E. E. Eyler, W. C. Stwalley, M. Aymar, and O. Dulieu. Detection by two-photon ionization and magnetic trapping of cold rb2 triplet state molecules. *The European Physical Journal D - Atomic, Molecular, Optical and Plasma Physics*, 39 (2):261–269, Aug 2006. ISSN 1434-6079. doi: 10.1140/epjd/e2006-00084-4. URL https://doi.org/10.1140/epjd/e2006-00084-4.

[275] Robert J. Le Roy and Geoffrey T. Kraemer. University of waterloo chemical physics research report cp-650r^2. 2004. URL http://scienide2.uwaterloo.ca/~rleroy/bcont/DraftMan.pdf.

[276] V.B. Sovkov, D. Li, V.S. Ivanov, A.S. Skublov, F. Xie, Li Li, and S. Magnier. Two-photon excitations of the cs2 state: Assignment and analysis with the deformed ab initio potential. *Chemical Physics Letters*, 557:66–70, 2013. ISSN 0009-2614. doi: https://doi.org/10.1016/j.cplett.2012.12.030. URL https://www.sciencedirect.com/science/article/pii/S0009261412014510.

[277] A. R. Janzen and R. A. Aziz. An accurate potential energy curve for helium based on ab initio calculations. *The Journal of Chemical Physics*, 107(3):914–919, 1997. doi: 10.1063/1.474444. URL https://doi.org/10.1063/1.474444.

[278] B. Woratschek, W. Sesselmann, J. Küppers, G. Ertl, and H. Haberland. Singlet to triplet conversion of metastable he atoms during deexcitation at a cs-covered surface. *Phys. Rev. Lett.*, 55:611–614, Aug 1985. doi: 10.1103/PhysRevLett.55.611. URL https://link.aps.org/doi/10.1103/PhysRevLett.55.611.

[279] Thomas Ruchti, Berton E. Callicoatt, and Kenneth C. Janda. Charge transfer and fragmentation of liquid helium droplets doped with xenon. *Phys. Chem. Chem. Phys.*, 2:4075–4080, 2000. doi: 10.1039/B002051F. URL http://dx.doi.org/10.1039/B002051F.

[280] Jakob D. Asmussen, Rupert Michiels, Ulrich Bangert, Nicolas Sisourat, Marcel Binz, Lukas Bruder, Miltcho Danailov, Michele Di Fraia, Raimund Feifel, Luca Giannessi, Oksana Plekan, Kevin C. Prince, Richard J. Squibb, Daniel Uhl, Andreas Wituschek, Marco Zangrando, Carlo Callegari, Frank Stienkemeier, and Marcel Mudrich. Time-resolved ultrafast interatomic coulombic decay in superexcited sodium-doped helium nanodroplets. *The Journal of Physical Chemistry Letters*, 13(20):4470–4478, 2022. doi: 10.1021/acs.jpclett.2c00645. URL https://doi.org/10.1021/acs.jpclett.2c00645. PMID: 35561339.

[281] Ghazal Jabbari, Kirill Gokhberg, and Lorenz S. Cederbaum. Competition between interatomic coulombic decay and autoionization of doubly-excited atoms. *Chemical Physics Letters*, 754:137571, 2020. ISSN 0009-2614. doi: https://doi.org/10.1016/j.cplett.2020.137571. URL https://www.sciencedirect.com/science/article/pii/S0009261420304863.